

Tesi di Dottorato di DANIELA POLINO  
Matricola 753430

**POLITECNICO DI MILANO**



**DIPARTIMENTO  
DI  
CHIMICA,  
MATERIALI  
E  
INGEGNERIA CHIMICA  
"Giulio Natta"**

**Dottorato di Ricerca in  
Chimica Industriale e  
Ingegneria Chimica (CII)**

XXV ciclo

**DEVELOPMENT OF  
METHODOLOGIES FOR THE  
ACCURATE ESTIMATION OF  
REACTION RATE COEFFICIENTS**

Coordinatore: prof. Tiziano Faravelli

Tutore: prof. Maurizio Masi

Relatore: prof. Carlo Cavallotti



*Your eyes are windows into your body  
If you open your eyes in wonder and belief, your body fills up with light*



# Acknowledgements

---

I would like to thank all the people that have been with me in the last three years, which have been probably the best three years of my life so far.

First, I am deeply grateful to my advisor Prof. Carlo Cavallotti. To work with you has been a great pleasure and most times a lot of fun. Thank you for your teachings and your guidance; they have affected and shaped my life. You have believed in me and challenged me to go beyond my limits and never settle for less than excellence. Thank you.

I want to thank also Dr. Stephen Klippenstein. Thank you for the opportunity I have been given to work with you. Thank you for your precious help and assistance during my visit at Argonne National Laboratory. Along with Dr. Stephen Klippenstein I want to thank all the scientists in the chemical dynamics group at ANL that I have met: Steve, Larry, Yuri, Joe, Glen, Ron, Al, Rob, Raghu and last, but not least I cannot forget Jim, the funniest officemate I have ever had! Thanks to all of you. It has been a great privilege to meet you.

I want to thank Franco the person that shared with me this adventure from the closest side. Thank you for your patience, for your encouragement, for being there when I needed someone to rely on. I am looking forward to live more of these adventures, as long as we are together.

Special thanks are for my parents and for my brother Davide. You do not know just how important your presence has been these last three years. You are the best family I could ever wish for!

I want to thank the CFA group and the friends and colleagues that have been with me during these three years and made this experience unique: Filippo, Marco, Matteo, Danilo, Tommaso, Stefano, Raffaele, Vangelis, Tushar, Claudio, Ruggiero e Silvia.

I want also to thank the people I have met in Chicago during my visit at Argonne that have assisted me to settle down and enjoy my permanence there. Thank you to my new second mom Lina, Sebastian and Martha, Martin, Christian, Colin, Francesc, Chris, Patrick and Gokhan, Amit and Mike.

Finally, I want to thank the One who put this dream in my heart and made it become true. The One who has been with me every single moment, never letting me go. Thank you Jesus, because in the end I owe it all to you.

Daniela



# Publications and Conferences

---

1. *On the kinetics of the  $C_5H_5 + C_5H_5$  reaction*  
Cavallotti C., **Polino D.**, Proceedings of the Combustion Institute, 2012 in press
2. *Is Quantum Tunneling Relevant in Free Radical Polymerization?*  
Cuccato D., Dossi M., **Polino D.**, Cavallotti C., Moscatelli D. Macromolecular Reaction Engineering , 6, 496 (2012)
3. *Analysis of Some Reaction Pathways Active during Cyclopentadiene Pyrolysis*  
Cavallotti C., **Polino D.**, Frassoldati A., Ranzi E. J. Phys. Chem. A, 116, 3313 (2012)
4. *Toluene and benzyl decomposition mechanisms: elementary reactions and kinetic simulations*  
Derudi M., **Polino D.** and Cavallotti C., Phys Chem Chem Phys , 13, 21308 (2011)
5. *Fulvenallene Decomposition Kinetics*  
**Polino D.** and Cavallotti C., J. Phys. Chem. A, 115, 10281 (2011)
6. *Analysis of the Reactivity on the  $C_7H_6$  Potential Energy Surface*  
**Polino D.**, Famulari A. and Cavallotti C., J. Phys. Chem. A, 115, 7928 (2011)
7. *Theoretical investigation of germane and germylene decomposition kinetics*  
**Polino D.**, Barbato A. and Cavallotti C., Phys. Chem. Chem. Phys., 12, 10622 (2010)
8. *An Ab Initio RRKM/Master Equation Investigation of  $SiH_4$  and  $GeH_4$  Decomposition Kinetics Using a Kinetic Monte Carlo Approach*  
Cavallotti C., **Polino D.** and Barbato B., ECS Transactions 25 (8 PART 1), 445-452 (2009)
9. *On the kinetics of the  $C_5H_5 + C_5H_5$  reaction.* Cavallotti C. and **Polino D.** , 34th International Symposium on Combustion, Warsaw, University of Technology, Poland, July 29 – August 3 2012
10. *An RRKM/ME analysis of the decomposition kinetics active on the  $C_7H_6$  potential energy surface.* **Polino D.**, Derudi M., Cavallotti C., 7th International Conference on Chemical Kinetics, MIT, Cambridge, MA, US, 10-14 July 2011

11. *Predictive theory for the addition kinetics of  $^1\text{CH}_2$  with unsaturated hydrocarbons.* **Polino D.**, Georgievskii Y., Klippenstein S.J. 22nd International Symposium on Gas Kinetics, Boulder, CO, US, 18-22 June 2012
12. *Reactivity of silicon surfaces in presence of adsorbed hydrogen and chlorine.* Cavallotti C. and **Polino D.** 241st National Meeting and Exposition of the American Chemical Society (ACS), Anaheim, CA, US, 27-31 March 2011
13. *An ab initio RRKM/master equation investigation of  $\text{SiH}_4$  and  $\text{GeH}_4$  decomposition kinetics using a kinetic Monte Carlo approach.* Cavallotti C. **Polino D.**, Barbato A. 17th International Chemical Vapor Deposition Symposium 216th Meeting of the Electrochemical Society; Vienna; 4-9 October 2009

# Table of Contents

---

<b>Acknowledgements</b> .....	<b>iii</b>
<b>Publications and Conferences</b> .....	<b>v</b>
<b>Table of Contents</b> .....	<b>vii</b>
<b>List of Figures</b> .....	<b>xi</b>
<b>List of Tables</b> .....	<b>xix</b>
<b>Abstract</b> .....	<b>xxi</b>
<b>1 Introduction</b> .....	<b>1</b>
<b>2 Theoretical Gas Phase Chemical Kinetics: The State of the Art</b> .....	<b>3</b>
2.1. Quantum Mechanics in Theoretical Kinetics .....	3
2.2. Kinetic Theories .....	6
2.2.1. Basic Concepts .....	6
2.2.2. Transition State Theory .....	9
2.2.3. Microscopic Rate Coefficients – The RRKM theory .....	12
2.2.4. The Variable Reaction Coordinate – Transition State Theory .....	16
2.2.5. Solution of the Master Equation.....	16
<b>3 Methods</b> .....	<b>19</b>
3.1. Computational Quantum Chemistry.....	20
3.1.1. The Hamiltonian Operator.....	20
3.1.2. The Born-Oppenheimer Approximation .....	21
3.1.3. Hartree-Fock Theory .....	21
3.1.4. Basis Set Approximation.....	22
3.1.5. Electron Correlation Methods .....	22
3.2. Kinetic Theories .....	28
3.2.1. MCRRKM – Theory and Implementation .....	28
3.3. Overcoming TST Limitations – MCRRKM Development.....	33
3.3.1. Spin Forbidden Reactions .....	33
3.3.2. The 1D Hindered Rotor Approximation .....	36
3.3.3. Multi-well Reactions .....	40
3.3.4. Tunneling Effect.....	42
3.3.5. Bimolecular Reactions .....	53
3.3.6. Variable Reaction Coordinate Transition State Theory – VRC-TST.....	54
<b>4 Germane and Germylene Decomposition Kinetics</b> .....	<b>59</b>
4.1. Introduction .....	59
4.2. Methodology .....	62

4.3.	Results and Discussion.....	64
4.3.1.	<i>Ab initio</i> Calculations and Evaluation of High-pressure Rate Constants .....	64
4.3.2.	GeH <sub>4</sub> and GeH <sub>2</sub> Decomposition Kinetics .....	70
4.4.	Conclusions .....	76
<b>5</b>	<b>Toluene Decomposition: Secondary Chemistry.....</b>	<b>77</b>
5.1.	Introduction .....	77
5.2.	Computational Methodology.....	80
5.2.1.	Electronic Structure Methods.....	80
5.2.2.	Kinetic Theories .....	81
5.3.	Fulvenallene Decomposition.....	82
5.3.1.	Analysis of the Reactivity on the C <sub>7</sub> H <sub>6</sub> Potential Energy Surface.....	82
5.3.2.	Fulvenallene Decomposition Kinetics.....	94
5.4.	Benzyl Decomposition .....	101
5.5.	Kinetic Simulations of Toluene and Benzyl Decomposition .....	105
5.5.1.	Kinetic Model.....	105
5.5.2.	Comparison with Experiments .....	107
5.6.	Concluding Remarks .....	112
<b>6</b>	<b>New Reaction Pathways Active in Cyclopentadiene Pyrolysis.....</b>	<b>115</b>
6.1.	Introduction .....	115
6.2.	Computational Methodology.....	117
6.2.1.	Electronic Structure Calculations.....	117
6.2.2.	RRKM/Master Equation Calculations.....	119
6.2.3.	Kinetic Mechanism and Experimental Data Simulations .....	121
6.3.	Kinetics of the cC <sub>5</sub> H <sub>5</sub> + cC <sub>5</sub> H <sub>6</sub> Reaction .....	121
6.3.1.	Analysis of the Potential Energy Surface .....	122
6.3.2.	Master Equation Integration and Rate Constant Estimation .....	128
6.4.	The Kinetics of the C <sub>5</sub> H <sub>5</sub> + C <sub>5</sub> H <sub>5</sub> Reaction.....	131
6.4.1.	Analysis of the Potential Energy Surface .....	131
6.4.2.	ME/RRKM Simulations .....	135
6.5.	Comparisons between Model Predictions and Experimental Data.....	137
6.5.1.	Pyrolysis in Georgia Flow Reactor.....	138
6.5.2.	Pyrolysis and Oxidation Study in Princeton Flow Reactor .....	139
6.6.	Concluding Remarks .....	141
<b>7</b>	<b>Quantum Tunneling in Hydrogen Transfer Reactions: A Study on the CH<sub>4</sub>+H Reaction. 143</b>	
7.1.	Introduction .....	143
7.2.	Computational Methodology.....	146
7.3.	Sensitivity Analyses .....	147
7.3.1.	Level of <i>Ab initio</i> Theory .....	148
7.3.2.	Level of Approximation for IRC Calculations.....	154
7.4.	Comparison with Experiments and Accurate Theories .....	157
7.5.	Concluding Remarks .....	159

<b>8 Singlet Methylene Addition to Unsaturated Hydrocarbons .....</b>	<b>161</b>
8.1. Introduction .....	161
8.2. Methodology .....	164
8.2.1. Kinetic Theory.....	164
8.2.2. Electronic Structure Methods.....	166
8.3. Results and Discussion.....	168
8.3.1. Tests for $^1\text{CH}_2 + \text{C}_2\text{H}_2$ and $\text{C}_2\text{H}_4$ .....	168
8.3.2. Comparison with Experiment for $^1\text{CH}_2 + \text{pC}_3\text{H}_4$ , $\text{C}_3\text{H}_6$ , $\text{aC}_3\text{H}_4$ , $\text{C}_4\text{H}_6$ , $\text{C}_6\text{H}_6$ .....	175
8.3.3. General observations .....	179
8.4. Conclusion.....	181
<b>9 Conclusions .....</b>	<b>183</b>
<b>References .....</b>	<b>187</b>



# List of Figures

---

<b>Figure 1.</b> Surface mesh plot of the potential energy surface for the collinear $H+H_2$ reaction taken from ref 44. ....	7
<b>Figure 2.</b> Collinear triatomic system.....	7
<b>Figure 3.</b> Representation, in the $(r_{AB}, r_{BC})$ plane of the triatomic system, of the new set of reaction coordinates $(s,u)$ . ....	8
<b>Figure 4.</b> Potential along the reaction coordinate $s$ for a reaction with a barrier $E_0$ .....	8
<b>Figure 5.</b> Potential energy surface for reactions with a) a tight transition state and b) a loose transition state.....	9
<b>Figure 6.</b> Determination of the transition state through the variational approach. ....	11
<b>Figure 7.</b> Schematic illustration of the pressure dependence of thermal rate coefficient. ....	12
<b>Figure 8.</b> Scheme showing collision and reaction events among levels of reactant $A$ with energy $E$ . ....	13
<b>Figure 9.</b> Schematic representation of energy levels of a reactant molecule between 0 and 2000 $cm^{-1}$ , illustrating density of states. ....	15
<b>Figure 10.</b> Representation of a generic reactive PES, taken from ref [60]. ....	17
<b>Figure 11.</b> Illustration of the complete active space (CAS) selection. ....	25
<b>Figure 12.</b> MCRRKM protocol for the simulation of a unimolecular reaction. ....	31
<b>Figure 13.</b> Schematic crossing of a singlet-triplet crossing. ....	33
<b>Figure 14.</b> Schematization of singlet-triplet state crossing with evidence on the transition region. ....	34
<b>Figure 15.</b> Scheme of internal rotations for the 1-octyl radical and the potential energy surface for the rotation around the dihedral angle $\phi_2$ . ....	37
<b>Figure 16.</b> Schematic representation of the axis considered for each $n$ index introduced by East and Radom. ....	38
<b>Figure 17.</b> Scheme of a unimolecular multiple well reaction where reactant $A$ needs to interconvert into complex $B^*$ and $C^*$ , through transition states $TS1$ and $TS2$ , before transforming into the product $D$ . ....	40
<b>Figure 18.</b> Example of Eckart Potential as a function of the reaction coordinate $x$ . In evidence are the forward activation energy $E_1$ and the backward activation energy $E_{-1}$ . ....	43
<b>Figure 19.</b> Plot of the potential energy contours for the $H + H_2 \rightarrow H_2 + H$ using the Porter–Karplus <sup>96</sup> surface taken from ref <sup>88</sup> . Solid line is the reaction path. Dotted line is the $t$ -curve. The	

point $P$ and $P'$ denote the initial and final tunneling points on the $t$ -curve for a particular total energy. The corresponding points on the reaction path are $Q$ and $Q'$ .	45
<b>Figure 20.</b> Potential energy associated to the vibrational motion along $\rho$ .	46
<b>Figure 21.</b> Cartoon of the two ways the hydrogen atom can attack the methyl radical in the $\text{CH}_3 + \text{H}$ reaction.	56
<b>Figure 22.</b> Composite dividing surface for the $\text{CH}_3 + \text{H}$ reaction.	57
<b>Figure 23.</b> Germane and germylene decomposition kinetics were studied with stochastic RRKM/master equation simulations based on <i>ab initio</i> reaction parameters.	59
<b>Figure 24.</b> Transition state structures for the decomposition of (a) $\text{SiH}_4$ and (b) $\text{GeH}_4$ to $\text{SiH}_2$ and $\text{GeH}_2$ determined at the B3LYP/aug-cc-pVTZ level. Distances in Angstrom and angles in degrees.	67
<b>Figure 25.</b> PES of the $\text{GeH}_4$ (a) and $\text{GeH}_2$ (b) dissociation to $\text{GeH}_3$ and $\text{GeH}$ calculated at the CASTP2 level using the cc-pVQZ basis set and corrected with ZPE calculated using vibrational frequencies determined at the same level of theory.	69
<b>Figure 26.</b> Microcanonical RRKM kinetic constants calculated for the reaction of decomposition of $\text{GeH}_4$ to $\text{GeH}_2$ and $\text{GeH}_3$ , reported in $\text{s}^{-1}$ .	70
<b>Figure 27.</b> Comparison between the energy distribution function calculated for the $\text{GeH}_4$ reactive system at 1 bar and 1400 K and the Boltzmann population. The energy thresholds for reaction 1 and 2 are shown to highlight the dramatic decrease of population of the excited states that takes place above the first reaction threshold.	72
<b>Figure 28.</b> Comparison of the calculated decomposition kinetic constants of $\text{GeH}_4$ to $\text{GeH}_2$ and $\text{H}_2$ with the experimental data measured (a) by Votintsev <sup>132</sup> and Smirnov <sup>131</sup> at 1.5 bar in the presence of (1) 1.0% $\text{N}_2\text{O}$ and (2) 3.0% $\text{N}_2\text{O}$ and by Newman <sup>130</sup> at 5.3 bar. In (b) it is reported the comparison with the experimental data reported by Smirnov at 1.5 bar for the decomposition of $\text{GeH}_2$ to $\text{Ge}$ and $\text{H}_2$ .	73
<b>Figure 29.</b> Comparison of the calculated concentrations with experimental data measured after variable reaction times (240-390 $\mu\text{s}$ ) with an initial fraction of $\text{GeH}_4$ of 1.1% (a,c) and 0.5% (b,d) at a pressure of 1.5 bar. Points are experimental data, squares were obtained not considering reaction 5, while triangles were obtained introducing reaction 5 in the kinetic scheme.	74
<b>Figure 30.</b> Calculated kinetic constant for the decomposition of (a) $\text{GeH}_4$ to $\text{GeH}_2$ and $\text{H}_2$ and (b) $\text{GeH}_2$ to $\text{Ge}$ and $\text{H}_2$ reported as the ratio with respect to the high-pressure limit.	75
<b>Figure 31.</b> A kinetic analysis based on <i>ab initio</i> and RRKM/ME calculations shows that toluene decomposition involves fulvenallene and benzyne as intermediates.	77
<b>Figure 32.</b> PES for the dissociation of fulvenallene into the fulvenallenyl radical and hydrogen computed at two different levels of theory and corrected for ZPE.	83

<b>Figure 33.</b> PES for the first mechanism of interconversion of fulvenallene to cycloheptatetraene. Energies were calculated at the CCSD(T)/CBS level for B3LYP/6-31+G(d,p) structures. ....	84
<b>Figure 34.</b> Second and most energetically favored mechanism of interconversion of fulvenallene to cycloheptatetraene and phenylcarbene. ....	85
<b>Figure 35.</b> PES for the second mechanism of interconversion of fulvenallene to cycloheptatetraene. Energies were calculated at the CCSD(T)/CBS level for B3LYP/6-31+G(d,p) structures. ....	86
<b>Figure 36.</b> PES for the mechanism of interconversion of fulvenallene to benzocyclopropene ( <b>11</b> ) and several 6-membered cyclic species susceptible to Diels-Alder decomposition. Energies were calculated at the CCSD(T)/CBS level for B3LYP/6-31+G(d,p) structures. ....	88
<b>Figure 37.</b> PES of a possible mechanism, alternative to pathway 4, of interconversion of fulvenallene to several intermediates susceptible to Diels-Alder decomposition. Energies were calculated at the CCSD(T)/CBS level for B3LYP/6-31+G(d,p) structures. ....	91
<b>Figure 38.</b> Reactivity on the $C_7H_6$ triplet PES. Energies were calculated at the CCSD(T)/CBS level on B3LYP/6-31+G(d,p) structures. ....	92
<b>Figure 39.</b> Summary of the reactions that can take place on the $C_7H_6$ potential energy surface. ....	95
<b>Figure 40.</b> Portion of the $C_7H_6$ PES considered in the simulations. Energies were calculated at the CCSD(T) level using the cc-pVDZ and cc-pVTZ basis sets and extrapolated to the complete basis set limit. ZPE corrections are included and were calculated using vibrational frequencies determined at the B3LYP/6-31+G(d,p) level. ....	96
<b>Figure 41.</b> Overall kinetic constants for $C_7H_6$ decomposition. Simulations were performed: a) accounting for intersystem crossing using Landau Zener theory; b) assuming that intersystem crossing is fast. ....	98
<b>Figure 42.</b> Branching reaction constants for channel 1 and 2 calculated a) accounting for intersystem crossing using Landau Zener theory and b) assuming that intersystem crossing is fast. ....	99
<b>Figure 43.</b> Energy distribution functions of <b>W1</b> and <b>W18</b> calculated at 1 bar and 1700 K and Boltzmann population of <b>W1</b> . ....	99
<b>Figure 44.</b> Product branching ratio as a function of temperature and pressure calculated accounting for intersystem crossing using Landau Zener theory (lowest points) and assuming that intersystem crossing is fast (upper points). ....	100
<b>Figure 45.</b> PES considered for the $C_7H_7$ decomposition simulations. Energies (in kcal/mol) were calculated at the CCSD(T) level using the cc-pVDZ and cc-pVTZ basis sets and extrapolated to the complete basis set limit. ZPE corrections at the B3LYP/6-31+G(d,p) level are included. ....	101

<b>Figure 46.</b> a) Global kinetic constant for benzyl decomposition calculated by integrating the master equation as a function of temperature and pressure. b) Comparison between calculated and literature <sup>153,155,157,179-181,218</sup> kinetic constants for benzyl decomposition. ....	103
<b>Figure 47.</b> Branching ratio of the $C_7H_6+H$ channel over the global decomposition rate of $C_7H_7$ as a function of temperature and pressure. ....	104
<b>Figure 48.</b> Comparison between H-atom experimental data <sup>186</sup> (symbols) and model predictions (dashed lines: without $H_{SO}$ ; solid line: with $H_{SO}$ ); $T = 1573$ K, $P = 0.67$ bar, $[C_6H_5CH_2Br]_0 = 1.585 \times 10^{12}$ molecule/cm <sup>3</sup> . ....	108
<b>Figure 49.</b> Decomposition pathway of the benzyl radical at 1573 K and 0.67 bar calculated for the simulations of the experimental data of <b>Figure 48</b> ; the thickness of the arrows is proportional to the channeled reactive flux. ....	108
<b>Figure 50.</b> Comparison between H-atom yield time profile measured during the pyrolysis of toluene <sup>171</sup> (symbols) and model predictions (dashed lines: without $H_{SO}$ ; solid line: with $H_{SO}$ ) for different conditions: a) $T = 1705$ K, $P = 0.1$ bar, $[C_6H_5CH_3]_0 = 4 \times 10^{-12}$ mol/cm <sup>3</sup> ; b) $T = 1602$ K, $P = 1.6$ bar, $[C_6H_5CH_3]_0 = 1.2 \times 10^{-11}$ mol/cm <sup>3</sup> . ....	109
<b>Figure 51.</b> Comparison between measured H-atom production <sup>152</sup> (symbols) and model predictions (dashed lines: without $H_{SO}$ ; solid line: with $H_{SO}$ ) for various conditions, namely: a) $T = 1465$ K, $P = 7.01$ bar, $[C_6H_5CH_3]_0 = 4.2$ ppm; b) $T = 1545$ K, $P = 1.91$ bar $[C_6H_5CH_3]_0 = 5$ ppm; c) $T = 1555$ K, $P = 1.92$ bar, $[C_6H_5CH_3]_0 = 19.3$ ppm. ....	110
<b>Figure 52.</b> Decomposition pathway of toluene at 1602 K and 1.6 bar (solid lines) calculated for the simulations of the experimental data of <b>Figure 50b</b> ; dashed lines represent the reactions that contribute to the production of H atoms. The thickness of the arrows is proportional to the channeled reactive flux. ....	111
<b>Figure 53.</b> $\beta$ -opening reaction mechanism leads to the formation of major pyrolysis products within the cyclopentadienyl plus cyclopentadiene reaction. ....	115
<b>Figure 54.</b> Potential energy surface of the C5-C7-C6 reaction pathway. Energies [kcal/mol] include ZPE corrections, were computed at the CCSD(T)/cc-pVDZ level, and extrapolated to the CBS limit. ....	123
<b>Figure 55.</b> Potential energy surface of the $\beta$ -opening reaction pathway. Energies include ZPE corrections, were computed at the CCSD(T)/cc-pVDZ level, and extrapolated to the CBS as described in equation 138. Energies [kcal/mol] calculated for key transition states at the ROCBS-QB3 level and used in the master equation calculations are reported between square brackets. .	125
<b>Figure 56.</b> Potential energy surface of two mechanisms that proceed in parallel to the main $\beta$ -opening reaction pathway. The first connects W9 to W10, while the second provides a mechanism for decomposition of W10 alternative to those sketched in <b>Figure 55</b> , which leads to 6-vinyl fulvene	

and the vinyl radical. Energies [kcal/mol] include ZPE corrections, were computed at the CCSD(T)/cc-pVDZ level, and extrapolated to the CBS limit. Energies calculated for key transition states at the ROCBS-QB3 level and used in the master equation calculations are reported between square brackets. .... 127

**Figure 57.** Potential energy surface of a mechanism of formation of phenyl butadiene that is parallel to that of **Figure 55**. Energies [kcal/mol] include ZPE corrections, were computed at the CCSD(T)/cc-pVDZ level, and extrapolated to the CBS limit. Energies calculated for key transition states at the ROCBS-QB3 level and used in the master equation calculations are reported between square brackets. .... 128

**Figure 58.** Kinetic constants [ $\text{cm}^3 \text{mol}^{-1} \text{s}^{-1}$ ] calculated at 1 bar for the reaction between  $\text{cC}_3\text{H}_5$  and  $\text{cC}_5\text{H}_6$  for the different reaction channels. The kinetic constant for the reaction of decomposition to reactants is not reported as it is almost superimposed to the global kinetic constant, which is equal to the rate for the addition of  $\text{cC}_3\text{H}_5$  to  $\text{cC}_5\text{H}_6$  to give W1. .... 129

**Figure 59.** Potential energy surface of the *n*-H-fulvalenyl mechanism. Energies, expressed in kcal/mol, were computed at the CBS-QB3 level. .... 131

**Figure 60.** Potential energy surface of the *n*-H-azulyl mechanism. Energies, expressed in kcal/mol, were computed at the CBS-QB3 level. .... 134

**Figure 61.** Kinetic constants [ $\text{cm}^3 \text{mol}^{-1} \text{s}^{-1}$ ] calculated at 1 bar for the reaction between  $\text{cC}_3\text{H}_5$  and  $\text{cC}_5\text{H}_5$ . The kinetic constant for the decomposition to reactants is not reported as it is almost superimposed to the global kinetic constant, which is equal to the high-pressure rate of the entrance channel. .... 136

**Figure 62.** Cyclopentadiene conversion and yields of major aromatic products versus reactor temperature.<sup>250</sup> .... 138

**Figure 63.** Concentration profiles of major species for the pyrolysis (lines and filled symbols) and oxidation at  $\Phi \sim 1$  (dashed lines and empty symbols) of cyclopentadiene.<sup>249,273</sup> (Experimental runs #7 and #12. Initial temperature=1190-1200 K, initial fuel= $\sim 2000$  ppmv.) .... 139

**Figure 64.** Concentration profiles of major species for the pyrolysis (lines and filled symbols) and oxidation at  $\Phi \sim 1$  (dashed lines and empty symbols) of cyclopentadiene.<sup>249,273</sup> (Experimental runs #3 (a) and #10 (b). Initial temperature =  $\sim 1150$  K, initial fuel =  $\sim 3000$  ppmv.) .... 140

**Figure 65.** Major reaction paths of cyclopentadiene pyrolysis at 1200 K and 50% conversion. Conditions of experimental run #12.<sup>249</sup> .... 141

**Figure 66.** Experimental literature rate coefficients for the  $\text{CH}_4 + \text{H}$  reaction. .... 145

**Figure 67.** The potential energy along the MEP ( $V_{\text{MEP}}(s)$ ) as function of the reaction coordinate  $s$  calculated at different levels of theory. .... 150

<b>Figure 68.</b> Plot of the reaction path curvature and effective reduced mass as functions of the reaction coordinate $s$ .....	153
<b>Figure 69.</b> Plots of the two lowest generalized vibrational frequencies ( $\omega_{10}$ and $\omega_{11}$ ) as function of the reaction coordinate $s$ corresponding to the bending motions of the H atom as illustrated on the right. ....	153
<b>Figure 70.</b> Plots of the effective reduced mass calculated with different step sizes as a function of the reaction coordinate expressed in mass weighted coordinates. ....	155
<b>Figure 71.</b> Plots of the effective reduced mass calculated from LQA and HPC based IRC calculations. ....	157
<b>Figure 72.</b> Experimental literature rate coefficient compared with our predicted rate. ....	158
<b>Figure 73.</b> Plots of the theoretical literature rate coefficients compared with our predicted rate and the experimental data of Sutherland et al.....	158
<b>Figure 74.</b> Pivot points number and locations used for each fragment a) methylene, b) acetylene, c) ethylene, d) propyne, e) propene, f) allene, g) butadiene, h) benzene. Distances are in bohr. ....	165
<b>Figure 75.</b> One-dimensional potential energy surface for $^1\text{CH}_2 + \text{C}_2\text{H}_2$ with CASPT2/cc-pVDZ (blue dotted), CAS+I+2+QC/cc-pVDZ (red dashed) and CCSD(T)/cc-pVDZ (green solid) calculations. ....	169
<b>Figure 76.</b> Potential energy surface for $^1\text{CH}_2 + \text{C}_2\text{H}_2$ with CASPT2/cc-pVDZ calculations using either a (2e2o) active space (blue dotted) or a (6e6o) active space (red solid). ....	169
<b>Figure 77.</b> Potential energy surface for $^1\text{CH}_2 + \text{C}_2\text{H}_2$ with CASPT2(2e,2o) calculations employing a cc-pVDZ (blue dotted), cc-pVTZ (red dashed) or cc-pVQZ (green solid) basis set. .	170
<b>Figure 78.</b> Comparison of the VRC-TST calculated rate coefficients for (a) $^1\text{CH}_2 + \text{C}_2\text{H}_2$ and (b) $^1\text{CH}_2 + \text{C}_2\text{H}_4$ reactions using CASPT2/cc-pVDZ (green solid), CASPT2/cc-pVDZ+Corr (red fine-dashed), CASPT2/cc-pVTZ (black dashed) and CASPT2/cc-pVTZ+Corr (blue dotted) interaction energies. ....	171
<b>Figure 79.</b> VRC-TST rate predictions for $^1\text{CH}_2 + \text{C}_2\text{H}_2$ with CASPT2(2e2o)/cc-pVDZ (black fine-dashed) and CCSD(T)/cc-pVDZ energies (red solid) including the potential correction.....	171
<b>Figure 80.</b> VRC-TST rate predictions for $^1\text{CH}_2 + \text{C}_2\text{H}_2$ with (a) CASPT2/cc-pVDZ and (b) CASPT2/cc-pVTZ direct sampling including only the relaxation correction (black dotted), only the method correction (red dashed), both relaxation and method corrections (blue fine-dashed) and no correction (green solid). Correction ratio evaluated for (c) CASPT2/cc-pVDZ and (d) CASPT2/cc-pVTZ direct sampling based VRC-TST rate coefficients. ....	172
<b>Figure 81.</b> Energy correction ratio for the $^1\text{CH}_2 + \text{C}_2\text{H}_2$ reaction accounting for the method correction at the cc-pVTZ level (blue dashed) and cc-pVDZ level (light blue dotted) and for the	

<i>relaxation correction at the cc-pVTZ level (dark red solid) and at the cc-pVDZ level (red fine-dashed).</i> .....	173
<b>Figure 82.</b> <i>VRC-TST high-pressure limit rate coefficient for the <math>^1\text{CH}_2 + \text{C}_2\text{H}_2</math> reaction (solid red line) with 10% confidence limit compared with experimental measurements (symbols) and other theoretical predictions (lines).</i> .....	174
<b>Figure 83.</b> <i>VRC-TST high-pressure limit rate coefficient for the <math>^1\text{CH}_2 + \text{C}_2\text{H}_4</math> reaction (solid red line) with 10% confidence limit compared with experimental measurements (symbols).</i> .....	175
<b>Figure 84.</b> <i>VRC-TST high-pressure limit rate coefficient (solid red line) for (a) <math>^1\text{CH}_2 + \text{pC}_3\text{H}_4</math> and (b) <math>^1\text{CH}_2 + \text{C}_3\text{H}_6</math> with 10% confidence limit compared with experimental measurements (symbols).</i> .....	177
<b>Figure 85.</b> <i>VRC-TST high-pressure limit rate coefficient (solid red line) for (a) <math>^1\text{CH}_2 + \text{aC}_3\text{H}_4</math> and (b) <math>^1\text{CH}_2 + \text{C}_4\text{H}_6</math> with 10% confidence limit compared with experimental measurements (symbols).</i> .....	177
<b>Figure 86.</b> <i>Potential energy surface for the <math>^1\text{CH}_2 + \text{C}_6\text{H}_6</math> reaction evaluated at the CASPT2/cc-pVDZ level (blue fine dashed) and CCSD(T)/CBS level (red dashed) keeping the geometries of the approaching fragments fixed, and at the CASPT2/cc-pVDZ level (green solid) allowing the relaxation of the internal degrees of freedom of the two reactants.</i> .....	178
<b>Figure 87.</b> <i>VRC-TST predicted high-pressure limit rate coefficient (solid red line) for <math>^1\text{CH}_2 + \text{C}_6\text{H}_6</math> with 10% limit confidence compared with experimental measurements (symbols).</i> .....	179
<b>Figure 88.</b> <i>Temperature dependent VRC-TST high-pressure limit rate coefficients for all the <math>^1\text{CH}_2 + \text{R}</math> reactions considered in this work.</i> .....	179



# List of Tables

---

<b>Table 1.</b> Energetic, structural and reaction parameters adopted to determine the high-pressure rate constant of reaction 2. H1 and H2 are the reacting hydrogen atoms. Energies are reported in Hartrees, vibrational frequencies in $\text{cm}^{-1}$ , and rotational constants in GHz. Activation energies are corrected with ZPE. Geometry parameters are evaluated at B3LYP/aug-cc-pVTZ. In parenthesis are displayed geometry parameters evaluated at CASPT2/aug-cc-pVTZ and the energies calculated with these parameters. ....	65
<b>Table 2.</b> Activation energies and 0 K enthalpy changes for the decomposition of $\text{GeH}_4$ to $\text{GeH}_2$ and $\text{H}_2$ . Theoretical data corrected with ZPE. Energies expressed in kJ/mol. ....	66
<b>Table 3.</b> High-pressure kinetic constants of the considered reactive events interpolated between 300 and 2200 K to the modified Arrhenius expression ( $k = AT^n \exp(-E_a/RT(K))$ ). Activation energies and reaction enthalpies are reported in kJ/mol. The bimolecular kinetic constant has dimensions of $\text{cm}^3/\text{mol}\cdot\text{s}$ . ....	69
<b>Table 4.</b> Fit of the $\text{GeH}_4$ and $\text{GeH}_2$ kinetic parameters to the Troe formalism: high-pressure ( $\text{s}^{-1}$ ), low pressure ( $\text{cm}^3 \text{mol}^{-1} \text{s}^{-1}$ ) and FC parameters for the broadening factor ( $T^{**}$ was set to 0 in the regression). Activation energies in kJ/mol. ....	76
<b>Table 5.</b> High-pressure upper limits to the kinetic constants for fulvenallene decomposition. ..	94
<b>Table 6.</b> Kinetic constants for the two fulvenallene reaction channels calculated considering explicitly intersystem crossing ( $p_{\text{hop}} = \mathcal{A}(P_{LZ})$ ) and under the assumption that it is fast ( $p_{\text{hop}} = 1$ ). Kinetic constants expressed as $k = A \times T(K)^\alpha \times \exp(-E_a(\text{kcal/mol})/RT)$ in $\text{s}^{-1}$ . ....	101
<b>Table 7.</b> Kinetic constants for benzyl decomposition reactions interpolated between 1500 and 2000 K as $k = AT^\alpha \exp(-E_a(\text{kcal/mol})/RT)$ in $\text{s}^{-1}$ . ....	104
<b>Table 8.</b> Atmospheric pressure reaction mechanism for toluene pyrolysis and benzyl decomposition <sup>a</sup> .....	106
<b>Table 9.</b> Thermochemical data used for the kinetic simulations. ....	107
<b>Table 10.</b> Kinetic constants for the reaction between $c\text{C}_5\text{H}_5$ and $c\text{C}_5\text{H}_6$ interpolated between 900 and 2000 K as $k = AT^\alpha \exp(-E_a(\text{cal/mol})/RT)$ in $\text{cm}^3 \text{mol}^{-1} \text{s}^{-1}$ . ....	130
<b>Table 11.</b> High-pressure kinetic constants of the overall reacting system investigated interpolated between 1000 and 2000 K as $k = A T^\alpha \exp(-E_a(\text{kcal/mol})/RT)$ in $\text{s}^{-1}$ for unimolecular reactions and $\text{cm}^3 \text{mol}^{-1} \text{s}^{-1}$ for bimolecular reactions. ....	136
<b>Table 12.</b> Kinetic constants for the reaction between $c\text{C}_5\text{H}_5$ and $c\text{C}_5\text{H}_5$ interpolated between 1100 and 2000 K as $k = AT^\alpha \exp(-E_a(\text{cal/mol})/RT)$ in $\text{cm}^3 \text{mol}^{-1} \text{s}^{-1}$ . ....	137

<b>Table 13.</b> Activation energies (kcal/mol) without ZPE correction of the CH <sub>4</sub> + H reaction calculated with different electronic structure methods adopting the 6-311+G(2d,2p) basis set. ..	148
<b>Table 14.</b> CVT/SCT rate coefficients for the CH <sub>4</sub> + H reaction calculated using different electronic structure methods and adopting the 6-311+G(2d,2p) basis set compared with the suggested value of Sutherland et al. <sup>280</sup> .....	148
<b>Table 15.</b> CVT/SCT rate coefficients for the CH <sub>4</sub> + H reaction calculated using different electronic structure methods adopting the 6-311+G(2d,2p) basis set for structures, vibrational frequencies and ZPE. The CCSD(T)/CBS activation energy was adopted for all cases. Results are compared with the suggested values of Sutherland et al. <sup>280</sup> .....	149
<b>Table 16.</b> SCT tunneling corrections evaluated using different electronic structure methods adopting the 6-311+G(2d, 2p) for the CH <sub>4</sub> + H reaction. ....	150
<b>Table 17.</b> CVT/SCT rate coefficients for the CH <sub>4</sub> + H reaction calculated using different electronic structure method adopting the 6-311+G(2d,2p) basis set for structures, vibrational frequencies and ZPE. The CCSD(T)/CBS activation energy and the CCSD(T)/aug-cc-pVTZ//WB97XD/6-311+G(2d,2p) MEP were adopted for all cases. The results are compared with the suggested values of Sutherland et al. <sup>280</sup> .....	151
<b>Table 18.</b> Ratio of CVT/SCT rate constants over the reference value calculated for the CH <sub>4</sub> + H reaction using different electronic structure methods and adopting the 6-311+G(2d,2p) (BS1) and the aug-cc-pVTZ (BS2) basis sets for structures, vibrational frequencies and ZPE. The CCSD(T)/CBS activation energy and the CCSD(T)/aug-cc-pVTZ//WB97XD/6-311+G(2d,2p) MEP were adopted for all cases. ....	152
<b>Table 19.</b> SCT tunneling correction and ratio of CVT/SCT rate constants over the reference value <sup>280</sup> ( $k_{ref}$ ) calculated for the CH <sub>4</sub> + H reaction using the M062X method and adopting the 6-311+G(2d,2p) basis set without (case 1) and with the ultrafine grid (case 2). ....	154
<b>Table 20.</b> SCT tunneling corrections evaluated adopting different step sizes for the calculation of the MEP. ....	155
<b>Table 21.</b> SCT tunneling corrections evaluated adopting different reaction coordinate intervals for the calculation of the MEP and adopting a step size of 0.01 bohr. ....	156
<b>Table 22.</b> SCT tunneling corrections evaluated adopting LQA and HPC based IRC solutions. ....	157
<b>Table 23.</b> Contributions of physical deactivation to the removal of <sup>1</sup> CH <sub>2</sub> by the reactants considered in this study. ....	176
<b>Table 24.</b> Direct addition bond strengths for <sup>1</sup> CH <sub>2</sub> + unsaturated hydrocarbons. ....	181

# Abstract

---

This PhD thesis has been focused on the theoretical and computational modeling of gas phase chemical reactions and specifically on the accurate estimation of reaction rate coefficients. The ability to determine accurately the rate coefficients of key elementary reactions has become in fact gradually more important over the past years. In this field, transition state theory (TST) coupled with *ab initio* electronic structure methods has been a powerful tool to calculate the rate coefficient of gas phase elementary reactions due to the simplicity and efficiency by which it is characterized. However, TST is characterized by several limitations and this reduces the accuracy and reliability of its predictions. Moreover, also the precision of the electronic structure calculations play a relevant role on the accuracy of the predicted rate coefficient. Taking into account these factors, TST calculations proved to give rate coefficients that in general have an uncertainty factor of 3.

In this scenario, the goal of the present work has been to address the major limitations of transition state theory and to develop and implement ad hoc methodologies in order to overcome these issues, with the intent of reducing the uncertainty from a factor of 3 down to less than a factor of 2. Specifically, we concentrated on the solutions of the following topics: spin forbidden reactions, hindered rotors, multi-well and multi-channel potential energy surfaces, tunneling corrections and a microcanonical description of bimolecular reactions.

The methods adopted for each one of these issues have been validated against literature data and tested on chemical reactions of interest. The rate coefficients thus predicted were compared when possible with experimental rates. Otherwise, they were introduced in detailed kinetic schemes in order to reproduce experimental concentration profiles of the species of interest evolving in complex systems, such as toluene or cyclopentadiene pyrolysis. The results obtained allowed us to improve our understanding on the kinetic aspects of a number of reactions of scientific interest.



# 1 Introduction

---

Gas phase reactions play a major role in many reacting systems. Among them, combustion processes, atmospheric chemistry and polymerization technologies are just a few examples. From a chemical engineering point of view, it can be of fundamental importance to know the consumption or production rate of key species in the reacting system under study. This information can be used to design new chemical reactors, engines or burners in order to obtain the best performances at the minimum cost. In addition, they can help reduce the production of dangerous or undesired byproducts. For example, for what concerns combustion processes, many studies are centered nowadays on the formation and growth of polycyclic aromatic hydrocarbons, as they are the source of the formation of soot that has been proved to cause a long series of diseases. In addition, the knowledge of the kinetic aspects of a chemical process can be helpful during its optimization, which gives engineers the opportunity to find the operative conditions that grant better yields or degree of purity in the desired products.

It is important to remark that the information on the chemical kinetics of the reactions needed by the process engineers consists in global rates of production or consumption, yet the collection of these data depends in the end on the rate coefficients of the elementary reactions that actually take place within the reacting system under investigation.

In this scenario, the ability to determine accurately the rate coefficients of elementary key reactions has become progressively more important. A very powerful tool that has assisted the scientists in the past decades in calculating the rate coefficient of gas phase elementary reactions is transition state theory (TST). This theory has been deemed successful for the simplicity and efficiency by which is characterized. Unlike other theoretical approaches that were time-consuming and dedicated only to very small systems, this theory could be applied also to systems with more than three or four atoms and it has been widely adopted since quantum chemistry software packages have become more accessible. Such packages offer, in fact, the possibility to calculate with relative ease those parameters necessary to apply the theory, such as the equilibrium geometrical structures and the corresponding energies of the molecules of interest.

Nevertheless, the theoretical estimation of a rate coefficient is not univocally and straightforwardly resolved for all kind of gas phase reactions. In particular, its accuracy depends on two fundamental factors: the accuracy of the electronic structure calculations and the level of the kinetic theory that depends on the assumptions made.

The level of accuracy of the electronic structures calculation can be decisive in determining the precision of the final rate coefficient. The level of improvement of such *ab initio* methods, both in

the methodology and computer technology, has been dramatic over the last years and this allows for the computation of energies and structural properties with increasing speed and accuracy. Even so, it is important to choose the appropriate method for each reaction investigated between the several available.

From the point of view of kinetic theory, classical TST provides reasonably accurate rate coefficients. Unfortunately, we can find a number of additional complications for which conventional transition state theory proves to be insufficient. Thus, during recent years much work has been dedicated to its improvement and generalization leading to the formulation of several theories which hold in common all or a part of the assumptions that lay under the transition state theory.

In this framework, the purpose of the present work, that is the accurate prediction of the rate coefficient of elementary gas phase reactions, has been approached with the following strategy: (1) the identification of those situations that go beyond the TST assumptions; (2) the search in the literature of new methods and theories that have been proposed to overcome these issues; (3) the implementation of such methods and theories that permit to build an efficient protocol in calculating an accurate rate coefficient; (4) the validation of the predicted rate coefficient for a number of test cases against the available experimental data.

The dissertation will thus be organized as follow. First, a brief exposition of the state of the art of electronic structure methods and kinetic theories will be reported with the intention to illustrate the scenario in which the present research project has been developed. This will be followed by Chapter 3 that will focus on the methods and theories adopted specifically in this work thesis and will provide the details of their implementation. Successively a series of reaction case studies will be presented. In particular the results obtained will be reported for:

- Chapter 4: Germane and Germylene decomposition kinetics
- Chapter 5: Toluene decomposition secondary chemistry
- Chapter 6: New reaction pathways active in cyclopentadiene pyrolysis
- Chapter 7: Quantum tunneling in hydrogen transfer reactions
- Chapter 8: Singlet methylene addition to unsaturated hydrocarbons

For each of these case studies a new feature will be analyzed and implemented, thus offering the possibility to validate and discuss the properness and accuracy of the methodologies adopted.

Finally, a concluding chapter will review the significant goals achieved within this research project and provide some perspectives on future improvements of the methods developed here.

# 2 Theoretical Gas Phase Chemical Kinetics: The State of the Art

---

The central theme of this thesis focuses on the theoretical estimation of gas phase reaction rate coefficients. In this chapter will follow a thorough description of the state of the art for the current methods and theories that have been developed in the past decades to evaluate accurate rate coefficients and which are the issues that are up to date still challenging kinetic scientists.

## 2.1. Quantum Mechanics in Theoretical Kinetics

Accurate rate coefficient estimations cannot be obtained without a proper knowledge of the potential energy surface on which the reaction takes place. Hence, we must have a good understanding of the quantum mechanical methods commonly adopted to obtain the needed information. The aim of the following section is to enclose this vast subject within the boundaries of kinetic applications with some insight on when a particular method is expected to be reliable and when it can fail.

The application of the kinetic theories foresees the knowledge of the properties of the molecules (reactants, products and transition states) involved in the reaction under investigation. In particular, fundamental information are:

- The geometrical arrangement of the nuclei that corresponds to a stable configuration of the molecule.
- The vibrational frequencies corresponding to the stable configuration.
- The relative energies between different stable configurations (e.g. reaction energy).

Theoretical chemistry offers the possibility to calculate these properties *ab initio* through the direct solution of the electronic Schrödinger equation. This equation gives as a result the electronic energy of the molecule for a particular configuration of the nuclei (single point energy). To determine the properties of interest, however, it is necessary to have information also about the energy gradient and hessian.

The energy gradient, for example, indicates the strength and the direction by which the electronic energy acts on the nuclei. This information is essential to finding a stable configuration of a molecule, because starting from a guess structure it will lead the nuclei towards their equilibrium position. Furthermore, to carry out a vibrational analysis and get the vibrational frequencies of the mol-

ecule it is necessary to know the hessian, which is the second derivative matrix of the electronic energy.

These and other features are nowadays commonly implemented in several software packages, such as Gaussian<sup>1,2</sup>, Molpro<sup>3,4</sup>, and Gamess<sup>5,6</sup>. These program suites offer the possibility to choose among many methods developed over the years to solve the Schrödinger equation. Thus, it is important to know which one of those available is the most effective in the treatment of the problem at hand and what is the range of uncertainty that can be expected.

A brief overview and a first classification of the quantum mechanical methods available follows in the next paragraph. The aim is to illustrate the scenario in which the present thesis has been developed and help understand the reasons behind the choices made throughout the work.

### **Schrödinger Equation**

The electronic energy of a molecule can be obtained solving the time independent Schrödinger equation for the electrons here expressed in a simplified notion as:

$$(\mathbf{T}_e + \mathbf{H}_{e-e} + \mathbf{H}_{n-e})\Psi_e = \mathbf{E}_e\Psi_e \quad (1)$$

where  $E_e$  is the electron energy,  $T_e$  is the electron kinetic energy,  $H_{n-e}$  is the nuclei-electron interaction potential,  $H_{e-e}$  is the electron-electron interaction potential and  $\Psi_e$  is the electron wave function. In this formula the contribution given by the electron-electron interaction energy is the most difficult to determine.

### **Electronic Correlation Energy**

The Hartree-Fock (HF) method is the basic method for solving the Schrödinger equation. However, it generates solutions where the electron-electron interaction is replaced by an average interaction and, as such, these solutions are able to cover up to 99% of the total energy (using an adequately large basis set). Unfortunately, though, the last 1% is significant for a correct description of molecular chemical properties. The difference between the energy obtained through a HF calculation and the energy obtained including explicitly the electron-electron interaction is called electronic correlation (EC) energy.

Over the years, many methods have been developed in order to calculate the electron correlation energy, usually called Post Hartree-Fock methods. Among them, it is important to distinguish between two classes as they can deal with different chemical phenomena: (1) single reference methods and (2) multi-reference methods.

The development of multi-reference methods comes from the necessity to overcome an issue that arises in the treatment of bond dissociation reactions called “spin contamination”. For a more detailed description of the phenomenon refer to chapter 4 of Jensen’s book “Introduction to Computational Chemistry”<sup>7</sup>. Here, suffice it to say that this problem may severely distort the shape of

the potential energy. Multi-reference methods, however, which include also the excitation contribution to the computation of the wave function, do not suffer from “spin contamination” due to the possibility of have molecular orbitals that correspond to different electronic configurations. Methods such as CASPT2<sup>8-11</sup>, with an adequate basis set, have been proved accurate enough in the treatment of radical-radical recombinations<sup>12-14</sup>. Unfortunately, these methods are less straightforward in their application and it is necessary to know which orbitals may be affected by a change of energy as the reaction takes place.

When the wave function does not show multireference effects, single reference methods can be applied with confidence. In particular, among the several available, CCSD(T)<sup>15</sup> has proven to be the most reliable, with energy deviation of ~1 kcal/mol if large enough basis set is employed.

The major problem of the Post Hartree-Fock methods is the high computational effort required for the treatment of molecular systems with more than 10 heavy atoms. For these systems, it is necessary to move to another class of methods that will be the subject of the next paragraph.

### **Density Functional Theory – DFT methods**

The basis for density functional theory is the Hohenberg and Kohn theorem<sup>16</sup> stating that the electronic energy is determined completely by the electron density. This approach introduces a significant simplification in the treatment of a many-body problem, because the number of the degrees of freedom is reduced from  $3N$  (with  $N$  the number of electrons) to 3. This is because electron density is a scalar function only of the space coordinates. Therefore, if the complexity of a wave function increases with the number of electrons, the electron density has the same number of variables, independently of the system size. The only problem associated with the theory is that it is not known what functional creates a one-to-one correspondence between electron density and end electron energy. Thus, the purpose of DFT methods is to design functionals able to approximately create this connection.

Among the most utilized density functional is the B3LYP<sup>17,18</sup> functional. This method has been extensively adopted to produce geometries and vibrational frequencies of molecular structures. In particular, in combustion science it has been very useful in surveying complex potential energy surfaces. However, one problem with DFT methods is the neglect of dispersion interactions. This makes DFT results much less accurate (~3 kcal/mol), especially in the case of large polyatomic systems. In order to rectify this problem, new DFT functionals have been recently proposed, such as the M05-2X and M06-2X of Zhao and Truhlar<sup>19</sup>, and first results indicate that the discrepancy with higher level methods has been reduced.

## Extrapolation Procedures

As we have already mentioned, DFT methods offer energy values with an accuracy level of the order of  $\sim 3$  kcal/mol, while high level post Hartree-Fock methods are computationally demanding. These findings have pressed the development of several approximate procedures. These procedures foresee the combination of different levels of theory with the goal of producing energy differences accurate to about 1 kcal/mol. Among these procedures, it is worth mentioning the G1-G4 series<sup>20-26</sup> and the CBS series<sup>27-33</sup> of Petersson and coworkers.

In addition, lately two different research groups have been focused on the development of new procedures able to reach an accuracy of about 0.1 kcal/mol. These procedures are known as the W1-W4 methods series proposed by Martin's group<sup>34-39</sup> and the HEAT protocol formulated by Stanton and coworkers<sup>40-42</sup>. Their high level of accuracy is reached through the adoption of CCSD(T) for the geometry optimization and the successive inclusion of very high level energy corrections and basis set extrapolations. At the moment, though, these methods can be applied only to small molecules, although some recent work has attempted to extend the applicability ranges to larger molecules. For example, Martin's group was able to compute heat of formation of polycyclic aromatic compounds with up to four rings with a mean deviation of 0.2 kcal/mol<sup>39</sup>.

In conclusion, we can observe that there is a joint effort in producing increasingly accurate energy results and this follows the general tendency present within the scientific community to reach higher levels of understanding of the chemical phenomena that rule the behavior of many systems of scientific interest.

## 2.2. Kinetic Theories

In the following section the kinetic theories available in the literature will be listed and discussed in order to provide the state of the art in which is collocated the present work. Moreover, the advantages and limitations of each theory will be presented with the intention of revealing the perspective that encouraged this study. A detailed description of the kinetic theories encountered is beyond the scope of this introduction, thus to the interested reader the book "Theory of unimolecular and recombination reaction" of Gilbert and Smith<sup>43</sup> is suggested as an exhaustive reference on the subject.

### 2.2.1. Basic Concepts

It can be helpful at this point to first introduce some basic aspects that lay at the foundation of the methods and theories exploited here.

## Potential Energy Surfaces

One of the fundamental concepts on which chemical dynamics is based is the Born-Oppenheimer approximation for which the atoms within the molecules move according to forces derived from a potential field that is determined by the electronic energy. Theoretically, the electronic energy can be mapped out as a function of the nuclear positions solving the Schrödinger equation for a number of different nuclear configurations. The plot of the electronic potential as a function of the nuclear coordinates is referred to as a “potential energy surface” (PES). For example, **Figure 1** illustrates the PES for a collinear reaction. In this simple case, the potential depends only on two nuclear coordinates producing a three-dimensional plot.

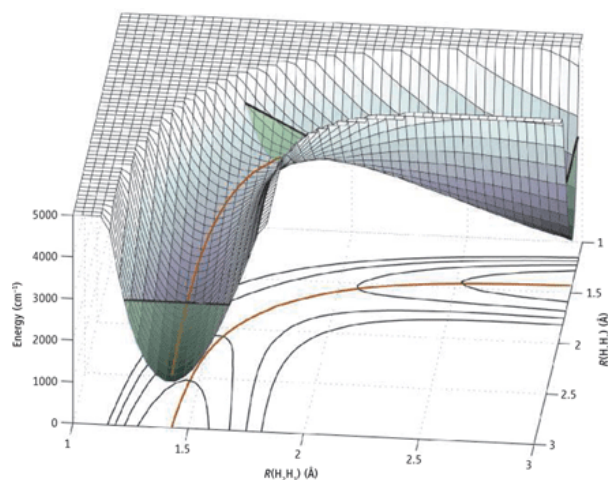


**Figure 1.** Surface mesh plot of the potential energy surface for the collinear  $H+H_2$  reaction taken from ref 44.

## The Reaction Coordinate

The reaction coordinate, usually denoted as  $s$ , is a curvilinear coordinate that links the reactant region of the potential energy surface to the product region as depicted in **Figure 3**, where for simplicity we again consider a collinear reaction as described in the scheme of **Figure 2**.



**Figure 2.** Collinear triatomic system

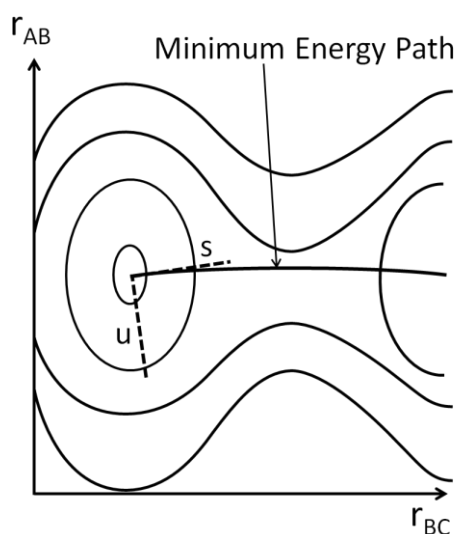


**Figure 3.** Representation, in the  $(r_{AB}, r_{BC})$  plane of the triatomic system, of the new set of reaction coordinates  $(s, u)$ .

From **Figure 3** we can deduce that the reaction coordinates  $(r_{AB}, r_{BC})$  are correlated to the set of new coordinates  $(s, u)$ . The reaction coordinate  $s$  is defined as the coordinate that follows the minimum energy path (MEP). Slicing the PES along this direction we obtain the familiar “reaction profile” illustrated in **Figure 4**.

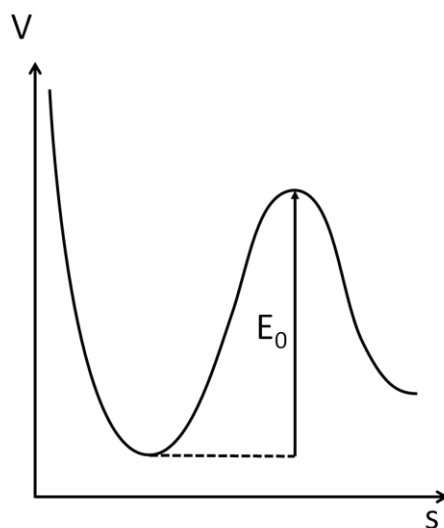


**Figure 4.** Potential along the reaction coordinate  $s$  for a reaction with a barrier  $E_0$ .

## Reaction Classification

A first approach to classifying gas phase reactions is realized by dividing them into unimolecular and bimolecular. Unimolecular reactions proceed through the chemical transformation of one molecule into another one or more different species. The various unimolecular reactions can be distinguished as dissociations, eliminations or isomerizations. Bimolecular reactions, on the other hand,

take place when two molecules collide and generate different species. In the specific case of addition or insertions we have one new molecule and two new molecules for substitutions or abstractions.

Another way to classify chemical reactions is based on the shape of the potential energy surface that connects the reactants to the products. First, the energy surface can show a maximum that clearly divides the reactants from the products as shown in **Figure 5a**. In this case, we have a “simple barrier reaction” or a reaction that passes through a “tight” transition state.

On the other hand, the energy surface can also smoothly change from reactants to products with no evident maximum (**Figure 5b**). In this second case we have a “reaction without an intrinsic potential barrier” or more simply a “loose” transition state.

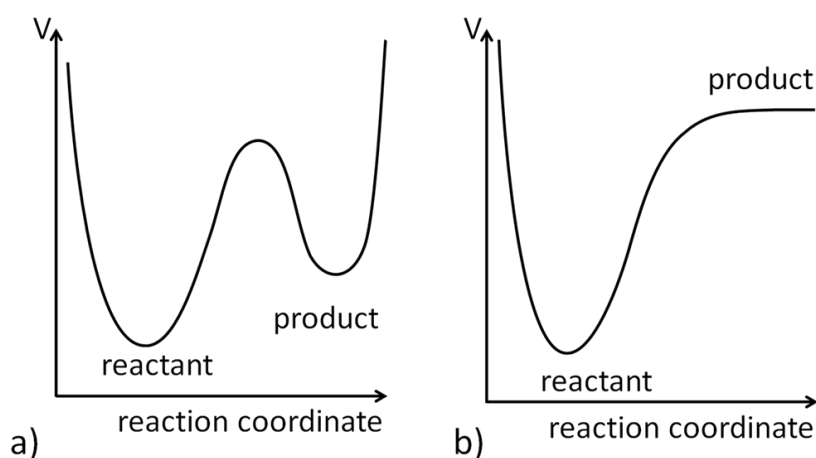


**Figure 5.** Potential energy surface for reactions with a) a tight transition state and b) a loose transition state.

With the basis of these fundamental concepts, we can now pass to the description of the kinetic theories that represent the foundations on which the current research project was build.

### 2.2.2. Transition State Theory

Transition-state theory (TST) provides a simple and useful way to understand and estimate the rates of chemical reactions. The theory as it was first proposed in 1935 by Eyring<sup>45</sup> and Evans and Polanyi<sup>46</sup> relies on the concept that there exists a transition state or “activated complex” that separates the reactants from the products. In other words, in order to convert into the products, the reactants need to reach a particular molecular configuration that corresponds to a saddle point on the potential energy surface. In fact, this configuration is characterized by a maximum along the reaction coordinate, but it is a minimum along all the other motions orthogonal to it, as we move along the minimum energy path.

In deriving the TST rate expression it is necessary to first introduce some basic assumptions. The first assumption, described in Wigner’s<sup>47</sup> words, is that “the comparatively slow motion of the

nuclei is followed by the rapid motion of the electrons to such an extent that they are, for every position of the nuclei, in the lowest quantum state". This explanation encloses two features. The first aspect is the possibility to separate the description of the motion of the nuclei from the motion of the electrons. The second one directly related to the first is the "adiabatic" aspect; in other words the theory assumes that the reacting molecule or molecules are always in the same lowest quantum state.

The second assumption comes as a result of the first. Given the possibility to separate the motion of the nuclei with respect to electrons, it can be deemed acceptable to describe it by classical mechanics. In particular, the nuclei will move under the action of the potential generated by the electronic energy of the reacting molecule in the lowest quantum state.

The third assumption says, "We can find a critical surface so that every trajectory passing through this surface started in the reactant valley and that these reactive trajectories do not re-cross the surface".

From this point on the theory can be derived and described following two different approaches. In the customary way, one would postulate a fourth quasi-equilibrium assumption between the transition state and the reactants. However, in 1938 Wigner<sup>47</sup> was able to derive the same theory adopting a dynamical approach that permitted to achieve the same result without the last assumption. This approach is the preferred one among the chemical kinetics community as (1) it gave the possibility to correlate the statistical TST theory and the already known dynamic theories and (2) successively turned out to be helpful in the generalization of the theory.

An important aspect of this derivation of TST rests in the classical definition of the reactive flux, which passes through a dividing surface in the configuration space. Wigner, in fact, was able to connect this expression to the more common TST formula.

The main result of TST theory is the following expression for the thermal rate coefficient:

$$k = \frac{k_B T}{h} \frac{Q^\ddagger}{Q^R} \exp\left(\frac{-E_A}{k_B T}\right) \quad (2)$$

where  $Q^R$  and  $Q^\ddagger$  are the partition functions of the reactants and transition state, respectively,  $k_B$  is Boltzmann's constant,  $T$  the temperature,  $h$  is Planck's constant and  $E_A$  the activation energy.

### Variational Transition State Theory (VTST)

The canonical transition state theory can be applied also to reactions that do not present an evident saddle point, or in other words reactions that present a *loose* transition state. In this case, as we cannot identify univocally the molecular configuration of the transition state it is necessary to apply the variational principle to the computation of the rate coefficient. In fact, the transition state corresponds in terms of reactive flux to the minimum flux of reactive molecules that pass from reactants to products per unit of time. This principle allows us to locate the transition state, choosing the po-

sition along the reaction coordinate that minimizes the canonical rate coefficient,  $k$ , as illustrated in **Figure 6**.

This procedure requires only a little more effort than the standard TST, as one repeats the calculation of  $k$  for a number of different transition states, until the position giving the minimum value for  $k$  is determined.

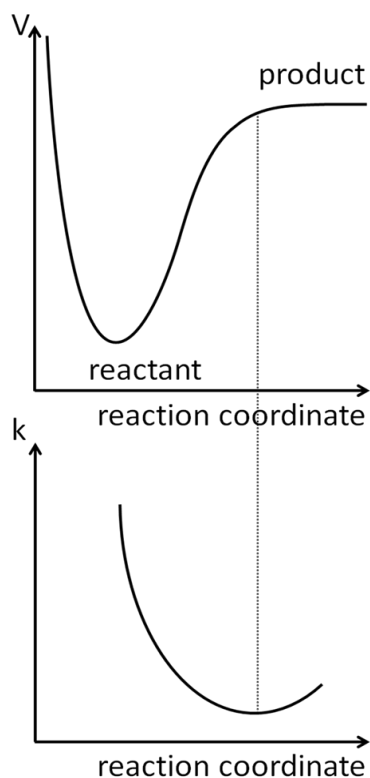


**Figure 6.** *Determination of the transition state through the variational approach.*

### Transition State Theory Limitations

TST and its variational form are both characterized by the same limitations since they are founded on the same hypothesis. These limitations are:

- ✓ The non re-crossing assumption. This is the most limiting one, as it is not always verified. As it is, hence, TST provides only an upper bound value to the actual rate coefficient.
- ✓ The adiabatic assumption. This assumption leaves out all the spin forbidden reactions. In other words, those reactions that involve a jump from one potential energy surface to another, like singlet-to-triplet reactions.
- ✓ The use of classical mechanics for the nuclei motion. This approach excludes all those reactions characterized by quantum effects, such as quantum tunneling.

Other limitations, instead, come from the definition of the reactants and TS partition functions and in particular on how we decide to treat the internal modes of vibration of the molecules. Commonly, within the TST approach, the internal motions of the molecule are treated with the harmon-

ic oscillator approximation (HO). This approximation, though, is not always legitimate. For example, when we have a torsional vibration, characterized by a very low frequency, we are in the presence of a hindered rotor that cannot be treated as a harmonic oscillator.

Finally, conventional transition state theory, as it has been presented here does not take into consideration any pressure dependence of the rate coefficient. However, it has been demonstrated that for many gas phase reactions, especially those involving small molecules, the rate coefficient can show a strong dependence with pressure. This realization drove scientists to formulate new theories in order to treat this particular behavior. The combined master equation-RRKM approach came out as the most effective one and as such, it will be the focus of the next paragraph.

### 2.2.3. Microscopic Rate Coefficients – The RRKM theory

As we have seen in the previous paragraph, a molecule that actually undergoes reaction must have a high internal energy and at least it has to exceed the barrier existing between reactant and products. Molecules in the gas phase can increase their internal energy through excitation induced by collision with other molecules in the bath gas. Hence, a reaction is the combination of two steps:

- The addition or removal of energy by collision:  $A + M \leftrightarrow A^* + M$
- The actual reaction event:  $A^* \rightarrow \text{products}$

(where A is the reactant, M is the bath gas and \* denotes internal excitation).

Lindemann<sup>48</sup>, in 1922, was the first to propose such a mechanism to explain the dynamics of gas phase unimolecular reactions. At the same time he also pointed out that this assumption leads to the pressure dependence illustrated in **Figure 7**, that only later was observed experimentally by Ramsperger (1927).<sup>49</sup>

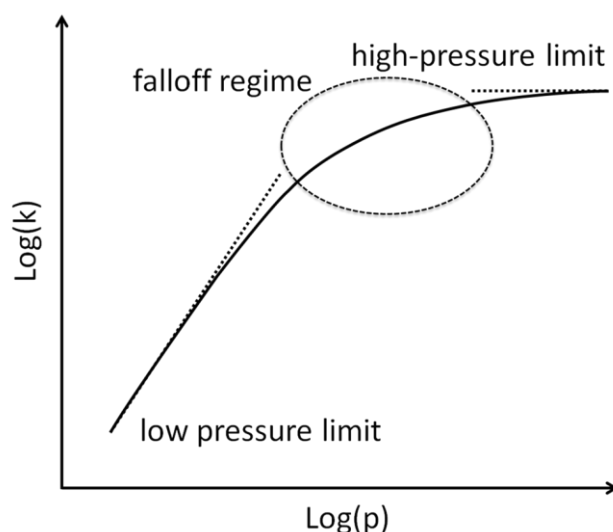


**Figure 7.** Schematic illustration of the pressure dependence of thermal rate coefficient.

We can explain the rate coefficient behavior with pressure as follows. At high pressures, collisional activation and deactivation are very fast, hence the rate-determining step of the mechanism is the reaction event and as such, the overall rate coefficient will correspond to the rate coefficient of the reaction event. Since this does not involve the bath gas, the overall rate coefficient will be independent of pressure. At low pressure, the situation is inverted. In this case, in fact, the collisional activation and deactivation is the rate-determining step and the overall rate coefficient will thus be proportional to the bath gas pressure. In the intermediate region, we observe a falloff regime.

The Lindemann description, however, gives only a qualitatively correct behavior of the pressure dependence, but does not fit quantitatively the experimental data. This problem comes as a consequence of the assumption that  $A$  and  $A^*$  are the only possible levels, while it is necessary to include all the energy levels of the molecule  $A$  and the higher ones that correspond to  $A^*$  as illustrated in **Figure 8**.

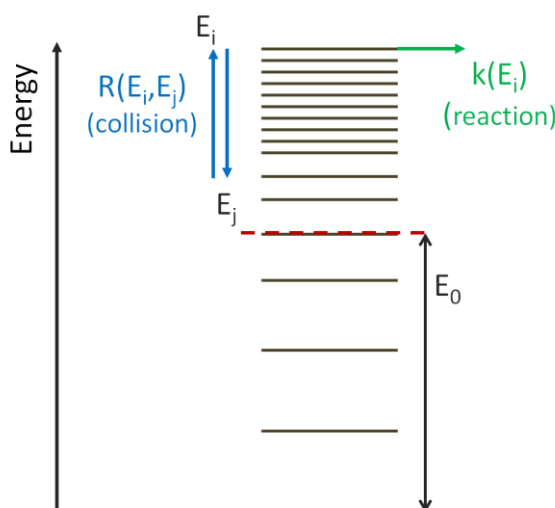


**Figure 8.** Scheme showing collision and reaction events among levels of reactant  $A$  with energy  $E$ .

In order to deduce the rate equation that describes this mechanism we must consider the microscopic rates of collisional energy transfer from energy level  $E_j$  to another level with energy  $E_i$ ,  $R(E_i, E_j)$ , and the microscopic rate of reaction from a level with energy  $E_i$ ,  $k(E_i)$ . It is necessary to take into account that only molecules that reach an energy level higher than the  $E_0$  level, corresponding to the activation energy of the reaction, can react. Introducing the population of each energy level,  $g_i$ , we can formulate a population balance for each energy level:

$$\frac{dg_i}{dt} = [M] \sum_j (g_j R_{ij} - g_i R_{ji}) - k_i g_i \quad (3)$$

with  $[M]$  as the concentration of the bath gas.

This is the most basic form of the master equation. Solving this equation it is possible to extract information about the phenomenological rate coefficient, in other words the measurable rate constant of the considered reaction as a function of temperature and pressure. Nevertheless, the solution of this equation can be attempted only if information about the microscopic reaction ( $k(E_i)$ ) and the collisional energy transfer ( $R_{ij}$ ) are known.

Collisional energy transfer can be determined theoretically from classical trajectories simulations. This type of calculation, however, requires a significant computational effort and provides more information than what is actually needed. Hence, numerous approximate models have been developed in the last decades, which permit to evaluate  $R_{ij}$  with much less computational cost, although at a cost in reliability.

The microscopic reaction rate, previously considered as a function of the energy level  $E_i$ , is actually a function of not just the energy  $E$ , but also of the angular momentum  $J$  (where  $E$  is the total energy of the molecule minus the contribution given by the rotational energy). This parameter, as for the collisional energy transfer can be obtained exactly from complete classical trajectories calculations. However, the most commonly employed and widely accepted approximate description of the dynamics of the reaction step is RRKM theory, named for Rice, Ramsperger, Kassel and Marcus<sup>49-52</sup>, who are the scientists that contributed the most to its formulation.

RRKM theory lays on two basic assumptions:

❖ *The ergodicity assumption.*

In the ergodicity assumption, we postulate that the vibrational energy is randomized rapidly on the timescale of the reaction throughout all the vibrational degrees of freedom. This assumption implies that all initial distributions of internal modes of vibration with energy  $E$  become rapidly equivalent and they carry equal weighting in the expression of the microscopic rate coefficient.

❖ *The transition state approximation.*

The transition state approximation assumes that all trajectories that cross a surface dividing reactants from products will have started in the reactants region and will go directly to the products region without recrossing the dividing surface.

The final RRKM result is:

$$k(E, J) = \frac{\int_0^{E-E_0+R-R^\ddagger} \rho^\ddagger(E_+, J) dE_+}{h \rho(E, J)} \quad (4)$$

where  $J$  is the angular momentum,  $E$  is the energy,  $R$  is the rotational energy,  $\rho(E, J)$  is the density of states and the  $\ddagger$  superscript denotes evaluation at the transition state.

It is important to highlight the definition of a basic concept: the density of states of a molecule. As is known from quantum mechanics, the energy levels accessible for a molecule are quantized. Hence, given a set of quantum states, such as those represented in **Figure 9**, we can define an energy range  $dE$  (for example  $500 \text{ cm}^{-1}$ ) in which we can count the number of states having energy

comprised between  $E$  and  $E+dE$ . The number of states per unit of energy is defined as the density of states. The same count for the angular momentum  $J$ , hence  $\rho(E, J)$  is the number of states per unit of  $E$  and  $J$ .

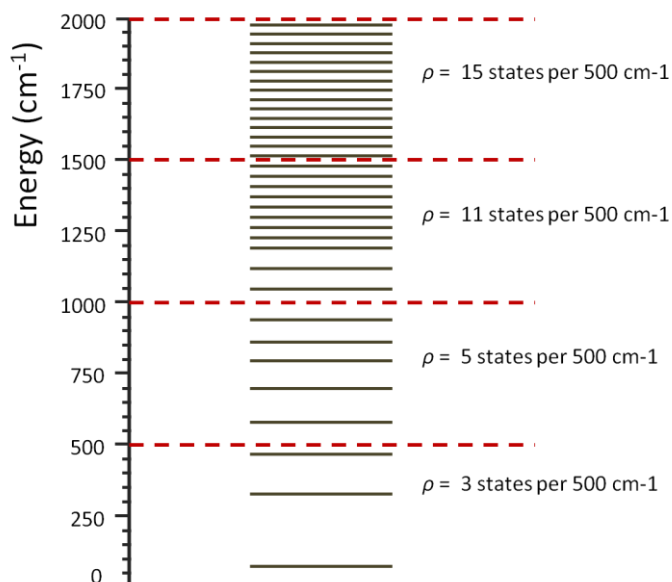


**Figure 9.** Schematic representation of energy levels of a reactant molecule between 0 and 2000  $\text{cm}^{-1}$ , illustrating density of states.

RRKM theory combined with the solution of the master equation is a very effective method for predicting the rate coefficient of gas phase reactions in terms of both computational cost and accuracy. However, this theory, being based on the transition state approximation, inevitably suffers the same limitations. Hence, for example, this theory is not able to treat spin-forbidden reactions or to account for quantum effects, such as tunneling. Still, it is possible to consider these cases by generalization of the RRKM result; however, this will be a topic of later discussion.

Another feature that RRKM theory shares with TST is the requirement of an evident saddle point. In the presence of a barrierless reaction it is, thus, necessary to use a variational implementation of RRKM theory, which is usually called the microcanonical variational transition state theory ( $\mu$ VTST) that is the analogue of VTST. In the presence of barrierless reactions, though, both standard implementations of VTST and  $\mu$ VTST fail to reproduce experimental data with an accuracy that is less than a factor of 2. The reason behind this discrepancy comes from the adoption of the harmonic oscillator to model the internal degrees of freedom of the bimolecular adduct.

In order to overcome this limit Klippenstein formulated a new approach called the variable reaction coordinate transition state theory (VRC-TST) developing the idea behind the Phase space integral based-TST. This new approach will be briefly presented in the next paragraph, while a detailed description will be exposed in the Methods section.

### 2.2.4. The Variable Reaction Coordinate – Transition State Theory

In the presence of barrierless reactions, it is particularly important to provide a proper treatment of the variation of the location of the transition state. In fact, in such reactions the transition state can be located at interfragment separations of tens of angstroms at low energies, down to 2-3 Å at higher energies.

A key concept introduced to describe better this behavior is the separation of the modes into the vibration of the fragments, termed the *conserved* modes, and the relative and overall rotation and relative translation of the fragments, called the *transitional* modes. This separation permits to compute the number of states of the transition state as a convolution of the number of states corresponding to the transitional modes and the number of states of the conserved modes, which are calculated for a number of points along the reaction coordinate. In the first version of this approach, the reaction coordinate was taken as the separation between the centers of mass of the two reacting fragments. This approximation is valid for large separations, but breaks down for shorter separations distances.

The VRC-TST approach<sup>53-57</sup> explicitly considers the variation in the form of the reaction coordinate. This is accomplished by introducing a variable reaction coordinate defined in terms of the distance between two variably located pivot points, with one pivot point for each fragment. An optimization is then carried out not only of the value of the reaction coordinate, but also of the definition of the reaction coordinate in terms of the location of the two pivot points. This VRC-TST approach can thus better represent the reaction coordinate also at close separation of the two reacting fragment.

In the last two decades Klippenstein and coworkers further improved the present approach, also validating its accuracy against a large set of experimental data available on a number of bimolecular barrierless reactions, such as radical-radical recombination reactions.<sup>12-14,41,58,59</sup> This process of improvement and validation yielded the currently most effective approach for the determination of accurate rate coefficients for barrierless bimolecular reactions.

### 2.2.5. Solution of the Master Equation

As mentioned in the previous paragraph, a number of chemical reactions occur with non-equilibrium energy distributions (non-Boltzmann), in other words the chemical reaction time-scale is comparable to the collision time-scale. A successful approach that has been developed to model this class of reactions is the time dependent, multiple well master equation, in which a coarse-grained description of the energy levels accessible to the molecules is adopted.

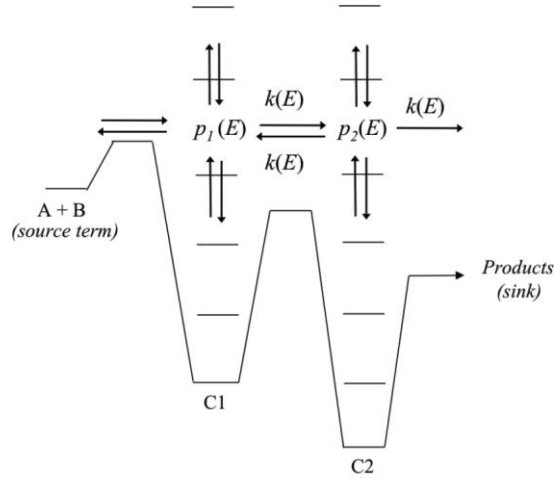


**Figure 10.** Representation of a generic reactive PES, taken from ref [60].

Considering the representation of a generic reactive system illustrated in **Figure 10**, it is possible to formulate the master equation for a generic isomer  $m$  on the reactive PES, as:

$$\begin{aligned} \frac{dp_m(E)}{dt} = & Z \int_0^\infty P(E; E') p_m(E') dE' - Z p_m(E) + \sum_{n \neq m}^M k_{m,n}(E) p_n(E) - \sum_{n \neq m}^M k_{n,m}(E) p_m(E) \\ & - k_{S,m}(E) p_m(E) + K_{R,m}^{eq} k_{R,m}(E) \frac{\rho(E) e^{-\frac{E}{k_B T}}}{Q_m(T)} n_A p_B - k_{R,m}(E) p_m(E) \end{aligned} \quad (5)$$

Here,  $p_m(E)$  is the rovibrational population density within a particular energy grain  $E$ . On the right side of the equation we have seven terms, three are positive and correspond to the flux into  $p_m(E)$ , while the other four terms are negative and correspond to outward fluxes. The first two terms are correlated to the gain or loss of the population density due to collisional energy transfer phenomena with the bath gas. The second two terms are the inward flux coming from an adjacent intermediate  $n$  and the outward flux due to the conversion of the isomer  $m$  into another isomer  $n$ . The fifth term is reaction in to the products and is considered if intermediate  $m$  is directly connected to the products. Finally, the last two terms are related to the bimolecular association source term and apply only to those isomers that are populated through a bimolecular association reaction, in which it is assumed that reactant A is in significant excess compared to reactant B.

Equation ( 5 ) as it is written does not represent a closed system of differential equation since  $p_B$  is not specified. Thus, if a bimolecular reaction is included in the reaction network, then it is necessary to include an additional equation:

$$\frac{dp_B}{dt} = \sum_{m=1}^M \int_0^\infty k_{R,m}(E) p_m(E) dE - n_A p_B \sum_{m=1}^M K_{R,m}^{eq} \int_0^\infty k_{R,m}(E) \frac{\rho(E) e^{-\frac{E}{k_B T}}}{Q_m(T)} dE \quad (6)$$

Over the entire set of energy grains and intermediates, equations ( 5 ) and ( 6 ) give a set of coupled ordinary differential equations that may be solved using different approaches. Among the master equation solvers present in the literature, we can distinguish them by the approach they adopt: stochastic approaches like kinetic Monte-Carlo or matrix diagonalization techniques.

In the first class of master equation solvers, we find the Multiwell Program Suite of Barker and coworkers<sup>61</sup> that employs Gillespie's exact stochastic method and the solver described by Vereecken et al.<sup>62</sup> In the second class of master equation solvers are comprised the VariFlex code of Klippenstein and coworkers<sup>63</sup>, the MESMER code of Pilling's group<sup>60</sup> and the code implemented by Frankcombe and Smith.<sup>64</sup>

# 3 Methods

---

The following chapter reports the theories and methods adopted in this work.

Firstly, the electronic structure methods used throughout this research project will be presented and discussed. In particular, we will focus on the description of the coupled cluster theory, as it has been largely employed to calculate accurate energy values.

Details about the CASPT2 method will be also reported. This method, in fact, has been adopted to study reactions characterized by a multireference nature. In particular, it has been considered significant to provide a few details about its derivation, which can assist the understanding of its implementation that is necessary for a correct utilization. However, for a complete and exhaustive description of these theories we suggest the book “Introduction to Computational Chemistry” of Frank Jensen from which we report here only a brief extraction.<sup>7</sup>

In addition, an exhaustive report on the kinetic theories implemented will follow. Specifically the theoretical background and the details of implementation of the original MCRRKM homemade code will be described. Successively, we will illustrate the building blocks that have been progressively added to create a program suite able to address the majority of the gas phase reactions one may encounter. In particular, these building blocks include the treatment of:

- *Spin-forbidden reactions.*
- *Hindered rotor approximation.*
- *Multi-well and multi-channel potential energy surfaces.*
- *Tunneling correction.*
- *Bimolecular reactions.*

Finally, the variable reaction coordinate transition state theory formulated and implemented by Klippenstein and coworkers will be described. This theory, in fact, has been applied to study a particular set of bimolecular reactions with the intent to confirm its reliability in the treatment of reactions characterized by loose transition states.

## 3.1. Computational Quantum Chemistry

### 3.1.1. The Hamiltonian Operator

The energy estimation of a multi-atom multi-electron system as a function of the atomic coordinates can be obtained integrating the time-independent Schrödinger equation that can be expressed in a compact form as:

$$H\Psi = E\Psi \quad (7)$$

where  $H$  represents the Hamiltonian operator,  $\Psi$  is the wave function and  $E$  the energy.

The Hamiltonian operator can be obtained by writing down the total energy (kinetic plus potential) for the system of interest as a function of the positions and momentum variables. Subsequently, any momentum  $\vec{p}$  for a particle of mass  $m$  can be substituted with the operator  $(\hbar/i)\vec{\nabla}$ .

For a system with  $M$  nuclei the positions are identified by  $\vec{R}_k$  and charges by  $Z_k e$ . If we indicate the momentum as  $\vec{P}_k$  and the mass  $M_k$  for each nucleus, then the kinetic energy becomes  $(P_k^2/2M_k)$ . Equivalently, we have  $N$  electrons with the same charge,  $-e$ , and the same mass  $m_e$ . The position of the  $i$ -th electron is denoted by  $\vec{r}_i$  and its momentum by  $\vec{p}_i$ , so that its kinetic energy is  $(p_i^2/2m_e)$ .

The total kinetic energy is therefore:

$$E_{kin} = \sum_{k=1}^M \frac{P_k^2}{2M_k} + \sum_{i=1}^N \frac{p_i^2}{2m_e} \quad (8)$$

The potential energy of the system is given by the electrostatic energy due to the interactions between the charges. For the system of our interest, with two types of particles nuclei and electrons, we obtain:

$$E_{pot} = \frac{1}{2} \sum_{k_1 \neq k_2=1}^M \frac{1}{4\pi\epsilon_0} \frac{Z_{k_1} Z_{k_2} e^2}{|\vec{R}_{k_1} - \vec{R}_{k_2}|} + \frac{1}{2} \sum_{i_1 \neq i_2=1}^N \frac{1}{4\pi\epsilon_0} \frac{e^2}{|\vec{r}_{i_1} - \vec{r}_{i_2}|} + \frac{1}{2} \sum_{k=1}^M \sum_{i=1}^N \frac{1}{4\pi\epsilon_0} \frac{Z_k e^2}{|\vec{R}_k - \vec{r}_i|} \quad (9)$$

The first term on the right-hand side is the nucleus-nucleus interaction, the second one is the electron-electron interaction and the last one is the nucleus-electron interaction.

In the total energy expression:

$$E_{tot} = E_{kin} + E_{pot} \quad (10)$$

We insert the operator  $(\hbar/i)\vec{\nabla}$  and then obtain the Hamiltonian operator:

$$H = \sum_{k=1}^M \frac{\hbar}{2M_k} \nabla_{\vec{R}_k}^2 + \sum_{i=1}^N \frac{\hbar}{2m_e} \nabla_{\vec{r}_i}^2 + \frac{1}{2} \sum_{k_1 \neq k_2=1}^M \frac{1}{4\pi\epsilon_0} \frac{Z_{k_1} Z_{k_2} e^2}{|\vec{R}_{k_1} - \vec{R}_{k_2}|} + \frac{1}{2} \sum_{i_1 \neq i_2=1}^N \frac{1}{4\pi\epsilon_0} \frac{e^2}{|\vec{r}_{i_1} - \vec{r}_{i_2}|} + \frac{1}{2} \sum_{k=1}^M \sum_{i=1}^N \frac{1}{4\pi\epsilon_0} \frac{Z_k e^2}{|\vec{R}_k - \vec{r}_i|} \quad (11)$$

We can write the Hamiltonian in a compact form accordingly as:

$$H = T_n + T_e + V_{n-n} + V_{e-e} + V_{n-e} \quad (12)$$

### 3.1.2. The Born-Oppenheimer Approximation

The solution of the Schrödinger equation depends on the spin and position coordinates of all the electrons

$$(\vec{r}_1, \sigma_1, \vec{r}_2, \sigma_2, \dots, \vec{r}_N, \sigma_N) \equiv (\vec{x}_1, \vec{x}_2, \dots, \vec{x}_N) \equiv \vec{x} \quad (13)$$

and the nuclei

$$(\vec{R}_1, \Sigma_1, \vec{R}_2, \Sigma_2, \dots, \vec{R}_M, \Sigma_M) \equiv (\vec{X}_1, \vec{X}_2, \dots, \vec{X}_M) \equiv \vec{X} \quad (14)$$

We can express the Schrödinger as:

$$H\Psi = (T_n + T_e + V_{n-n} + V_{e-e} + V_{n-e})\Psi(\vec{X}, \vec{x}) = E \cdot \Psi(\vec{X}, \vec{x}) \quad (15)$$

We can group the Hamiltonian operators in two parts so that the equation becomes:

$$[(T_n + V_{n-n}) + (T_e + V_{e-e} + V_{n-e})]\Psi(\vec{X}, \vec{x}) = E \cdot \Psi(\vec{X}, \vec{x}) \quad (16)$$

The first term depends only on the nuclear spins and positions, the second part depends only on the spin and position of the electrons. Thus, we can introduce the Born-Oppenheimer approximation. The physical idea is that the electrons move much faster than the nuclei, hence it is possible for the electrons to find their “equilibrium position” before the nuclei move.

The Schrödinger equation can consequently be solved as the product given by the two wave functions contributions: one offered by the nuclei that depends only on the nuclear position and a second one that corresponds to the electrons and depends on both sets of coordinates:

$$\Psi(\vec{X}, \vec{x}) = \Psi_n(\vec{X})\Psi_e(\vec{X}, \vec{x}) \quad (17)$$

Introducing this functional form, we can write the Schrödinger equation for the electrons:

$$(T_e + V_{e-e} + V_{n-e})\Psi_e(\vec{X}, \vec{x}) = E_e(\vec{X}) \cdot \Psi_e(\vec{X}, \vec{x}) \quad (18)$$

Finally, the total energy  $E$  is found:

$$E = \frac{(T_n + V_{n-n})\Psi_n(\vec{X})}{\Psi_n(\vec{X})} + E_e(\vec{X}) \quad (19)$$

The advantage of this assumption is the possibility to treat the nuclei as classical particles that give rise to a total energy contribution and an electrostatic field in which the electrons move.

### 3.1.3. Hartree-Fock Theory

To solve the Schrödinger equation it is necessary to introduce a functional form for the solution that is a functional form for the wave function. The Hartree-Fock theory is based on approximating the N-electron wave function with a simple functional that allows the satisfaction of the antisymmetry condition, which is the Slater determinant

$$\Phi(\vec{x}_1, \vec{x}_2, \dots, \vec{x}_N) = \frac{1}{\sqrt{N!}} \begin{vmatrix} \phi_1(\vec{x}_1) & \phi_2(\vec{x}_1) & \dots & \phi_N(\vec{x}_1) \\ \phi_1(\vec{x}_2) & \phi_2(\vec{x}_2) & \dots & \phi_N(\vec{x}_2) \\ \vdots & \vdots & \ddots & \vdots \\ \phi_1(\vec{x}_N) & \phi_2(\vec{x}_N) & \dots & \phi_N(\vec{x}_N) \end{vmatrix} \quad (20)$$

Here  $\Phi$  stands for the approximate solution to the real wave function  $\Psi$  and  $\phi_i$  is the molecular spin-orbital wave function for the  $i$ -th electron.

The Hartree-Fock method consists then of the solution to the Schrödinger equation through the utilization of the variational principle assuming the functional form of the wave function corresponding to one Slater determinant. This implies that the electron-electron interaction is considered as an average effect. The Hartree-Fock method is also called, especially in the older literature, the self-consistent field method (SCF) because the solutions to the resulting non-linear equations are solved by means of an iterative algorithm assuming that each particle is subjected to the mean field created by all other particles.

### 3.1.4. Basis Set Approximation

In order to make a wave function calculation possible for systems with more than two atoms, however, it is necessary to approximate the molecular orbitals  $\phi_i$  in terms of a set of known functions. Hence, each molecular orbital can be expressed as an expansion of  $N_b$  basis function,  $\chi_i$

$$\phi_k(\vec{x}) = \sum_i^{N_b} c_{ik} \chi_i(\vec{x}) \quad k = 1, \dots, N_b \quad (21)$$

The number of orbitals obtained with this procedure is determined by the basis set dimension. However, not all of the orbitals will be occupied by electrons, but only those at lower energy.

### 3.1.5. Electron Correlation Methods

As it has been already pointed out, the Hartree-Fock method generates solutions to the Schrödinger equation that account for the electron-electron interaction as an average effect. Adopting an appropriately large basis set it is possible to reach 99% of the solution, but the 1% that is left can still be very significant to the description of chemical phenomena. This energy difference is often called electron correlation energy and from a physical point of view is correlated to the description of the relative motion of the electrons being correlated.

This correlation can be of two types:

- Intra-orbital – considered between electrons of the same molecular orbital
- Inter-orbital – considered between electrons of different molecular orbitals

These two contributions correspond to electrons with opposite spin. In addition, the interaction between electrons with equal spin can also be considered, but its contribution is much less signifi-

cant. In this framework, the Hartree-Fock solution is regarded as a starting point for improvements to the approximation of the exact solution. In particular, the first method that has been proposed for calculating the electron correlation energy is based on an increase in the number of Slater determinants.

The wave function is thus expressed as a linear combination of  $N_d$  Slater determinants following the scheme:

$$\begin{aligned} \chi &\rightarrow \phi \rightarrow \Phi \rightarrow \Psi \\ \phi_k(\vec{x}) &= \sum_i^{N_b} c_{ik} \chi_i(\vec{x}) \\ \Psi &= a_0 \Phi_{\text{HF}} + \sum_i^{N_d} a_i \Phi_i(\vec{x}) \end{aligned} \quad (22)$$

In the HF computation, only one Slater determinant is used, which is built with the lowest energy molecular orbitals. However, a new series of determinants can be generated by replacing the molecular orbitals that are occupied in the HF determinant with molecular orbitals that are unoccupied, (virtual orbitals). Depending on how many molecular orbitals have been replaced we will generate Slater determinants that are singly, doubly, triply etc. excited with respect to the HF determinant.

The total number of determinants that can be generated depends on the basis set dimension. A larger basis set, in fact, corresponds to a larger number of virtual orbitals, allowing the possibility to build more determinants that are excited.

There are three main methods for calculating the electron correlation: Configuration Interaction (CI), Many-Body Perturbation Theory (MBPT), and Coupled Cluster (CC).

### Configuration Interaction – CI<sup>65</sup>

The configuration interaction method is based on the variational principle analogous to the HF method. The wave function is written as a linear combination of Slater determinants, with the expansion coefficients determined by imposing as a condition the minimization of the energy.

$$\Psi_{\text{CI}} = a_0 \Phi_{\text{HF}} + \sum_S a_S \Phi_S + \sum_D a_D \Phi_D + \sum_T a_T \Phi_T + \dots = \sum_i a_i \Phi_i \quad (23)$$

The molecular orbitals adopted to build the excited Slater determinants are taken from HF calculations and kept fixed. Subscripts S, D, T etc. denote determinants singly, doubly, triply etc. excited with respect to the HF configuration.

Taking into consideration all the possible excited determinants, we obtain the *full CI* wave function. In this solution, there are no approximations in the correlation correction computation, aside

from the one introduced by the dimension of the basis set chosen to represent the single electron wave function. This result, however, is obtained only with a high computational effort.

To develop a model able to give reasonable results at a lower computational cost the number of determinants in the CI expansion must be truncated. Introducing only single excited determinants does not give significant improvements over the Hartree-Fock solution. If only doubly excited determinants are added, yielding the CID model, there is an improvement. Moreover, this addition made in conjunction with the introduction of also singly excited determinants leads to even better solutions with low additional effort. This method is denoted as CISD. Sequentially, triply and quadruply excited determinants can also be added leading to the CISDT and CISDTQ methods. The last one is very accurate since its results are close to Full CI limit, but it is still very demanding in term of computational cost and it can be applied only to small molecules and small basis sets.

### **Multi-Configuration Self Consistent Field<sup>66</sup>**

The Multi-Configuration Self Consistent Field (MCSCF) method can be regarded as a generalization of the CI method. Within this method, in fact, not only the coefficients in front of the Slater determinants are optimized following the variational principle, but also the molecular orbitals that compose the Slater determinants. In this way many configurations or combinations of molecular orbitals can be distinguished. This property is especially useful when treating molecules like ozone that present different resonance structures which are important in the definition of the wave function.

These methods find also a large application in the energy description of homolytic dissociation reactions as Hartree-Fock wave functions are known to be poorly suited for the task. The problem is that using the common HF method we restrict the wave function to have only doubly occupied orbitals (e.g. restricted HF). Calculating the bond separation energy as a function of the bond distance with such a method leads to results characterized by a spurious ionic character. Without imposing such restrictions, e.g. adopting the unrestricted version of the HF method, the wave function obtained suffers from spin contamination. Hence, it is necessary to adopt a method capable to take into account the changes of the wave function configuration along the reaction coordinate. This is accomplished with MCSCF methods.

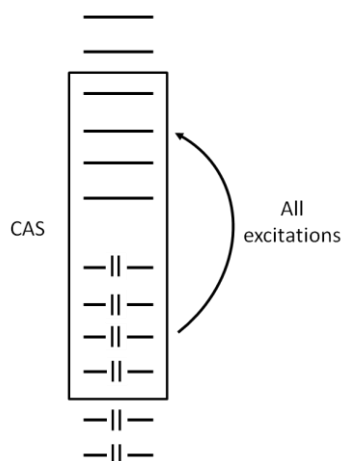


**Figure 11.** Illustration of the complete active space (CAS) selection.

The major problem of MCSCF methods is the selection of the configurations to include in the calculation of the wave function, which are necessary to describe correctly the property of interest. One of the most popular approaches is the *Complete Active Space Self Consistent Field* (CASSCF) method. To generate the configurations needed, here the molecular orbitals are partitioned into active and inactive spaces. Generally, the active orbitals are the lowest unoccupied and the highest occupied orbitals from a HF calculation, as depicted in **Figure 11**.

The selection of the molecular orbitals to include in the active space must be done manually taking into account the problem at hand and the computational resources necessary to carry out the calculation. When several points along the dissociating bond are needed, for example, the orbitals that will undergo significant changes must be included to describe properly the potential energy surface.

It is important to highlight that the correlation energy can be separated into two contributions:

- *Static* – generated by the effect of allowing orbitals to become partly singly occupied or even unoccupied instead of forcing double occupation.
- *Dynamic* – generated by taking into account the correlation in the motion of the electrons.

In this framework, MCSCF methods are adopted to recover the correct “static” part of the correlation energy but they neglect the dynamic contribution. Thus, they cannot be used to obtain quantitatively accurate correct results, but they can offer a qualitatively correct wave function that can be used as a reference for successive more accurate calculations. In the next section, we will present a method that exploits this feature.

## Multi-Reference Configuration Interaction

CI methods generally have an HF wave function as a reference, e.g. we generate the excited configurations from a single Slater determinant. It is possible, however to use a different reference

wave function. Adopting the MCSCF wave function as a reference for a configuration interaction calculation generates a new method called Multi-Reference Configuration Interaction (MRCI). In fact, the number of references changes with the number of configurations included in the MCSCF wave function. MRCI calculations that include a large number of configurations in the MCSCF reference generate very accurate results, but are also computationally very expensive.

It is interesting to notice that, as for the CI method, the same approach can be applied also to other single-reference electron correlation methods. For example, including the MCSCF as reference wave function to the perturbation method MP2, which will be described in the next section, leads to the method called CASPT2.

### Many Body Perturbation Theory – Møller-Plesset Perturbation Theory<sup>67</sup>

The main idea behind the perturbation methods is that the problem at hand differs only slightly from an already solved one. Hence, the solution of the given problem will not be too distant from the solution of the already known system. This idea can be mathematically described by defining a Hamiltonian operator formed by two terms, the reference ( $H_0$ ) and the perturbation ( $H'$ ).

$$\begin{aligned} H &= H_0 + \lambda H' \\ H_0 \Phi_i &= E_i \Phi_i \quad i = 0, 1, 2, \dots, \infty \end{aligned} \quad (24)$$

where  $\lambda$  is a variable parameter that indicates the level of perturbation. The perturbed Schrödinger equation is defined as

$$H\Psi = W\Psi \quad (25)$$

If  $\lambda = 0$ , then  $H = H_0$ ,  $\Psi = \Phi_0$  and  $W = E_0$  and we obtain an unperturbed wave function. Increasing  $\lambda$  from 0 to 1 and 2 we obtain respectively first order and second order perturbed wave functions. When applying this theory to the calculation of the correlation energy the Hamiltonian operator must be chosen. A common choice for  $H_0$  is the sum of Fock operators, whose specification is found in the derivation of Hartree-Fock theory. In particular, the first order of perturbation corresponds to the HF result and in order to recover some of the electron correlation energy it is necessary to go to order 2, thus obtaining the MP2 method.

### Coupled Cluster<sup>68</sup>

Perturbation methods add all types of correction (S, D, T, Q, etc.) to the reference wave function to a given order (2, 3, 4, etc.). The idea of Coupled Cluster (CC) methods is to include all type of corrections for an infinite order of perturbation.

We can start by defining a cluster operator T:

$$T = T_1 + T_2 + T_3 + \dots + T_{N_{elec}} \quad (26)$$

The  $T_i$  operator acting on the reference wave function generates all the  $i$ -th excited Slater determinants.

$$T_1\Phi_0 = \sum_i^{occ} \sum_a^{vir} t_i^a \Phi_i^a \quad (27)$$

$$T_2\Phi_0 = \sum_{i<j}^{occ} \sum_{a<b}^{vir} t_{ij}^{ab} \Phi_{ij}^{ab} \quad (28)$$

The CC wave function thus becomes:

$$\Psi_{CC} = e^T \Phi_0$$

$$e^T = 1 + T + \frac{1}{2}T^2 + \frac{1}{6}T^3 + \dots = \sum_{k=0}^{\infty} \frac{1}{k!} T^k \quad (29)$$

Combining equation (26) and equation (29) we obtain:

$$e^T = 1 + T_1 + \left(T_2 + \frac{1}{2}T_1^2\right) + \left(T_3 + T_1T_2 + \frac{1}{6}T_1^3\right) +$$

$$+ \left(T_4 + T_3T_1 + \frac{1}{2}T_2^2 + \frac{1}{2}T_2T_1^2 + \frac{1}{24}T_1^4\right) + \dots \quad (30)$$

Here the first term generates the HF reference, the second all excited states generated by a single electron excitation, then the first parenthesis generates all the doubly excited states, in the second parenthesis we have all the triply excited states and so on. With this CC wave function, the Schrödinger equation becomes:

$$He^T\Phi_0 = Ee^T\Phi_0 \quad (31)$$

Introducing the previous expressions, then it is possible to search for the minimum of the energy by varying the  $t_i$  amplitudes.

To solve the problem, however, it is necessary to truncate the expansion of excitation levels, or in other words to decide how many terms to introduce in the T operator. If we introduce only the first term ( $T_1$ ) no improvement is reached with respect to the HF solution. Introducing only the second term some of the electron correlation energy is recovered and we have the CCD method. The singly excited term is not much more demanding in term of computational cost and yields a more complete method (the CCSD model). Introducing also the third excitation term we have the CCSDT method, that is quite computationally expensive and can be applied only to small molecules.

The CCSD(T) method, that has been extensively adopted throughout the present work, is an hybrid method that combines CCSD and MP4 methods. In particular, in this case the triples contribution is computed separately through the perturbation theory and added to the CCSD results. In addition, a term coming from the fifth order perturbation that describes the coupling between singles and triples is also included.<sup>15</sup>

In a Coupled Cluster calculation, it is possible to recover information about the multireference character of the wave function through the calculation of the T1-diagnostic. If this parameter is less than 0.02 then the CCSD(T) wave function is expected to give results close to the full CI limit, otherwise is necessary to employ a multi-reference method.

Summarizing, in terms of accuracy with a medium sized basis set, the following order is generally observed:<sup>7</sup>

$$\text{HF} \ll \text{MP2} < \text{CISD} < \text{MP4(SDQ)} \sim \text{CCSD} < \text{MP4} < \text{CCSD(T)}$$

All of these are single reference methods. Multi-reference methods are not easily classified as their accuracy strongly depends on the number of configurations chosen in the reference wave function.

## 3.2. Kinetic theories

### 3.2.1. MCRRKM – Theory and Implementation

The MCRRKM code is a homemade code implemented within the Chimica Fisica Applicata CFA research group and in particular has been the subject of a previous PhD thesis “Multi-scale simulations of the production process of advanced materials by chemical vapor deposition” by Alessandro Barbato<sup>69</sup> and of a recent paper by Barbato et al.<sup>70</sup> Hence, for a more detailed description of its implementation and validation we refer to these resources.

However, as this code has been used and further developed within this research project, we considered it worthwhile to present here a summary of the theory on which the program is based and a few details about its implementation.

#### RRKM-Master Equation theory

The calculation of pressure dependent rate constants with MCRRKM is based on the stochastic integration of the Master Equation (ME), which is performed discretizing the investigated rovibrational energy field into finite bins whose reacting properties are determined through RRKM theory. In particular, the form of the two-dimensional ME for a unimolecular reaction characterized by a single well is given by:

$$\begin{aligned} & -k(T, p) \cdot x(E, J) \\ & = Z \int_0^\infty \int_0^\infty [P(E, J; E^I, J^I) \cdot x(E^I, J^I) - P(E^I, J^I; E, J) \cdot x(E, J)] dE^I dJ^I \quad (32) \\ & - k(E, J)x(E, J) \end{aligned}$$

Here  $k(T, p)$  is the thermal rate constant,  $x(E, J)$  is the population distribution,  $Z$  is the collisional frequency of the reactant with the bath gas,  $P(E, J; E^I, J^I)$  is the probability that the collision yields to an energy jump from level  $E^I$  to level  $E$  and from angular momentum level  $J^I$  to level  $J$ . Finally  $k(E, J)$  is the RRKM rate coefficient.

This is the complete formulation of the master equation, in fact, it takes into account both energy and angular momentum conservation. However, the solution of the master equation in this form is

still a challenge for the scientific community. The problem comes from the absence of a correct description of the J dependency of the transfer probability  $P(E, J; E^I, J^I)$ .

The approach here adopted to overcome this issue is the E,J model of Miller et al.,<sup>71</sup> that exploits the “initial J independence” assumption for which  $P(E, J; E^I, J^I)$  can be calculated as:

$$P(E, J; E^I, J^I) = P(E, E^I)\varphi(E, J) \quad (33)$$

This expression means that the transfer probability does not depend on the angular momentum of the molecule before the collision,  $J^I$ , from this the name “initial J independence”.

Including equation (33) within the 2D-ME, it is possible to obtain a master equation dependent only on the total energy E, i.e. a one-dimensional master equation.

$$-k(T, p) \cdot \bar{x}(E) = Z \int_0^\infty [P(E, E^I) \cdot \bar{x}(E^I) - P(E^I, E) \cdot \bar{x}(E)] dE^I - \bar{k}(E)\bar{x}(E) \quad (34)$$

where the J-averaged quantities  $\bar{k}(E)$  and  $\bar{x}(E)$  are defined as

$$\bar{x}(E) = \sum_J x(E, J) \quad (35)$$

$$\bar{k}(E) = \frac{\sum_J k(E, J)y(E, J)}{\sum_J y(E, J)} \quad (36)$$

with  $y(E, J)$  equal to

$$y(E, J) = \frac{\varphi(E, J)}{Z + k(E, J)} \quad (37)$$

and  $\varphi(E, J)$  is given by

$$\varphi(E, J) = \frac{\rho(E, J)}{\sum_J \rho(E, J)} \quad (38)$$

In this expression  $\rho(E, J)$  represents the rovibrational density of states of the molecule at energy E and angular momentum J. Rotational and vibrational density of states and the degeneracy of each energetic level E are computed with the Beyer-Swinehart algorithm.

The implementation of this approach still requires the *microcanonical rate coefficient*,  $k(E, J)$ , the *transition probability* between different energy levels,  $P(E, E^I)$ , and the *collision frequency*, Z.

The **microcanonical rate constant** can be computed through RRKM theory as:

$$k(E, J) = \frac{N^\ddagger(E, J)}{h\rho(E, J)} \quad (39)$$

where h is Planck's constant and  $N^\ddagger(E, J)$  is the sum of states at the transition state.

The **transition probability** for the downward transfer,  $P(E, E^I)$  with  $E^I > E$ , can be computed by adopting any one of several functional forms. Here we have decided to implement the common “single exponential down” model as:

$$P(E, E^I) = \frac{1}{C_N(E^I)} \exp\left(-\frac{E^I - E}{\Delta E_{down}}\right) \quad E \leq E^I \quad (40)$$

In this expression  $C_N(E^I)$  is a normalization factor and  $\Delta E_{down}$  is the mean energy transferred in a deactivating collision. Microscopic reversibility can be imposed to recover also the probability for upwards energy transfer, i.e. using the condition:

$$f(E^I)P(E, E^I) = f(E)P(E^I, E) \quad (41)$$

here  $f(E)$  is the Boltzmann distribution function, which is computed as:

$$f(E) = \frac{\rho(E)}{Q} \exp\left(-\frac{E}{k_B T}\right) \quad (42)$$

with:

$$Q = \int \rho(E) \exp\left(-\frac{E}{k_B T}\right) dE \quad (43)$$

where  $k_B$  is the Boltzmann's constant.

The **collision frequency** of the molecule with the bath gas is computed using Lennard-Jones collision rates as:

$$Z = \pi \sigma^2 \sqrt{\frac{8k_B T}{\pi \mu}} [M] \Omega^{(2,2)} \quad (44)$$

where  $\sigma$  is the hard sphere diameter,  $\mu$  is the reduced mass,  $[M]$  is the bath gas concentration and  $\Omega^{(2,2)}(\sigma, \varepsilon)$  the collision integral of Reid et al.<sup>72</sup> defined as:

$$\Omega^{(2,2)} = \frac{1.16145}{T^{*0.14874}} + \frac{0.52487}{\exp(0.7732 \cdot T^*)} + \frac{2.16178}{\exp(2.437887 \cdot T^*)} \quad (45)$$

with  $T^* = k_B T / \varepsilon$

Once the parameters,  $k(E, J)$ ,  $P(E, E^I)$  and  $Z$  are known it is possible to integrate the 1D master equation of equation (34).

### Implementation of the RRKM Theory and Solution of the Master Equation

The MCRRKM code is based on the stochastic integration of the master equation, which is performed by discretizing the investigated rovibrational internal molecular energy into finite bins whose reacting properties are determined as mentioned previously with RRKM theory.

In the designed computational protocol all reaction and transitional collisional properties are calculated before starting the ME integration cycle with an integration energy step of  $1 \text{ cm}^{-1}$ . Then they are averaged over discrete energy bins whose size is determined through a series of test calculations, which are needed to find a reasonable compromise between computational efficiency and numerical accuracy.

After this evaluation and averaging processes we move to the main ME integration cycle. The simulation starts by assuming at time 0 a reactant molecule is at an assigned energy  $E_{in}$  and under-

goes a collision event. The collision can eventually yield to a complex excited at energy  $E$  with probability  $P$  defined as:

$$P_i = \frac{R_i}{\sum_1^{\infty} R_i} \quad (46)$$

Here  $R_i$  is any possible transition event for the activated complex, which, in the first implementation of the code were: excitation to a higher energy level, de-excitation to a lower energy level, or reaction to products. To limit the total number of possible transitions of the excited adduct, a maximum value  $JM$  for the collisional energy transfer events was fixed.

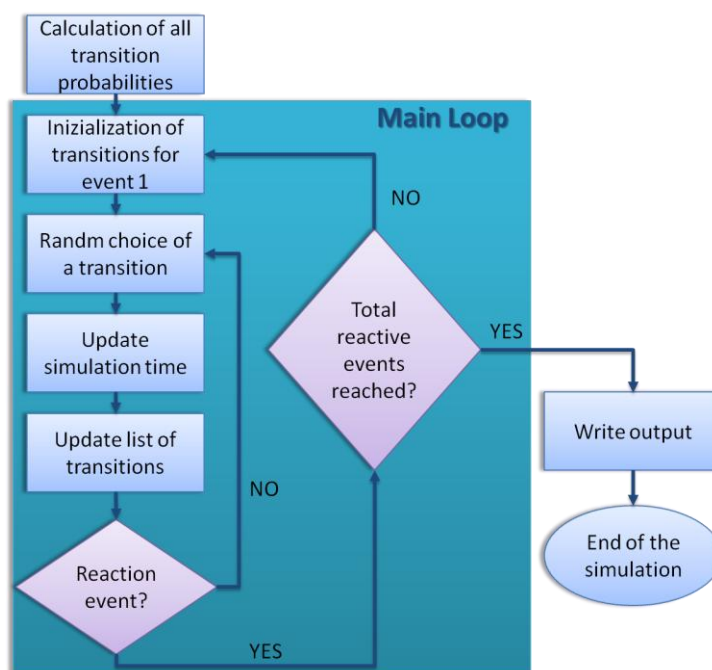


**Figure 12.** MCRRKM protocol for the simulation of a unimolecular reaction.

The transition event of the activated complex is searched randomly using a rejection free algorithm. In particular, a random number  $U$  comprised between 0 and 1 is generated and the transition event is chosen among the  $N_{tot}$  events that satisfy the following condition:

$$\sum_{i=1}^{j-1} R_i < U * \sum_{i=1}^{N_{tot}} R_i < \sum_{i=1}^j R_i \quad (47)$$

the simulation time is then updated with a real time increment  $\Delta t$  calculated as:

$$\Delta t = -\frac{\ln(U)}{\sum_{i=1}^{N_{tot}} R_i} \quad (48)$$

The simulation terminates when a reactive event occurs. After this a new simulation can be started until the total number of the desired reactive events has taken place as reported schematically in **Figure 12**. The random number generator adopted is the Mersenne Twister.

After solving the RRKM/master equation combined system using the approach described before it is necessary to extract information about the thermal rate constant of the overall reaction.

The first version of the code foresaw a post processing of the output data at the end of a stochastic ME simulation to obtain the rate coefficient desired. In particular, the kinetic constant was calculated taking advantage of the solution of the mass balance for a population of  $N$  reacting molecules, which for a unimolecular reaction with rate coefficient  $k_{uni}$  can be expressed as:

$$\frac{dN}{dt} = k_{uni}N \quad (49)$$

This equation can be integrated analytically obtaining the expression:

$$\ln\left(\frac{N}{N_0}\right) = -k_{uni}t \quad (50)$$

The kinetic constant can be calculated performing a linear regression over the simulation time that each molecule takes to react.

This feature was changed within the course of the present project with the incorporation of the calculation of the rate coefficient “on the fly” in the main ME cycle. This modification yielded to the formulation of a new procedure for the determination of the convergence criteria that allowed obtaining more accurate and robust solutions.

In particular, three different approaches available can be used to determine the kinetic constant. The first is the one mentioned before, which is based on a linear regression. The second is the approach adopted by Barker and coworkers in the Multiwell program suite,<sup>61</sup> for which the kinetic constant is calculated as the inverse of the sum of the time that each molecule has taken to react divided by the total simulation time. The third is the direct evaluation of the kinetic constant from RRKM rates weighted over the energy distribution function calculated stochastically from the time spent in each energy bin.

The convergence criteria can thus be defined as the limit at which the rate coefficients calculated using the three different approaches reach a constant value, which was defined as the iteration at which the student’s  $t$  test limit has a 1% confidence limit.

The adoption of a discrete formulation of the master equation and its direct stochastic integration has several advantages over direct numerical integration, among which the most significant is the possibility to solve the ME without introducing any restrictive approximation to the set of integral-differential equations considered, which is often necessary to make the ME numerically tractable. A second advantage of this approach is that both transitions among energy bins and reactions are treated similarly as independent events characterized by a specific transition frequency. This permits us to avoid the normalization of the collisional transfer matrix over the total number of collisions. Lastly, since one molecule at time is considered for each simulation and successive simulations are independent, it is possible to run the simulations in parallel on multiple processors.

### 3.3. Overcoming TST Limitations – MCRRKM Development

The following paragraph presents the theories adopted to overcome the transition state limitations encountered in the course of the present project and the details of their implementation in to the MCRRKM code.

#### 3.3.1. Spin Forbidden Reactions

Spin forbidden reactions are a particular class of reactions in which a change of spin state occurs. They are said to be non-adiabatic in the sense that they occur on multiple energy surfaces. Generally, to undergo a transformation from reactant to products these systems need to “hop” from one energy surface, corresponding to the spin state of the reactant, to another one, that corresponds to the spin state of the product. However, reactions that require more than one hop can also occur, which means that a reaction with reactants and products that have the same spin state may also be spin forbidden.

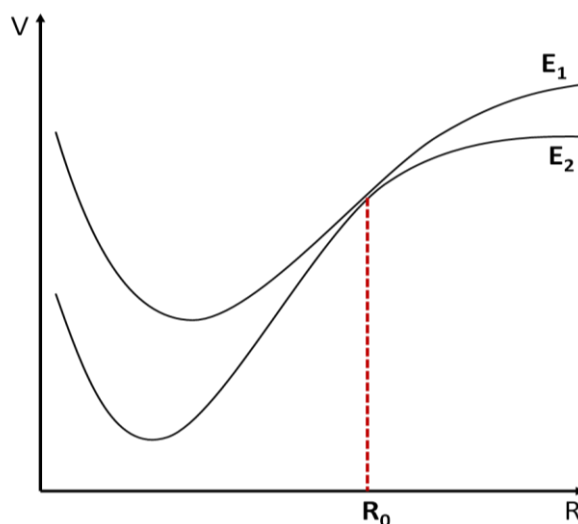


**Figure 13.** *Schematic crossing of a singlet-triplet crossing.*

Still, the essential features of a spin forbidden reaction may be illustrated in the crossing of a singlet and triplet state of a molecule, as represented in **Figure 13**.

#### Derivation of the Hopping Probability – Landau-Zener Theory

Let  $\psi_1(x/R)$  and  $\psi_2(x/R)$  be the two electronic wave functions of the molecule and let them have the following properties:

- (1)  $\psi_1(x/R)$  is a singlet state for  $R < R_0$  and a triplet state for  $R > R_0$ .
- (2)  $\psi_2(x/R)$  is a triplet state for  $R < R_0$  and a singlet state for  $R > R_0$ .

The adiabatic theorem says that if the molecule is initially in state  $\psi_2$  and  $R$  changes infinitely slowly from  $R < R_0$  to  $R > R_0$  then the molecule will remain in state  $\psi_2$ . However, if  $R$  changes with finite velocity, the final state will be a linear combination of the two.

Let  $\phi_1$  and  $\phi_2$  be such linear combination of  $\psi_1$  and  $\psi_2$ , that for all values of  $R$ ,  $\phi_1$  has the characteristics which  $\psi_1$  has at  $R > R_0$ , while  $\phi_2$  has the characteristics which  $\psi_2$  has at  $R > R_0$ . In this way  $\phi_1$  is a pure triplet state while  $\phi_2$  is a pure singlet state.

In this framework the Schrödinger equation for  $\phi_1$  and  $\phi_2$  can be written as:

$$\begin{cases} H\phi_1 = \varepsilon_1\phi_1 + \varepsilon_{12}\phi_2 \\ H\phi_2 = \varepsilon_{12}\phi_1 + \varepsilon_2\phi_2 \end{cases} \quad (51)$$

Introducing the following assumptions:

- $\varepsilon_{12}(R_0) \ll$  the relative kinetic energy of the two systems. With this condition, the motion of the centers of gravity of the two atoms can be treated as an external parameter.
- The transition region is small to the point that in it we may consider  $\varepsilon_1 - \varepsilon_2$  as a linear function of time and  $\varepsilon_{12}(R)$ ,  $\phi_1(x/R)$  and  $\phi_2(x/R)$  as independent of time. This is true if  $\varepsilon_{12}(R_0)$  is sufficiently small.

If the relative velocity of the two systems is constant, assumption b) leads to the relationship shown in **Figure 14** between  $\varepsilon_1(R)$ ,  $\varepsilon_2(R)$  and the eigenvalues of  $\psi_1$  and  $\psi_2$ , that are  $E_1(R)$  and  $E_2(R)$ .  $E_1(R)$  and  $E_2(R)$  are hyperbolae having  $\varepsilon_1(R)$  and  $\varepsilon_2(R)$  as asymptotes. The closest distance between  $E_1$  and  $E_2$ , that is,  $E_1(R_0) - E_2(R_0)$ , is given by  $2\varepsilon_{12}(R_0)$ .

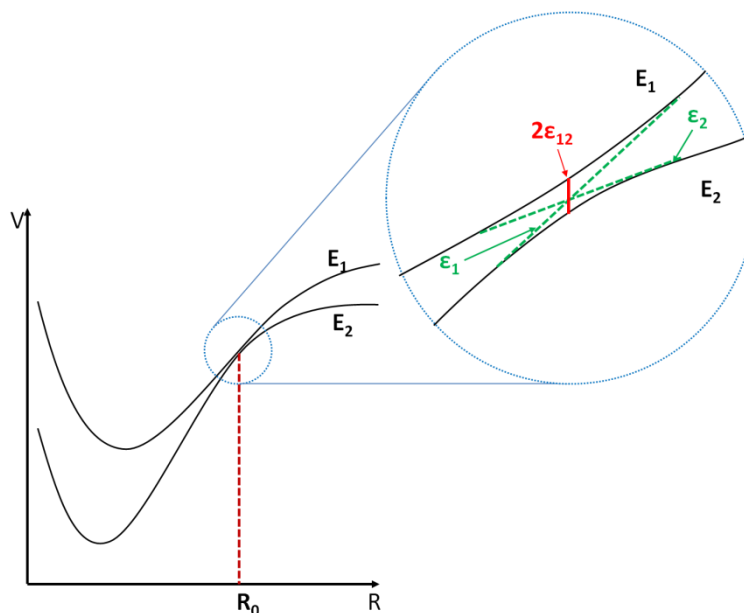


**Figure 14.** Schematization of singlet-triplet state crossing with evidence on the transition region.

With these assumptions, it is possible to solve the wave equation, obtaining the probability,  $P$ , of a non-adiabatic transition. The solution has been found analytically by Zener<sup>73</sup> in 1935 in the form:

$$P = \exp\left(-\frac{2\pi\varepsilon_{12}^2}{\hbar}\left/\left|\frac{d}{dt}(\varepsilon_1 - \varepsilon_2)\right|\right.\right) \quad (52)$$

and contemporarily Landau<sup>74</sup> obtained a very similar result

$$P \sim \exp\left(-\frac{\pi}{2h\nu}\frac{\Delta^2}{(F_1 - F_2)}\right) \quad (53)$$

with  $\nu$  the relative velocity,  $\Delta=2\varepsilon_{12}$  and  $F_1$  and  $F_2$  are the forces that act upon the two states.

With the identification of  $\frac{d}{dt}(\varepsilon_1 - \varepsilon_2) = \nu(F_1 - F_2)$ , the two formulas are identical with Landau's exponent being smaller only by a factor of  $2\pi$ . This expression takes the name Landau-Zener formula and it is commonly written as:

$$P_{LZ}(E) = \exp\left(-\frac{2\pi H_{SO}^2}{\hbar\Delta F}\sqrt{\frac{\mu}{2E}}\right) \quad (54)$$

where  $H_{SO}$  corresponds to  $\varepsilon_{12}$ , the off-diagonal spin-orbit coupling element of the Hamiltonian matrix between two general electronic states,  $\Delta F$  is the relative slope of the two surfaces at the crossing point.  $\nu = \sqrt{\frac{\mu}{2E}}$ , where  $\mu$  is the reduced mass and  $E$  the kinetic energy of the system as it moves through the crossing point.

The probability of hopping after a double passage is expressed as

$$p_{hop}(E) = (1 - P_{LZ})(1 + P_{LZ}) \quad (55)$$

that is the sum of the probability of hopping on the first pass ( $1 - P_{LZ}$ ) plus the probability of hopping not on the first but at the second pass ( $P_{LZ}(1 - P_{LZ})$ ).<sup>75</sup>

### Micro-canonical Rate Coefficients for Spin Forbidden Reactions

Once the probability to hop from an electronic state to another has been determined, it is relatively easy to introduce this element into the definition of the RRKM rate constant.

As in simple RRKM theory, the density of states can be expressed as the convolution of the densities of states of different separable degrees of freedom. Let us consider the single degree of freedom as the ‘‘hopping’’ coordinate, which is  $R$  in **Figure 13** and **Figure 14**, and assume it is separable from the ‘‘spectator’’ rotational and vibrational degrees of freedom. Then, we can compute the total density of states as a convolution between the probability of hopping from one surface to another at energy  $E$ ,  $p_{hop}(E)$ , and the rovibrational density of states  $\rho(E)$

$$N^\ddagger(E) = \int \rho^\ddagger(E - E^I)p_{hop}(E^I - E_0)dE^I \equiv \int \rho^\ddagger(E^I)p_{hop}(E - E^I - E_0)dE^I \quad (56)$$

Thus, the microcanonical rate coefficient,  $k(E, J)$ , can be written as:

$$k(E, J) = \frac{\int_0^{E-E_0} \rho^\ddagger(E^I, J)p_{hop}(E - E^I - E_0)dE^I}{h\rho(E, J)} \quad (57)$$

This approach made popular by Harvey<sup>75</sup> is named ‘‘Non-adiabatic Transition State Theory’’ and has the ability to extend the application of RRKM theory also to spin forbidden reactions.

## Details of Implementation

As stated before, the implementation of non-adiabatic transition state theory is quite straightforward once the hopping probability is known as a function of energy  $E$ . However, to determine the hopping probability with the expression given by Landau-Zener theory:

$$P_{LZ}(E) = \exp\left(-\frac{2\pi H_{SO}^2}{\hbar\Delta F} \sqrt{\frac{\mu}{2E}}\right) \quad (58)$$

we need the following parameters:

- $\Delta F$  – the relative slope of the energy surfaces of the two electronic states at the crossing point.
- $H_{SO}$  – the off-diagonal spin-orbit coupling element of the Hamiltonian matrix between the two states at the crossing point.

Both parameters are properties of the crossing point, thus, the first step in our protocol is the location of the minimum energy crossing point (MECP).

Several alternative ways to locate the crossing region have been suggested. In this procedure we have adopted the most common method also called by Harvey<sup>75</sup> the “partial optimization” method. This method in fact involves a series of geometry optimization on both potential energy surfaces with a particular reaction coordinate (that can be a bond length or an angle between two bonds) constrained to a series of different values. This scan of the two potential energy surfaces generates two cuts that may eventually cross at certain values of the chosen coordinate.

When the structure of the crossing point has been determined, it is possible to calculate the properties we are interested in and successively apply non-adiabatic transition state theory.

### 3.3.2. The 1D Hindered Rotor Approximation

One of the limitations of standard TST comes from the definition of the reactants and transition state partition functions, in which all-internal motions are treated in the harmonic oscillator approximation. This approximation however fails in the case of torsional modes that are characterized by very low frequencies.<sup>76</sup> These motions cannot be treated as vibrations, but have to be treated as internal rotations.

The internal rotations of a molecule can be distinguished into two classes: free rotors and hindered rotors. However, internal rotations are often subject to hindrances due to the steric interactions between the parts of the molecule that move relative to each other.

A common procedure<sup>77</sup> adopted for the treatment of hindered rotors starts with the assumption that it is possible to count separately the contribution of each degree of freedom. In this way, we assume that the possible internal rotations of a molecule are not coupled and we treat each rotor with an effective one-dimensional Hamiltonian. It is necessary to say that this is an approximate treatment and that using this assumption may sacrifice accuracy in cases of highly coupled rotations. However, the extreme difficulty of treating multidimensional problems, especially for large

systems, lets us presume that the assumption of uncoupled rotors will still be commonly exploited in the near future.

The steps of the adopted procedure are the following:

- (1) calculation of the rotational potential energy surface.
- (2) calculation of the reduced internal moment of inertia.
- (3) solution of the 1D rotational Schrödinger equation.
- (4) calculation of the partition function of the internal rotation energy levels.

### Rotational Potential Energy Surface

The first step in the hindered rotor approach is the computation of the potential energy surface for each rotation (an example is given in **Figure 15**).

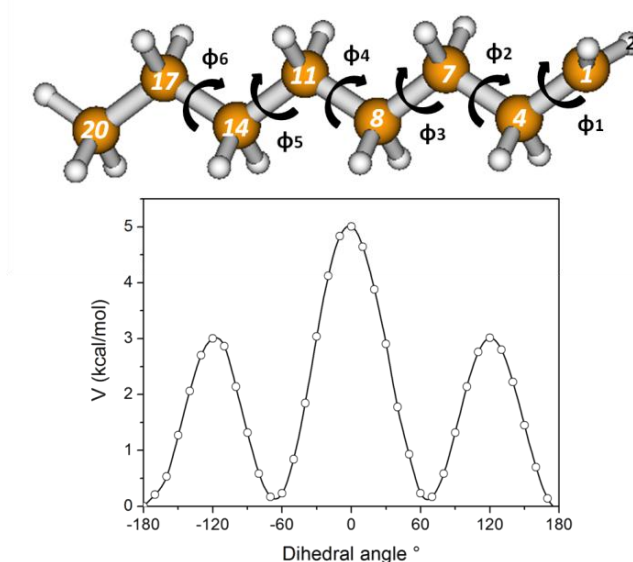


**Figure 15.** Scheme of internal rotations for the 1-octyl radical and the potential energy surface for the rotation around the dihedral angle  $\phi_2$ .

The potential energy surface for the rotation can be determined with constrained optimizations. More specifically, for a number of fixed values of the dihedral angle corresponding to the rotation of interest, one calculates the minimum energy structure of the molecule.

### Reduced Internal Moment of Inertia

Another important parameter that needs to be defined is the reduced moment of inertia. Even if the present approach does not account for potential coupling, it can account for kinetic coupling via reduction of the internal moments of inertia. A thorough exposition of this reduction and various approximations used to evaluate inertia moments for internal rotations was presented in a detailed analysis performed by East and Radom.<sup>78</sup>

They introduced the notation  $I^{(m,n)}$  to classify the various approximations available. Here  $n$  indicates the level of approximation for a rotor attached to a fixed frame before any reduction, while the  $m$  indicates the level of approximation of the coupling reduction. Moreover, since it is possible to arbitrarily choose either end (“left” or “right”) of the twisting bond also a subscript L or R was added.

If  $n = 1$ , the moment of inertia of the rotating group is computed about the axis containing the twisting bond. If  $n = 2$ ,  $I$  is computed about the axis parallel to the bond but passing through the center of mass of the rotating group. If  $n = 3$ ,  $I$  is computed about the axis passing through the centers of mass of the rotating group and the remainder of the molecule. An illustrative scheme is presented in **Figure 16**.

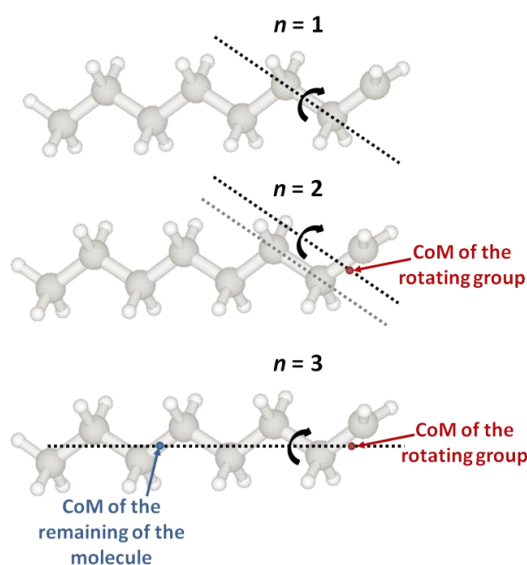


**Figure 16.** Schematic representation of the axis considered for each  $n$  index introduced by East and Radom.

If  $m = 1$ , the moment of inertia of the rotating group is not reduced. If  $m = 2$ , the reduced moment due to coupling with the overall rotation is approximated by

$$\frac{1}{I^{(2,n)}} = \frac{1}{I_L^{(1,n)}} + \frac{1}{I_R^{(1,n)}} \quad (59)$$

In their dissertation, East and Radom listed also approximations for  $m = 3$  and  $m = 4$ , that represent higher levels of approximation of the coupling reduction. However their description should require a deeper analysis and this goes beyond the scope of the present thesis, thus we refer to their paper for further details.<sup>78</sup>

In our procedure, we choose to calculate the moments of inertia of the systems investigated with  $m = 2$ . The reason behind this choice can be found in the robustness and the reasonable accuracy by which this method is characterized. In fact, once more East and Radom demonstrated that the mo-

ment of inertia calculated as  $I^{(2,1)}$ , with respect to  $I^{(3,1)}$  and  $I^{(4,1)}$ , generally lies within 5% of the best values and only in a small number of cases the error can be as large as 30%.

### 1D Rotational Schrödinger Equation

Once the potential and the moment of inertia have been obtained, the energy levels can be computed solving the 1D rotational Schrödinger equation:

$$-\frac{\hbar^2}{2I_r} \frac{\partial^2 \Psi}{\partial \phi^2} + V(\phi) \Psi(\phi) = \varepsilon \Psi(\phi) \quad (60)$$

where  $I_r$  is the reduced moment of inertia for the rotating top and  $V(\phi)$  is the rotational hindrance potential and  $\phi$  is the rotational angle.

The solution of the Schrödinger equation adopting a finite difference method and the rotational potential fitted with a Fourier series expansion was implemented and tested in a work<sup>79</sup> previous to this thesis, which was developed following the procedure suggested by Van Speybroeck et al.<sup>80</sup>

### Partition Function for an Internal Rotation

For each eigenvalue  $\varepsilon_k$  calculated there is a corresponding accessible rotational energy level and they can be used to calculate directly the partition function for the associated internal rotation  $i$ , which is expressed as:

$$q_{IR,i} = \frac{1}{\sigma_{IR}} \sum_k g_k \exp\left(-\frac{\varepsilon_k}{k_B T}\right) \quad (61)$$

where  $g_k$  is the degeneracy of the rotational energy level  $\varepsilon_k$  and  $\sigma_{IR}$  is the symmetry number of the internal rotation.

Internal rotations can be found both in the reactant and in the TS vibrational analysis. Hence, the procedure described so far can be applied to conventional transition state theory introducing the partition functions calculated for all the internal rotations of the system (both in the reactants and the TS) as follows:

$$k = \frac{k_B T}{h} \frac{Q_{IR}^\ddagger Q^\ddagger}{Q_{IR}^R Q^R} \exp\left(\frac{-E_A}{k_B T}\right) \text{ with } Q_{IR} = \prod_i q_{IR,i} \quad (62)$$

taking care to eliminate from the computation of the vibrational partition function the low frequencies corresponding to the internal rotations individuated.

The next paragraph describes the approach implemented in order to extend the present approximation to RRKM rate coefficients estimation.

### Hindered Rotor Approximation within the Microcanonical Ensemble

In order to include the 1D hindered rotor approximation in our combined ME/RRKM approach, we implemented a new algorithm within the MCRRKM code able to compute the density of states for each internal rotation separately and then calculate the overall rovibrational density of states.

It is known that the overall density of states can be expressed, within the approximation of separable degrees of freedom, as the convolution of the density of states of individual modes. Thus, we computed the density of states for the hindered rotors by direct count of the quantized energy levels that were within the energy range  $E$  to  $E+\Delta E$ , with  $\Delta E$  equal to  $1\text{ cm}^{-1}$ . The spectrum of eigenvalues for each hindered rotor is obtained by solving the 1D rotational Schrödinger equation as previously described. Moreover, for those species with more than one internal hindered rotation, we first sum the eigenvalues related to the degrees of freedom under consideration and then successively convolute the density of states as mentioned above.

Successively, this density was convoluted with the vibrational density of states using the Beyer-Swinehart algorithm with an initialization vector that contains the density of states previously evaluated for internal rotations, as suggested by Astholz et al.<sup>81</sup> Utilizing this estimation of the rovibrational density of states for both reactant and transition state in the presence of degenerate torsional modes it is possible to evaluate the microcanonical rate coefficient corrected by the hindered rotor approximation.

### 3.3.3. Multi-well Reactions

Here, the single well integration protocol of the master equation described previously has been extended to describe the unimolecular reaction dynamics that takes place over a multiple well potential energy surface.

Multi-well reactions take place when it is necessary to pass through several intermediates before reaching the reaction bottleneck. A schematic example of a multiple well reaction is depicted in **Figure 17**. In this scheme, in fact, we can observe how molecule A undergoes a series of jumps up and down the possible energy levels before converting into intermediate  $B^*$  through transition state TS1. This intermediate in turn can convert back into reactant A or transform into another isomer,  $C^*$ . Finally,  $C^*$  can also interconvert into  $B^*$  again or yield the product D, through TS3.

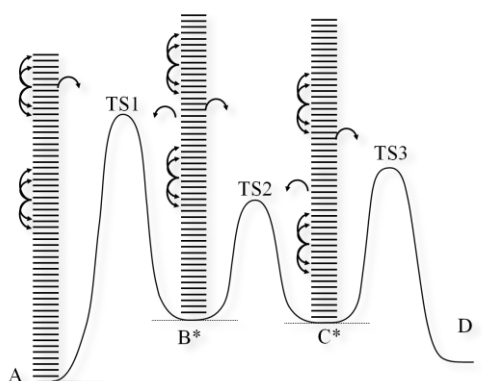


**Figure 17.** Scheme of a unimolecular multiple well reaction where reactant A needs to interconvert into complex  $B^*$  and  $C^*$ , through transition states TS1 and TS2, before transforming into the product D.

To simulate this process we updated the MCRRKM code allowing for the excited molecule (A) the possibility to react to a different energetic state or well (B\*), that has different collisional transitional probabilities between the energy levels and RRKM reaction rates. Moreover, the new energetic state reached through the reaction will differ from the starting one for the reaction energy change.

As we have described before, the computational procedure is designed so that reaction and transitional collisional properties for all the considered wells and transition states are calculated before the ME integration cycle. Afterwards, during the ME simulation information about previous collisional or reacting steps as well as the time spent in each energy level are also stored with an efficient binary tree algorithm.<sup>70</sup>

This protocol yields a computational efficiency that is independent of the size, in terms of the number of wells and transition states, of the PES and makes the present approach particularly apt to study complex reacting systems, in which many wells can be visited from an excited complex before a reaction takes place.

It is important to highlight that we consider a hypothetical circumstance in which all products are removed from the system the instant they appear. This allows us to calculate the rate coefficient assuming that the rate law can be expressed as:

$$\frac{dn_i}{dt} = -k_D n_i \quad (63)$$

where  $n_i$  is the concentration of the reactant. The rate coefficient  $k_D$  for each reaction channel is then calculated through a linear regression over the stochastic reaction times.

In calculating the rate coefficient using this equation we make two important assumptions, which are the elimination of the backward reactions and the hypothesis that the contribution to the rate coefficient from stabilized intermediate wells is not significant.

The rate coefficient determined through this approach represents a flux coefficient, i.e. the coefficient that multiplied by the reactant concentration gives the number of molecules that per unit time and volume are converted to the reaction product. As clearly explained by Widom<sup>82</sup> in a seminal paper published several decades ago, this coefficient is not equal to the phenomenological rate coefficient, which is the rate coefficient accessible to experimental measurements. The difference between phenomenological rate coefficients and reaction fluxes is subtle and counterintuitive, as reviewed recently by Miller and Klippenstein.<sup>83</sup> However, it is likely that this difference may not be too large for most of the cases investigated in the present project. In fact, the products of the decomposition reactions considered are usually present in very low concentrations in reaction environments in which these reactions are active due to fast secondary reactions channels, so that the irreversible sink assumption most probably holds. In addition, the stabilization of intermediate

wells is most of the times negligible, if otherwise it will be pointed out in the discussion of the results.

### 3.3.4. Tunneling Effect

From a molecular point of view, a reaction consists of a conformational rearrangement of the atoms that can be interpreted, according to transition state theory, as a relative motion of a part of the molecule along a reaction coordinate. Moving along the reaction coordinate from the configuration of the reactants to that of products there is an increase in the energy of the system. Then, if the formation of the products leads to stabilization, the energy of the system decreases. It is thus comparable to the motion of a particle along a potential energy surface in which the reacting event is contextual to the crossing of an energy barrier.

In classical mechanics, a particle in motion is able to overcome an energy barrier only if the sum of its kinetic and potential energy is higher than the height of the barrier itself. In quantum mechanics, the situation is different, since the same particle is able to overcome the barrier even if its energy is lower than the barrier. This phenomenon, which is purely quantum, is known as tunneling.

Various methods have been developed to account for the tunneling effect in reaction rate estimation. They can be classified in two categories depending on the approach adopted to solve the Schrödinger equation. The first class includes the early methods proposed in literature. They are based on the solution of the 1D Schrödinger equation introducing a parabolic function to approximate the potential energy barrier. The quantum mechanical transmission coefficient through this barrier is obtained with both approximated<sup>84,85</sup> and analytical solutions.<sup>86</sup> Another similar approach has been formulated by Eckart.<sup>87</sup> In detail, Eckart proposed a new functional form to approximate the shape of the potential energy barrier and its asymptotic properties. Notably, he also provided the analytical solution of the associated Schrödinger equation, leading to the formulation of a relatively simple expression for the microcanonical transmission probability.

In the following decades, a new class of methods has been introduced in order to account for tunneling in reacting systems with improved accuracy. It had in fact been shown that the integration of the 1D Schrödinger equation over the standard transition state theory tunneling path, which is the minimum energy path (MEP), leads to significant underestimation of the tunneling coefficient. To explain this effect Marcus and Coltrin proposed for the  $\text{H}_2 + \text{H}$  reaction an alternative tunneling path, removed from the MEP by an orthogonal displacement equal to the maximum vibrational amplitude.<sup>88</sup> Successively Truhlar and co-workers extended the Marcus and Coltrin path to a multiatomic system using the harmonic vibrational frequencies of the Hessian defined by the reaction path Hamiltonian proposed in a seminal paper by Miller, Handy, and Adams.<sup>89</sup> The Truhlar theory was named Small Curvature Tunneling (SCT) and it is currently among the most effective approaches for the calculation of accurate quantum tunneling effects.<sup>90,91</sup>

In this work, we implemented two approaches to estimate tunneling correction coefficients that will be described here: the Eckart model and SCT theory.

### Eckart Model

The tunneling effect is a quantum mechanical phenomenon that can be evaluated by solving the Schrödinger equation for a particle moving in a one-dimensional direction in the presence of an energetic barrier  $V(x)$ :

$$\frac{\hbar^2}{2m} \frac{\partial^2 \Psi}{\partial x^2} + V(x)\Psi = E\Psi \quad (64)$$

where  $\hbar$  is Planck's constant,  $m$  is the mass of the moving particle,  $E$  is the energy and  $x$  is the reaction coordinate.  $V(x)$  is the potential energy surface.

The tunneling effect takes place when the particle can pass the barrier even for energy values lower than the potential energy. The probability that such an event happens is called the transmission probability. The functional form of the asymmetric potential proposed by Eckart is illustrated in **Figure 18** and expressed as:

$$V(x) = -A \frac{\xi}{1-\xi} - B \frac{\xi}{(1-\xi)^2} \quad \text{with} \quad \xi = -\exp\left(\frac{2\pi x}{l}\right) \quad (65)$$

where  $A$ ,  $B$  and  $l$  are parameters.

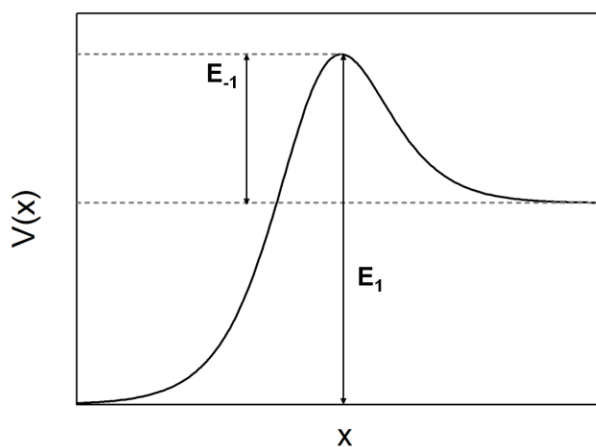


**Figure 18.** Example of Eckart Potential as a function of the reaction coordinate  $x$ . In evidence are the forward activation energy  $E_1$  and the backward activation energy  $E_{-1}$ .

Eckart integrated Equation ( 64 ) analytically using hyper geometric series. The wave function determined is the sum of an incident and a reflected wave function. The ratio of their amplitudes gives the reflection probability, from which the transmission or tunneling probability can be computed as:

$$P(E) = 1 - \frac{\cosh(2\pi(\alpha - \beta)) + \cosh(2\pi\delta)}{\cosh(2\pi(\alpha + \beta)) + \cosh(2\pi\delta)} \quad (66)$$

Where

$$\alpha = \frac{1}{2} \left( \frac{E}{C} \right)^{1/2}, \beta = \frac{1}{2} \left( \frac{E-A}{C} \right)^{1/2}, \delta = \frac{1}{2} \left( \frac{B-c}{C} \right)^{1/2} \text{ and } C = \frac{\hbar^2}{8\mu l^2} \quad (67)$$

The parameters  $A$ ,  $B$ , and  $l$  can be computed applying three conditions to the Eckart potential energy surface. The first one equals the asymptotic limit of the PES to the reaction energy and allows calculating  $A$  as:

$$A = E_1 - E_{-1} \quad (68)$$

The second condition equals the maximum on the PES to the forward activation energy and gives  $B$ :

$$B = (\sqrt{E_1} - \sqrt{E_{-1}})^2 \quad (69)$$

Finally, it is possible to determine  $l$  imposing that the imaginary frequency is equal to the value of the second derivative of the PES with respect to the reaction coordinate:

$$l = \frac{1}{|v|} \sqrt{\frac{2E_1 E_{-1}}{\mu} \frac{1}{\sqrt{E_1} + \sqrt{E_{-1}}}} \quad (70)$$

It is possible to notice that the only parameters necessary to apply the Eckart model for the estimation of the transmission probability are  $E_1$  and  $E_{-1}$ , that are the activation energy barriers for the forward and backward reactions and  $v$ , that is the TS imaginary frequency.

### Centrifugal-Dominant Small Curvature Tunneling Theory – SCT

The Schrödinger equation for a particle moving in a one-dimensional direction in the presence of an energetic barrier  $V(x)$  can be expressed also in the form:

$$\Psi''(x) + Q(x)\Psi(x) = 0 \quad (71)$$

with

$$Q(x) = \frac{2m}{\hbar^2} (E - V(x)) \quad (72)$$

where  $m$  is the mass of the particle in motion and  $E$  is the energy of the particle.

The Small Curvature Tunneling theory proposed by Truhlar and coworkers<sup>90</sup> starts from the semiclassical solution of the Schrödinger equation. Within this approximation, the transmission probability has the form:<sup>92-95</sup>

$$P(E) = \frac{1}{1 + e^{2\theta(E)}} \quad (73)$$

with

$$\theta(E) = \int \sqrt{-Q(x)} dx = \frac{1}{\hbar} \int \sqrt{2m(V(x) - E)} dx \quad (74)$$

where  $\theta(E)$  is the imaginary action integral, i.e. the imaginary part of the integral of the conjugated momentum. It is possible to extend this result, valid for a particle in 1D motion, to the relative motion of two reacting molecules by substituting the mass of the particle  $m$  with the reduced mass

of the reacting moieties  $\mu$  and adopting as the direction of motion the reaction coordinate  $s$ . The imaginary action integral becomes:

$$\theta(E) = \frac{1}{\hbar} \int_{s1}^{s2} \sqrt{2\mu(V(s) - E)} ds \quad (75)$$

where  $s1$  and  $s2$  are the turning points for which holds  $V(s) = E$ . The potential energy that needs to be considered is the sum of the electronic energy at the ground state along the minimum energy path,  $V_{MEP}$ , plus the zero-point energy of the reacting molecules along the reaction coordinate  $s$ :

$$V(s) = V_{MEP}(s) + \frac{1}{2} \sum_i^{3N-7} \hbar\omega_i(s) \quad (76)$$

with  $\omega_i = 2\pi\nu_i$  as the frequency of the  $i$ -th mode of vibration and the sum made over all the vibrational modes orthogonal to the reaction coordinate at  $s$ . Details about the computation of the  $V_{MEP}$  and the frequencies along the reaction path will be discussed later.

Marcus and Coltrin<sup>88</sup> were the first to suggest the possibility that when tunneling takes place the reacting molecules do not move along the minimum energy path (the  $s$ -curve or MEP) but along a shorter path that they called “tunneling path” ( $t$ -curve). They applied their method to the collinear  $H + H_2$  reaction, which potential energy is depicted in **Figure 19**.

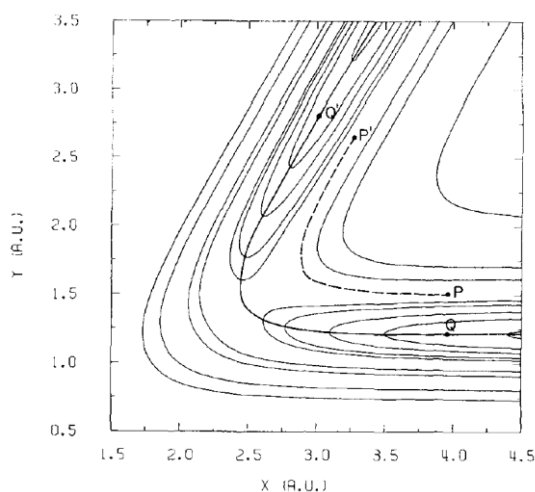


**Figure 19.** Plot of the potential energy contours for the  $H + H_2 \rightarrow H_2 + H$  using the Porter–Karplus<sup>96</sup> surface taken from ref<sup>88</sup>. Solid line is the reaction path. Dotted line is the  $t$ -curve. The point  $P$  and  $P'$  denote the initial and final tunneling points on the  $t$ -curve for a particular total energy. The corresponding points on the reaction path are  $Q$  and  $Q'$ .

In this figure in particular are depicted two lines: the one connecting  $Q'$  and  $Q$  represents the MEP while the other one connecting  $P'$  and  $P$  is the tunneling path or  $t$ -curve. The  $t$ -curve is positioned on the concave side of the MEP because it has been observed that in the presence of tunneling there is a negative centrifugal effect that allows the molecules to cut the corner of the reaction path increasing the reaction velocity.<sup>97,98</sup>

To ease the comprehension of the method it is opportune to introduce a coordinate perpendicular to the  $s$ -curve, denoted by  $\rho(s)$ , as a measure of the distance from the tangent to the  $s$ -curve and the potential energy associated to the vibrational motion along  $\rho$ , represented by  $V_2(s, \rho)$

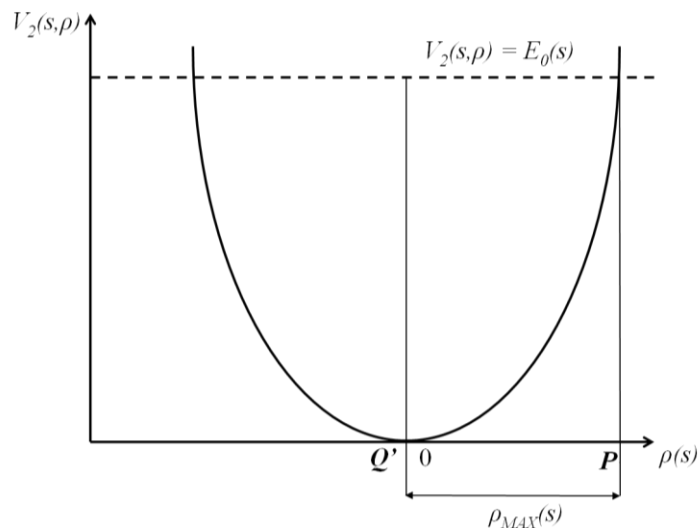


**Figure 20.** Potential energy associated to the vibrational motion along  $\rho$ .

Marcus and Coltrin<sup>88</sup> identified the  $t$ -curve defining its distance from the MEP as a function of the reaction coordinate. This distance corresponds to the maximum vibrational amplitude at a given  $s$ ,  $\rho_{MAX}(s)$ , that is reached when  $V_2(s, \rho)$  is equal to the zero point energy at  $s$ ,  $E_0(s)$ , as it is represented in **Figure 20** in correspondence of the  $Q'$  point on the  $s$ -curve shown in **Figure 19**.

$V_2(s, \rho)$  can be expressed as:

$$V_2(s, \rho) = \frac{1}{2} k(s) \rho^2 \quad (77)$$

where  $k(s)$  is the force constant associated to the vibrational motion, that can be written as

$$k(s) = 4\pi^2 \nu^2(s) \mu \quad (78)$$

Here  $\nu(s)$  is the vibrational frequency associated to the motion in the  $\rho$  direction and  $\mu$  is the mass correspondent to the moving moiety. The zero-point energy correspondent to the same vibrational motion is

$$E_0(s) = \frac{1}{2} h \nu(s) \quad (79)$$

The value of  $\rho$  for which the condition  $V_2(s, \rho) = E_0(s)$  is satisfied is

$$\rho_{MAX}(s) = \sqrt{\frac{h}{4\pi^2 \nu(s) \mu}} = \sqrt{\frac{\hbar}{\omega(s) \mu}} \quad (80)$$

The family of points  $[\rho_{MAX}(s), s]$  describes the  $t$ -curve.

Once the  $t$ -curve is known, the imaginary action integral can be calculated over this path, thus taking into account the contribution of the curvature while computing the transmission probability.

The method described thus far is valid for systems where the curvature is small and is mainly confined to a single normal mode of vibration orthogonal to the reaction coordinate.

Truhlar and coworkers<sup>90</sup> generalized this method introducing the concept for which the curvature of the MEP and the negative centrifugal effect associated can be thought of as a lowering of the effective mass of the motion along the s-curve. In order to apply this concept they first formulated the geometrical relationship between the s-curve and the t-curve as:

$$d\xi = \sqrt{(1 - \kappa(s) \cdot t(s))^2 + \left(\frac{dt(s)}{ds}\right)^2} ds \quad (81)$$

where  $\xi$  is the distance along the tunneling path,  $t(s)$  is the distance of the t-curve from the MEP (and corresponds to the  $\rho_{MAX}(s)$  of Marcus and Coltrin<sup>88</sup>) and  $\kappa(s)$  is the curvature of the s-curve.

Defining the effective reduced mass as:

$$\mu_{eff}(s) = \mu \left( (1 - \kappa(s) \cdot t(s))^2 + \left(\frac{dt(s)}{ds}\right)^2 \right) \quad (82)$$

it is possible to compute the imaginary action integral not over the tunneling path, but over the minimum energy path:

$$\theta(E) = \frac{1}{\hbar} \int_{s_1}^{s_2} \sqrt{2\mu_{eff}(s)(V(s) - E)} ds \quad (83)$$

With the intention of removing singularities and taking only those results for which  $\mu_{eff} < \mu$  Truhlar group in the work of Skodje et al.<sup>90</sup> expressed  $\mu_{eff}$  as:

$$\mu_{eff}(s) = \mu \cdot \min \left\{ \exp \left( -2(\kappa(s) \cdot t(s)) - (\kappa(s) \cdot t(s))^2 + \left(\frac{dt(s)}{ds}\right)^2 \right), 1 \right\} \quad (84)$$

In addition, in Lu et al.<sup>91</sup> they improved this method by adding the possibility that more than one normal mode of vibration can have an appreciable reaction path curvature. They first defined the curvature  $\kappa$  as:

$$\kappa(s) = \left( \sum_{i=1}^{3N-7} [\kappa_i(s)]^2 \right)^{1/2} \quad (85)$$

with  $\kappa_i(s)$  as the component of the reaction path curvature due to the i-th mode of vibration and subsequently substituting  $t(s)$  with  $\bar{t}(s)$  defined as:

$$\bar{t}(s) = \kappa(s)^{1/2} \left( \sum_{i=1}^{3N-7} [\kappa_i(s)]^2 [t_i(s)]^{-4} \right)^{-1/4} \quad (86)$$

where  $t_i(s)$  is the vibrational turning point of mode i. Remembering the definition of  $\rho_{MAX}$ , that is the equivalent of  $t(s)$ , we can express  $t_i(s)$  in the same way by just using the frequency of the i-th mode:

$$t_i(s) = \sqrt{\frac{\hbar}{\omega_i(s)\mu}} \quad (87)$$

Introducing this definition in equation ( 86 ) we can rewrite  $\bar{t}(s)$  as

$$\bar{t}(s) = \left( \frac{\kappa(s)\hbar}{\mu} \right)^{1/2} \left( \sum_{i=1}^{3N-7} [\kappa_i(s)]^2 [\omega_i(s)]^2 \right)^{-1/4} \quad (88)$$

Furthermore, we can introduce the variable  $\bar{a}(s)$  defined as follows:

$$\bar{a}(s) = |\kappa(s) \cdot \bar{t}(s)| \quad (89)$$

So finally, we can write the  $\mu_{eff}$  as:

$$\mu_{eff}(s) = \mu \cdot \min \left\{ \exp \left( -2\bar{a}(s) - \bar{a}(s)^2 + \left( \frac{dt(s)}{ds} \right)^2 \right) \right. \\ \left. 1 \right\} \quad (90)$$

At this point the only information necessary are the potential energy surface  $V_{MEP}(s)$ , the frequencies of the generalized normal mode of vibration  $\omega_i(s)$  calculated along the reaction path and the curvature components associated to each mode of vibration  $\kappa_i(s)$ . The computation of these parameters will be the subject of the following sections.

### Generalized normal mode analysis – $\omega_i(s)$

The first thing that is necessary to do once the IRC calculation has been carried out is to compute the center of mass of the system and translate it to the origin. We can calculate the center of mass as:

$$\vec{R}_{CoM} = \frac{\sum_i^N m_i \vec{R}_i}{\sum_i^N m_i} \quad (91)$$

with  $N$  the number of atoms of the system and  $\vec{R}_i = \{x_i, y_i, z_i\}$  the Cartesian coordinates of atom  $i$ , and  $m_i$  the mass of atom  $i$ . It is then straightforward to translate the  $\vec{R}_{CoM}$  to the origin

$$\vec{r}_i = \vec{R}_i - \vec{R}_{CoM} \quad (92)$$

with  $\vec{r}_i = \{x_i, y_i, z_i\}$  as the coordinates in the new reference system. It is convenient at this point to calculate the moments of inertia tensor

$$\mathbf{I} = \begin{pmatrix} I_{xx} & I_{xy} & I_{xz} \\ I_{yx} & I_{yy} & I_{yz} \\ I_{zx} & I_{zy} & I_{zz} \end{pmatrix} = \begin{pmatrix} \sum_i m_i (y_i^2 + z_i^2) & -\sum_i m_i (x_i y_i) & -\sum_i m_i (z_i x_i) \\ -\sum_i m_i (x_i y_i) & \sum_i m_i (x_i^2 + z_i^2) & -\sum_i m_i (y_i z_i) \\ -\sum_i m_i (z_i x_i) & -\sum_i m_i (y_i z_i) & \sum_i m_i (x_i^2 + y_i^2) \end{pmatrix} \quad (93)$$

By diagonalization of this matrix, we obtain the principal moment of inertia as the eigenvalues and a  $3 \times 3$  matrix ( $\mathbf{X}$ ) made up of the normalized eigenvectors of  $\mathbf{I}$ .

Now we can calculate the frequencies of the generalized normal modes of vibration along the reaction path. This was realized implementing the normal mode analysis proposed by Miller, Handy and Adams<sup>89</sup> in their study on the reaction path Hamiltonian. The Hessian, also called the force constant matrix, is acquired from the IRC calculation and contains the second partial derivatives of

the potential  $V$  with respect to the displacements of atoms in Cartesian coordinates (CART). It can be written as:

$$F_{CARTij} = \left( \frac{\partial^2 V}{\partial \xi_i \partial \xi_j} \right) \quad (94)$$

This is a  $3N \times 3N$  matrix, with  $N$  the number of atoms, where  $\xi_1, \xi_2, \dots, \xi_{3N}$  are the displacements in Cartesian coordinates, i.e.  $\Delta x_1, \Delta y_1, \Delta z_1, \dots, \Delta x_N, \Delta y_N, \Delta z_N$ . Firstly, we need to convert the force constant matrix to mass weighted Cartesian coordinates (MWC),  $q_i = \sqrt{m_i} \xi_i$ :

$$F_{MWCij} = \left( \frac{\partial^2 V}{\partial q_i \partial q_j} \right) = \frac{F_{CARTij}}{\sqrt{m_i m_j}} \quad (95)$$

For saddle points and minima of potential surfaces it is common to carry out normal mode frequency analyses by diagonalizing the force constant matrix in mass weighted Cartesian coordinates after having separated out external translations and rotations. However, to obtain the normal coordinates for vibrations orthogonal to the reaction path it is necessary to also project out the motion along the reaction coordinate.

Miller, Handy and Adams<sup>89</sup> proposed to calculate the projected force constant matrix as follows:

$$\mathbf{F}_{MWC}^P = (\mathbf{1} - \mathbf{P}) \cdot \mathbf{F}_{MWC} \cdot (\mathbf{1} - \mathbf{P}) \quad (96)$$

where  $\mathbf{F}_{MWC}$  is the matrix whose elements are  $F_{MWCij}$ ,  $\mathbf{1}$  is the identity matrix and  $\mathbf{P}$  is the projector matrix. The projector  $\mathbf{P}$  is a  $3N \times 3N$  matrix made up of three terms, one for the translations  $P_T$ , one for the rotations  $P_R$  and one for the reaction coordinate  $P_{rc}$ :

$$P_{ij} = P_{ij,T} + P_{ij,R} + P_{ij,rc} \quad (97)$$

The translational term can be written as:

$$P_{ij,T} = L_{i,T_x} \cdot L_{j,T_x} + L_{i,T_y} \cdot L_{j,T_y} + L_{i,T_z} \cdot L_{j,T_z} \quad (98)$$

where

$$\begin{aligned} L_{\alpha x, T_x} &= \sqrt{\frac{m_\alpha}{\sum_\alpha m_\alpha}} & L_{\alpha x, T_y} &= 0 & L_{\alpha x, T_z} &= 0 \\ L_{\alpha y, T_x} &= 0 & L_{\alpha y, T_y} &= \sqrt{\frac{m_\alpha}{\sum_\alpha m_\alpha}} & L_{\alpha y, T_z} &= 0 \\ L_{\alpha z, T_x} &= 0 & L_{\alpha z, T_y} &= 0 & L_{\alpha z, T_z} &= \sqrt{\frac{m_\alpha}{\sum_\alpha m_\alpha}} \end{aligned} \quad (99)$$

with  $\alpha = 1, \dots, N$ ,  $T_x$  corresponding to translation along the  $x$  axis,  $T_y$  along the  $y$  axis and  $T_z$  along the  $z$  axis.

The rotational term similarly can be written as:

$$P_{ij,R} = L_{i,R_x} \cdot L_{j,R_x} + L_{i,R_y} \cdot L_{j,R_y} + L_{i,R_z} \cdot L_{j,R_z} \quad (100)$$

where

$$\begin{aligned}
L_{\alpha x, R_x} &= q_{\alpha z}(\mathbf{I}^{-1/2})_{xy} - q_{\alpha y}(\mathbf{I}^{-1/2})_{xz} & L_{\alpha x, R_y} &= q_{\alpha z}(\mathbf{I}^{-1/2})_{yy} - q_{\alpha y}(\mathbf{I}^{-1/2})_{yz} & L_{\alpha x, R_z} &= q_{\alpha z}(\mathbf{I}^{-1/2})_{zy} - q_{\alpha y}(\mathbf{I}^{-1/2})_{zz} \\
L_{\alpha y, R_x} &= q_{\alpha x}(\mathbf{I}^{-1/2})_{xz} - q_{\alpha z}(\mathbf{I}^{-1/2})_{xx} & L_{\alpha y, R_y} &= q_{\alpha x}(\mathbf{I}^{-1/2})_{yz} - q_{\alpha z}(\mathbf{I}^{-1/2})_{yx} & L_{\alpha y, R_z} &= q_{\alpha x}(\mathbf{I}^{-1/2})_{zz} - q_{\alpha z}(\mathbf{I}^{-1/2})_{zx} \\
L_{\alpha z, R_x} &= q_{\alpha y}(\mathbf{I}^{-1/2})_{xx} - q_{\alpha x}(\mathbf{I}^{-1/2})_{xy} & L_{\alpha z, R_y} &= q_{\alpha y}(\mathbf{I}^{-1/2})_{yx} - q_{\alpha x}(\mathbf{I}^{-1/2})_{yy} & L_{\alpha z, R_z} &= q_{\alpha y}(\mathbf{I}^{-1/2})_{zx} - q_{\alpha x}(\mathbf{I}^{-1/2})_{zy}
\end{aligned} \tag{101}$$

with again  $\alpha = 1, \dots, N$ ,  $R_x$  corresponding to rotation around the  $x$  axis,  $R_y$  around the  $y$  axis and  $R_z$  around the  $z$  axis and  $\mathbf{I}$  as the inertia tensor previously calculated. The third and last term, which corresponds to the motion along the reaction coordinate, is

$$P_{ij, r_c} = L_{i, r_c} \cdot L_{j, r_c} \tag{102}$$

with  $L_{i, r_c}$  equal to the normalized energy gradient

$$L_{i, r_c} = \frac{g_i}{C_N} \tag{103}$$

where  $C_N$  is the normalization constant

$$C_N = \left( \sum_i^{3N} g_i^2 \right)^{1/2} \tag{104}$$

and  $g_i$  is the  $i$ -th component of the energy gradient vector in mass weighted Cartesian coordinates

$$g_i = \frac{\partial V}{\partial q_i} \tag{105}$$

Once we have built the projector matrix we can compute the projected force constant matrix  $\mathbf{F}_{\text{MWC}}^{\text{P}}$  and diagonalize it. Thus, we have:

$$\mathbf{L}^\dagger \mathbf{F}_{\text{MWC}}^{\text{P}} \mathbf{L} = \mathbf{\Lambda} \tag{106}$$

obtaining thus the  $3N-7$  generalized normal modes of vibration (normalized eigenvectors matrix  $\mathbf{L}$ ) with the corresponding  $3N-7$  non-zero frequencies that can be extracted from the calculated eigenvalues, i.e. the elements of the diagonal matrix  $\mathbf{\Lambda}$ . In fact, if we call  $\lambda_i$  the eigenvalues, the frequencies in  $\text{s}^{-1}$  can be calculated as

$$\nu_i = \sqrt{\frac{\lambda_i}{4\pi^2}} \tag{107}$$

It is important to notice that using the Hessians and gradients taken from the output of a Gaussian calculation it is necessary to use the appropriate conversion factors to convert atomic units in SI units. The procedure that goes from equation ( 91 ) to equation ( 107 ) needs to be repeated for each point calculated along the minimum energy path. It is important to store not just the calculated values of  $\nu_i$  as a function of  $s$ , but also the calculated normalized eigenvectors matrix  $\mathbf{L}$  for each  $s$  point, because they will be necessary for the computation of the curvature vector of the reaction path, as we will see in the next section.

Reaction path curvature vector –  $\kappa_i(s)$ 

The other information that we need is the reaction path curvature vector whose elements  $\kappa_i$  were defined by Miller et al.<sup>89</sup> as

$$\kappa_i = \sum_{j=1}^{3N-6} L'_{j,i} \cdot L_{j,r_c} \quad \text{with } i = 1, \dots, 3N-7 \quad (108)$$

where  $L_{i,j}$  are the components of the eigenvector matrix  $\mathbf{L}$ . This formulation, however, was found to be problematic as it was necessary to evaluate the first derivative with respect to the reaction coordinate  $s$  of the  $\mathbf{L}$  matrix. In fact, alteration of the sequence of the eigenvectors within the matrix led to errors in the computation of this term.

Due to the orthogonality property of the coupling matrix (see Miller et al.<sup>89</sup> eq 2.19) the curvature vector can also be written as:

$$\kappa_i = \sum_{j=1}^{3N-6} L'_{j,r_c} \cdot L_{j,i} \quad \text{with } i = 1, \dots, 3N-7 \quad (109)$$

In this way it is not necessary to compute the derivative of the  $\mathbf{L}$  matrix but only of  $L_{i,r_c}$  i.e. the normalized gradient vector in mass weighted Cartesian coordinates.

However, this formulation also presented some problems. In particular, near the saddle point, where the gradient is almost zero, difficulties arise for the numeric evaluation of its derivative. For this reason the expression of Page and McIver<sup>99</sup> for the curvature vector was finally employed (see Page and McIver<sup>99</sup> eq. (48)), which can be written as

$$\kappa_i = -\frac{1}{C_N} \sum_j \frac{g_i}{C_N} \left( \sum_k L_{k,i} F_{MWC_{k,j}} \right) \quad (110)$$

where all the elements present are the same as those that were previously declared.

It is interesting to notice that within this formulation no derivatives need to be employed, thus reducing the possibility of introducing numerical errors. Moreover, as it is suggested by the same Page and McIver<sup>99</sup>, in the proximity of the saddle point a more reliable expression for the reaction path curvature components was used (see Page and McIver<sup>99</sup> eq. (49)), defined here as:

$$\kappa_i = -\sum_k \sum_j D_{i,k} \cdot \frac{g_k}{C_N} \delta_{k,j} \quad (111)$$

where

$$D_{j,i} = \sum_k L_{k,i} \cdot \Delta_{INV_{k,j}} \quad (112)$$

with

$$\Delta_{INV} = \Delta^{-1} \quad \text{and} \quad \Delta_{k,j} = \begin{cases} 2f_v - F_{MWC_{k,j}} & k = j \\ F_{MWC_{k,j}} & k \neq j \end{cases} \quad (113)$$

and  $f_v$  defined as

$$f_v = \sum_k^{3N} \sum_j^{3N} \left( \frac{g_k}{C_N} \right)^2 F_{MWC_{k,j}} \quad (114)$$

While  $\delta$  is defined as

$$\delta_{k,j} = \begin{cases} dF_{MWC_{k,j}} - 2df_v & k = j \\ dF_{MWC_{k,j}} & k \neq j \end{cases} \quad (115)$$

with

$$df_v = \sum_k^{3N} \sum_j^{3N} \left( \frac{g_k}{C_N} \right)^2 dF_{MWC_{k,j}} \quad (116)$$

and  $dF_{MWC}$  is the first derivative of the mass weighted force constant matrix with respect to the reaction coordinate  $s$ .

### Tunneling Correction within MCRRKM

The main result of the previous models is the possibility for calculating the transition or tunneling probability as a function of energy,  $P(E)$ . This probability either can be used to calculate a tunneling coefficient to correct the canonical TST rate coefficient, or can eventually be included in the computation of the microcanonical RRKM rate coefficient.

In the first case, the tunneling coefficient,  $q_{tunn}$ , is defined as the ratio between quantum and classical fluxes across the energy barrier as follows:

$$q_{tunn}(T) = \frac{\int_0^\infty P(E) \exp\left(\frac{-E}{k_B T}\right) dE}{\int_{E_0}^\infty \exp\left(\frac{-E}{k_B T}\right) dE} \quad (117)$$

With this parameter it is thus possible to correct the transition state theory rate coefficient as follows:

$$k(T) = q_{tunn}(T) \frac{k_B T}{h} \frac{Q^\ddagger}{Q^R} \exp\left(\frac{-E_0}{k_B T}\right) \quad (118)$$

It is possible to also include the tunneling effect in the computation of the microcanonical  $k(E,J)$  rate constant. In the MCRRKM code, in particular, the RRKM rate coefficient in absence of tunneling is evaluated as:

$$k(E,J) = \frac{\int_0^{E-E_0} \rho^\ddagger(E^*,J) dE^*}{h \rho^{well}(E+E_0,J)} = \frac{\int_{E_0}^E \rho^\ddagger(E-E^*,J) dE^*}{h \rho^{well}(E+E_0,J)} \quad (119)$$

where  $\rho(E,J)$  is the density of states,  $E_0$  is the activation energy, the energy is measured from the first non zero term of  $k(E,J)$ .

To include tunneling effects,  $k(E,J)$  should be rigorously calculated as:

$$k(E,J) = \frac{\int_0^E P(E^*) \rho^\ddagger(E-E^*,J) dE^*}{h \rho^{well}(E,J)} \quad (120)$$

Here the energy of the well and the first non zero term of  $k(E,J)$  coincide. The direct implementation of equation ( 120 ) in the code is simple, but computationally expensive, as it requires to cal-

culate  $P(E)$  for each energy  $E$  of the  $k(E, J)$  vector, for each  $J$  value. A large containment of the computational cost can be obtained by observing that  $P(E)$  is significantly larger than 0 and smaller than 1 only for a restricted interval of the energy vector, centered on  $E_0$ . The calculation of  $k(E, J)$  can then be simplified by including the tunneling contribution only for an energy interval  $E_{\text{delta}}$ . The microcanonical rate constant can then be computed as:

$$k(E, J) = \frac{\int_{E_0 - E_{\text{delta}}}^{E_0 + E_{\text{delta}}} P(E^*) \rho^\ddagger(E - E^*, J) dE^*}{h \rho^{\text{well}}(E + E_0 - E_{\text{delta}}, J)} + \frac{\int_{E_0 + E_{\text{delta}}}^E \rho^\ddagger(E - E^*, J) dE^*}{h \rho^{\text{well}}(E + E_0 - E_{\text{delta}}, J)} \quad (121)$$

for  $E > E_0 + E_{\text{delta}}$

and as:

$$k(E, J) = \frac{\int_{E_0 - E_{\text{delta}}}^E P(E^*) \rho^\ddagger(E - E^*, J) dE^*}{h \rho^{\text{well}}(E + E_0 - E_{\text{delta}}, J)} \quad (122)$$

for  $0 < E < E_0 + E_{\text{delta}}$ .

In equations (121) and (122), the energy is measured with respect to the first non zero term of  $E$ , as in equation (119), which is assumed to be at an energy  $E_{\text{delta}}$  below the energy barrier  $E_0$ . The calculation of tunneling effects can be made as accurate as desired increasing the energy interval  $E_{\text{delta}}$ .

### 3.3.5. Bimolecular Reactions

In the present work the integration protocol previously adopted to investigate the unimolecular dynamics on a multi-well PES has been extended to also treat bimolecular reactions.

For this purpose we first compute the microcanonical rate constant  $k_{\text{add}}(E)$  for a hypothetical entrance channel (A + B giving the AB adduct) through microscopic reversibility from the adduct decomposition reaction  $k_{\text{dec}}(E)$  as:

$$k_{\text{add}}(E) = k_{\text{dec}}(E) \cdot \frac{Q_{\text{AB}}^{\text{tras}}}{Q_{\text{A}}^{\text{tras}} Q_{\text{B}}^{\text{tras}}} \cdot \frac{\text{DOS}_{\text{AB}}^{\text{RV}}(E + E_0)}{\sum_{E^*=0}^{E+E_0-E_{\text{rea}}} \text{DOS}_{\text{A}}^{\text{RV}}(E - E^*) \text{DOS}_{\text{B}}^{\text{RV}}(E^*)} \quad (123)$$

where  $Q_i^{\text{tras}}$  is the translational partition functions of adducts and reactants.  $\text{DOS}_{\text{AB}}^{\text{RV}}(E + E_0)$  is the  $1 \text{ cm}^{-1}$  spaced rovibrational density of states of the adduct, and it is divided by the convoluted density of states of the two reactants. The energy  $E$  of  $k_{\text{dec}}(E)$  is measured from its first non zero term (i.e. at the PES saddle point),  $E_0$  is the activation energy of the reaction calculated with respect to AB, and  $E_{\text{rea}}$  is the reaction energy change. Afterwards, the master equation calculation is started from the entrance well AB at an energy  $E$  determined by stochastically sampling the microcanonical reaction rates calculated assuming a Boltzmann population of the reactants. The probability  $P(E)$  to enter the simulations at an energy level  $E$  was calculated as:

$$P(E) = \frac{k_{\text{add}}(E) \sum_{E^*=0}^{E+E_0-E_{\text{rea}}} \text{DOS}_{\text{A}}^{\text{RV}}(E - E^*) \text{DOS}_{\text{B}}^{\text{RV}}(E^*) \cdot \exp\left(-\frac{E+E_0-E_{\text{rea}}}{k_{\text{B}}T}\right)}{\sum_{E=0}^{\infty} \left( k_{\text{add}}(E) \sum_{E^*=0}^{E+E_0-E_{\text{rea}}} \text{DOS}_{\text{A}}^{\text{RV}}(E - E^*) \text{DOS}_{\text{B}}^{\text{RV}}(E^*) \cdot \exp\left(-\frac{E+E_0-E_{\text{rea}}}{k_{\text{B}}T}\right) \right)} \quad (124)$$

The entrance energy level was determined using a rejection free algorithm, according to which the reaction probabilities are stored in a vector  $P_{\text{add}}$ . This vector is discretized as the energy bin size so that each component  $i$  corresponds to the energy level  $E = i\Delta E_{\text{bin}}$ . Each term  $P_{\text{add}}(i)$  is equal to the sum of all the probabilities  $P(E^*)$  for  $E < E^*$ .

The entrance energy level is then selected choosing a random number  $t_1$  and scanning the probability vector until a value  $j$  for which hold  $P_{\text{add}}(j) > t_1$  and  $P_{\text{add}}(j+1) < t_1$  is found. The random entrance energy is then  $E = j\Delta E_{\text{bin}}$ .

In the course of this project, the present approach has been applied to both tight and loose transition state reactions. However, it is known that for loose transition state reactions it can introduce a significant error in the estimation of bimolecular rate coefficients. An effective way to treat these classes of reaction is the variable reaction coordinate transition state theory that will be the subject of the next section.

### 3.3.6. Variable Reaction Coordinate Transition State Theory – VRC-TST

The variable reaction coordinate TST approach find its basis in the main concept of variational transition state theory (VTST), in which the transition state dividing surface is obtained by minimization of the predicted TST reactive flux. The central focus of VTST is the estimation of this reactive flux through an arbitrary dividing surface that separates reactants from the products. It is important to notice that the reactive flux at energy  $E$  and total angular momentum  $J$  is commonly interpreted as the number of states available with energy less than  $E$  and the specified angular momentum  $J$ ,  $N(E,J)$ , while, traditionally, the dividing surface is defined in terms of a single parameter, that is the reaction coordinate  $s$ . The minimization of the reactive flux is thus performed with respect to the reaction coordinate  $s$ .

For barrierless reactions, however, it is difficult to obtain quantitatively accurate estimations of the reactive flux with the standard VTST approach. The reasons are the following: (1) the value and the form of the reaction coordinate for the optimal dividing surface varies greatly with  $E$  and/or  $J$ ; (2) the relative motions of the two fragments can be of large amplitude.

The variable reaction coordinate implementation of VTST<sup>56,100</sup> considers in the optimization of the reactive flux, not only the value of the reaction coordinate but also how the reaction coordinate is defined. Within this scheme, the dividing surfaces are defined in terms of the distance between individual pivot points located on each of the two reacting fragments. The variational optimization, therefore, is performed with respect to both the distance between the pivot points and their location. This scheme allows the reaction coordinate to vary from that appropriate at large separations to that appropriate at small separations of the reacting fragments.

A separation of the modes into conserved and transitional modes is a key simplifying assumption within the VRC-TST approach.<sup>101</sup> The conserved modes correspond to the internal vibrational

modes of the two reacting system. The contribution of these vibrational modes does not change significantly during the reacting process and as such they can be left out of the definition of the variational dividing surface. In contrast, the remaining transitional modes include the rotations of both fragments as well as their relative translational motion, which change from free rotation and translation at infinite separations of the fragments into vibrational motion and overall rotation upon the formation of the bond between the fragments.

With the assumption of separability of the transitional and conserved modes, the overall number of states can be expressed as:<sup>101</sup>

$$N(E, J) = \int \rho^{(c)}(E - E') N^{(t)}(E', J) dE' \quad (125)$$

where  $\rho^{(c)}(E)$  is the density of states of the conserved modes and  $N^{(t)}(E, J)$  is the number of states of the transitional modes. The density of states of the internal vibrational modes can be computed by direct counting of the quantum states. The number of states of the transitional modes, on the other hand, can be computed using the classical phase space integral formalism, due to the low frequency nature by which they are characterized.

The number of states of the transitional modes can thus be written as:<sup>102</sup>

$$N^{(t)}(E, J) = (2\pi)^{-\alpha} \int d^\alpha \mathbf{q} d^\alpha \mathbf{p} \delta(s(\mathbf{q}) - s') \delta(H(\mathbf{q}, \mathbf{p}) - E) \delta(\hat{J}(\mathbf{q}, \mathbf{p}) - J) \dot{s} \Theta(\dot{s}) \quad (126)$$

where  $\mathbf{q}$  and  $\mathbf{p}$  are vectors containing generalized coordinates and corresponding conjugate momenta and  $\alpha$  is the number degrees of freedom for the transitional modes.  $H(\mathbf{q}, \mathbf{p})$  is the Hamiltonian function of the system,  $\hat{J}(\mathbf{q}, \mathbf{p})$  is the total angular momentum,  $\delta$  is the delta function and  $\Theta$  is the Heaviside step function for which:

$$\Theta(\dot{s}) = \begin{cases} 1, & \dot{s} > 0 \\ 0, & \dot{s} < 0 \end{cases} \quad (127)$$

and the dot denotes the time derivative,  $\dot{s} \equiv ds/dt$ .

The evaluation of such phase space integrals can be computationally very expensive and in the course of the last decades, various studies have derived efficient means to evaluate them.<sup>100,103,104</sup> However, for a more effective implementation of the VRC-TST approach Klippenstein and coworkers have derived a more efficient method for evaluating the transitional mode contribution to the number of states by analytical integration over the generalized momenta.<sup>54</sup>

Within this scheme, the number of states corresponding to the transitional modes is expressed as:

$$N^{(t)}(E, J) = \langle N_q(E, J, \mathbf{q}) \rangle_\Omega \quad (128)$$

where  $\langle \dots \rangle_\Omega$  denotes the averaging over all possible orientations of the fragments and the vector  $s$  connecting the pivot points. The quantity  $N_q(E, J, \mathbf{q})$  can be viewed as a number of states for a specific configuration  $\mathbf{q}$  that can be evaluated straightforwardly using the expression obtained by analytical integration in equation (2.39) of reference 54.

To perform the averaging a simple Monte Carlo sampling method can be used:

$$N^{(t)}(E, J) = M^{-1} \sum_{i=1}^M N_q(E, J, \mathbf{q}_i) \quad (129)$$

where  $M$  is the number of samplings.

The VRC-TST formalism has been further extended to treat reactions where there are multiple binding sites, or for those cases when further flexibility in the description of the dividing surface is desirable. This generalization simply foresees the possibility to include multi pivot points for each reacting fragment. The result is a properly variational multifaceted dividing surface approach which allows the incorporation and optimization of different dividing surfaces shapes for each binding site.<sup>53</sup>

As a simple example of multiple binding sites, Georgievskii and Klippenstein considered the reaction of methyl radical with a hydrogen atom:  $\text{CH}_3 + \text{H} \rightarrow \text{CH}_4$ . This reaction can proceed in two ways depending on which side of the  $\text{CH}_3$  plane the hydrogen approaches as shown in **Figure 21**.

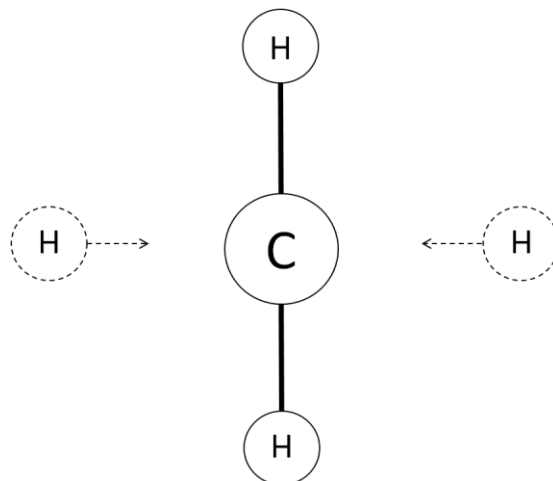


**Figure 21.** *Cartoon of the two ways the hydrogen atom can attack the methyl radical in the  $\text{CH}_3 + \text{H}$  reaction.*

Two pivot points can be positioned on each side of the plane formed by the  $\text{CH}_3$  fragment. In this way, we create two spheres: one sphere centered on the pivot point of one side and the other centered on an equivalent pivot point on the other side. The two spheres intersect on the  $\text{CH}_3$  plane. Thus, the dividing surface used for the optimization can be viewed as a composite of the two surfaces, consisting of the outer surface of the union of the two spheres, as illustrated in **Figure 22**.

In the flux calculation, one integrates only over that part of each facet of the dividing surface, which is on the side corresponding to its pivot point. This procedure is translated into a modification of equation (128) as follows,

$$N^{(t)}(E, J) = F \langle N_q(E, J, \mathbf{q}) \rangle_{\Omega} \quad (130)$$

where  $F$  is the fraction of the dividing surface that is exposed to the flux. Within the Monte Carlo sampling  $F$  can be written as

$$F = \frac{M'}{M} \quad (131)$$

where  $M'$  is the number of accepted samplings.

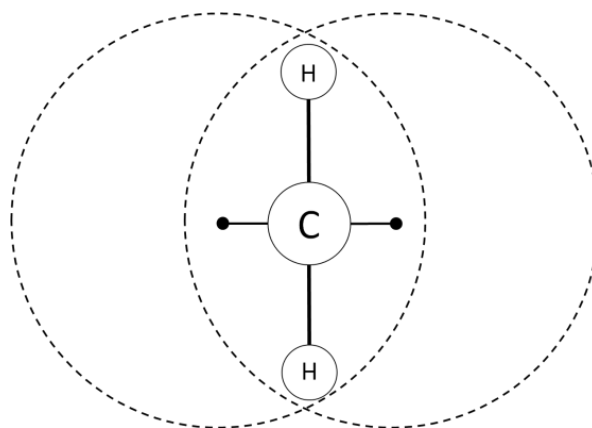


**Figure 22.** Composite dividing surface for the  $\text{CH}_3 + \text{H}$  reaction.

The use of additional pivot points within this scheme makes the dividing surface more flexible and increases the accuracy of the VTST rate coefficient estimation. This improvement, however, come at the cost of increased computational cost, because the flux must be evaluated for each dividing surface.

The present implementation of the VRC-TST approach has been applied in the course of this project in collaboration with Dr Stephen J. Klippenstein to study the kinetics of a particular set of chemical reactions that will be the subject of Chapter 8.



# 4 Germane and Germylene Decomposition Kinetics

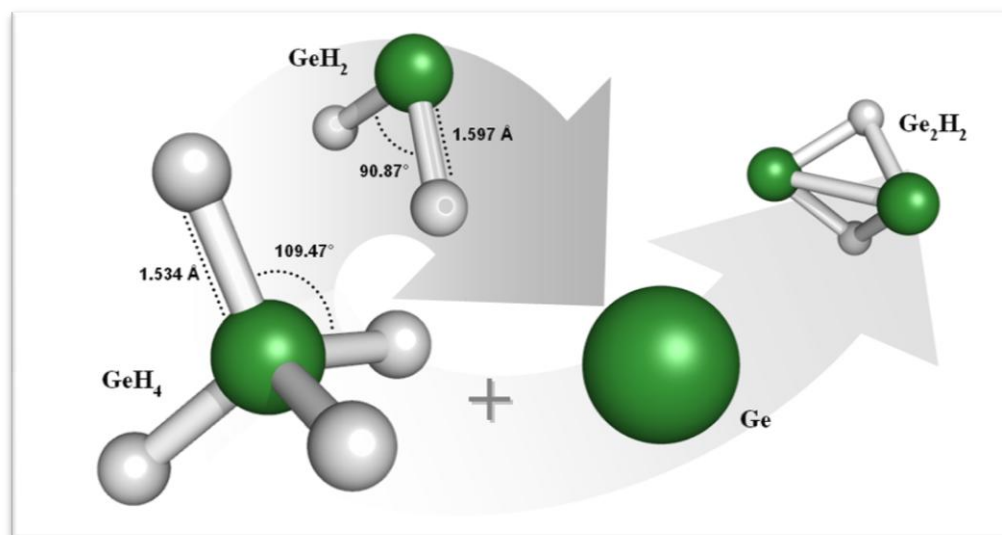


**Figure 23.** Germane and germylene decomposition kinetics were studied with stochastic RRKM/master equation simulations based on *ab initio* reaction parameters.

## 4.1. Introduction

Germane is among the most adopted gases for the chemical vapor deposition (CVD) of germanium or silicon/germanium thin films used in the manufacturing of semiconductor devices, such as diodes or transistors. The optimization of the Si/Ge growth processes can be facilitated by an accurate knowledge of germane thermochemistry and kinetics.<sup>105</sup> This has motivated considerable research in this field, so that several studies on the molecular properties of germane and its decomposition products can be found in the literature.<sup>106-126</sup>

Thermochemistry was among the first germane properties to be investigated. The heat of formation of  $\text{GeH}_4$  was experimentally determined for the first time through bomb calorimetric measurement in 1961 by Gunn and Green<sup>113</sup> ( $90.4 \pm 2 \text{ kJ mol}^{-1}$  at 298 K). Successively, Ruscic et al.<sup>120</sup> estimated heats of formation and Ge–H bond energies of  $\text{GeH}_4$ ,  $\text{GeH}_3$ ,  $\text{GeH}_2$  and  $\text{GeH}$  through photoionization mass spectrometry. The  $\text{GeH}_3\text{--H}$  bond energy determined at 0 K was  $343.3 \pm 8.4 \text{ kJ mol}^{-1}$ , thus in good agreement with the value determined by Reed and Brauman<sup>127</sup> ( $339.1 \pm 15.5 \text{ kJ mol}^{-1}$  at 0 K), who derived the bond energy by measuring the  $\text{GeH}_4$  gas-phase acidity. Also Noble and Walsh,<sup>118</sup> investigating the iodination of germane, determined a similar value for the bond dis-

sociation energy of the first hydrogen atom of GeH<sub>4</sub> ( $345.4 \pm 8.4$  kJ mol<sup>-1</sup> at 0 K). According to Berkowitz et al.,<sup>128</sup> who reviewed the field, the bond energy determined by photoionization mass spectrometry is the most accurate. Almost no experimental data are available for the other GeH<sub>x</sub> hydrides, with the exception of the bond energy of 276.3 kJ mol<sup>-1</sup> determined by Ruscic et al.<sup>120</sup> for the GeH–H bond.

The GeH<sub>x</sub> thermochemical data determined through experiments were confirmed by early theoretical studies performed using several high level *ab initio* theories, ranging from MP2 to the hybrid G1 and G2 computational schemes.<sup>106,117,129</sup> Recently, Duchowicz and Cobos<sup>110</sup> determined the enthalpies of formation of germane and of its fluoro–chloro derivatives at the G3//B3LYP level. In the same work bond dissociation energies and barrier heights were estimated for the lowest dissociations pathways at 0 K. Wang and Zhang<sup>123</sup> investigated the homolytic dissociation of germane and of its fluoro–chloro derivatives at the same level of theory. Ricca and Bauschlicher<sup>119</sup> computed the heats of formation for the GeH<sub>n</sub> and Ge<sub>2</sub>H<sub>n</sub> species using coupled cluster theory including single double and a perturbative estimation of triple excitations (CCSD(T)) with extrapolation to the complete basis set limit (CBS) introducing corrections for spin orbital, thermal and scalar relativistic effects. Also Koizumi et al.<sup>115</sup> evaluated the heat of formation of germane at the CCSD(T) level of theory at the complete basis set limit, with explicit calculation of relativistic effects, core valence correlation, spin orbital effect and zero-point energy. Finally, Chambreau and Zhang<sup>107</sup> determined the energies of the thermal decomposition reactions of germane at the G3 level of theory with geometries and zero-point energies determined at the QCISD/cc-pVTZ level. These studies showed that energy and structures of GeH<sub>x</sub> molecules can be calculated at a quantitative level of accuracy if molecular structures are determined at least at the density functional theory (DFT) level and if energies are computed adopting a high level theory, such as coupled cluster or configuration interaction, and large basis sets. The calculated GeH<sub>x</sub>–H bond dissociation energies are compared to those determined in the present work in the Results and discussion section.

While germane thermodynamics is well established, only a few experimental and theoretical works are available in the literature on its decomposition kinetics.<sup>129-132</sup> These studies revealed that the germane decomposition mechanism is similar to that of silane for many aspects. Its main reaction step is the dissociation to GeH<sub>2</sub> and H<sub>2</sub>, which mimics the SiH<sub>4</sub> dissociation reaction to SiH<sub>2</sub> and H<sub>2</sub>. Furthermore, both reactions proceed through a well defined tight transition state. In the present investigation we also considered as competitor channel the simple dissociation of GeH<sub>4</sub> to GeH<sub>3</sub> and H, in analogy with our recent study on SiH<sub>4</sub> decomposition kinetics.<sup>70</sup>

Thus, the decomposition of GeH<sub>4</sub> can be described as a combination of two processes:



Reaction (R2) was first proposed as the germane main decomposition channel by Newman et al. This conclusion was based on an experimental investigation of GeH<sub>4</sub> thermal decomposition through a single pulse shock tube operating at 5.3 bar in the 950–1060 K temperature range. Successively Newman et al. analyzed the overall reaction stoichiometry and found it to be:



Thus, it was reasonably hypothesized that reaction (R2) is followed by GeH<sub>2</sub> decomposition through one of (or both) the following reactions:



The analysis of the experimental results leads to the conclusion that the decomposition of GeH<sub>2</sub> is about 9 times faster than that of GeH<sub>4</sub>. Votintsev et al.<sup>132</sup> studied the kinetics of germane decomposition, conducting shock tube experiments and detecting the formation of Ge atoms through atomic absorption spectrometry at 1.5 bar in the 1060–1300 K temperature range. The possibility to measure the formation of atomic germanium allowed the authors to further assess the reaction mechanism. It was thus confirmed that reactions (R2) and (R4) are the most important steps and that reaction (R2) is the rate-determining step of the overall decomposition process. More recently Smirnov<sup>131</sup> expanded the results of his previous study carrying out experiments at similar pressures and temperatures measuring chemiluminescence kinetics during germane dissociation behind shock waves. This work confirmed the results obtained by Votintsev et al.<sup>132</sup> A rate expression for reaction (R4) was also proposed for the first time.

From a theoretical standpoint, only one work carried out by Simka et al.<sup>129</sup> investigated directly the decomposition kinetics of germane. Calculations were performed at the MP2 level to determine molecular structures and thermochemical data, while kinetic constants were calculated with classic transition state theory. Pressure effects were determined using RRKM theory as implemented in the Unimol suite of programs.<sup>43</sup>

Neither experimental nor theoretical kinetic data could be found for reactions (R1) and (R3), which are thus investigated for the first time in the present study.

In this framework, we decided to study germane thermal decomposition in order to improve our understanding of this important process. In particular, we calculated the kinetic constants for the decomposition of GeH<sub>4</sub> through reactions (R1) and (R2) and for GeH<sub>2</sub> decomposition through reactions (R3) and (R4) adopting a combined RRKM/master equation approach using data determined through *ab initio* calculations. The results of the calculations were then validated through comparison with literature experimental data. The chapter is organized in two sections. In the Methods section are reported the details about *ab initio* theories used to perform the calculations and the kinetic theory level adopted to compute the rate constants. Then, in the Results and discussion section, we

report first the results of *ab initio* and high-pressure kinetic constants calculations and successively the results of the master equation investigation of the GeH<sub>4</sub> and GeH<sub>2</sub> decomposition kinetics.

## 4.2. Methodology

The chemical reactivity of GeH<sub>4</sub> and GeH<sub>2</sub> was investigated adopting potential energy surfaces (PES) determined through *ab initio* calculations. Structures of reactants, transition states and reaction products were calculated both using density functional theory (DFT) with B3LYP functionals<sup>17,18</sup> and the augmented correlation consistent aug-cc-pVTZ basis set<sup>133</sup> and at the CASPT2<sup>134,135</sup> level with the cc-pVTZ basis set. Vibrational frequencies of relevant wells and transition states were determined at the B3LYP/aug-cc-pVTZ level of theory without adopting correction factors. Energies were calculated at the CCSD(T)<sup>15</sup> level using the aug-cc-pVTZ and aug-cc-pVQZ basis sets for wells and transition states and then extrapolated to the infinite basis set adopting the scheme suggested by Martin as:<sup>136</sup>

$$E(\infty) = E(l_{max}) - B/(l_{max} + 1)^4 \quad (132)$$

in which  $l_{max}$  is the basis set maximum angular momentum quantum number (4 and 3 for the aug-cc-pVQZ and aug-cc-pVTZ basis sets, respectively) and  $B$  a proportionality constant that can be calculated solving equation ( 132 ) for the two  $l_{max}$  values on which the infinite basis set extension is performed.

All energies were corrected with zero point energies (ZPE) calculated at the B3LYP/aug-cc-pvtz level. The overall expression adopted to calculate the energy was thus:

$$\begin{aligned} E(\infty) = & E(\text{CCSD(T)}/\text{aug-cc-pVQZ}) \\ & + 0.6938[E(\text{CCSD(T)}/\text{aug-cc-pVQZ}) \\ & - E(\text{CCSD(T)}/\text{aug-cc-pVTZ})] + \text{ZPE (B3LYP/aug-cc-pVTZ)} \end{aligned} \quad (133)$$

The analysis of the PES of the reactions of decomposition of GeH<sub>4</sub> and GeH<sub>2</sub> to GeH<sub>3</sub> and GeH showed that they do not have a chemical barrier, and thus a transition state. The kinetic constants of these reactions were thus determined using the microvariational form of transition state theory on a PES determined adopting an *ab initio* theory with multireference character, which can account more properly for the contribution of virtual orbitals to the molecular wave function than a single reference approach, such as DFT or CCSD(T). Thus intermediate structures and energies were calculated as a function of the reaction coordinate at the CASPT2 level using the cc-pVQZ basis set including in the active space all the valence electrons. Frequencies were computed at the same level of theory. CASPT2 energies were then re-scaled to fit the overall binding energy determined at the CCSD(T) level, which was found in this and previous studies to predict bond energies that are in good agreement with those experimentally measured.<sup>119</sup> All DFT calculations were carried out

adopting the Gaussian 03 computational suite<sup>1</sup>, while CASPT2 and CCSD(T) calculations were performed adopting the Molpro 2008.1 computational suite.<sup>3</sup>

RRKM microcanonical rate constants  $k(E,J)$  were computed from the convoluted rotational and vibrational density of states as a function of energy  $E$  and angular momentum  $J$ . All the vibrational and external rotational degrees of freedom were considered in the calculation of  $k(E,J)$  for reactions with a chemical barrier. This is based on the hypothesis that the intramolecular rotational–vibrational energy transfer is fast. The high-pressure rate coefficients were calculated both integrating  $k(E,J)$  over the Boltzmann population and from the classic TST expression, as they give the same result. The approach adopted to determine  $k(E,J)$  for the reactions proceeding without passing from a chemical barrier is the  $E,J$  model proposed by Miller et al.<sup>71</sup>

The density of states related to the transitional  $\text{GeH}_3\text{--H}$  and  $\text{GeH--H}$  bending motions were treated in the harmonic oscillator approximation using the vibrational frequencies calculated at the CASPT2 level. A similar approach applied to the study of the decomposition of  $\text{CH}_4$  to  $\text{CH}_3$  and  $\text{H}$  led to a good fit of experimental data. Despite this, the harmonic approximation is probably unrealistic for this class of reactions and we plan in the near future to update our computational approach by implementing a hindered rotor approximation.

However, as will be discussed later on, the present calculations predict that decompositions to  $\text{GeH}_3$  and  $\text{GeH}$  have a minor impact on the overall decomposition kinetics and therefore the uncertainty associated to the above assumption is likely to have a small influence on the overall rate constants calculated in the present work.

The transition state for reaction (R4) corresponds to the Minimum Energy Crossing Point (MECP) of the singlet and triplet PES of  $\text{GeH}_2$  and is therefore formally spin forbidden. The singlet–triplet transition of  $\text{GeH}_2$  has been the subject of several theoretical studies in the literature and it is expected to proceed rapidly because of the large spin–orbit coupling between the two states.<sup>137</sup> As discussed in the previous chapter, the probability of intersystem crossing was included in our microcanonical calculation by evaluating the  $k(E,J)$  microcanonical rate as:<sup>75</sup>

$$k(E,J) = \frac{\int_0^{E-E_0} \rho^\ddagger(E',J) p_{hop}(E - E' - E_0) dE'}{h\rho(E,J)} \quad (134)$$

where  $\rho$  is the density of states,  $J$  the angular momentum,  $E$  the rovibrational energy, and  $p_{hop}$  the probability of intersystem hopping, which was calculated from Landau–Zener<sup>73,74</sup> theory as the probability of hopping in a double pass through the MECP as:

$$p_{hop}(E) = (1 - P_{LZ})(1 + P_{LZ}) \quad (135)$$

in which the Landau–Zener transition probability was calculated as:

$$P_{LZ}(E) = \exp\left(-\frac{2\pi H_{SO}^2}{\hbar\Delta F} \sqrt{\frac{\mu}{2E}}\right) \quad (136)$$

where  $H_{\text{SO}}$  is the off-diagonal spin-orbit coupling element of the  $4 \times 4$  Hamiltonian matrix between the singlet and triplet state,  $\Delta F$  is the relative slope of the triplet and singlet PES at the MECP,  $\mu$  is the reduced mass of the reacting moieties, and  $E$  is the system kinetic energy. The spin-orbit matrix element  $H_{\text{SO}}$  was calculated adopting spin-orbit singlet and triplet wave functions determined using multireference configuration interaction (MRCI)<sup>138,139</sup> theory including all valence electrons in the active space adopting the cc-pVTZ basis set.<sup>140</sup> The forces at the MECP were calculated at the B3LYP/aug-cc-pvtz level.

Master equation (ME) calculations were performed adopting the 1D master equation formulation proposed by Miller et al.,<sup>71</sup> which was derived by J-averaging the E,J 2D master equation and is implemented in our computational code as described in detail in Chapter 3.

### 4.3. Results and Discussion

The results are presented in two sections. In the first we report and discuss the *ab initio* simulations and the calculation of high-pressure rate constants adopting classic transition state theory and microvariational J-resolved transition state theory, while in the second we report the results of the investigation of the pressure dependence of the decomposition rate constant for the two systems considered.

#### 4.3.1. Ab initio Calculations and Evaluation of High-pressure Rate Constants

Energies, vibrational frequencies, structural and reaction parameters of reactants and transition states for  $\text{GeH}_4$ ,  $\text{GeH}_2$ , and reactions (R2) and (R4) are summarized in **Table 1**.

The energy change and activation energies of reaction (R2) have been determined experimentally and theoretically by several authors and were thus used to discuss the level of accuracy of the present calculations.

Experimentally it was found that the reaction enthalpy should be higher than  $147 \text{ kJ mol}^{-1}$  and a most probable value of  $163.3 \text{ kJ mol}^{-1}$  was proposed, though the uncertainty was great ( $41.9 \text{ kJ mol}^{-1}$ ). Enthalpy changes determined through first principle calculations are comprised between  $150.7$  and  $171.7 \text{ kcal mol}^{-1}$ . The most accurate theoretical value is most likely the  $157.4 \text{ kJ mol}^{-1}$  enthalpy change determined by Ricca and Bauschlicher<sup>119</sup>, which includes relativistic and spin-orbit corrections as well as extension to the infinite basis set. The enthalpy change calculated in the present study,  $164.5 \text{ kJ mol}^{-1}$ , is thus in reasonable agreement with both the theoretical best estimate and the available experimental data. Also, the calculated activation energy of reaction (R2) ( $217.7 \text{ kJ mol}^{-1}$ ) is in good agreement with that experimentally evaluated by Votintsev et al.<sup>132</sup> ( $218.1 \text{ kJ mol}^{-1}$ ) and Newman et al.<sup>130</sup> ( $209.3\text{--}227.3 \text{ kJ mol}^{-1}$ ), while it is slightly larger than that determined by Smirnov<sup>131</sup> ( $208.1 \text{ kJ mol}^{-1}$ ) and in good agreement with that computed by Simka et al.<sup>129</sup>

through MP2 calculations (224.8 kJ mol<sup>-1</sup>). The inverse process, the direct insertion of H<sub>2</sub> in GeH<sub>2</sub>, was studied by Becerra et al.<sup>141,142</sup> The energy barrier calculated at the QCISD/6-311+G(3df,2pd) level is 57.8 kJ mol<sup>-1</sup>, thus in good agreement with the 53.2 kJ mol<sup>-1</sup> determined in the present study.

Few experimental studies are available in the literature on the GeH<sub>2</sub> decomposition thermochemistry. Ruscic et al.<sup>120</sup> determined experimentally the GeH<sub>2</sub> heat of formation, through which a decomposition reaction energy of 110.5 kJ mol<sup>-1</sup> was determined using the heat of formation of atomic germanium experimentally evaluated by Glushko et al.<sup>143</sup>

**Table 1.** Energetic, structural and reaction parameters adopted to determine the high-pressure rate constant of reaction 2. H1 and H2 are the reacting hydrogen atoms. Energies are reported in Hartrees, vibrational frequencies in cm<sup>-1</sup>, and rotational constants in GHz. Activation energies are corrected with ZPE. Geometry parameters are evaluated at B3LYP/aug-cc-pVTZ. In parenthesis are displayed geometry parameters evaluated at CASPT2/aug-cc-pVTZ and the energies calculated with these parameters.

	GeH <sub>4</sub>	TS1	GeH <sub>2</sub>	TS2
E(B3LYP/aug-cc-pVTZ)	-2079.448136	-2079.399178	-2078.221807	-2078.166323
E(CCSD(T)/cc-pVTZ)	-2077.891355 (-2077.891437)	-2077.804709 (-2077.804722)	-2076.649686 (-2076.649695)	-2076.585637 (-2076.586851)
E(CCSD(T)/cc-pVQZ)	-2077.901066 (-2077.901128)	-2077.814192 (-2077.814154)	-2076.656941 (-2076.656949)	-2076.592733 (-2076.593820)
ZPE(B3LYP/aug-cc-pVTZ)	0.029318	0.025137	0.010716	0.00738
E(CCSD(T)/CBS)	-2077.878486 (-2077.878533)	-2077.795635 (-2077.795558)	-2076.651259 (-2076.651261)	-2076.586494 (-2076.591274)
Eact (B3LYP/aug-cc-pVTZ)	-	117.65 kJ/mol	-	136.91 kJ/mol
Eact (CCSD(T)/CBS)	-	217.67 kJ/mol (217.98 kJ/mol)	-	160.21 kJ/mol (157.59 kJ/mol)
Distance Ge-H1	1.534 (1.543) Å	1.568 (1.584) Å	1.597 (1.599) Å	1.747 (1.793) Å
Distance Ge-H2	1.534 (1.543) Å	1.722 (1.756) Å	1.597 (1.599) Å	1.748 (1.793) Å
Distance-H1-H2	2.505 (2.520) Å	1.249 (1.225) Å	2.276 (2.298) Å	0.991 (1.107) Å
Angle H1-Ge-H2	109.47 (109.47)	44.34 (42.65)	90.87 (91.87)	32.94 (35.941)
Vibrational Frequencies (cm <sup>-1</sup> )				
1	824.82	-1248.84	935.2888	-1449.6667
2	824.82	649.39	1880.6462	1486.9354
3	824.82	713.38	1888.0151	1752.3038
4	925.83	881.55	-	-
5	925.83	943.05	-	-
6	2130.21	1556.01	-	-
7	2137.61	2056.75	-	-
8	2137.61	2104.99	-	-
9	2137.61	2128.82	-	-
Rotational Constant (GHz) I1	79.89	92.95	205.02346	1021.03578
Rotational Constant (GHz) I2	79.89	73.46	193.5894	91.65519
Rotational Constant (GHz) I3	79.89	63.98	99.57123	84.10531
Rotational symmetry number	12	1	2	1
Symmetry Group	T <sub>D</sub>	C <sub>1</sub>	C <sub>2v</sub>	C <sub>s</sub>

**Table 2.** Activation energies and 0 K enthalpy changes for the decomposition of GeH<sub>4</sub> to GeH<sub>2</sub> and H<sub>2</sub>. Theoretical data corrected with ZPE. Energies expressed in kJ/mol.

$\Delta H_0$ (0 K)	E <sub>a</sub>	Method	Reference
164.5	217.7	CCSD(T)/CBS //CASPT2/aug-cc-pVTZ	This work
163.3 ± 41.9	209.3-227.3	Single pulse shock tube GeH <sub>4</sub> detection through mass spectrometry	Newman et al. <sup>130</sup>
>147.0		Photoionization mass spectrometry	Ruscic et al. <sup>120</sup>
	218.1±13	Shock tube Ge atoms detection by atomic absorption	Votintsev et al. <sup>132</sup>
	208.1	Shock tube Chemiluminescence detection	Smirnov et al. <sup>131</sup>
171.7	224.8	MP2/BC(1d,1f)	Simka et al. <sup>129</sup>
150.7		G3//QCISD/cc-pVTZ	Chambreau et al. <sup>107</sup>
153.1		G3//B3LYP/6-31G(2df,p)	Wang et al. <sup>123</sup>
152.8	208.1	G3//B3LYP/6-31G(2df,p)	Duchowicz et al. <sup>110</sup>
165.8		MP4/962(d,p)//HF/641(d)	Binning et al. <sup>106</sup>
157.4		CCSD(T)/CBS//B3LYP/6-311++G(2df,2p)	Ricca et al. <sup>119</sup>
165	218	QCISD(T)/6-311G++(3df,2pd)// QCISD/6-311G(d,p)	Becerra et al. <sup>141</sup>

Several theoretical studies were dedicated to the thermochemical investigation of this reaction.<sup>107,110,116,119,123</sup> In particular Ricca and Bauschlicher<sup>119</sup> calculated an energy change of 123.9 kJ mol<sup>-1</sup>, while Chambreau and Zhang<sup>107</sup> and Wang and Zhang<sup>123</sup> both determined a 117.2 kJ mol<sup>-1</sup> energy change. More recently, Duchowicz and Cobos computed the heats of formation of germane derivatives with the alternative approach of the isodesmic reaction scheme, through which they determined a reaction energy of 131.0 kJ mol<sup>-1</sup>. The enthalpy change here calculated (133.5 kJ mol<sup>-1</sup>) is in good agreement with that found by Duchowicz and Cobos, but overestimates by about 10 kJ mol<sup>-1</sup> the one determined by Ricca and Bauschlicher. The GeH<sub>2</sub> bond dissociation energy was determined experimentally through photoionization mass spectrometry by Ruscic et al.,<sup>120</sup> who reported an upper bound of 288.5 kJ mol<sup>-1</sup> and a most probable value of 276.3 kJ mol<sup>-1</sup>. This energy is slightly smaller than that calculated through first principle calculations reported in the literature,<sup>107,109,110,123</sup> which all fall all in a range comprised between 282.6 to 289.7 kJ mol<sup>-1</sup>. The bond dissociation energy computed in the present work (291.8 kJ mol<sup>-1</sup>) is thus in good agreement with the theoretical estimates and near the upper bound of the energy determined experimentally.

On the basis of the discussion reported above, we conclude that a reasonable uncertainty level of the energies computed on the GeH<sub>4</sub> and GeH<sub>2</sub> PES is about 7 and 10 kJ mol<sup>-1</sup>, respectively.

The transition state for the reaction of decomposition of  $\text{GeH}_4$  to  $\text{GeH}_2$  and  $\text{H}_2$  was determined both at the B3LYP/aug-cc-pvtz and CASTP2/cc-pvtz levels. It was interesting to find that the geometries determined at the two levels of theory are extremely similar, as they differ by less than 0.03 Å and that the computed activation energies are in practice undistinguishable.

As there are many similarities between germane and silane, it is interesting to compare the parameters determined for the  $\text{GeH}_4$  decomposition reaction with those calculated for  $\text{SiH}_4$  in a previous study.<sup>70</sup> The transition state structures of the two reactions are shown in **Figure 24**.

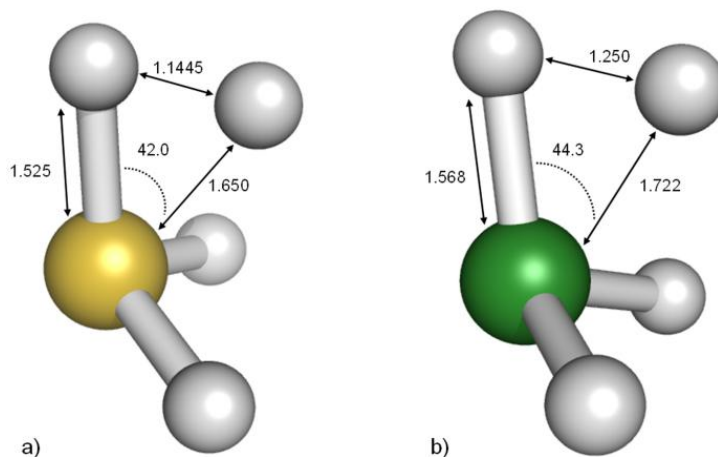


**Figure 24.** Transition state structures for the decomposition of (a)  $\text{SiH}_4$  and (b)  $\text{GeH}_4$  to  $\text{SiH}_2$  and  $\text{GeH}_2$  determined at the B3LYP/aug-cc-pVTZ level. Distances in Angstrom and angles in degrees.

As it can be observed, at a first sight they appear to be qualitatively similar: both structures have no rotational symmetry; the two Si–H and Ge–H bonds involved in the reactions differ only by about 0.12–0.15 Å; the two SiH and GeH bonds not participating in the reaction are positioned in a plane perpendicular to that formed by the other two bonds; the H–H distance in the  $\text{GeH}_4$  transition state is only 0.1 Å larger than that calculated for  $\text{SiH}_4$ .

Despite the similarities, the two systems differ substantially from an energetic standpoint. First, the activation energy calculated at the CCSD(T) level and extrapolated to the infinite basis set is 238.6  $\text{kJ mol}^{-1}$  for  $\text{SiH}_4$  and 217.7  $\text{kJ mol}^{-1}$  for  $\text{GeH}_4$ , and thus does not scale with the calculated bond dissociation energy, which is 234.5  $\text{kJ mol}^{-1}$  for  $\text{SiH}_4$  and 164.5 for  $\text{GeH}_4$  (0 K bond dissociation energy corrected with zero point energy). The relatively high activation energy for the  $\text{GeH}_4$  reaction, which is only 21  $\text{kJ mol}^{-1}$  smaller than that determined for  $\text{SiH}_4$  despite a reaction energy change about 71.2  $\text{kJ mol}^{-1}$  smaller, is unlikely to be determined by the energy required to distort the reacting hydrogen atoms from their minimum energy position, as the H–H distance in  $\text{SiH}_4$  and  $\text{GeH}_4$ , 2.421 Å and 2.505 Å, are very similar, as well as the associated bending vibrational frequencies, which are 918 and 824  $\text{cm}^{-1}$ , respectively. A more reasonable explanation is that the for-

mation of the hydrogen molecule is partially hindered in GeH<sub>4</sub> by a repulsive interaction between the electronic density of the Ge atom and that of the forming H<sub>2</sub> molecule, which is likely to be larger than that experienced by SiH<sub>4</sub>, as the GeH<sub>4</sub> electronic density is considerably more diffuse.

The presence of a significant barrier to the recombination of H<sub>2</sub> and GeH<sub>2</sub> is likely to favor the formation of this reactive species in atmospheres in which the hydrogen concentration is relatively high and will hinder the attainment of chemical equilibrium between GeH<sub>4</sub>, GeH<sub>2</sub> and H<sub>2</sub> in a reactive gas phase, since even a small activation energy will decrease exponentially the reaction rate of the GeH<sub>2</sub> and H<sub>2</sub> recombination process.

The transition state for the decomposition of GeH<sub>2</sub> to Ge and H<sub>2</sub> was determined on the singlet PES using an unrestricted B3LYP formalism and a broken symmetry guess wavefunction. Differently from what was found for GeH<sub>4</sub>, the transition state has C<sub>2v</sub> symmetry and the spin contamination  $\langle S^2 \rangle$  of the converged wave function is 0.56, thus indicating a significant multireference character. A saddle point search performed on the GeH<sub>2</sub> PES at the CASTP2/cc-pvtz level showed that no transition state leading to the direct dissociation of GeH<sub>2</sub> to Ge and H<sub>2</sub> could be located both on the singlet (<sup>1</sup>A<sub>1</sub>) and triplet (<sup>3</sup>B<sub>1</sub>) PES, though a transition state with a structure similar to that found using the unrestricted DFT approach, whose structural parameters are reported in **Table 1**, was determined for the singlet <sup>1</sup>B<sub>1</sub> excited state. SCF energies indicate that both transition states are located in proximity of the conical intersection of the triplet and singlet PES, which implies that the progress of the reaction requires intersystem crossing between the singlet and triplet states. The hopping probability was determined as described in the Method section using Landau–Zener theory. The spin–orbit matrix element HSO calculated at the MECP is 282 cm<sup>-1</sup>, thus in good agreement with the 310 cm<sup>-1</sup> determined by Matsunaga et al.<sup>137</sup> for GeH<sub>2</sub> using a relativistic potential energy surface and an effective core potential basis set. The difference between the forces acting on the two states, calculated at the B3LYP/aug-cc-pvtz level, is 115.6 kJ mol<sup>-1</sup> Å<sup>-1</sup>. Given the high spin coupling value, it is reasonable to expect that the hopping probability is fast and that it will not affect considerably the system reactivity. This is indirectly confirmed by the good agreement found between the calculated and experimental activation energies. The activation energy calculated for reaction (R4) (160.2 kJ mol<sup>-1</sup>) in fact only slightly overestimates that evaluated by Votintsev<sup>132</sup> ( $\leq 146.9$  kJ mol<sup>-1</sup>) and Smirnov<sup>131</sup> (134.8 kJ mol<sup>-1</sup>), both determined by fitting of experimental data.

For the dissociation of GeH<sub>4</sub> and GeH<sub>2</sub> to GeH<sub>3</sub> and GeH we determined the rate constants in the high-pressure limit adopting micro-variational transition state theory on the PES calculated at the CASPT2 level. The PES for GeH<sub>4</sub> and GeH<sub>2</sub> homolytic decomposition reactions are sketched in **Figure 25** as a function of the length of the breaking bond. According to Berkowitz et al.,<sup>128</sup> the best estimate of the GeH<sub>3</sub>–H bond energy, determined through photoionization mass spectrometry, is 344.1 ± 8.4 kJ mol<sup>-1</sup> at 0 K. This result was confirmed by several theoretical studies, which re-

ported values comprised between 355.9 and 347.9 kJ mol<sup>-1</sup>,<sup>106,107,109-112,117,119,123</sup> and by the present calculations (349.6 kJ mol<sup>-1</sup>).

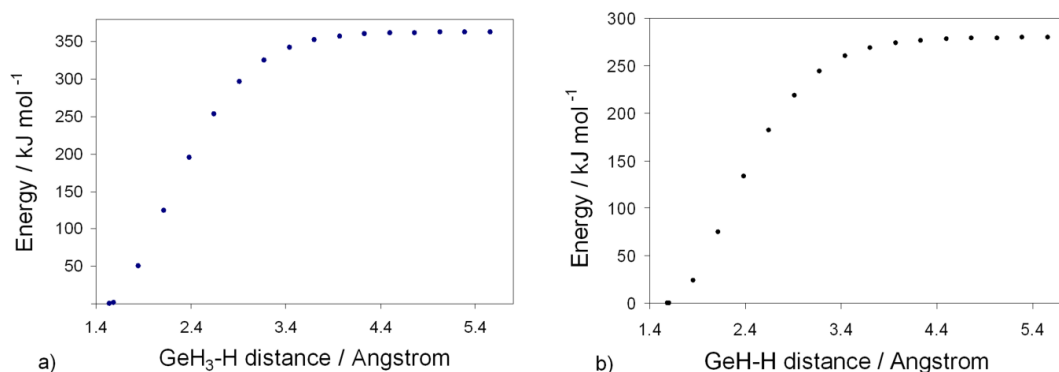


**Figure 25.** PES of the  $\text{GeH}_4$  (a) and  $\text{GeH}_2$  (b) dissociation to  $\text{GeH}_3$  and  $\text{GeH}$  calculated at the CASTP2 level using the  $cc\text{-}pVQZ$  basis set and corrected with ZPE calculated using vibrational frequencies determined at the same level of theory.

The high-pressure kinetic constants were calculated for reactions (R1)–(R4) using both classic and microcanonical transition state theory. The kinetic constants determined using the microcanonical approach were interpolated between 300 and 2200 K and are reported in **Table 3**. It was found that the E,J resolved microvariational determination of the kinetic constants of reactions (R1) and (R3) leads to a slight decrease of about 15% of the kinetic constants determined using classic variational transition state theory.

A more significant effect was found for the spin forbidden reaction  $\text{GeH}_2 \rightarrow \text{Ge} + \text{H}_2$ , in which the high-pressure kinetic constant decreases with respect to that determined using classic transition state theory by a factor of about 2 because of the inclusion of the intersystem crossing probability in the calculations.

**Table 3.** High-pressure kinetic constants of the considered reactive events interpolated between 300 and 2200 K to the modified Arrhenius expression ( $k = AT^n \exp(-E_a/RT(K))$ ). Activation energies and reaction enthalpies are reported in kJ/mol. The bimolecular kinetic constant has dimensions of  $\text{cm}^3/\text{mol/s}$ .

	A	N	E <sub>a</sub>	ΔH (0K)
$\text{GeH}_4 \rightarrow \text{GeH}_2 + \text{H}_2$	$6.4 \times 10^{13}$	0.272	221.90	164.54
$\text{GeH}_4 \rightarrow \text{GeH}_3 + \text{H}$	$6.12 \times 10^{16}$	-0.168	355.88	349.60
$\text{GeH}_2 \rightarrow \text{Ge} + \text{H}_2$	$9.09 \times 10^{12}$	0.203	164.12	133.56
$\text{GeH}_2 \rightarrow \text{GeH} + \text{H}$	$2.29 \times 10^{31}$	-4.43	345.83	291.82

### 4.3.2. GeH<sub>4</sub> and GeH<sub>2</sub> Decomposition Kinetics

The GeH<sub>4</sub> and GeH<sub>2</sub> decomposition kinetics was studied by integrating the master equation for a pure Argon bath gas, adopting an exponential down model for the collisional energy transfer, and using as Lennard-Jones collision parameters for bath gas and reactants the literature values of  $\sigma = 3.75 \text{ \AA}$  and  $\varepsilon = 98.3 \text{ cm}^{-1}$  for Argon, and  $\sigma = 4.30 \text{ \AA}$  and  $\varepsilon = 166.1 \text{ cm}^{-1}$  for GeH<sub>4</sub>.<sup>144</sup> The Lennard-Jones parameters of GeH<sub>2</sub> were determined by scaling those of GeH<sub>4</sub> in the same manner as they scale for SiH<sub>4</sub> with respect to SiH<sub>2</sub>. The values so determined are  $\sigma = 3.93 \text{ \AA}$  and  $\varepsilon = 106.3 \text{ cm}^{-1}$ . Since energy transfer parameters are not well known for GeH<sub>x</sub> molecules, we assumed as first guess that the mean downward transfer energy is  $170 \times (T/298 \text{ K})^{0.85} \text{ cm}^{-1}$  for both systems. This functional form was found to yield good agreement with experimental data for our previous investigation of the SiH<sub>4</sub> dissociation reaction<sup>70</sup> and by Matsumoto when studying the Si<sub>2</sub>H<sub>6</sub> reactivity.<sup>145</sup> Since, among the others, this parameter is the most uncertain, its impact on the calculations was investigated through a sensitivity analysis.

The  $k(E,J)$  kinetic constants were calculated at E and J steps of  $1 \text{ cm}^{-1}$  and 1, for E and J comprised between 1 and  $50000 \text{ cm}^{-1}$  and 1 and 150, respectively. The microcanonical kinetic constants were then averaged over J as proposed by Miller et al.<sup>71</sup> and the  $k(E)$  so determined were finally averaged in discrete reaction bins. The J averaged  $k(E)$  RRKM kinetic constants for the reactions of dissociation of GeH<sub>4</sub> to GeH<sub>2</sub> and GeH<sub>3</sub> are reported in **Figure 26** as a function of the internal energy. In order to determine the effect of the bin size on the accuracy of the calculations two different tests were performed. The first was the check of the consistency of the high-pressure rate constants calculated assuming a Boltzmann energy distribution both for the  $1 \text{ cm}^{-1}$  E spaced  $k(E,J)$  kinetic constants and for those averaged over  $100 \text{ cm}^{-1}$  bins.

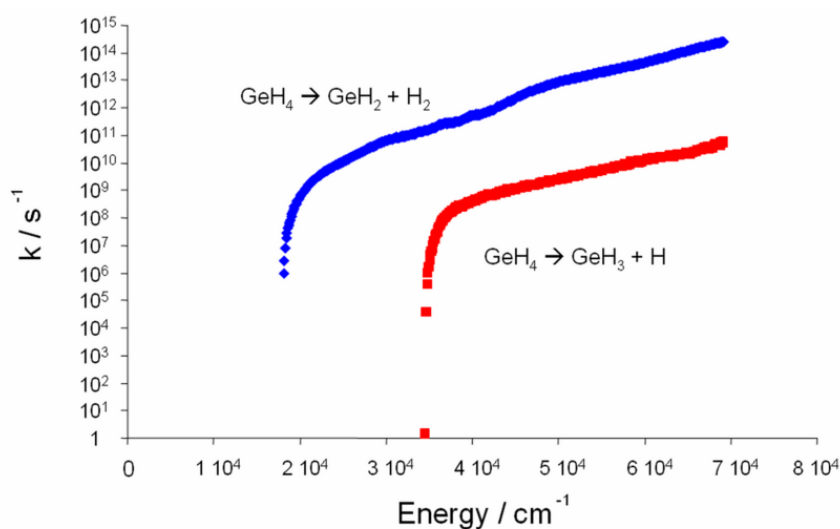


**Figure 26.** Microcanonical RRKM kinetic constants calculated for the reaction of decomposition of GeH<sub>4</sub> to GeH<sub>2</sub> and GeH<sub>3</sub>, reported in s<sup>-1</sup>.

The high-pressure rate constants calculated using the microcanonical  $k(E,J)$  kinetic constants and the J-averaged kinetic constants were always in quantitative agreement with those determined using classic transition state theory (i.e. when no intersystem crossing was considered), while those determined with the  $100\text{ cm}^{-1}$  binned rate constants differed by the expected values by no more than 5%. The second test consisted in performing several simulations (i.e.  $\text{GeH}_4$  and  $\text{GeH}_2$  decomposition between 1100 and 1700 K at 1 bar) by systematically reducing the bin size to 50 and  $25\text{ cm}^{-1}$ . It was found that the effect of the bin size is negligible (i.e. the deviation from the  $100\text{ cm}^{-1}$  reference value is smaller than 5%) as long as the maximum energy change allowed for a single jump is at least  $4500\text{ cm}^{-1}$ , which corresponds to a max jump parameter of 45 (which means that a maximum of 92 transitions are stored in the binary tree for each stochastic event).

Simulations were performed studying explicitly the dynamics of  $N$  parallel systems, each composed of a single molecule, starting the simulations from an unexcited state. The pressure dependent kinetic constant was then determined by regression over the reaction time, using the linear regression algorithm over reacted molecules as a function of reaction time we introduced in our protocol (see Chapter 3 section 3.2) The number of reactive events needed to reach a converged solution was determined dynamically, as it changes with temperature and pressure, by adopting as convergence parameter the student's t-test with a 1% confidence limit. At least about 500 events and  $10^8$  random transitions were generally necessary to reach converged solutions for most simulations. Simulations were performed for temperatures comprised between 1100 and 1700 K and pressures comprised between  $10^{-3}$  and 10 bar. Some specific simulations were performed at 1600 K and at 1700 K at increasing pressures to check both the internal consistency of the code in terms of capability to predict the high-pressure limit as well as to determine the pressure at which the high-pressure limit is finally reached. The calculated kinetic constants reached smoothly the limiting rates for pressures of about  $2 \times 10^4$  bar for both simulation sets. The calculated high-pressure rate constants were about 95% of those computed with TST, which confirms that the stochastic code is able to predict the correct high-pressure behavior for the conditions in which the Boltzmann equilibrium distribution is reached.

Interestingly, we did not observe any reactive event leading to the direct decomposition of  $\text{GeH}_4$  to  $\text{GeH}_3$  and H in the investigated temperature and pressure range. This result could in part be expected since, analyzing the high-pressure rate constants of these reactions, it can be observed that the rate constant of the simple dissociation reaction is from 5 to 2 orders of magnitude lower than that of the reaction that produces  $\text{GeH}_2$  and  $\text{H}_2$ . A similar result was found also for  $\text{GeH}_2$  decomposition. A second less evident reason is that, in the investigated temperature and pressure range, both the reactive systems considered are deep in their fall off regime. In this situation, the population of the most excited states is significantly depleted with respect to the Boltzmann population, so that it is extremely difficult for an excited state to reach the reaction energy threshold of the most activat-

ed dissociation reaction. This can be directly observed from the analysis of the calculated population of the excited energy states for a  $\text{GeH}_4$  reacting system, which is reported in **Figure 27** where it is compared with the Boltzmann population.

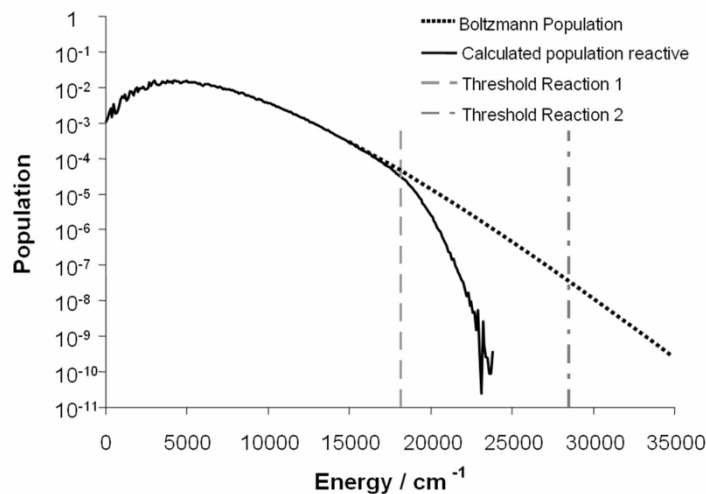


**Figure 27.** Comparison between the energy distribution function calculated for the  $\text{GeH}_4$  reactive system at 1 bar and 1400 K and the Boltzmann population. The energy thresholds for reaction 1 and 2 are shown to highlight the dramatic decrease of population of the excited states that takes place above the first reaction threshold.

A specific set of simulations was performed with the aim of determining the effect that the inclusion of the intersystem crossing probability in the estimation of the microcanonical kinetic constants has on the decomposition kinetics. It was interesting to find out that, though the high-pressure rate constants decrease by a factor of 2 upon inclusion of the  $p_{\text{hop}}$  probability in equation (134), the effect on the master equation simulations is much smaller, with a decrease of the kinetic constants calculated in the investigated temperature and pressure ranges of about 15% with respect to the rates computed without accounting for the intersystem crossing probability. The motivation for this small impact of intersystem crossing on the rate constant is that in the fall off regime prevailing in these conditions the high rovibrational energy levels are depleted and the reactivity is determined mostly by the energy states located just above the reaction energy threshold. For these states the kinetic energy available for the transitional modes is little, so that PLZ is small and  $p_{\text{hop}}$  approaches unity.

The comparison between the RRKM/ME calculations and the first set of experimental data considered (Votintsev et al.<sup>132</sup> and Smirnov et al.<sup>131</sup>), measured over the 1060–1500 K temperature range and at a pressure of 1.5 bar, concerns the  $\text{GeH}_4$  and  $\text{GeH}_2$  decomposition kinetic constants and is reported in **Figure 28**.

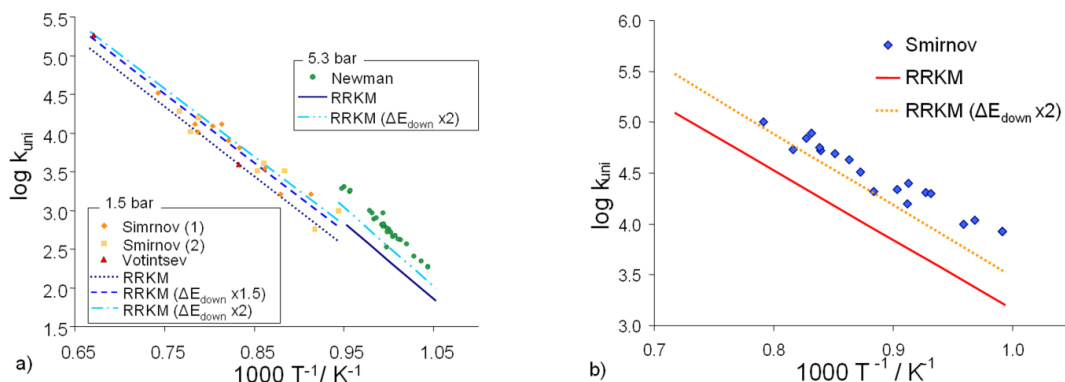


**Figure 28.** Comparison of the calculated decomposition kinetic constants of  $\text{GeH}_4$  to  $\text{GeH}_2$  and  $\text{H}_2$  with the experimental data measured (a) by Votintsev<sup>132</sup> and Smirnov<sup>131</sup> at 1.5 bar in the presence of (1) 1.0%  $\text{N}_2\text{O}$  and (2) 3.0%  $\text{N}_2\text{O}$  and by Newman<sup>130</sup> at 5.3 bar. In (b) it is reported the comparison with the experimental data reported by Smirnov at 1.5 bar for the decomposition of  $\text{GeH}_2$  to  $\text{Ge}$  and  $\text{H}_2$ .

As it can be observed, the calculations under predict the measured kinetic constants by an average factor of 1.6 for  $\text{GeH}_4$  decomposition, which more than doubles for  $\text{GeH}_2$  decomposition. A possible explanation for the observed disagreement is the choice of the energy transfer parameter for the collision energy transfer process, on which, as mentioned above, there is considerable uncertainty. Thus, we decided to perform a sensitivity analysis in order to investigate what is the effective impact of this parameter on the calculated rate constants.

It was found that increasing the energy transfer up to a factor of two leads to a decrease of the difference between calculations and experimental data from a factor of 1.6 to 1.3 in the case of  $\text{GeH}_4$  decomposition, thus within the experimental uncertainty, and from 3.5 to 1.6 for  $\text{GeH}_2$  decomposition. Increasing the energy transfer parameter above a factor of two did not affect significantly the computational results. Also for the second set of simulations an underestimation of experimental data, measured in a different temperature range (950–1060 K) and at a higher pressure (5.3 bar) with respect to those reported by Smirnov, was observed. The disagreement is significantly larger than that found for the first set of data simulated. The discrepancies between calculations and experiments for the data reported by Newman et al.<sup>130</sup> for the  $\text{GeH}_4$  decomposition is in fact a factor of 2.5, which reduces to 1.7 increasing the energy transfer parameter. These differences were detected also by Simka et al.<sup>129</sup> who carried out a RRKM study of germane decomposition. The underestimation of the experimental data, a factor of 4.5, is larger than that calculated in the present study and can mostly be ascribed to the lower value of the high-pressure rate constants, in which the pre-exponential is a factor of two smaller than that computed in the present work (most probably because its temperature dependence was neglected) while the activation energy is about 7  $\text{kJ mol}^{-1}$  higher (calculations were performed at a lower level of theory, as reported in **Table 2**).

To further study the origin of the discrepancy between experimental and theoretical data, we investigated whether it might be determined by the presence of secondary reactions.

A peculiarity of this reaction system is in fact represented by the rate at which  $\text{GeH}_2$  dissociates to  $\text{Ge}$  and  $\text{H}_2$ , which is significantly faster than the rate of dissociation of  $\text{GeH}_4$ . It becomes thus possible that, if  $\text{Ge}$  atoms react with  $\text{GeH}_4$  sufficiently rapidly, they may accelerate the overall  $\text{GeH}_4$  decomposition rate. Since it is well known that  $\text{Si}$  can react rapidly (with almost collisional efficiency) with  $\text{SiH}_4$  to form  $\text{Si}_2\text{H}_2$ ,<sup>146,147</sup> we hypothesized that a similar reaction may also be active for this system. We thus simulated both sets of experimental data adopting a kinetic scheme constituted by reactions (R1)–(R4) with the addition of the following reaction:

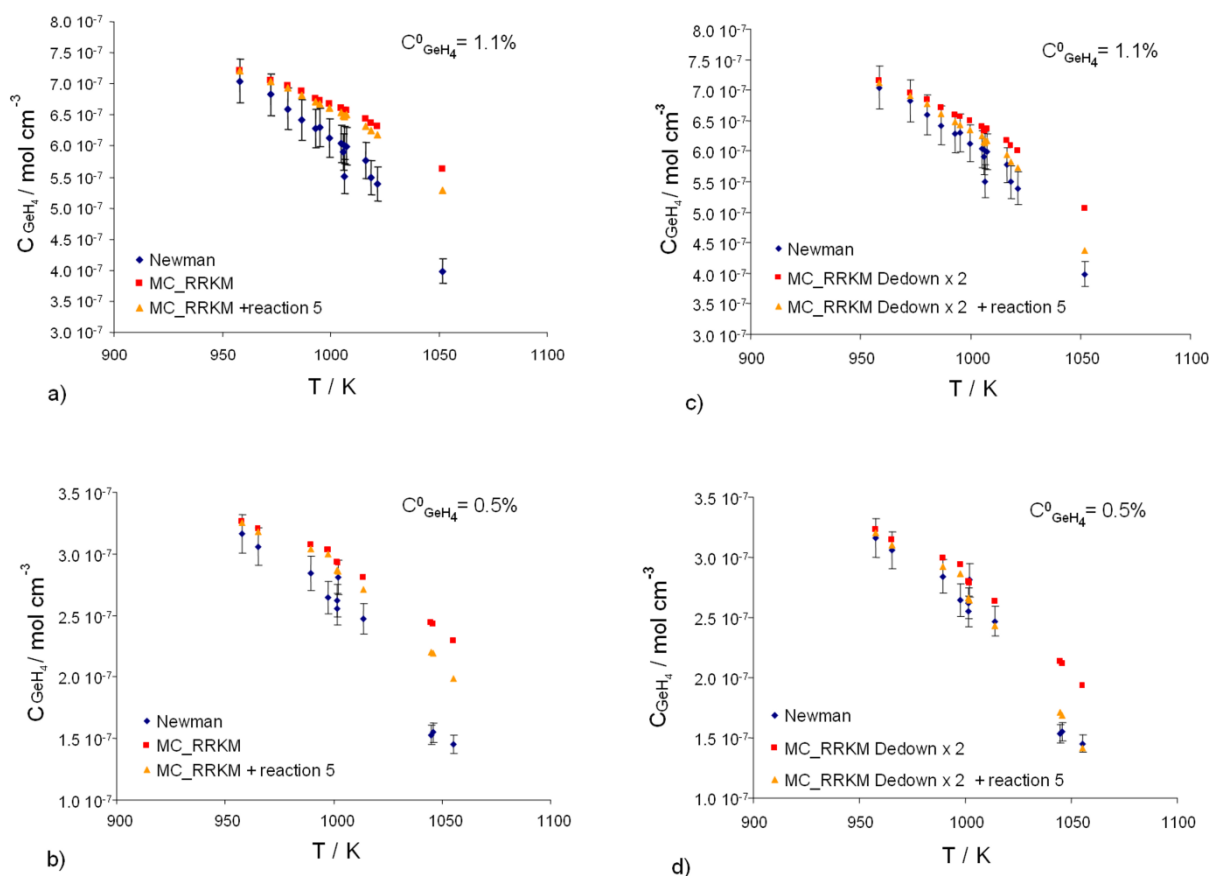


**Figure 29.** Comparison of the calculated concentrations with experimental data measured after variable reaction times (240–390  $\mu\text{s}$ ) with an initial fraction of  $\text{GeH}_4$  of 1.1% (a,c) and 0.5% (b,d) at a pressure of 1.5 bar. Points are experimental data, squares were obtained not considering reaction 5, while triangles were obtained introducing reaction 5 in the kinetic scheme.

The kinetic constant adopted for reaction (R5) was first assumed to be equal to that reported by Dollet and de Persis<sup>146</sup> for the reaction of  $\text{SiH}_4$  with atomic  $\text{Si}$ , while for the other reactions we used the kinetic constants evaluated in this study.

The simulations of the first set of experimental data did not evidence any impact of the introduction of reaction (R5) on the rate of decomposition of  $\text{GeH}_4$ , even when increasing the reaction rate up to the collisional limit. The situation changed however for the second set of experimental data, which were measured performing the experiments using an initial  $\text{GeH}_4$  concentration significantly higher than that adopted by Smirnov. The results of the simulations are compared with experimental data in **Figure 29**.

In **Figure 29a** and **b** are reported the results of the simulations of the second set of experimental data performed adopting reactions (R1)–(R5) with the kinetic constants determined with the reference energy transfer parameter. As it can be observed, the presence of reaction (5) reduces the difference between the calculated and experimental data, though a certain disagreement can still be observed, especially at high temperatures.

Increasing the energy transfer parameter by a factor 2, which gave a satisfactory agreement with the first experimental data set, leads also in this case to a good reproduction of the experimental data. The results are shown in **Figure 29c** and **d**. Interestingly, a sensitivity analysis on the kinetic constant of reaction (R5) revealed that even decreasing significantly its value did not affect the computational results. This is determined by the relatively high concentration of  $\text{GeH}_4$  used for the experiments (0.5–1%  $\text{GeH}_4$  mixtures in Ar), in which decomposition leads to the formation of a concentration of Ge atoms sufficient to react quantitatively with the precursor.

The data reported in **Figure 30** show that the  $\text{GeH}_4$  and  $\text{GeH}_2$  decomposition rates are in their fall off regime for the whole temperature and pressure range considered in this study, which covers in practice all the operating conditions in which Ge films are deposited from this precursor.

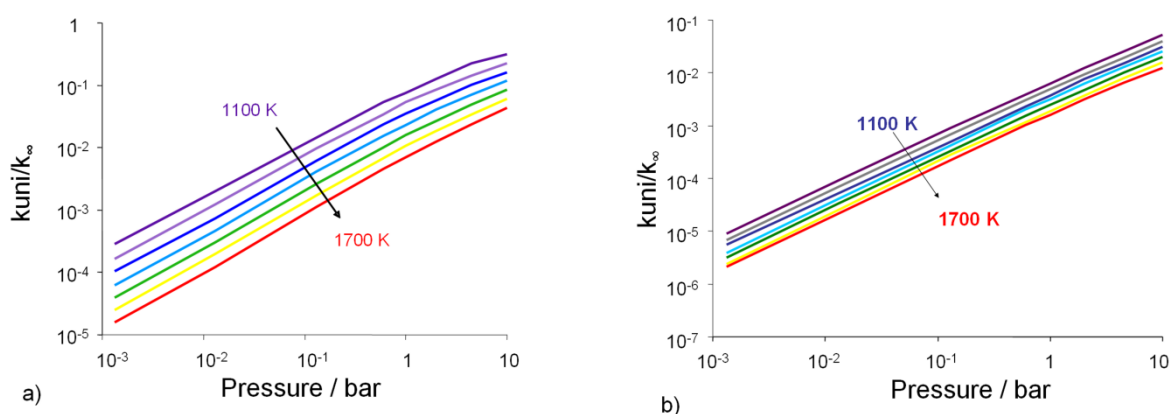


**Figure 30.** Calculated kinetic constant for the decomposition of (a)  $\text{GeH}_4$  to  $\text{GeH}_2$  and  $\text{H}_2$  and (b)  $\text{GeH}_2$  to  $\text{Ge}$  and  $\text{H}_2$  reported as the ratio with respect to the high-pressure limit.

Since the accurate knowledge of these decomposition parameters is of practical importance in order to study the gas phase kinetics active during the deposition of Ge films, we have fitted the decomposition rate constant to the Troe form so that it is possible to calculate for any range of op-

erating parameters the correct decomposition rates. The interpolated low-pressure kinetic constant and FCent parameters are reported in **Table 4**.

**Table 4.** Fit of the  $\text{GeH}_4$  and  $\text{GeH}_2$  kinetic parameters to the Troe formalism: high-pressure ( $s^{-1}$ ), low pressure ( $\text{cm}^3\text{mol}^{-1}\text{s}^{-1}$ ) and FC parameters for the broadening factor ( $T^{**}$  was set to 0 in the regression). Activation energies in kJ/mol.

$\text{GeH}_4$	A	N	Ea	T-range (K)
$k_\infty$	$6.4 \times 10^{13}$	0.272	221.90	300-2200
$k_0$	$2.75 \times 10^{48}$	-9.055	263.35	1100-1700
	A	$T^{***}$	$T^*$	
Fcent	0.216	626.55	$-2.59 \times 10^7$	1100-1700
$\text{GeH}_2$	A	N	Ea	T-range (K)
$k_\infty$	$9.09 \times 10^{12}$	0.203	164.12	300-2200
$k_0$	$1.6 \times 10^{26}$	-3.06	175.6	1100-1700
	A	$T^{***}$	$T^*$	
Fcent	0.018	$1.222 \times 10^3$	$-6.125 \times 10^2$	1100-1700

#### 4.4. Conclusions

The decomposition rate of  $\text{GeH}_4$  and  $\text{GeH}_2$  was studied through RRKM/ME simulations using structural and energetic parameters determined from *ab initio* simulations. Our calculations confirm that in the considered temperature and pressure ranges both reactions are in the fall off regime. It was found that  $\text{GeH}_2$  decomposes faster than  $\text{GeH}_4$  and that, at sufficiently high partial pressures, the Ge atoms so produced are likely to react with  $\text{GeH}_4$  to enhance its decomposition. A good agreement between experimental data and calculated  $\text{GeH}_4$  and  $\text{GeH}_2$  decomposition rates could be obtained assuming that the energy transfer parameter is  $340 \times (T/298 \text{ K})^{0.85} \text{ cm}^{-1}$  for both  $\text{GeH}_4$  and  $\text{GeH}_2$ . This parameter is in reasonable agreement with that used in several RRKM studies on the  $\text{GeH}_2$  reactivity, in which it was adopted a temperature independent energy transfer parameter of  $800 \text{ cm}^{-1}$ .<sup>148,149</sup>

Finally, despite the increase of the energy transfer parameter, our calculations still under predict the  $\text{GeH}_2$  decomposition rate by a factor of 1.6, well within the uncertainty range of these calculations, which have been estimated to be about a factor of 2 and 4 for the  $\text{GeH}_4$  and  $\text{GeH}_2$  decomposition reactions, respectively, due to the uncertainty of the calculated energies and transition state structures. Since in this case the validation of the computational results is based on the comparison with a single set of experimental data and  $\text{GeH}_2$  is an extremely reactive molecule, we think that further studies will be necessary to definitely assess the kinetic constant for this reaction.

# 5 Toluene Decomposition: Secondary Chemistry

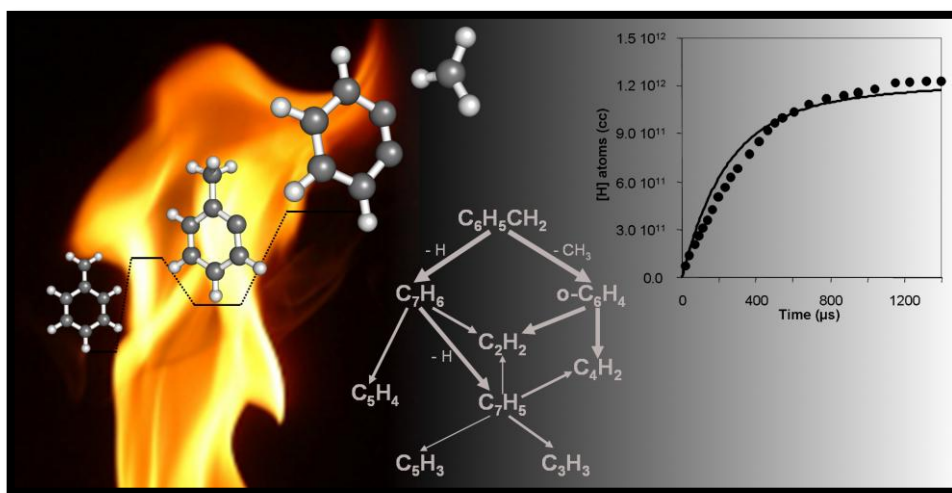


**Figure 31.** A kinetic analysis based on *ab initio* and RRKM/ME calculations shows that toluene decomposition involves fulvenallene and benzyne as intermediates.

## 5.1. Introduction

The gas phase kinetics of toluene has been the subject of much experimental and theoretical research in the last years.<sup>59,150-169</sup> Toluene is in fact not only the simplest alkylated aromatic species, but it is also found in considerable concentration in crude oils as well as in jet fuels and in gasoline and it is formed easily in the gas phase during the pyrolysis or combustion of hydrocarbons. A detailed understanding of its decomposition kinetics and of its secondary chemistry would thus be extremely useful to model the initial stages of combustion or pyrolysis of the mentioned fuels as well as to understand if and how it can contribute to the nucleation and growth of soot.

Currently, there is a general consensus on what are the main products formed through the unimolecular decomposition of toluene: the benzyl and the phenyl radicals. The kinetic constant for the overall decomposition of toluene has been determined experimentally by several authors,<sup>59,152,154,157,159-162,170-173</sup> with a few also reporting the branching ratios between the benzyl and the phenyl reaction channels. It was found that the dominant product is benzyl, with the phenyl contribution rising with the temperature from about 10% at 1000 K to 30-40 % at 2000 K.

Several theoretical studies were devoted to the investigation of the reactivity on the  $C_7H_8$  potential energy surface (PES), though the focus was more on the interconversion kinetics between the

different toluene isomers, norbornadiene and cycloheptatriene,<sup>174-176</sup> than on decomposition reactions. More recently the experimental data have been interpreted through refined *ab initio* and kinetic calculations, accounting explicitly for intermolecular energy transfer and thus extending the experimental estimates to an ample pressure and temperature range.<sup>59</sup>

However, the secondary chemistry started by toluene decomposition, in particular for what concerns the benzyl radical, is understood at a lower level of detail. In addition, the interpretation of the benzyl decomposition mechanism has been controversial for many years. Experimental and computational studies were particularly conflicting. More specifically, investigations focused on the initial steps of benzyl decomposition evidenced that it is consistent with dissociation to hydrogen and a C<sub>7</sub>H<sub>6</sub> species.<sup>153,157,177-179</sup> On the other hand, kinetic simulations of the overall decomposition process showed that good fits of experimental data can be obtained only if it is assumed that the main decomposition products are acetylene and the cyclopentadienyl radical.<sup>165,166</sup>

An advancement in the comprehension of benzyl reactivity came from a recent proposal by Cavallotti et al.<sup>180</sup>, formulated on the basis of theoretical calculations, that the main decomposition product of benzyl is fulvenallene. This prediction found support in successive theoretical calculations<sup>181</sup> and simulations of experimental data,<sup>182</sup> which showed that a kinetic mechanism incorporating a C<sub>7</sub>H<sub>6</sub> pathway can predict mole fraction profiles experimentally measured in a rich toluene flame.

Still, agreement with experimental data could be obtained only by assuming that fulvenallene reacts rapidly with atomic hydrogen to form acetylene and the cyclopentadienyl radical. Furthermore, the proposed kinetic constant for this reaction channel is extremely high,  $3 \times 10^{14}$  cm<sup>3</sup>/mol/s, which is about a factor of 50 higher than the one calculated from first principles.<sup>180</sup> This overestimation seems excessive not only considering the uncertainty associated with first principles calculations, but also in the light of the fact that a similar reaction channel had already been tested unsuccessfully by Brezinsky and co-workers to simulate the shock tube decomposition of toluene.<sup>165</sup>

To improve our understanding of the fulvenallene reaction channel we investigated the reactivity on the C<sub>7</sub>H<sub>6</sub> PES using *ab initio* calculations<sup>183</sup> and then examining the C<sub>7</sub>H<sub>6</sub> decomposition kinetics integrating the master equation (ME).<sup>184</sup> Through this analysis we found that, in addition to decomposing to the fulvenallenyl radical (C<sub>7</sub>H<sub>5</sub>) and atomic hydrogen, as suggested by da Silva and Bozzelli,<sup>185</sup> fulvenallene can also decompose to acetylene and the cyclopentadienyliene di-radical (cC<sub>5</sub>H<sub>4</sub>). Though the latter is the main reaction channel, the decomposition to C<sub>7</sub>H<sub>5</sub> and H contributes between 20% and 50% to the global fulvenallene decomposition rate, depending on temperature and pressure.

According to these results, the decomposition of each benzyl radical should lead to the formation of 1.2-1.5 H atoms, of which one is due to the decomposition to fulvenallene and 0.2-0.5 to fulvenallene decomposition to the fulvenallenyl radical. This is in contrast with the very recent H-

ARAS experiments performed by Sivaramakrishnan et al. at very low partial pressures of benzyl bromide and of its partially deuterated analogue,  $C_6H_5CD_2Br$ .<sup>186</sup> In these conditions, the contribution of secondary reactions to the production or consumption of H is negligible, so that an accurate measure of each H atom produced per decomposed benzyl molecule is possible. It was found that about 0.8 H+D atoms are produced for each decomposed benzyl molecule. Moreover, the observed minor production of D atoms could be explained only by the participation of the deuterated  $CD_2$  group to the decomposition reaction. A mechanism that is not energetically feasible on the PES we proposed, according to which the scrambling of H atoms of the benzyl methylene group requires overcoming an activation energy larger than that leading to benzyl decomposition.<sup>180</sup> The theoretical and experimental evidences can thus be reconciled only assuming that benzyl can decompose through a second reaction channel, possibly involving scrambling, that does not have H atoms among its products. In light of these evidences, we decided to investigate again at higher level of theory the benzyl potential energy surface and in particular, we searched for a decomposition channel alternative to that leading to fulvenallene.

After much search, a potential new pathway accessible to benzyl decomposition that leads to the formation of benzyne and a methyl radical has been discovered. Including this newfound reaction path in our ME/RRKM calculations we estimated the overall benzyl decomposition rate constant and the branching ratio for each specific decomposition channel at different temperatures and pressures. Good agreement was obtained comparing the results of our predicted rate coefficients with the experimental measures.<sup>187</sup>

To prove the reliability of this finding, we also formulated a kinetic mechanism, which comprises the benzyl and toluene decomposition reactions together with the proposed fulvenallene decomposition mechanism and some reactions describing the secondary chemistry originated by the decomposition products. With this kinetic mechanism we simulated the production of H atoms measured in a wide pressure and temperature range using different experimental set ups. The calculated and experimental data were found to be in good agreement.<sup>187</sup>

To summarize, in the present work two potential energy surfaces were investigated that are of great importance for the determination of toluene secondary chemistry: the  $C_7H_6$  (fulvenallene) and  $C_7H_7$  (benzyl) PESs. A combined RRKM/ME approach has been adopted to analyze the reaction dynamics that takes place on these energy surfaces and to estimate the overall and channel specific rate coefficients of fulvenallene and benzyl decomposition. The predicted rate constants have been successively introduced in a detailed kinetic scheme in order to simulate experimental conditions and the direct comparison between the calculated and the measured values allowed us to confirm the mechanism proposed.

The present chapter is organized as follows. In section 5.2 is presented a brief description of the electronic structure methods and the kinetic theories here adopted. In section 5.3 and 5.4 are report-

ed the analyses of the C<sub>7</sub>H<sub>6</sub> and C<sub>7</sub>H<sub>7</sub> PESs, respectively, and the estimation of the channel specific rate constants as a function of pressure and temperature. In section 5.5 is reported the kinetic mechanism formulated to simulate toluene and benzyl decomposition and the comparison with the experimental measurements. Finally, some concluding remarks will be discussed in section 5.6.

## 5.2. Computational Methodology

### 5.2.1. Electronic Structure Methods

The computational strategy adopted to investigate the C<sub>7</sub>H<sub>6</sub> and C<sub>7</sub>H<sub>7</sub> PESs consists in the systematic determination of all the possible reaction pathways that can depart from the minimum energy well, which are fulvenallene and benzyl respectively. The structures and vibrational frequencies of all the considered wells and transition states have been determined using density functional theory (DFT) at the B3LYP/6-31+G(d,p)<sup>17,18,188</sup> level and are reported as supplementary information in ref<sup>183</sup>. All transition states have been located using a synchronous transit guided saddle point search algorithm<sup>189</sup> and are characterized by a single imaginary frequency. The energies of all wells and transition states have been then calculated using coupled cluster theory at the CCSD(T) level<sup>15</sup> using the correlation consistent double and triple  $\zeta$  basis sets cc-pVDZ and cc-pVTZ<sup>190</sup> and extrapolated to the complete basis set limit (CBS) using the scaling coefficients suggested by Martin<sup>136</sup> including B3LYP/+6-31g(d,p) zero point energy (ZPE) corrections as:

$$\begin{aligned} E(\infty) = & E(\text{CCSD(T)}/\text{cc-pVTZ}) \\ & + 0.463[E(\text{CCSD(T)}/\text{cc-pVTZ}) - E(\text{CCSD(T)}/\text{cc-pVDZ})] \quad (137) \\ & + \text{ZPE (B3LYP/6-31+G(d,p))} \end{aligned}$$

The energies of all the open shell wells and saddle points have been estimated with an unrestricted formalism in the case of DFT calculations and a restricted open shell wave function for the coupled cluster calculations.

The decomposition of fulvenallene to the fulvenallenyl radical proceeds through a loose transition state, thus its potential energy surface has been determined by scanning the reaction coordinate, defined as the length of the breaking bond, at steps of 0.1 Å starting from a C-H distance of 2.0 Å.

Two different approaches have been used to determine the final result. At a lower level of theory, structures, energies, and vibrational frequencies have been determined with the unrestricted B3LYP/6-31+G(d,p) method on the singlet PES using a broken symmetry guess for the wave function. At a higher level of theory, in order to account properly for the contribution of excited states, structures and vibrational frequencies have been calculated at the CASSCF/6-311G(d,p) level<sup>8,9</sup>, while energies have been determined using CASPT2 theory<sup>134,135</sup>. The considered active space con-

sists of 10 electrons and 10 orbitals, thus including all the electrons populating the four  $\pi$  orbitals of fulvenallene and those of the  $\sigma$  orbital of the breaking bond together with the respective antibonding orbitals. The CASPT2 calculations have been performed in the C1 symmetry group using the cc-pVTZ basis set.

The energies thus obtained have been successively scaled to the bond dissociation energy estimated at the CCSD(T)/CBS level, as the coupled cluster approach is expected to be more accurate in determining bond energies than CASPT2 theory. The same approach has been used to calculate the activation energy for transition states with a significant multireference character.

In addition, among the elementary reactions that take place on the  $C_7H_7$  potential energy surface, the dissociation of the 2-methylphenyl radical into methyl and benzyne does not have a saddle point. Its potential energy surface has been thus determined as a function of the reaction coordinate, defined as the length of the breaking bond, with steps of 0.05 Å starting from a C-C distance of 2.5 Å. Intermediate geometries, vibrational frequencies and energies have been determined at the B3LYP/6-31+G(d,p) level using an unrestricted formalism. Successively energies have been scaled with the bond dissociation energy determined at the CCSD(T)/CBS level.

All DFT calculations were performed using the Gaussian 03 suite of programs<sup>1</sup>, while CASPT2 and CCSD(T) calculations were accomplished using Molpro 2008<sup>3</sup>.

### 5.2.2. Kinetic Theories

Within the scheme implemented in the MCRRKM code, the microcanonical rate constants  $k(E, J)$  are computed from the convoluted rotational and vibrational density of states as a function of energy  $E$  and angular momentum  $J$  considering all the vibrational and external rotational degrees of freedom. In particular, the degeneration of low vibrational frequencies into torsional rotors has been treated with the hindered rotor approximation. We investigated the PES associated to the torsional modes of vibration and when necessary we calculated the density of states for the internal rotations with a direct count algorithm over the energy levels determined solving the 1D rotational Schrödinger equation. In addition, the densities of state calculated were convoluted if more than one hindered rotations was present, as described in section 3.3.2 of Chapter 3.

One of the main pathways found to be active within fulvenallene decomposition occurs in correspondence of the intersection between the singlet and the triplet state of the  $C_7H_6$  PES. This reaction has been thus treated with the non-adiabatic transition state theory approach proposed by Harvey<sup>75</sup> that has been described in Chapter 3. There we established that the parameters necessary to compute the hopping probability are the off-diagonal spin-orbit coupling element of the  $4 \times 4$  Hamiltonian matrix between the triplet and singlet state evaluated at the crossing point,  $H_{SO}$ , and the relative slope of the two surfaces at the MECP,  $\Delta F$ . In particular, here,  $H_{SO}$  has been determined adopting singlet and triplet wave functions calculated using the multireference configuration inter-

action<sup>139,191</sup> (MRCI) theory including six orbitals and six electrons in the active space and a 6-31G basis set, while  $\Delta F$  has been calculated at the B3LYP/6-31+G(d,p) level.

Master equation (ME) calculations have been performed adopting the 1D master equation formulation proposed by Miller et al.<sup>71</sup> and implemented in our computational code as described in detail in Chapter 3. In particular, for the current investigation, the single well integration protocol of the master equation implemented in our previous works was extended to describe the unimolecular reaction dynamics on a multiple well PES as described in section 3.3.3 of Chapter 3.

In brief, this has been accomplished by allowing the excited molecule to react to a different energetic state, differing from the reacting well for the reaction energy change, with updated collisional transitional probabilities between different energy levels and RRKM reaction rates. The computational protocol is designed so that reaction and transitional collisional properties for all the considered wells and transition states are calculated before starting the ME integration cycle using an integration energy step of  $1 \text{ cm}^{-1}$ , and are then averaged over discrete energy bins.

It is important to highlight that the rate coefficient determined through our approach is a flux coefficient, i.e. the coefficient that multiplied by the reactant concentration gives the number of molecules that per unit time and volume are converted to the reaction product and differs from the value of the phenomenological rate constant.<sup>82,83</sup> However, it is likely that this difference may not be too large for the cases investigated here. In fact, the products of the decomposition reactions considered are usually present in very low concentrations in reaction environments in which these reactions are active due to fast secondary reactions channels, so that the irreversible sink assumption most probably holds. In addition, the stabilization of intermediate wells is likely to be negligible.

## 5.3. Fulvenallene Decomposition

### 5.3.1. Analysis of the Reactivity on the $\text{C}_7\text{H}_6$ Potential Energy Surface

The investigation of the reaction pathways that can be originated by fulvenallene and eventually lead to its dissociation can be rationalized in terms of six reaction channels, which are described below in detail. The global high-pressure decomposition rate constants are then calculated in order to determine which are the most probable decomposition channels. Afterwards, ME/RRKM calculations have been performed to estimate the rate coefficients of the main decomposition channels as a function of temperature and pressure.

#### **Reaction Pathway 1: Fulvenallene Dissociation to Fulvenallenyl and Hydrogen**

The decomposition of fulvenallene to fulvenallenyl is a unimolecular reaction without reverse barrier, as has been determined by scanning the PES as a function of the C-H breaking bond. A preliminary estimation of the kinetic constant using macrocanonical variational transition state theory

showed that the portion of the PES relevant for the estimation of the kinetic constant (i.e. the interval of the reaction coordinate along which the minimum kinetic constant is found) is comprised between 2.0 and 3.0 Å. The PES has thus been determined for 11 structures for which the minimum energy conformation was searched scanning the reaction coordinate at 0.1 Å steps. The PES calculated using CASPT2 energies corrected with ZPE and scaled with respect to the CCSD(T) reaction energy change is shown in **Figure 32**.

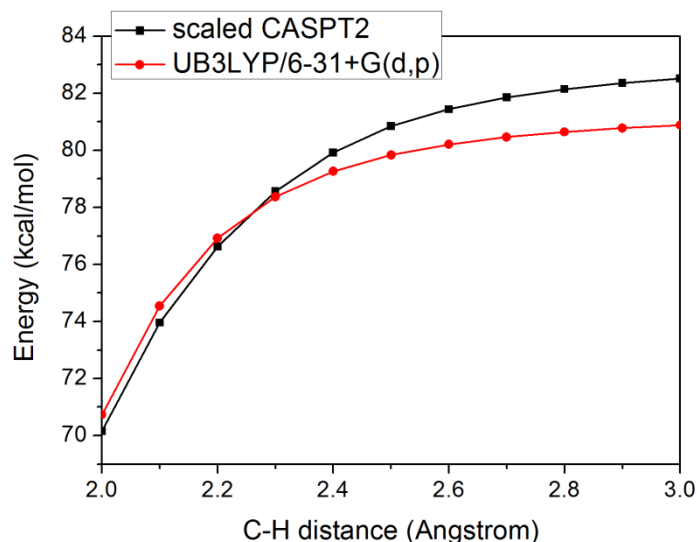


**Figure 32.** PES for the dissociation of fulvenallene into the fulvenallenyl radical and hydrogen computed at two different levels of theory and corrected for ZPE.

As can be observed, the two surfaces are almost overlapped between 2.0 and 2.3 Å, while they differ increasingly with the increase of the reaction coordinate. This difference rises up to 1.8 kcal/mol at a C-H distance of 3.0 Å, which can be ascribed to the different reaction energies predicted by DFT and CCSD(T) calculations. The reaction energy change calculated at the CCSD(T)/CBS level, 81.6 kcal/mol (corrected for ZPE), is similar to the 81.2 kcal/mol determined by da Silva and Bozelli using G3SX theory,<sup>185</sup> while the CASPT2 reaction energy change is about 5 kcal/mol smaller than the CCSD(T) estimate. Additional calculations revealed that this discrepancy could not be ascribed to the dimension of the active space or to the number of electrons. As coupled cluster and G3 theories are generally accurate in estimating reaction energy changes, it has thus been decided to rescale the CASPT2 to the CCSD(T) energies.

### Reaction Pathway 2: First C5 → C7 Ring Expansion Mechanism

It is known that fulvenallene can interconvert to cycloheptatetraene and vice versa. We found two possible reaction pathways that can lead to the formation of C7 cyclic species. The PES of the first investigated mechanism is sketched in **Figure 33**.

The reaction is initiated by the formation of bicyclic intermediate **2**, which is about 69.7 kcal/mol less stable than **1**. This is a relatively unstable species as the barriers to convert to **3** or give back **1** are small, about 10 kcal/mol.

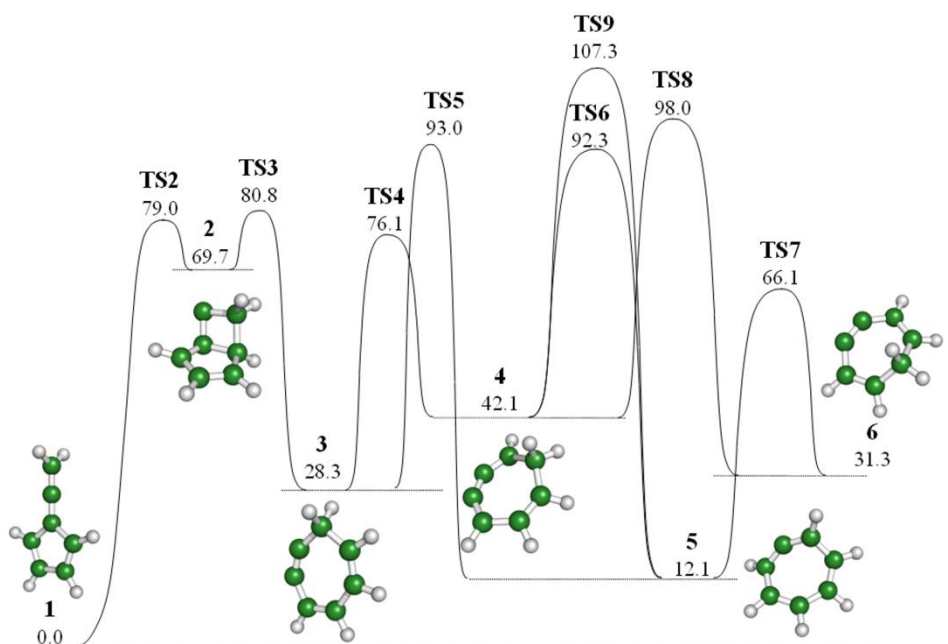


**Figure 33.** PES for the first mechanism of interconversion of fulvenallene to cycloheptatetraene. Energies were calculated at the CCSD(T)/CBS level for B3LYP/6-31+G(d,p) structures.

Isomer **3** needs to undergo several hydrogen transfer reactions before forming cycloheptatetraene. All the considered hydrogen transfer reactions are, however, significantly activated as they require a ring distortion that is contrasted by the allenic group, which favors a planar arrangement of ligands, as described by Johnson in his review on cyclic cumulenes.<sup>192</sup> The 1,4 H transfer reaction is the least activated, as its transition state involves the formation of a C6 ring structure, which has the lowest strain among the intramolecular H-transfer reactions considered here. This is consistent with *ab initio* calculations showing that the bending potential of cyclic allenes is soft up to 20°, after which it quickly raises.<sup>192</sup>

Successive reactions are, however, needed to convert **4** to cycloheptatetraene, which brings the overall energy required for this reaction pathway to a level higher than that necessary to dissociate fulvenallene to fulvenallenyl and H. It is thus unlikely that this reaction pathway will proceed beyond TS4 and the formation of intermediate **4**.

### Reaction Pathway 3: Second C5→C7 Ring Expansion Mechanism and Phenylcarbene formation

The second reaction pathway through which fulvenallene (**1**) can interconvert to cycloheptatetraene (**5**) is initiated by the migration of one of the hydrogen atoms of the allene

group to the neighboring carbon center through **TS10**. This reaction gives rise to a complex reaction chemistry consisting of 10 wells connected by 10 transition states that is summarized in **Figure 34**, while the corresponding PES is represented in **Figure 35**.

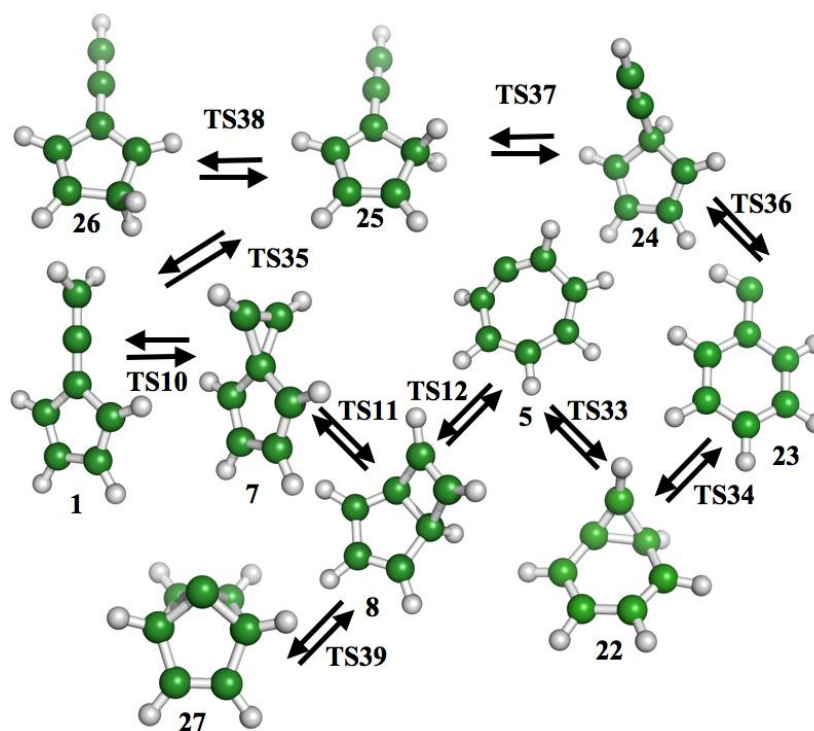


**Figure 34.** Second and most energetically favored mechanism of interconversion of fulvenallene to cycloheptatetraene and phenylcarbene.

This reaction pathway is the most energetically favored among those considered in this study, which is confirmed by the fact that the stability and existence of most of its energy wells, such as 7-norbornadienylidene (**27**), phenylcarbene (**23**), 1,2,4,6 cycloheptatetraene (**5**), and the three ethynylcyclopentadiene isomers (**24**, **25**, **26**) was experimentally confirmed.<sup>193-200</sup>

The reaction pathway found here is also similar to that proposed by Wong and Wentrup<sup>201</sup> and in part investigated by Schreiner et al.<sup>202</sup> and Matzinger et al.,<sup>203</sup> though several notable differences are present. The first is that, according to our calculations, **TS10** connects the fulvenallene (**1**) and spiro[2.4]heptatriene (**7**) wells, rather than **1** and the bicyclic adduct **8**.

The minimum energy path traveled by **1** after passing **TS10**, investigated with intrinsic reaction coordinate calculations, leads to an almost planar vinylcarbene intermediate, energetically unstable as a singlet but stable as a triplet. Energy minimization of the singlet vinylcarbene intermediate leads to **7**, which has been thus considered as the main well connected to **1** through **TS10**. Spiroheptatriene can then undergo ring expansion and form cycloheptatetraene passing through **8**.

The highest energy barrier along the pathway connecting **1** and **5** is given by **TS10** and is 63.2 kcal/mol, which is in good agreement with the 62.8 kcal/mol calculated by Wong and Wentrup at the G2MP2 level. The activation energy of **TS10** is more than 15 kcal/mol smaller than that of

**TS2**, which makes this reaction pathway significantly less activated than that examined in the previous section.

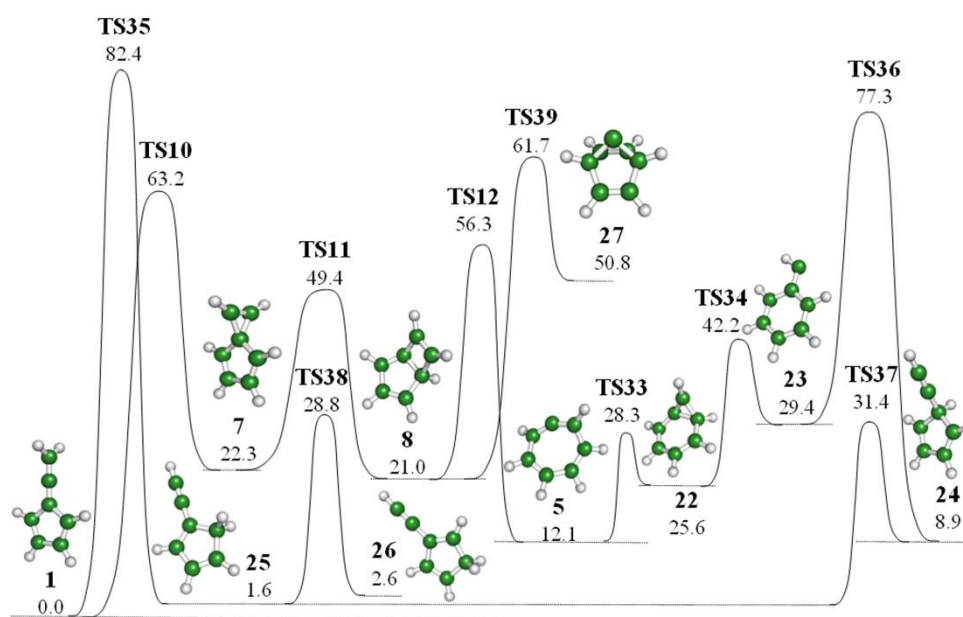


**Figure 35.** PES for the second mechanism of interconversion of fulvenallene to cycloheptatetraene. Energies were calculated at the CCSD(T)/CBS level for B3LYP/6-31+G(d,p) structures.

Cycloheptatetraene (**5**) can then be converted to phenylcarbene (**23**) passing, also in this case, through a bicyclic intermediate (**22**). The structure and energy of phenylcarbene here considered are those of its singlet  $^1A_1$  state, though the ground state is the  $^3A_1$  triplet, as the interconversion kinetics takes place on a singlet PES. It is however likely that, after being formed as a singlet, **23** will undergo intersystem crossing to form the triplet. The singlet-triplet energy difference calculated at the CCSD(T)/CBS level is in fact only 3.5 kcal/mol, which is within the 2-5 kcal/mol experimentally predicted<sup>204</sup> and near the best theoretical estimates of 2.7 kcal/mol made by Schreiner et al.<sup>202</sup> and the  $2.5 \pm 1$  kcal/mol of Nguyen et al.<sup>205</sup>

It appears thus that ring expansion and ring contraction reactions on the  $C_7H_6$  PES proceed in two steps and involve the formation of bicyclic intermediates. An exception to this rule is given by the energetically most favored pathway for the formation of ethynylcyclopentadiene, which proceeds through a concerted mechanism from phenylcarbene through **TS36**. This reaction pathway, which requires overcoming an activation energy of 77.3 kcal/mol, is energetically favored with respect to that proposed by Wong and Wentrup,<sup>201,206</sup> which consists in the direct hydrogen transposition from the allene group of fulvenallene through **TS35** and has an activation energy of 82.4 kcal/mol. It is however interesting to observe how the reactions that admit the formation of bicyclic

intermediates have overall activation energies significantly smaller than those proceeding directly through concerted mechanisms.

Three different ethynylcyclopentadiene isomers exist, namely 1- (**25**), 2- (**26**) and 5- (**24**) ethynylcyclopentadiene. The minimum energy pathway proceeds through the formation of **24**, followed by **25** and **26** generated through intramolecular H-transfer reactions proceeding through **TS37** and **TS38**, respectively. The 1- and 2- ethynylcyclopentadiene isomers are the second and third most stable isomers on the whole  $C_7H_6$  PES. Despite this, it is unlikely that these species are formed in considerable concentrations at the high temperatures at which fulvenallene is generated by benzyl decomposition. The activation energy necessary to form **25** and **26**, 77.3 kcal/mol, is in fact comparable to that required to dissociate fulvenallene into the fulvenallenyl radical and H and the pre-exponential factor of a homolytic barrierless dissociation reaction will be at least an order of magnitude larger than that of **TS36**, as this is a highly activated concerted reaction.

On the other side, the reactions of interconversion of **1** into **7**, **8**, **5**, **22**, and **23** will all be active in the same temperature range, so that all these  $C_7H_6$  isomers can be produced through isomerization reactions from fulvenallene once it is generated from benzyl decomposition. Though, given the high temperatures at which benzyl decomposes (above 1500 K), their lifetime will be limited.

Finally, it is interesting to observe that, in agreement with the proposal advanced by Brown and Jones,<sup>193</sup> also 7-norbordienylidene (**27**) can be produced from bicyclic intermediate **8** through **TS39** with an activation energy of 61.7 kcal/mol with respect to **1**, which is relatively low considering that **27** lies 50.8 kcal/mol above **1**.

The role of cycloheptatrienylidene in the molecular rearrangements of phenylcarbene has been the subject of much discussion, since heptafulvalene, its formal dimer, is among the main products of the decomposition of phenylcarbene precursors.<sup>196,197,207</sup> It was thus initially expected that it could be a stable reaction intermediate, also because of aromatic stabilization.<sup>208,209</sup> Further investigations demonstrated however that this was not the case.<sup>202,210</sup> In agreement with previous theoretical studies,<sup>201,202</sup> we found in fact that cycloheptatrienylidene is not a stable well in its singlet state and it is thus not reported in Figs 32 and 33. Though, it has been shown that its  $^1A_2$  state, calculated to be about 20.5 kcal/mol higher in energy than **5** at the CASPT2N/6-311g(2d,p) level of theory,<sup>202</sup> is a transition state for the racemization of **5**.

As mentioned, one of the purposes of this study is to investigate which are the most likely decomposition channels active on the  $C_7H_6$  PES. However, among the minimum energy structures found investigating this specific reaction pathway, none could be considered as a precursor to dissociation comparable to reaction pathway 1. For example, it might be argued that ethynylcyclopentadiene isomers may dissociate to the cyclopentadienyl radical and  $C_2H$ . However the high enthalpy change of this reaction, more than 115 kcal/mol, makes the rate of this pathway much slower than that of pathway 1. Similar considerations hold for dissociation to CH and  $C_6H_5$ .

Hence, alternative reaction pathways that could lead to energetically stable dehydrogenated products, such as acetylene, have been searched and are the subject of the next two sections.

### Reaction Pathway 4: Benzocyclopropene Reactivity and Diels-Alder Decomposition Mechanisms

The dissociation of a highly dehydrogenated molecule such as  $C_7H_6$  will involve most likely acetylene among the products, because of its high thermodynamic stability at elevated temperatures and high carbon to hydrogen ratio. This is also indirectly confirmed by the fact that acetylene is among the most abundant chemical species detected during toluene pyrolysis, though it is difficult to assess whether this is due to the secondary chemistry active in these conditions.

Dissociation to acetylene implies the contextual formation of a  $C_5H_4$  isomer. The four  $C_5H_4$  isomers whose possible formation has been investigated are, in order of energetic stability: 1,3-pentadiyne, 1,2,3,4-pentatetraene, penta-1,4-diyne, and the cyclopentadienylidene radical, which has a triplet  $^3B_1$  ground state. The electronic structure of cyclopentadienylidene and of its excited singlet states has been theoretically investigated by several authors, as it represents the simplest example of the union of a methylene with a conjugated alkene.<sup>211,212</sup> The PES of the first mechanism investigated is sketched in **Figure 36** and involves the formation of several 6 membered ringed structures.

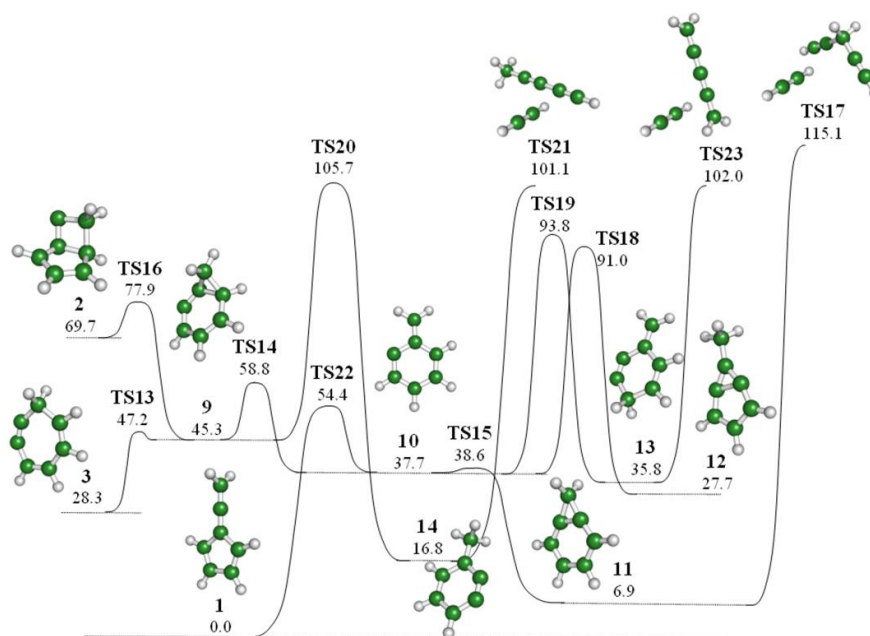


**Figure 36.** PES for the mechanism of interconversion of fulvenallene to benzocyclopropene (**11**) and several 6-membered cyclic species susceptible to Diels-Alder decomposition. Energies were calculated at the CCSD(T)/CBS level for B3LYP/6-31+G(d,p) structures.

The C<sub>7</sub>H<sub>6</sub> isomers that can be a precursor to the decomposition into acetylene and one of the mentioned C<sub>5</sub>H<sub>4</sub> isomers can be originated by several of the stable isomers or intermediates that can be accessed through the pathways described in the previous sections. A key compound of this reaction pathway, 6-methylenecyclohexa-2,4-dienylidene (**10**), can be formed both directly from fulvenallene through **TS22**, a reaction which has a relatively small activation energy of 54.4 kcal/mol, and from **2** and **3** through **9**. Benzocyclopropene (**11**) can then be formed easily from **10** since the rotation of the methylene group with respect to the C<sub>6</sub> plane is only slightly hindered. The possibility to convert **11** into **1** with high yields has been proved experimentally through FVT.<sup>213</sup>

While the formation of all the mentioned compounds is likely to take place as they are connected by transition states lying well below the dissociation threshold, significant energy barriers hinder the further reactivity of **10**, **11**, and **9**. Benzocyclopropene can in fact dissociate to 1,3-pentadiyne and acetylene through **TS17**. This reaction however requires overcoming a high energy barrier of 108.2 kcal/mol. Though the structure of **11** has C<sub>2v</sub> symmetry, the transition state is asynchronous, as is often the case for concerted<sup>214</sup> and Diels Alder<sup>215</sup> reactions.

**TS17** lies 115.1 kcal/mol above the energy level of fulvenallene, thus about 31.7 kcal/mol above the reaction enthalpy change. The high energy barrier for the insertion of acetylene into 1,3-pentadiyne is mostly due to the energy required to distort the reactants from their minimal energy structure to that of the transition state, which is tight (the C-C distances of the forming bonds are 2.17 and 2.19 Å, respectively). Though this transition state may have diradical character and it may thus be inappropriate to study it using a single reference wave function, the activation energy calculated at the CCSD(T)/CBS limit is so much higher than that of the competing reaction channel (pathway 1, about 80 kcal/mol), that it can be safely excluded that the decomposition rate along **TS17** may compete with pathway 1.

The situation is different for **TS23** and **TS21**, which connect the intermediate structures **13** and **14** with the C<sub>7</sub>H<sub>6</sub> decomposition products 1,3-pentadiyne and 1,2,3,4-pentatetraene. The activation energies relative to fulvenallene are in fact 101 and 102 kcal/mol, thus smaller than that calculated for **TS17**. In addition, in this case the transition states are not as tight as found for **TS17**, since the pre-exponential factors calculated at 300K using transition state theory are significantly larger. This can be attributed in the case of **TS23** to two low vibrational frequencies of 63 cm<sup>-1</sup> and 125 cm<sup>-1</sup>, related to the stretching of one of the two breaking C-C bonds and to the wagging of the two methylene groups, and in the case of **TS21** to three low vibrational frequencies of 21 cm<sup>-1</sup>, 67 cm<sup>-1</sup> and 139 cm<sup>-1</sup>, the lowest corresponding also in this case to the stretching of one of the two breaking bonds and the others to the rotation and wagging of the methyl group, respectively. The high pre-exponential factors suggest that these reactions may compete with pathway 1, in particular should the activation energy be slightly smaller. For this reason the activation energies of **TS21** and **TS23** have been computed at the CASPT2 level using the cc-pVTZ basis set. The energy barriers so de-

terminated are 98.2 and 101.5 kcal/mol, thus only slightly smaller than those calculated at the CCSD(T) level.

However, a comparison of the kinetic constants of **TS21** and **TS23** with that of the intermediate reactions that precede them on the fulvenallene PES shows that the effective rate determining steps for these two reaction channels are **TS20** and **TS19**, respectively, both because of the high activation energies and the low pre-exponential factors. All these considerations lead to the conclusion that decomposition to  $C_3H_4$  and acetylene through **TS21** and **TS23** does not compete with pathway 1. However, should an alternative pathway be found on the  $C_7H_6$  PES that could connect fulvenallene to **13** or **14** through smaller activation energies, the conclusion might be different.

Finally, it can be observed that intermediate **10** can transpose a hydrogen atom to the methylene group and form the bicyclic adduct **12** through **TS18**. However, also in this case the activation energy is significantly larger than that of decomposition pathway 1, so that intermediate **12** will be difficult to form.

### Reaction Pathway 5: Alternative Pentatetraene Formation Mechanisms

The analysis of the  $C_7H_6$  PES performed in the previous section has shown that there is potential for decomposition of fulvenallene to acetylene and 1,3-pentadiyne or 1,2,3,4-pentatetraene, though these reaction channels are slowed down considerably by high energy barriers, which prevent the formation of the precursors. Therefore, we have searched for alternative routes to potential precursors to dissociation to  $C_5H_4$  and  $C_2H_2$ . A first possibility is represented by the reaction pathway sketched in **Figure 37**.

The reaction mechanism is initiated by a hydrogen transposition on the C5 ring of fulvenallene to form a carbene intermediate (**15**), which can then undergo ring expansion or ring contraction through **TS25** and **TS27** to form two cyclic intermediates, characterized by 6 and 4 membered rings (**16** and **13**). The two intermediates are susceptible to decompose directly to the same product, 1,2,3,4-pentatetraene, either through **TS26** or, similarly to what found in the previous section, through **TS23**.

Also in this case activation energies have been computed at the CASPT2(10e,10o)/cc-pVTZ level. It has been found that **TS26** has the smallest activation energy among the acetylene decomposition channels examined, 98.6 kcal/mol at the CCSD(T)/CBS level and 93.8 kcal/mol at the CASPT2 level, while that of **TS23** is 101.5 kcal/mol. **TS26** appears thus as a significant competitor to pathway 1, also because of the two low vibrational frequencies of the transition state, 79 and 115  $cm^{-1}$ , which contribute significantly to the pre-exponential factor of the kinetic constant by increasing the vibrational partition function of the transition state with respect to that of the reactant (for comparison, the two lowest vibrational frequencies of fulvenallene are 138 and 158  $cm^{-1}$ ). It is interesting to observe that the two lowest vibrational frequencies of **TS26** are similar to those of

**TS21** and **TS23**. It appears thus that this is an intrinsic property of the transition states of the  $C_7H_6$  PES leading to dissociation to acetylene and  $C_5H_4$ .

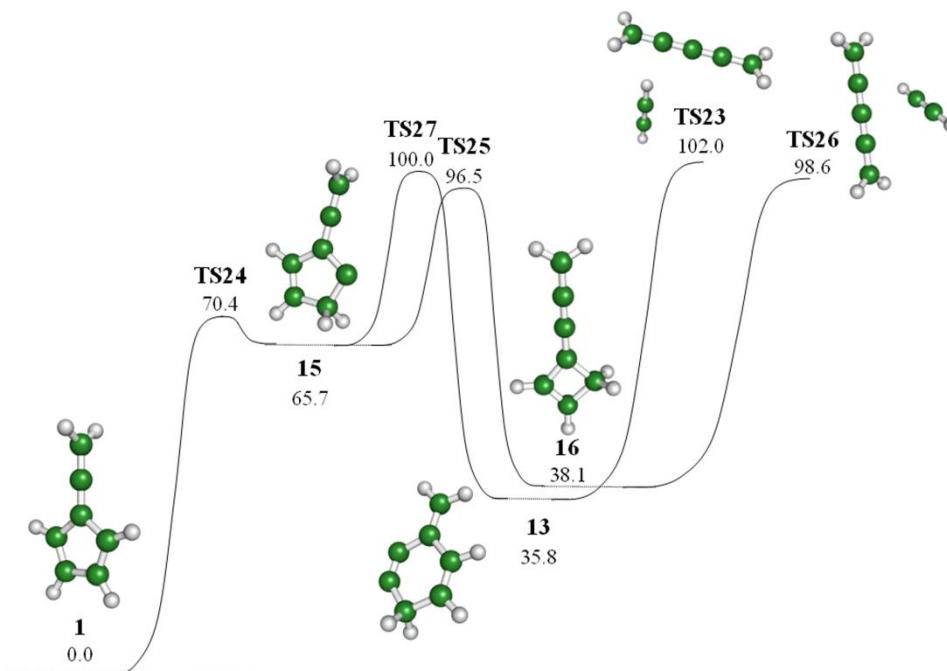


**Figure 37.** PES of a possible mechanism, alternative to pathway 4, of interconversion of fulvenallene to several intermediates susceptible to Diels-Alder decomposition. Energies were calculated at the CCSD(T)/CBS level for B3LYP/6-31+G(d,p) structures.

However, also in this case, the formation of **13** and **16** is hindered by the high energy barriers of **TS25** and **TS27** (96.5 and 100 kcal/mol), which must be overcome in order to connect fulvenallene with **16** and **13**. It appears that, also in this case, these two dissociation pathways are not competitive with pathway 1, at least as long as an alternative route to **13** and **16** is not found.

### Reaction Pathway 6: Reactivity on the Triplet Potential Energy Surface

Since one of the  $C_5H_4$  isomers that can be formed by the decomposition to acetylene, cyclopentadienylidene, is most stable in its triplet state, the reactivity of the  $C_7H_6$  triplet PES has been studied. The investigated PES is sketched in **Figure 38**.

The excitation of fulvenallene from the ground to the triplet state requires 45.9 kcal/mol and leads to the bending of the allene group, though the molecule remains planar. The migration of a hydrogen atom from the methylene group to the neighboring carbene requires 48.0 kcal/mol, which becomes 93.9 kcal/mol if measured with respect to the ground state of fulvenallene. **TS28** corresponds to **TS10** on the singlet PES of pathway 2, which energy barrier is however significantly smaller, 63.2 kcal/mol. The two transition states lead however to different products, which are spiroheptatriene for pathway 2 and vinylcarbene cyclopentadienylidene (**18**) on the triplet PES.

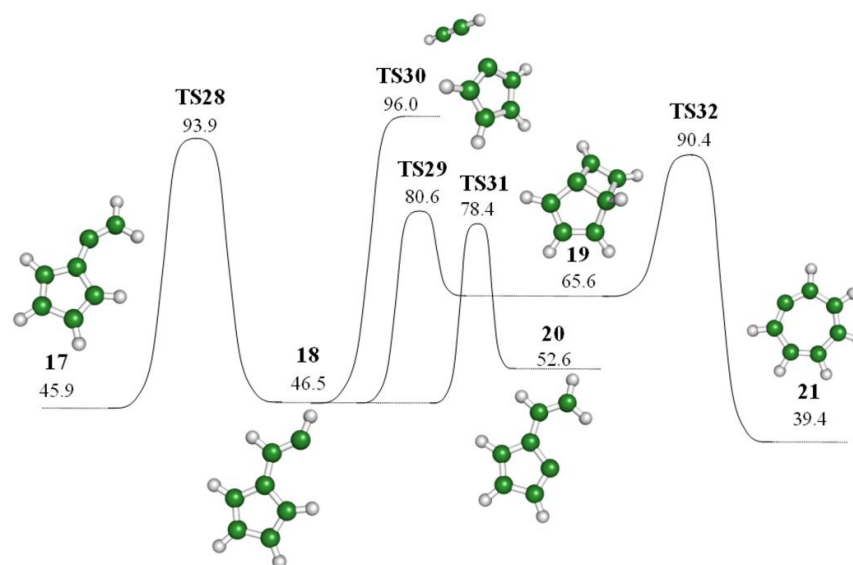


**Figure 38.** Reactivity on the  $C_7H_6$  triplet PES. Energies were calculated at the CCSD(T)/CBS level on B3LYP/6-31+G(d,p) structures.

Intermediate **18** can then follow four different reaction pathways: dissociation to cyclopentadienylidene and acetylene through **TS30**, ring closure to form **19**, H abstraction from the C5 ring to form intermediate **20**, and the backward pathway to **17**. A fifth pathway is given by intersystem crossing to the singlet PES followed by isomerization to spiroheptatriene or fulvenallene, as vinylcarbene cyclopentadienylidene is not an energy minimum on the singlet PES. The bicyclic intermediate **19** can further react through ring expansion to form cycloheptatrienylidene (**21**). Differently from cycloheptatetraene (**5**), **21** has a planar  $C_{2v}$  structure. The energy difference between **21** and **5** is 27.1 kcal/mol, in good agreement with the 27.2 kcal/mol calculated by Wong and Wentrup at the G2(MP2,SVP) level.

The activation energy for decomposition to acetylene and the cyclopentadienylidene radical is 96.0 kcal/mol (**TS30**), thus significantly higher than that of pathway 1 (about 80 kcal/mol). However, the activation energy of **TS30** is similar to the energy change, 91.8 kcal/mol, so that the energy barrier for the reverse reaction is relatively low (4.2 kcal/mol). This usually implies that the transition state is loose, i.e. that internal motions along the transitional degrees of freedom are only slightly hindered. This is confirmed by the three small vibrational frequencies calculated for **TS30**: 9.4, 51.3, and 89.0  $\text{cm}^{-1}$ . **TS30** has thus the potential to compete with pathway 1, as the high value of its vibrational partition function determined by its low vibrational frequencies can compensate for the high activation energy.

It is however unlikely that the well connected to **TS30**, **18**, is reached from the triplet state of fulvenallene, as **TS28** has both high activation energy and high vibrational frequencies. Moreover,

accessing **18** from **17** requires that intersystem crossing takes place between **1** and **17**, which, since the triplet and ground state of fulvenallene are separated by 45.9 kcal/mol, requires overcoming a significant energy barrier.

An analysis of the singlet PES around **TS10** performed following the internal reaction coordinate from **1** to **7** starting from the transition state evidenced that the energy difference between singlet and triplet states, calculated on the same geometry, is very small. In particular, the two states cross (less than 0.5 kcal/mol of difference) at about 0.05 Å (C-H distance of the forming bond) after **TS10** at a relative energy of 56.0 kcal/mol.

To test whether a conical intersection exists in proximity of this structure, which can be considered as a first guess, we used a procedure similar to the partial optimization method described by Harvey.<sup>75</sup> This approach, often used to locate conical intersections, consists in a set of partial geometry optimizations performed on the singlet and triplet PES at fixed values of the reaction coordinate. The crossing of the two PESs defines the conical intersection, though it can be considered only as a first level approximation since triplet and singlet geometries will differ somewhat.

In the present case it is difficult to define the reaction coordinate since, after the H transposition taking place in **TS10**, the evolution towards the minimum energy geometry of both the singlet and triplet states involves a rototranslation of the terminal CH group. This internal motion cannot be described with a single reaction coordinate, as both the HCCC dihedral angle and the HCC angle change during the reaction.

The following procedure has been adopted. First the singlet and triplet geometries have been relaxed starting from the first guess crossing point while keeping fixed the relative position of the CH group. Then two independent IRC scans have been performed starting from the respective optimized geometries at steps of 0.1 bohr. The two PESs crossed at the second step (energy difference less than 0.1 kcal/mol). The geometries were similar, as the XYZ atomic coordinates differ by less than 0.015 Å, while the energy was about 5 kcal/mol smaller than that determined at the first guess crossing point. This finding suggests that a conical intersection exists in proximity of **TS10**, though a more refined approach would be needed to determine its structure and energy at a higher level of approximation.

It is likely that, after jumping between the two adiabatic surfaces, the system will evolve toward the energy well lying in the closest proximity, which is **18**. It appears thus that no significant energy barrier precludes the accessibility to the well connected to **TS30**, though it is known that the intersystem crossing probability, determined by the spin orbit coupling coefficient, may affect considerably the transition frequency.

### 5.3.2. Fulvenallene Decomposition Kinetics

#### High-Pressure Rate Coefficients

At a first level of approximation, it is possible to determine the highest possible rate of the different decomposition channels by applying transition state theory using for the transition states the partition functions of the reaction channels and for the reactants the partition functions of the minimum energy well, which is fulvenallene. This approach allows determining the high-pressure rate constant for each decomposition reaction channel under the implicit assumptions that all the wells that must be visited by the rovibrationally excited  $C_7H_6$  molecule before reaching the target transition state are in thermodynamic equilibrium.

As mentioned in the previous sections, this is not the case for some reaction channels, since some bottlenecks on the PES hinder the accessibility to the decomposition transition states. Given the complexity of the  $C_7H_6$  PES, it is however difficult to exclude a priori that alternative reaction channels connecting fulvenallene to the well preceding the dissociation transition state might exist. On the other hand, the present calculation allows evaluating which is the upper limit to the kinetic constant for each possible reaction channel. The results of this calculation are summarized in **Table 5** in the 1500-2100 K temperature range, which is that at which fulvenallene decomposes at a significant rate.

**Table 5.** High-pressure upper limits to the kinetic constants for fulvenallene decomposition.

Reaction <b>1</b> $\rightarrow$	Activation En- ergy	Transition State	A $s^{-1}$	Ea	1500 K $s^{-1}$	1800 K $s^{-1}$	2100 K $s^{-1}$
$C_7H_5 + H$	82.5 <sup>b</sup>	<b>TS1</b>	$4.8 \times 10^{14}$	81.1	690	$6.5 \times 10^4$	$1.6 \times 10^6$
1,3-pentadiyne + $C_2H_2$	98.2 (101.1) <sup>c</sup>	<b>TS21</b>	$6.2 \times 10^{17}$	103.2	563.8	$1.8 \times 10^5$	$1.1 \times 10^7$
1,2,3,4-pentatetraene + $C_2H_2$	101.5 (102.0) <sup>c</sup>	<b>TS23</b>	$3.5 \times 10^{16}$	106.3	11.3	$4.3 \times 10^3$	$3.0 \times 10^5$
1,2,3,4-pentatetraene + $C_2H_2$	93.8 (98.6) <sup>c</sup>	<b>TS26</b>	$7.2 \times 10^{16}$	98.8	294	$7.4 \times 10^4$	$3.8 \times 10^6$
penta-1,4-diyne + $C_2H_2$	115.0	<b>TS17</b>	$2.2 \times 10^{16}$	119.8	0.08	61.6	7404.
cyclopentadienylidene + $C_2H_2$	96.0 <sup>b</sup>	<b>TS30</b>	$3.4 \times 10^{17}$	98.7	1520.	$3.5 \times 10^5$	$1.6 \times 10^7$

<sup>a</sup>The kinetic constants were fitted to the Arrhenius form as  $k = A \exp(-E_a / RT)$  between 1500 and 2000 K. Activation energies are in kcal/mol.

<sup>b</sup>PES calculated at the CASPT2/cc-pVTZ level scaled to the reaction energy change evaluated at the CCSD(T)/CBS level with CASPT2/cc-pVTZ ZPE.

<sup>c</sup>Activation energy calculated at the CASPT2/cc-pVTZ level; estimated CCSD(T)/CBS energy in parenthesis.

The analysis of the kinetic constants reported in **Table 5** shows that the fastest decomposition channel of fulvenallene leads to acetylene and cyclopentadienylidene. This reaction takes place on the triplet PES, so that intersystem crossing is necessary. The second fastest decomposition channels is given both by dissociation into the fulvalenyl radical and atomic hydrogen, which rate is comparable to that of dissociation to 1,3-pentadiyne and  $C_2H_2$  through **TS21**. The decomposition to 1,2,3,4-pentatetraene and  $C_2H_2$  through **TS26** is only slightly slower.

Of the four dissociation channels here identified as comparable in terms of decomposition rate constants, those corresponding to **TS26** and **TS21** are considerably slowed down by two bottlenecks, **TS25** and **TS20**, which kinetic constants calculated with respect to fulvenallene are more than two orders of magnitudes smaller. This leaves **TS30** and **TS1** as the two main decomposition channels of fulvenallene identified in the present work. Given the significantly higher activation energy of **TS30**, it is likely that eventual fall off effects would favor **TS1** with respect to **TS30**.

### ME/RRKM simulations

In this section we aim to determine what the main decomposition products of fulvenallene are and to evaluate the respective reaction rates as a function of temperature and pressure using a combined RRKM/ME approach.

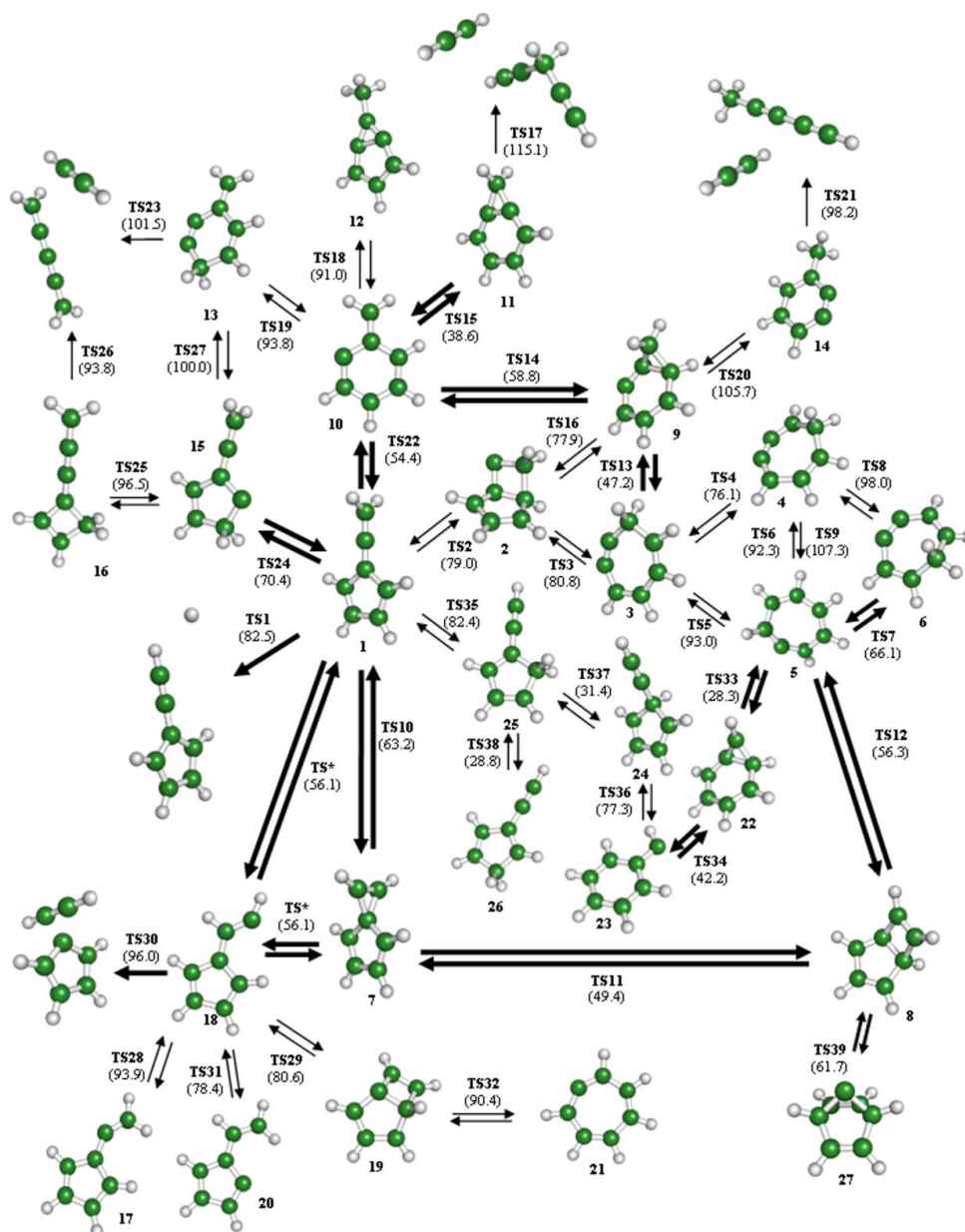


**Figure 39.** Summary of the reactions that can take place on the  $C_7H_6$  potential energy surface.

The  $C_7H_6$  PES on which the present calculations are based is illustrated in **Figure 39** and comprehends 27 wells connected through 39 paths. A preliminary analysis showed that only a small portion of this PES is likely to be visited for a reaction pathway started from the fulvenallene well, so that it can significantly be simplified without loss of accuracy.

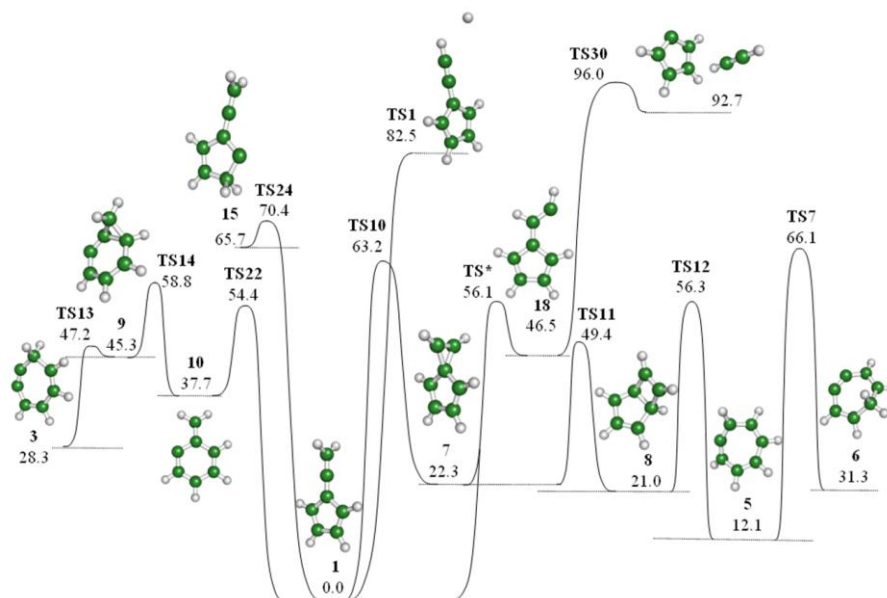


**Figure 40.** Portion of the  $C_7H_6$  PES considered in the simulations. Energies were calculated at the CCSD(T) level using the *cc-pVDZ* and *cc-pVTZ* basis sets and extrapolated to the complete basis set limit. ZPE corrections are included and were calculated using vibrational frequencies determined at the *B3LYP/6-31+G(d,p)* level.

The PES considered in the simulations is illustrated in **Figure 40**. It is composed of 10 wells connected by 11 transition states. Of the wells reported in **Figure 40**, only **W18** lies on the triplet surface. Two main decomposition channels appear thus competitive: the dissociation to fulvenallenyl and atomic hydrogen through **TS1** and the decomposition to cyclopentadienylidene and acetylene through **TS30**. Despite the higher activation energy, the second reaction channel is faster if the decomposition rate is computed assuming equilibrium between the involved wells. This comes as a result of its high pre-exponential factor. In fact **TS30** transition state has a loose character and is, therefore, characterized by five low vibrational frequencies, two of which degenerate into hindered rotors, as evinced by analysis of their rotational PESs.

To check whether the approach used to determine the **TS30** kinetic constant is consistent with experimental data, we calculated the kinetic constant of the inverse process, the addition of  $C_2H_2$  to  $C_5H_4$ , and compared it to the reaction of  $C_2H_2$  with  $C_2H$ . We believe that two reactions are similar in many ways; first, because one of the reactants,  $C_2H_2$ , is the same, then because in both reactions  $C_2H_2$  adds to highly unsaturated radicals,  $C_2H$  and  $C_5H_4$ , and finally for the fact that both reactions are almost barrierless. The kinetic constant measured for the addition of  $C_2H$  to  $C_2H_2$  at 1600 K by

Shin and Michael<sup>216</sup> is  $1.6 \times 10^{14}$  cm<sup>3</sup>/mol/s, while the one we calculated for the addition of C<sub>2</sub>H<sub>2</sub> to C<sub>5</sub>H<sub>4</sub> is  $6.3 \times 10^{13}$  cm<sup>3</sup>/mol/s. The similarity suggests that the transition state parameters determined for **TS30**, which are the same used to calculate the addition of C<sub>5</sub>H<sub>4</sub> to C<sub>2</sub>H<sub>2</sub>, are reasonable.

However, although **TS30** appears to yield a higher rate coefficient than **TS1**, it should be remembered that this reaction takes place on the triplet PES, so that intersystem crossing may be limiting. Moreover, eventual fall off effects would favor the first decomposition channel. Given the high rate of the **TS30** reaction channel, it is possible that also the decomposition to acetylene and the singlet state of C<sub>5</sub>H<sub>4</sub>, which lies 6.4 kcal/mol above the triplet and does not require intersystem crossing, may contribute to the overall C<sub>7</sub>H<sub>6</sub> decomposition, as the reaction is barrierless.

In the proposed reaction scheme, the reaction channel leading to the decomposition of C<sub>7</sub>H<sub>6</sub> into cC<sub>5</sub>H<sub>4</sub> + C<sub>2</sub>H<sub>2</sub> involves intersystem crossing from the singlet to the triplet state. The intersystem crossing frequency has been determined using Landau Zener theory as described in the method section. This approach requires as input the structure, energy, spin-orbit coupling coefficient, force constants and vibrational frequencies at the intersection linking the singlet and the triplet PES.

Conical intersections that may occur on the C<sub>7</sub>H<sub>6</sub> PES have been searched in proximity of the wells that may be reached from **W1** scanning the PES at the B3LYP/6-31+G(d,p) level. In the calculations we did not consider the well known singlet triplet crossing of phenylcarbene<sup>201</sup>, as it is unlikely that phenylcarbene may be accessed from **W1**. Among the several conical intersections that were located, the one with the highest spin-orbit coupling, **TS\***, has been found on the intrinsic reaction coordinate connecting **W1** to **W7**, after **TS10**. Hence, in the simulations we considered **TS\*** to be accessible both from **W1** and from **W7**.

The spin-orbit matrix element HSO calculated for the corresponding MECP is 9.3 cm<sup>-1</sup>. The difference between the forces acting on the two states is more difficult to determine, since an intrinsic reaction coordinate scan performed both on the triplet and singlet PESs showed that the conical intersection takes place contextually to a rotation of the terminal CH group, so that it is difficult to define a reaction coordinate. Taking into account this evidence, the force difference has been computed as the difference between the forces acting on the angle between the CH group and the C-C<sub>5</sub>H<sub>4</sub> moiety on the singlet and triplet surfaces, as the IRC analyses showed that is the coordinate that matches most closely the reaction path. The value so calculated is 9.4 kcal mol<sup>-1</sup>Å<sup>-1</sup>. The reduced mass used in the calculations is that of CH.

These parameters have been used in a first set of simulations. However, in order to take into account the possibility of the existence of an alternative fast intersystem crossing channel and considering the uncertainty of many parameters, we performed a second set of simulations assuming that intersystem crossing is fast, which was obtained by imposing the hopping probability equal to 1.

The master equation was solved assuming that the bath gas is pure Argon, adopting an exponential down model for the collisional energy transfer, and using Lennard-Jones collision parameters,

which were assumed to be the same as those of toluene for all the  $C_7H_6$  isomers.<sup>71,171,217</sup> Vibrational frequencies, rotational constants, and activation energies of the relevant intermediates and saddle points located on the investigated potential energy surface have been calculated from *ab initio* simulations as described in the method section. Since energy transfer parameters are not well known for these molecules, we assumed an empirical value for the mean downward transfer energy  $\langle\Delta E_{\text{down}}\rangle$  equal to  $2000\text{ cm}^{-1}$ , which has been used by da Silva et al.<sup>181</sup> to study the benzyl decomposition reaction. The sensitivity of the calculated rate constant to this parameter has been examined. Since we were interested in the initial product branching ratio of the  $C_7H_6$  decomposition reaction we used an “infinite sink” approximation for the two main products, i.e. the reverse  $C_2H_2 + C_5H_4$  and  $H + C_7H_5$  reactions have been neglected.

To solve the master equation the reported values have been first averaged over  $J$  as proposed by Miller et al. and then in discrete reaction bins. In order to determine the effect of the bin size on the accuracy of the calculations a sensitivity analysis was performed on this parameter. In particular, the bin size was systematically reduced from  $100\text{ cm}^{-1}$  to  $50$  and  $25\text{ cm}^{-1}$ . The simulations revealed that the rate constants determined by solving the ME are not particularly sensitive to the size of the energy bin (i.e. the deviation from the  $100\text{ cm}^{-1}$  reference value is smaller than 5%), as long as the maximum energy allowed for a collisional energy jump is at least  $9000\text{ cm}^{-1}$ .

In addition, we performed a sensitivity analysis on the  $\langle\Delta E_{\text{down}}\rangle$  parameter. It has been found that a variation of  $\pm 1000\text{ cm}^{-1}$  at 1 atm leads to a maximum change of the rate constant of about  $\pm 50\%$  at high temperatures (i.e. greater than 1900 K), while no significant changes are detected at low temperatures (i.e. lower than 1700 K). This behavior was expected as the variation of the  $\langle\Delta E_{\text{down}}\rangle$  parameter has an effect only when the rate constant is in deep fall off regime. Also the branching rate constants change accordingly, yielding a product branching ratio only slightly affected by the variation of  $\langle\Delta E_{\text{down}}\rangle$ . Unfortunately, as no experimental data are available for this reaction, it remains uncertain which is the most appropriate value.

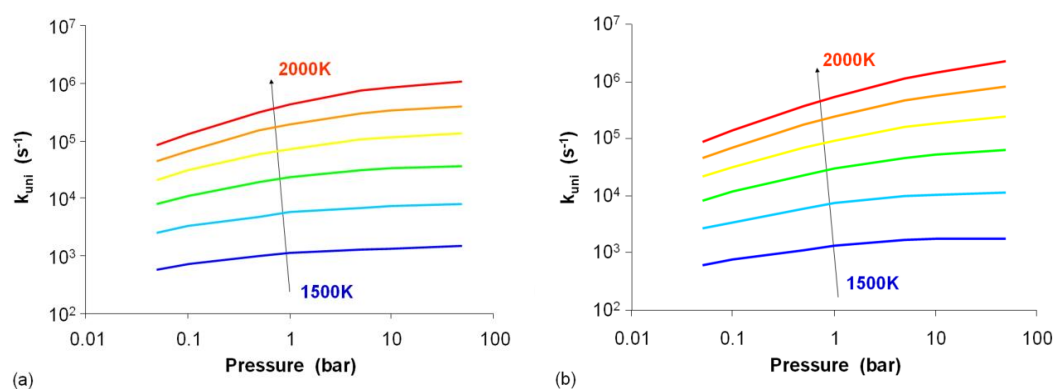


**Figure 41.** Overall kinetic constants for  $C_7H_6$  decomposition. Simulations were performed: a) accounting for intersystem crossing using Landau Zener theory; b) assuming that intersystem crossing is fast.

The global rate coefficients for  $C_7H_6$  decomposition determined both for the case in which inter-system crossing has been considered and when it has not are illustrated in **Figure 41**. Calculations were performed in the 0.05-50 bar pressure range and in the 1500 - 2000 K temperature range. The reaction is in its fall off regime for pressures up to 1-2 bar when intersystem crossing has been considered and up to 10 bar when it has not.

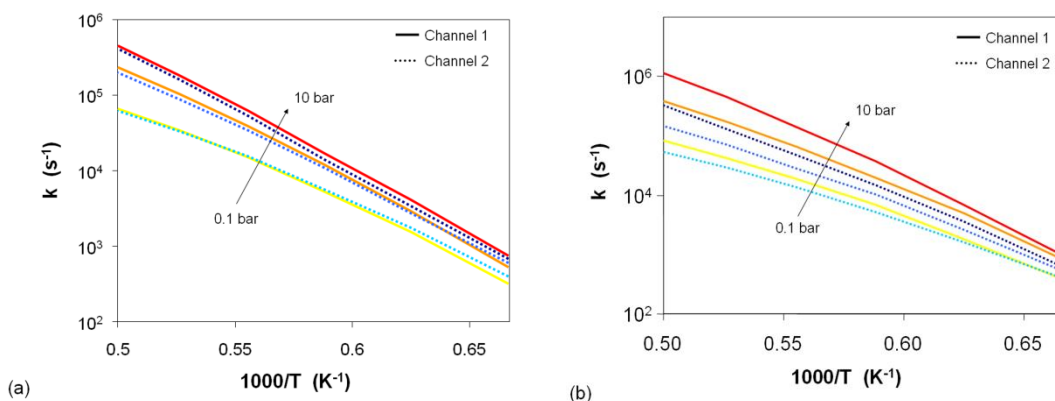


**Figure 42.** Branching reaction constants for channel 1 and 2 calculated a) accounting for inter-system crossing using Landau Zener theory and b) assuming that intersystem crossing is fast.

In addition to the total rate constant estimation, one of the attempts of the present study is to provide an insight into the mechanism and the product branching under different conditions. The channel specific rate constants for decomposition into cyclopentadienylidene and  $C_2H_2$  (channel 1) and into the fulvenallenyl radical (channel 2) are reported in **Figure 42**. It can be observed that the two pathways have similar rate coefficients for different pressures and temperatures if intersystem crossing is explicitly considered in the calculations, while if intersystem crossing is assumed to be fast channel 1 is up to a factor of three faster than channel 2.

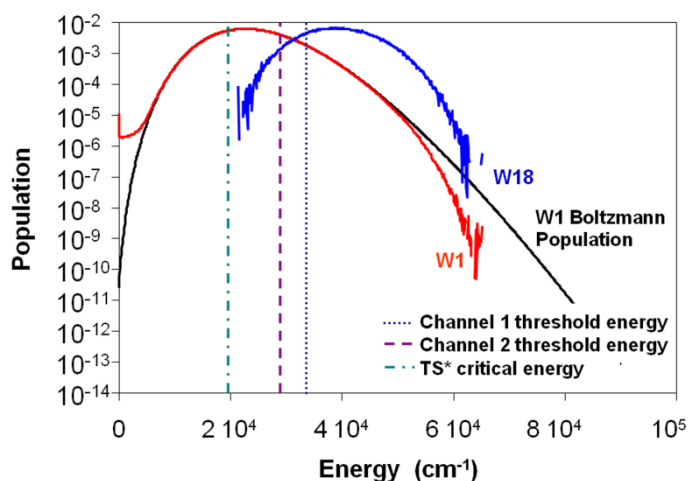


**Figure 43.** Energy distribution functions of *W1* and *W18* calculated at 1 bar and 1700 K and Boltzmann population of *W1*.

Furthermore, it is interesting to observe that the two channels exhibit a different pressure dependence. In fact, the homolytic dissociation reaction rate has a minor dependence with pressure compared to the other reaction. This can be also seen in **Figure 43** where are represented the population densities of wells **W1** and **W18** compared with the Boltzmann population of **W1**. It is thus interesting to observe that the population density of **W1** deviates from the Boltzmann population only at energies higher than the corresponding dissociation threshold energy, confirming that the direct decomposition to  $C_7H_5$  and H is hardly affected by fall off behavior even at high temperature. The second reaction channel, instead, involves the transition from well **W1** to **W18**. The population of the most excited states of **W18** is more depleted with respect to the threshold energy reached in **TS3**, which leads to a significant pressure dependence. The slight deviation of the **W1** energy distribution function from the Boltzmann population that can be observed at low energies can be ascribed to the fact that simulations are started from energy 0, which biases slightly the energy distribution function. It is also interesting to observe that no significant population of energies below the **TS\*** critical energy is observed for **W18**, which means that collisional stabilization is not significant.

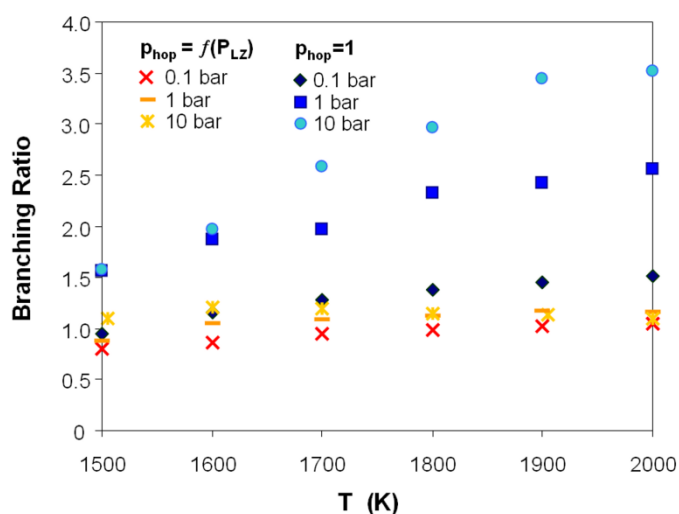


**Figure 44.** Product branching ratio as a function of temperature and pressure calculated accounting for intersystem crossing using Landau Zener theory (lowest points) and assuming that intersystem crossing is fast (upper points).

In **Figure 44** the product branching ratio, defined as the ratio of the number of molecules produced by channel 1 to the number of molecules produced by channel 2, is displayed as a function of pressure and temperature. When intersystem crossing is explicitly considered, the branching ratio is almost constant with both temperature and pressure with a mean value of 1.06. In the assumption of fast intersystem crossing, instead, the branching ratio varies proportionally with pressure and temperature, ranging from 0.8 up to 3.8. This behavior is motivated by two factors: channel 1 has a reaction energy barrier smaller than that of channel 2, hence the higher dependence of the

branching ratio with temperature, while channel 2, because of fall off effects, has a greater dependence on pressure than channel 1.

Channel specific rate constants were interpolated between 1500 and 2000 K and are reported at three different pressures as a function of temperature in **Table 6**.

**Table 6.** Kinetic constants for the two fulvenallene reaction channels calculated considering explicitly intersystem crossing ( $p_{hop} = f(P_{LZ})$ ) and under the assumption that it is fast ( $p_{hop} = 1$ ). Kinetic constants expressed as  $k = A \times T(K)^\alpha \times \exp(-E_a(\text{kcal/mol})/RT)$  in  $s^{-1}$ .

	P (bar)	$C_7H_6 \rightarrow C_5H_4 + C_2H_2$			$C_7H_6 \rightarrow C_7H_5 + H$		
		A	$\alpha$	$E_a$	A	$\alpha$	$E_a$
$p_{hop} = f(P_{LZ})$	0.1	130.10	-32.19	173.97	116.01	-28.46	157.86
	1	100.99	-23.86	154.21	66.69	-14.64	119.55
	10	61.12	-12.81	120.50	27.07	-3.54	89.15
$p_{hop} = 1$	0.1	135.37	-33.58	179.46	102.86	-24.94	144.42
	1	124.48	-30.18	176.46	108.80	-26.20	156.95
	10	129.63	-31.11	191.02	98.54	-23.11	153.51

## 5.4. Benzyl Decomposition

In this study we propose that the benzyl (**W1**) decomposition mechanism involves two competitive reaction pathways, reported on the left and right side of the  $C_7H_7$  potential energy surface shown in **Figure 45**.

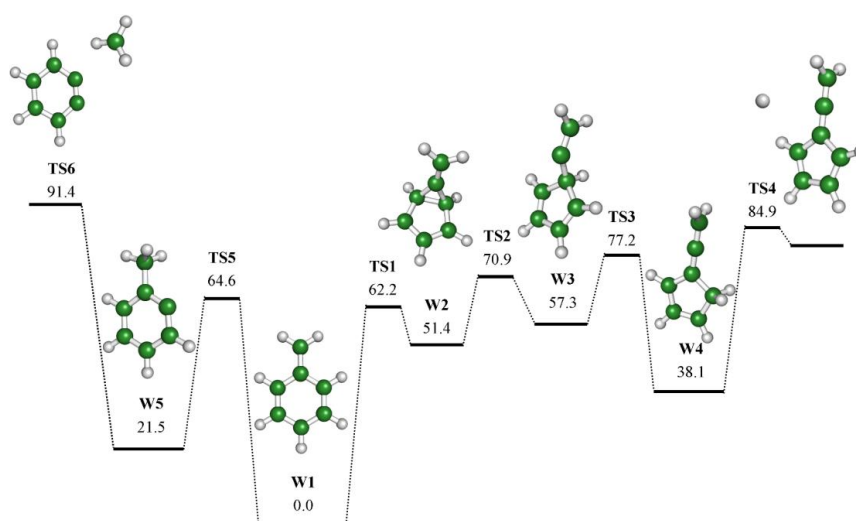


**Figure 45.** PES considered for the  $C_7H_7$  decomposition simulations. Energies (in kcal/mol) were calculated at the CCSD(T) level using the cc-pVDZ and cc-pVTZ basis sets and extrapolated to the complete basis set limit. ZPE corrections at the B3LYP/6-31+G(d,p) level are included.

The first is the one leading to fulvenallene and hydrogen. The reaction mechanism is initiated, as suggested by Jones et al.,<sup>218</sup> by benzyl cyclization to 6-methylenebicyclo[3.1.0]hex-3-en-2-yl (MBH) (**W2**), which has an activation energy of 62.2 kcal/mol, well below the benzyl dissociation threshold, and is rapidly followed by the C3 ring opening to give the 1,3-cyclopentadiene,5-vinyl-radical (**W3**). Successively this intermediate can make a 1,2-hydrogen transfer from the tertiary carbon atom within the C5 ring to form the 2-cyclopentene,5-ethenylidene-radical (**W4**). Though hydrogen transfer reactions over cyclic rings usually have activation energies of the order of 30 kcal/mol, in this particular case **TS3** has an energy barrier of only 19.9 kcal/mol, making this path easily accessible from the benzyl well. **W4** can then produce fulvenallene through a direct H dissociation from the CH<sub>2</sub> group of the C5 ring. This mechanism was first proposed in a previous work<sup>180</sup> of this group in which energies were calculated at the G2MP2 level. In this study energies have been updated to a higher level of accuracy by performing CCSD(T)/CBS calculations.

Following the motivations described in the introduction, the C<sub>7</sub>H<sub>7</sub> PES has been thoroughly investigated searching for a second benzyl decomposition pathway that may be competitive with the fulvenallene pathway. Among the possible reaction channels investigated, particular care was given to the study of H transfer reactions of the 1,3-pentadiene,5-ethenylidene linear isomer, whose formation requires overcoming an activation energy similar to that leading to the formation of fulvenallene. However the kinetic constants calculated for this portion of the PES are substantially lower than those of the first reaction channel.

It was interesting thus to discover that an alternative benzyl decomposition mechanism actually exists and consists in a sequence of two reactions, which final result is the barrierless decomposition to benzyne (cC<sub>6</sub>H<sub>4</sub>) and methyl. The first step consists in an internal 1,3-hydrogen abstraction from the CH<sub>2</sub> group to a vicinal CH group of the C6 ring leading to the 2-methylphenyl radical (**W5**). This reaction step has an activation energy of 64.6 kcal/mol, which is similar to that of benzyl cyclization to intermediate **W2** (62.2 kcal/mol). It is also important to observe that this reaction provides an efficient scrambling mechanism for the H atoms of the benzyl methylene group, which is absent in the first reaction pathway examined. Successively the 2-methylphenyl radical can decompose into benzyne and methyl by direct dissociation of the H<sub>3</sub>C-C<sub>6</sub>H<sub>4</sub> bond. This last reaction proceeds through a loose transition state, with an activation energy of 69.9 kcal/mol (91.4 kcal/mol with respect to benzyl). Though it has to overcome a larger barrier with respect to the one leading to fulvenallene (91.4 vs 84.9 kcal/mol), this reaction has a higher pre-exponential factor due to its loose nature. As mentioned in the method section, the kinetic constant for this reaction channel has been determined using variational transition state theory.

A quite important issue in the use of variational transition state theory is the treatment of the five transitional internal degrees of freedom, for which the harmonic approximation usually adopted in classic transition state theory is often not valid. In the present investigation one mode (the lowest)

has been treated as a 1D hindered rotor, while the other four were described as harmonic oscillators. In order to determine the level of error associated with this approximation the kinetic constant for the addition of methyl to the phenyl radical, a barrierless reaction similar to that involving methyl and benzyne, has been calculated at the same level of theory and compared with that determined by Klippenstein et al. using the more proper variable reaction coordinate (VRC) approach.<sup>59</sup> Within its scheme, in fact, the density of states of the transitional modes is determined by studying the reaction dynamics over a 5D PES. Through this comparison it has been found that the variational kinetic constant underestimates the VRC reference value by a factor of 3 in the investigated temperature range (1500-2000 K). As the variational kinetic constants for the addition of CH<sub>3</sub> to phenyl and to benzyne have similar values (addition to benzyne is only 20% slower than to phenyl), we decided to multiply the channel specific kinetic constant of benzyne decomposition by a constant correction factor of 3.

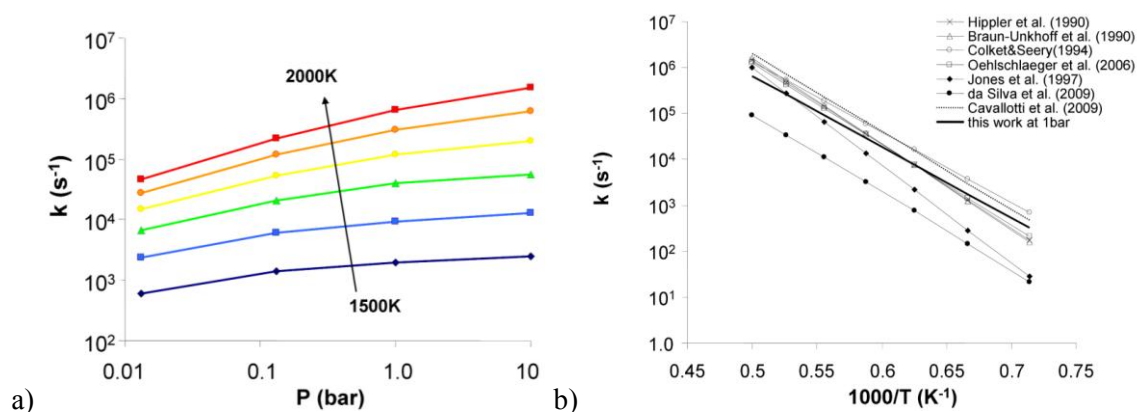


**Figure 46.** a) Global kinetic constant for benzyl decomposition calculated by integrating the master equation as a function of temperature and pressure. b) Comparison between calculated and literature<sup>153,155,157,179-181,218</sup> kinetic constants for benzyl decomposition.

The global and channel specific rate constants of the benzyl decomposition reaction have been estimated solving the master equation as described in the method section. The global kinetic constant so calculated is reported in **Figure 46a** as a function of temperature and pressure.

Simulations have been performed for temperatures comprised between 1500 and 2000 K and pressures of 0.013, 0.13, 1, and 10 bar. In this range of temperatures and pressures it is possible to observe that for this reaction it is important to account for fall off effects also in typical combustion conditions (1-10 bar).

Furthermore, the benzyl decomposition rate constant evaluated at 1 bar can be compared with a number of literature data, as shown in **Figure 46b**. It can be readily observed that our calculation is in agreement with the experimental rate constant of Hippler et al.,<sup>157</sup> and Oehlschlaeger et al.,<sup>179</sup> both determined through shock tube experiments and time resolved ultraviolet absorption. Our results are also in agreement with the kinetic constant of Braun-Unkhoff et al.,<sup>152</sup> obtained through

shock tube experiments and ARAS spectrometry, while they underestimate the rate constant determined by Colket and Seery.<sup>155</sup> The kinetic constant proposed by Colket and Seery was however determined through fitting a complex mechanism to experimental data under the hypothesis that benzyl decomposes to the cyclopentadienyl radical and acetylene, so it is reasonable to expect some uncertainty. The significant underestimation of experimental decomposition rates made by da Silva et al.<sup>181</sup> was unexpected, as the RRKM/ME calculations on which this estimate is based were performed using a PES similar to that used in this work, except for the benzyne channel, which would however account only for a factor of 2.

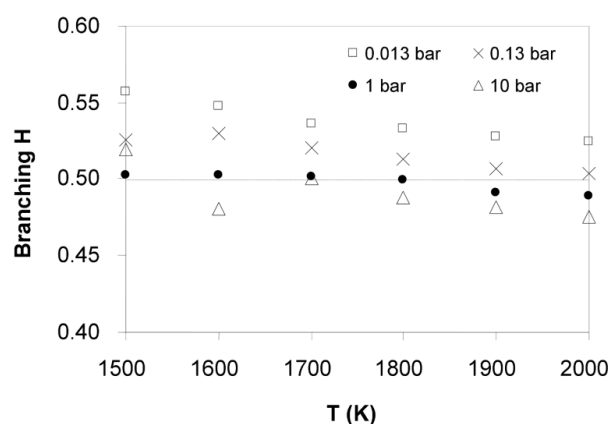


**Figure 47.** Branching ratio of the  $C_7H_6+H$  channel over the global decomposition rate of  $C_7H_7$  as a function of temperature and pressure.

Analyzing the branching ratio results shown in **Figure 47** it can be observed that the  $C_7H_6 + H$  and the  $C_6H_4 + CH_3$  channels contribute equally to benzyl decomposition. In fact, the ratio of production of fulvenallene and hydrogen is 0.5 at atmospheric pressure for the whole temperature range investigated and increases only slightly for lower pressures, reaching a maximum of 0.56 at 0.013 bar and 1500 K and a minimum of 0.48 at 10 bar and 2000 K.

Channel specific rate constant were interpolated between 1500 and 2000 K and are reported in the modified Arrhenius form in **Table 7** for the all the pressures investigated.

**Table 7.** Kinetic constants for benzyl decomposition reactions interpolated between 1500 and 2000 K as  $k = AT^\alpha \exp(-Ea(kcal/mol)/RT)$  in  $s^{-1}$ .

P (bar)	$C_7H_7 \rightarrow C_7H_6 + H$			$C_7H_7 \rightarrow C_6H_4 + CH_3$		
	Log A	$\alpha$	Ea	Log A	$\alpha$	Ea
<b>0.013</b>	129.65	-32.57	162.41	135.31	-34.08	169.13
<b>0.13</b>	123.11	-30.34	163.83	112.81	-27.50	155.36
<b>1</b>	97.47	-22.95	148.28	89.74	-20.82	141.68
<b>10</b>	39.10	-6.76	99.71	55.71	-11.23	116.58

## 5.5. Kinetic Simulations of Toluene and Benzyl Decomposition

### 5.5.1. Kinetic Model

A chemical kinetic mechanism consisting of elementary reactions has been assembled by embedding the reactions whose kinetic constants were determined from first principles here into a simple but sufficiently detailed kinetic scheme proposed in a previous work with the aim to include the most important reactions active during toluene decomposition.<sup>180</sup> The reactions used to build the kinetic mechanism are the decomposition of toluene and a subset of its reactions,<sup>179,219,220</sup> as well as the benzyl radical decomposition to produce o-benzyne or fulvenallene. The decomposition reactions of fulvenallene were included in the kinetic mechanism together with the H-addition reaction that leads to its conversion to acetylene and the cyclopentadienyl radical.<sup>180</sup> Moreover, a few reactions involving phenyl radicals,<sup>164,221</sup> the previously discussed H-addition or H-abstraction reactions to C<sub>5</sub> species, and the decomposition of cyclopentadienyl radical to propargyl and acetylene have been added to the mechanism.<sup>222</sup> The final kinetic model involves 20 species and 35 reactions, allowing the prediction of toluene and benzyl decomposition over the 1200-1900 K temperature range. The rate coefficients of the reactions listed in **Table 8** are valid for the 1-2 bar pressure range. In the simulations performed at higher or lower pressures the pressure sensitive rate coefficients were changed using the RRKM/ME pressure dependent values computed in this work or, for toluene and fulvenallene decomposition, in the referenced studies.<sup>59,184</sup>

The kinetic constants of reactions 12-26 are high-pressure limits. Moreover, it was assumed that the C<sub>5</sub>H<sub>5</sub> chemical species produced by the addition of H to any C<sub>5</sub>H<sub>4</sub> species rapidly isomerizes to the cyclopentadienyl radical. Though we acknowledge that these are rough assumptions, they helped us to check that these reactions do not contribute significantly to the overall chemical reactivity, in particular for what concerns the consumption of H atoms.

The proposed toluene decomposition mechanism is able to describe the key reaction steps involving toluene and benzyl as reactants as well as the main cyclopentadienyl and acetylene formation pathways. Since detailed mechanisms for the formation and consumption of smaller hydrocarbons and for the first aromatic ring formation are not incorporated into the kinetic model, it is not expected to predict quantitatively species like methane and benzene. This is true especially at temperatures higher than 1500 K, where other pyrolysis paths can be active to produce large molecules, such as polycyclic aromatic hydrocarbons and other soot precursors. The thermochemical data have been either estimated in this work through standard quantum chemistry methods or taken from the literature; in particular, **Table 9** reports a compilation of the thermodynamic parameters for the C<sub>7</sub> species of the model used in the simulations. All the simulations discussed in the following have been performed using the shock tube model available in the DSMOKE suite of programs.<sup>223</sup>

**Table 8.** Atmospheric pressure reaction mechanism for toluene pyrolysis and benzyl decomposition<sup>a</sup>.

	Reaction	log A	n	E <sub>a</sub>	Reference
(1)	$C_6H_5CH_3 \rightarrow C_6H_5CH_2 + H$	13.20	0.68	89.2	Harding et al. <sup>219 b</sup>
(-1)	$C_6H_5CH_2 + H \rightarrow C_6H_5CH_3$	13.82	0.07	-51.5	Harding et al. <sup>219</sup>
(2)	$C_6H_5CH_2 \rightarrow C_7H_6 + H$	97.47	-22.95	148.3	This study <sup>c</sup>
(-2)	$C_7H_6 + H \rightarrow C_6H_5CH_2$	8.94	1.20	-2.0	Cavallotti et al. <sup>180</sup>
(3)	$C_6H_5CH_2 \leftrightarrow o-C_6H_4 + CH_3$	89.74	-20.82	141.7	This study <sup>c</sup>
(4)	$C_6H_5CH_3 \leftrightarrow C_6H_5 + CH_3$	16.08	0	99.8	Ranzi et al. <sup>220 b</sup>
(5)	$C_6H_5CH_3 + H \leftrightarrow C_6H_5CH_2 + H_2$	15.10	0	14.8	Oehlschlaeger et al. <sup>179</sup>
(6)	$C_7H_6 + H \leftrightarrow C_5H_5 + C_2H_2$	8.03	1.35	-3.4	Cavallotti et al. <sup>180</sup>
(7)	$C_7H_6 \leftrightarrow C_7H_5 + H$	108.8	-26.2	156.9	This study <sup>c</sup>
(8)	$C_7H_6 \leftrightarrow C_5H_4 + C_2H_2$	124.48	-30.18	176.5	This study <sup>c</sup>
(9)	$C_7H_5 \leftrightarrow C_5H_3 + C_2H_2$	90.45	-21.38	135.62	This study
(10)	$C_7H_5 \leftrightarrow C_4H_2 + C_3H_3$	82.93	-19.18	125.34	This study
(11)	$o-C_6H_4 \leftrightarrow C_2H_2 + C_4H_2$	85.32	-19.6	69.9	Moskaleva et al. <sup>224 d</sup>
(12)	$C_5H_3 + H \rightarrow CH_2CCCCH_2$	11.60	0.69	-1.2	This study
(-12)	$CH_2CCCCH_2 \rightarrow C_5H_3 + H$	13.18	0.02	67.4	This study
(13)	$C_5H_3 + H \rightarrow CH_2CCHCCH$	13.28	0.05	-0.3	This study
(-13)	$CH_2CCHCCH \rightarrow C_5H_3 + H$	14.17	-0.05	80.3	This study
(14)	$C_5H_3 + H \rightarrow CH_3CCCCH$	13.66	0.05	-0.6	This study
(-14)	$CH_3CCCCH \rightarrow C_5H_3 + H$	13.9	-0.02	78.2	This study
(15)	$CH_2CCCCH_2 + H \rightarrow C_5H_5$	11.19	0.83	-0.6	This study
(16)	$CH_2CCCCH_2 + H \rightarrow C_5H_5$	9.44	1.47	10.2	This study
(17)	$CH_2CCCCH_2 + H \rightarrow C_5H_5$	9.39	1.49	12.7	This study
(18)	$CH_2CCHCCH + H \rightarrow C_5H_5$	9.05	1.44	3.9	This study
(19)	$CH_2CCHCCH + H \rightarrow C_5H_5$	9.12	1.44	4.3	This study
(20)	$CH_2CCHCCH + H \rightarrow C_5H_5$	8.81	1.43	6.1	This study
(21)	$CH_2CCHCCH + H \rightarrow C_5H_5$	9.04	1.46	5.8	This study
(22)	$CH_2CCHCCH + H \rightarrow C_5H_5$	11.39	0.73	-0.3	This study
(23)	$CH_3CCCCH + H \rightarrow C_5H_5$	11.06	1.00	4.2	This study
(24)	$CH_3CCCCH + H \rightarrow C_5H_5$	10.92	1.07	-0.2	This study
(25)	$CH_3CCCCH + H \rightarrow C_5H_5$	10.89	1.09	0.7	This study
(26)	$CH_3CCCCH + H \rightarrow C_5H_5$	11.73	0.85	-0.3	This study
(27)	$C_5H_4 + H \rightarrow C_5H_5$	12.82	0.3	0.77	This study
(-27)	$C_5H_5 \rightarrow C_5H_4 + H$	17.73	-0.55	115.5	This study
(28)	$C_5H_4 + C_6H_5CH_3 \leftrightarrow C_5H_5 + C_6H_5CH_2$	3.65	2.37	3.3	This study
(29)	$C_5H_5 \leftrightarrow C_3H_3 + C_2H_2$	13.80	-0.1	62.3	Kern et al. <sup>222</sup>
(30)	$C_6H_6 \leftrightarrow C_6H_5 + H$	16.76	0	116.0	Ranzi et al. <sup>220</sup>
(31)	$C_6H_6 + H \leftrightarrow C_6H_5 + H_2$	14.60	0	7.2	Sivaramakrishnan et al. <sup>164</sup>
(32)	$C_6H_5 \leftrightarrow o-C_6H_4 + H$	12.63	0.62	77.3	Wang et al. <sup>221 e</sup>
(33)	$C_6H_5CH_3 + H \leftrightarrow C_6H_6 + CH_3$	13.76	0	8.1	Oehlschlaeger et al. <sup>179</sup>
(34)	$CH_3 + C_6H_5CH_3 \leftrightarrow CH_4 + C_6H_5CH_2$	12.50	0	0	Oehlschlaeger et al. <sup>179</sup>
(35)	$C_6H_5 + C_6H_5CH_3 \leftrightarrow C_6H_6 + C_6H_5CH_2$	13.90	0	11.9	Oehlschlaeger et al. <sup>179</sup>

<sup>a</sup>Rate coefficients in the form  $k = AT^n \exp(-E_a/RT)$ , where A [cm, mol, s, K] and E<sub>a</sub> [kcal/mol].

<sup>b</sup>Rate coefficients reported by Klippenstein et al.<sup>59</sup> have been used for other pressure conditions.

<sup>c</sup>See text for rate coefficients that should be used for other conditions.

<sup>d</sup>Other rate coefficients reported by Moskaleva et al.<sup>224</sup> have been used for other pressure conditions.

<sup>e</sup>Rate coefficients reported by Zhang et al.<sup>225</sup> have been used for low pressure conditions.

**Table 9.** Thermochemical data used for the kinetic simulations.

Species	$\Delta H_f^0$ [kcal/mol]	$S_{298K}$ [cal/(mol K)]
$C_6H_5CH_3$	11.95 <sup>a</sup>	76.52 <sup>a</sup>
$C_6H_5CH_2$	49.00 <sup>b,c</sup>	76.04 <sup>d</sup>
$C_7H_6$	78.90	75.70
$C_7H_5$	108.1	77.00

<sup>a</sup>Thermodynamic data used for toluene and for all the other species not listed into the table are from the database of Burcat and Ruscic: Burcat A.; Ruscic B., Third Millennium Ideal Gas and Condensed Phase Thermochemical Database for Combustion with updates from Active Thermochemical Tables, ANL-05/20 and TAE 960 Technion-IIT, Aerospace Engineering, and Argonne National Laboratory, Chemistry Division, September 2005; [ftp://ftp.technion.ac.il/pub/supported/aetdd/thermodynamics](http://ftp.technion.ac.il/pub/supported/aetdd/thermodynamics);

<sup>b</sup>Sivaramakrishnan, R.; Tranter, R.S.; Brezinsky, K. J. Phys. Chem. A 2006, 110, 9388-9399;

<sup>c</sup>Braun-Unkshoff, M.; Frank, P.; Just, T. H. Ber. Bunsen-Ges. Phys. Chem. 1990, 94, 1417-1425;

<sup>d</sup>Ruscic, B.; Boggs, J.E.; Burcat, A.; Csaszar, A.G.; Demaison, J.; Janoschek, R.; Martin, J.M.L.; Morton, M.; Rossi, M.J.; Stanton, J.F.; Szalay, P.G.; Westmoreland, P.R.; Zabel, F.; Berces, T. J. Phys. Chem. Ref. Data 2005, 34, 573-656.

### 5.5.2. Comparison with Experiments

The kinetic mechanism of toluene pyrolysis reported in **Table 8** has been used to reproduce literature data measured in different shock tube experiments. Three datasets were considered: the H atom shock-tube-ARAS data of Sivaramakrishnan et al.,<sup>186</sup> Eng et al.,<sup>171</sup> and Braun-Unkshoff et al.<sup>152</sup>

Sivaramakrishnan et al.<sup>186</sup> studied the thermal benzyl decomposition using  $C_6H_5CH_2Br$  as benzyl radical precursor. As reported also by Jones et al.,<sup>218</sup> benzyl bromide decomposition is instantaneous, with no competing reactions, and produces benzyl radicals with concentrations equal to those of the  $C_6H_5CH_2Br$  precursor used for each experiment. Moreover, in these experiments very diluted reactant mixtures were used with the aim to avoid secondary reactions involving H-atoms produced during the pyrolysis. The reaction  $C_6H_5CH_2Br \rightarrow C_6H_5CH_2 + Br$  ( $k = 5 \times 10^{12} \exp(-25416 K/T)$ )<sup>218</sup> has been added to the kinetic scheme of **Table 8** to model the experiment performed at 1573 K and 0.67 bar. The H-atoms experimental trend and model predictions are compared in **Figure 48**.

The agreement between experimental data and model predictions in these diluted fuel conditions is good, in particular considering that no model parameter has been tuned to these experimental data. As mentioned, the kinetic constants reported in **Table 8** for fulvenallene have been taken from our study on fulvenallene decomposition kinetics.<sup>226</sup> It is worthwhile to remember that in that work two different sets of kinetic constant have been reported, which differ as in one case intersystem crossing (determined by the spin orbit coupling coefficient  $H_{SO}$ ) between the singlet and the triplet PES was considered in the calculations, while in the other it was assumed that intersystem crossing was not limiting. As it is difficult to calculate the effect of intersystem crossing on a rate constant accurately, simulations have been performed twice considering in the first case that intersystem crossing is not limiting (without  $H_{SO}$ ) and in the second accounting for intersystem crossing (with  $H_{SO}$ ). The production of H atoms is only slightly sensitive to intersystem crossing effects.

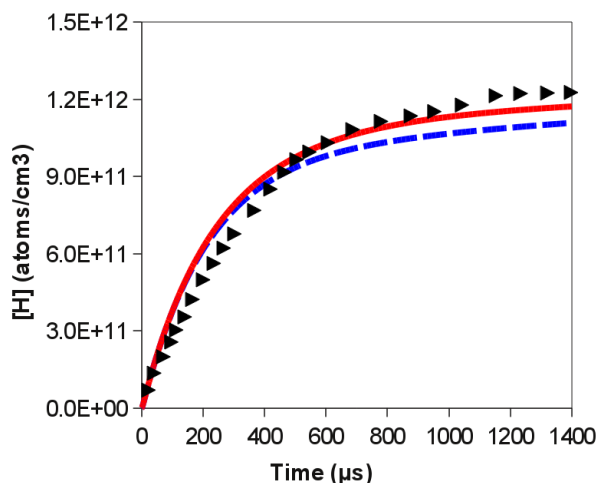


**Figure 48.** Comparison between H-atom experimental data<sup>186</sup> (symbols) and model predictions (dashed lines: without  $H_{SO}$ ; solid line: with  $H_{SO}$ );  $T = 1573$  K,  $P = 0.67$  bar,  $[C_6H_5CH_2Br]_0 = 1.585 \times 10^{12}$  molecule/cm<sup>3</sup>.

Rate of production analyses have been performed for the main species involved in the  $C_6H_5CH_2$  pyrolysis, evidencing that the two proposed decomposition channels are equally important at 1573 K and 0.67 bar. About 51% of the benzyl radicals decompose to form fulvenallene and atomic hydrogen, while the remaining part is decomposed via  $CH_3$  elimination to produce *o*- $C_6H_4$ . It is important to point out here that the relevance of the *o*- $C_6H_4$  channel relies in part on the scaling of the kinetic constant of this reaction to literature theoretical data for toluene decomposition, as discussed in the  $C_7H_7$  kinetic section. Neglecting this correction would decrease the importance of the *o*- $C_6H_4$  channel. The good agreement with the H production data reported in **Figure 48** however seems to support the reliability of the adopted procedure, as any change to the *o*- $C_6H_4$  kinetic constant would affect proportionally the production rate of atomic H.

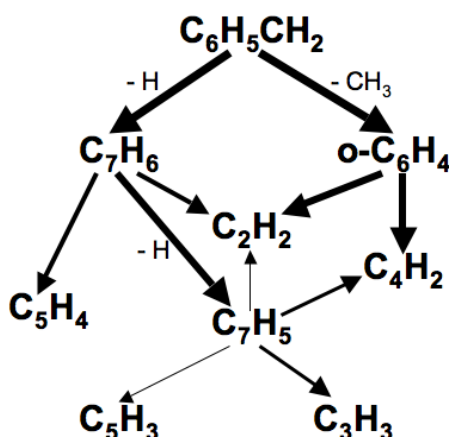


**Figure 49.** Decomposition pathway of the benzyl radical at 1573 K and 0.67 bar calculated for the simulations of the experimental data of **Figure 48**; the thickness of the arrows is proportional to the channeled reactive flux.

**Figure 49** summarizes the decomposition pathway of the benzyl radical at 1573 K. The main products of the benzyl radical decomposition,  $C_7H_6$  and  $o-C_6H_4$ , further decompose to  $C_7H_5$ ,  $C_5H_4$ ,  $C_4H_2$ , and  $C_2H_2$ . In particular, 71% of  $o-C_6H_4$  decomposes to  $C_4H_2$  and  $C_2H_2$ , making this the main channel for the production of acetylene in benzyl (and thus also toluene) pyrolysis in the investigated conditions. Consistently with these results, it can be observed that  $C_4H_2$  and  $C_2H_2$  are commonly detected in toluene pyrolysis<sup>164</sup> or rich flames and it is thus reasonable to ascribe their formation to the decomposition of  $o-C_6H_4$ .<sup>182</sup> However, the formation of  $o-C_6H_4$  is usually considered in kinetic mechanisms as a preliminary step toward polycyclic aromatic hydrocarbons and soot formation or it is associated with phenyl radical pyrolysis.<sup>221,224,225,227</sup> Since in these conditions  $C_6H_5$  is practically absent, it is possible that benzyl decomposition through  $o-C_6H_4$  could be the explanation for the presence of both  $C_2H_2$  and  $C_4H_2$  observed among the toluene pyrolysis products. On the other hand, it is confirmed that  $C_7H_6$  plays a key role in benzyl radical decomposition, though its direct contribution to  $C_2H_2$  formation is only partial; about 40% of  $C_7H_6$  directly produces  $C_2H_2$  and a cyclic  $C_5H_4$  species, while 54% decomposes to  $C_7H_5$  radicals and atomic H, thus affecting the overall H-atom production/consumption mass balance.

The proposed kinetic model was successively used to simulate some of the shock-tube experimental studies of toluene pyrolysis performed by Eng et al.<sup>171</sup> and Braun-Unkloff et al.<sup>152</sup> in a wide temperature (1465–1705 K) and pressure (0.1–7 bar) range. In toluene pyrolysis, more pathways than those active in benzyl decomposition can contribute to the production of H-atoms, so that it is interesting to check whether the simple mechanism of **Table 8** is able to reproduce experimental data.

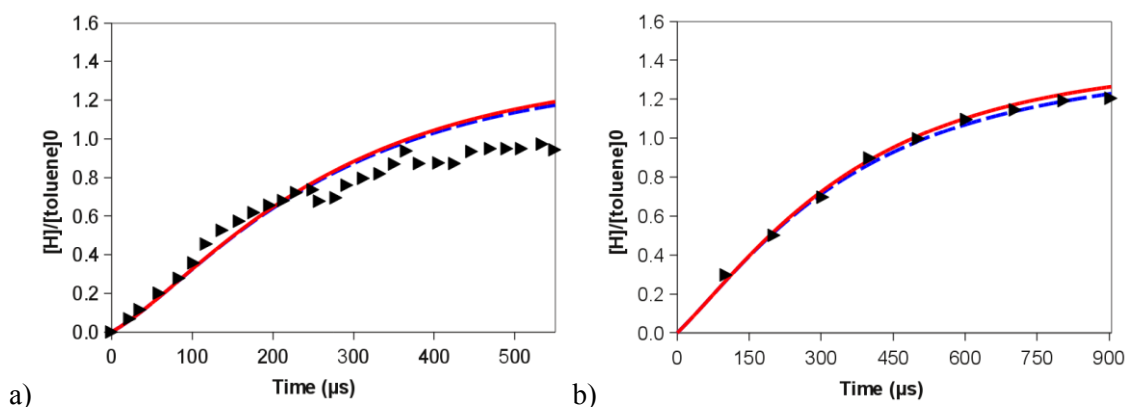


**Figure 50.** Comparison between H-atom yield time profile measured during the pyrolysis of toluene<sup>171</sup> (symbols) and model predictions (dashed lines: without  $H_{SO}$ ; solid line: with  $H_{SO}$ ) for different conditions: a)  $T = 1705$  K,  $P = 0.1$  bar,  $[C_6H_5CH_3]_0 = 4 \times 10^{-12}$  mol/cm<sup>3</sup>; b)  $T = 1602$  K,  $P = 1.6$  bar,  $[C_6H_5CH_3]_0 = 1.2 \times 10^{-11}$  mol/cm<sup>3</sup>.

**Figure 50** shows a comparison between the H-atom yield time profile measured during the pyrolysis of toluene by Eng et al.<sup>171</sup> and the model predictions. As the authors found a distinct incuba-

tion time (about 40  $\mu\text{s}$ ) in the H-atom measures performed at 0.1 bar, the experimental trend of **Figure 50a** has been shifted to remove this incubation period. Good agreement between experimental data and model predictions (it is worth noting again that no model parameter has been tuned on these experimental data) has also been obtained for this case. The model reproduced the trends obtained both at 0.1 and 1.6 bar, showing an excellent agreement over 900  $\mu\text{s}$  with the experimental profile found at 1602 K and 1.6 bar (**Figure 50b**).

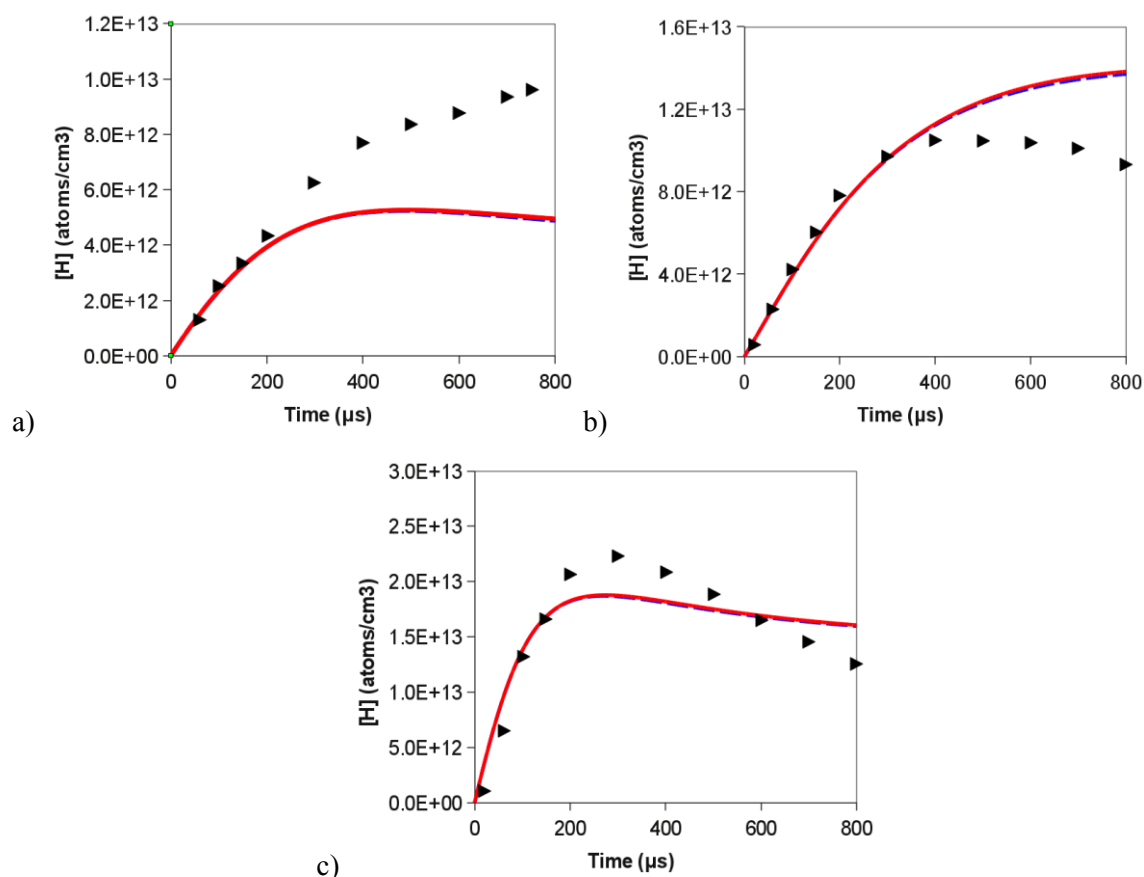


**Figure 51.** Comparison between measured H-atom production<sup>152</sup> (symbols) and model predictions (dashed lines: without  $H_{SO}$ ; solid line: with  $H_{SO}$ ) for various conditions, namely: a)  $T = 1465\text{ K}$ ,  $P = 7.01\text{ bar}$ ,  $[C_6H_5CH_3]_0 = 4.2\text{ ppm}$ ; b)  $T = 1545\text{ K}$ ,  $P = 1.91\text{ bar}$ ,  $[C_6H_5CH_3]_0 = 5\text{ ppm}$ ; c)  $T = 1555\text{ K}$ ,  $P = 1.92\text{ bar}$ ,  $[C_6H_5CH_3]_0 = 19.3\text{ ppm}$ .

Finally, the H-atom production experimentally measured by Braun-Unkhoff et al.<sup>152</sup> is compared with the kinetic model predictions in **Figure 51**. With respect to the previous two datasets, these experiments have been performed at lower temperatures (1465-1555 K), higher pressures (1.91-7.01 bar) and relatively high toluene concentrations (4.2-19.3 ppm), so that it is reasonable to expect an important influence of the secondary chemistry on the experimental results. A fairly good agreement between experimental data and model predictions has been obtained, especially in the short time scale (<200-300  $\mu\text{s}$ ) where a negligible contribution of other chemistry than that considered here is expected. It can be observed that H-atom formation is slightly underpredicted for

$T < 1500$  K (**Figure 51a**), where toluene is only partly consumed and benzyl and fulvenallene seem to be quite stable preventing the following dehydrogenation. H-atom formation on the other hand can be slightly over predicted at higher temperatures (**Figure 51b-c**), where both toluene and benzyl decompositions occur quantitatively and the most stable  $C_7$  species is  $C_7H_5$ .

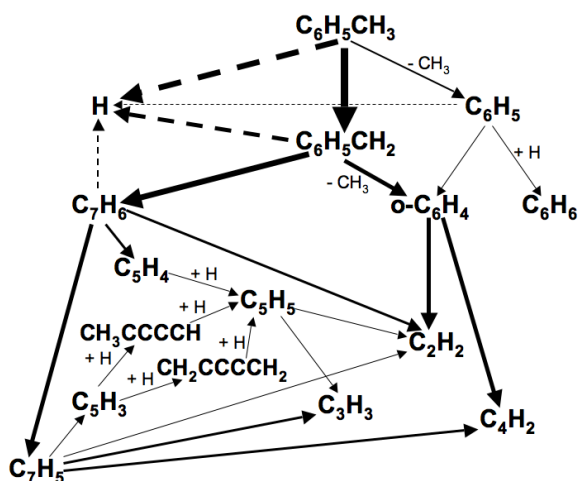


**Figure 52.** Decomposition pathway of toluene at 1602 K and 1.6 bar (solid lines) calculated for the simulations of the experimental data of **Figure 50b**; dashed lines represent the reactions that contribute to the production of H atoms. The thickness of the arrows is proportional to the channeled reactive flux.

The reactive fluxes corresponding to the experimental conditions of **Figure 50b** were investigated to determine the decomposition pathway of toluene (**Figure 52**). With respect to the analysis previously performed for the benzyl radicals, in this case the contribution of secondary reactions cannot be completely neglected because of the higher reactant concentration and pressure. The decomposition of toluene proceeds through two competing parallel reactions:  $C_6H_5CH_3 \rightarrow C_6H_5CH_2 + H$  and  $C_6H_5CH_3 \rightarrow C_6H_5 + CH_3$ . Benzyl formation is the dominant channel, in agreement with literature findings.<sup>59,171</sup>

As also depicted in **Figure 49**, benzyl radicals are involved in two decomposition channels: at 1602 K and 1.6 bar about 55% of  $C_6H_5CH_2$  undergoes H-elimination ( $C_6H_5CH_2 \rightarrow C_7H_6 + H$ ) to give fulvenallene, while the remaining part is decomposed via  $CH_3$  elimination to produce  $o-C_6H_4$ . The pathway that involves  $C_7$  species as intermediate products,  $C_6H_5CH_3 \rightarrow C_6H_5CH_2 \rightarrow C_7H_6 \rightarrow C_7H_5$ , has the main role in the H-atom production with an overall contribution of 96%. Only a minor contribution is due to the  $C_6H_5 \rightarrow o-C_6H_4$  channel. Concerning  $C_2H_2$  formation, the  $C_7H_6$  contribution is 23%, while the  $o-C_6H_4$  contribution is about 60%, confirming that the reaction  $o-C_6H_4 \rightarrow C_4H_2 + C_2H_2$  is the main channel for  $C_2H_2$  formation. **Figure 52** evidences the presence of a secondary active pathway that involves a few H-addition reactions to several linear or cyclic  $C_5$

species ( $C_5H_3 \rightarrow C_5H_4 \rightarrow C_5H_5$ ), followed by the cyclopentadienyl radical decomposition to  $C_3H_3$  and  $C_2H_2$ , which globally gives a 10% contribution to the overall acetylene production.

Summarizing, the good agreement (both qualitative and quantitative) between predicted values and experimental findings obtained with the new reaction pathways proposed in this work suggests that the subset of reactions here proposed and reported in **Table 8** can be used to complement more detailed and complex kinetic mechanisms for the description of high temperature reactions involving fulvenallene, benzyl radicals, toluene, and/or methyl-benzenes.

## 5.6. Concluding Remarks

The decomposition kinetics of fulvenallene and benzyl was investigated using RRKM/ME theory studying the reaction dynamics on a comprehensive PES in which have been included the most relevant intermediates and reactive paths. The structural and energetic parameters needed to carry out the simulations were determined through *ab initio* calculations.

It was found that  $C_7H_6$  can decompose mainly through two reaction channels: direct H-elimination to form the fulvenallenyl radical and decomposition to cyclopentadienylidene and  $C_2H_2$ . Our calculations demonstrate that both reactions are feasible and are likely to happen with almost equal probability if the intersystem crossing probability is explicitly considered in the calculations. However, if intersystem crossing is fast, the decomposition to cyclopentadienylidene and acetylene becomes significantly favored, in particular at high temperatures and pressures. Further experimental studies focusing directly on the  $C_7H_6$  high temperature reactivity would help greatly to achieve a better comprehension of the mechanism of this important reaction, in particular considering that several  $C_7H_6$  isomers, notably phenylcarbene, can be produced directly from the thermolysis or photolysis of phenyldiazomethane.<sup>206</sup>

Another main result is the identification of the two main benzyl decomposition pathways and the estimation of channel specific kinetic constants. The results of the *ab initio* and RRKM/ME calculations predict that benzyl decomposes to fulvenallene and benzyne with similar rates at temperatures and pressures comprised between 1500 and 2000 K and 0.013 and 10 bar. There is thus a remarkable symmetry between the toluene decomposition reactions, which lead to benzyl and phenyl and to the respective production of methyl and atomic hydrogen, and benzyl decomposition products, which involve as well the production of the same secondary products.

The combination of these two set of results led us to the formulation of a new kinetic mechanism for the pyrolysis of toluene and the decomposition of the benzyl radical. It is interesting to notice that the mechanism proposed here is not compatible with the assumption often used in the literature that benzyl decomposition can effectively be described through a lumped reaction whose products are the cyclopentadienyl radical and acetylene. The present calculations in fact show that, although

the cyclopentadienylidene diradical can be considered among the most important benzyl decomposition products and it is reasonable that in combustion environments it reacts rapidly to form the cyclopentadienyl radical, the propargyl radical and diacetylene are produced at higher rates. As diacetylene is often found among the products of toluene pyrolysis, it would be interesting to extend the present kinetic analysis to the study of the chemical composition evolution observed in toluene reactive environments. This however requires a significant extension of the secondary chemistry of the kinetic mechanism proposed here, as well as a detailed analysis of diacetylene reactivity.



# 6 New Reaction Pathways Active in Cyclopentadiene Pyrolysis

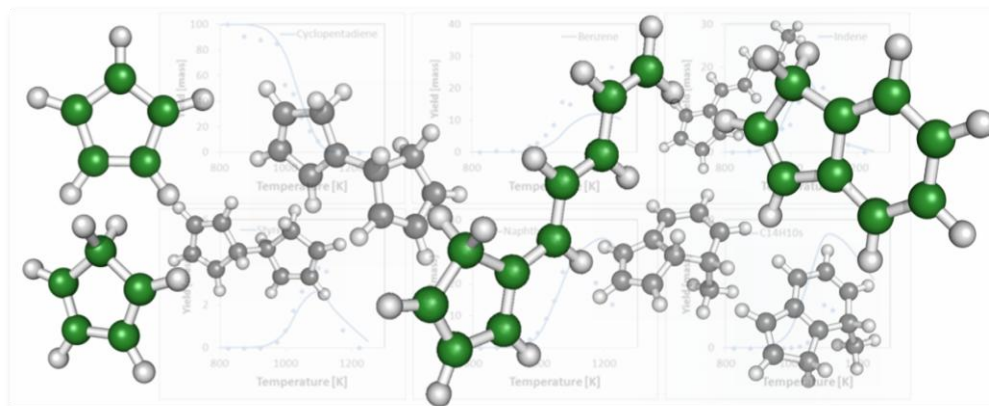


**Figure 53.**  $\beta$ -opening reaction mechanism leads to the formation of major pyrolysis products within the cyclopentadienyl plus cyclopentadiene reaction.

## 6.1. Introduction

The cyclopentadienyl radical ( $cC_5H_5$ ) is often formed in high concentrations during the combustion and pyrolysis of many hydrocarbons. Its chemical reactivity has thus been the subject of several experimental and theoretical investigations. The most studied  $cC_5H_5$  reactions include the addition of hydrogen to give cyclopentadiene ( $cC_5H_6$ ),<sup>219,228-230</sup> the reaction with methyl to form methylcyclopentadiene and its decomposition products,<sup>231-234</sup> the decomposition to acetylene and  $C_3H_3$ ,<sup>228,230,235-237</sup> the addition of acetylene to yield the cycloheptatrienyl radical ( $cC_7H_7$ ),<sup>174,238,239</sup> and the reactions with  $cC_5H_5$  and  $cC_5H_6$  to give naphthalene and indene.<sup>231,240-243</sup> Though it has been proposed that the two latter reactions play an important role in the initial stages of soot formation,<sup>231,240</sup> their reaction kinetics is still not fully understood.

The kinetics of the reaction between two  $cC_5H_5$  radicals has been the subject of several investigations since it was proposed by Melius et al.<sup>231</sup> that it can be one of the major production pathways for naphthalene. The insertion of this reaction path into complex kinetic mechanisms and the simulation of several sets of experimental pyrolysis data rapidly confirmed the consistency of the proposal,<sup>244-248</sup> so that this reaction is now present in most combustion mechanisms. While there is a general consensus in the combustion kinetics community that this reaction is an important path-

way for the formation of naphthalene for most combustion environments, its elementary kinetics has been the object of some discussion. A good example is given by the recent publication of Mebel and Kislov,<sup>243</sup> who proposed that the product of the  $cC_5H_5 + cC_5H_5$  reaction is not a direct naphthalene precursor, but a bicyclic  $C_{10}H_9$  isomer, the 9-H-fulvalenyl radical, which may yield naphthalene only after a successive H atom loss. In particular, the same authors propose that above the relatively low temperature threshold of 1000 K the major reaction product is fulvalene rather than naphthalene.

Similar computational approaches were used to investigate the potential energy surface (PES) of the reaction between  $cC_5H_5$  and  $cC_5H_6$ , identifying several possible reaction channels.<sup>240,242</sup> Though the calculations were performed at a relatively high level of theory, considering the complexity of the PESs and the large number of involved atoms, the reliability of the computational predictions suffers from the lack of an adequate quantitative comparison with experimental data.

Recently, two new experimental studies focused on the detection of the product of the pyrolysis of cyclopentadiene have been published,<sup>249,250</sup> giving a new set of data against which to validate theoretical kinetic predictions of possible reaction pathways for  $cC_5H_5$ . The first experimental work was published by Butler and Glassman and reports measurement of the major species produced during cyclopentadiene pyrolysis and oxidation in Princeton's adiabatic flow reactor.<sup>249</sup> The data were collected between 1100 K and 1200 K for different equivalence ratios. In the second work, performed by Kim et al.,<sup>250</sup> the main aromatic products of  $cC_5H_6$  pyrolysis between 823 K and 1223 K were collected and measured using gas chromatography coupled with mass spectroscopy. These studies provide an important source of experimental data to test and validate rate constants calculated for kinetic pathways involving  $cC_5H_5$  as a reactant.

In this framework, the purpose of the present work is to study the kinetics active during  $cC_5H_6$  pyrolysis. This goal has been accomplished using first principles calculations to investigate the reactive PESs, which has been followed by integration of the master equation to estimate channel specific kinetic constants and successive simulation of the available experimental data through a detailed kinetic mechanism. More specifically, the aim of this study has been focused on the analysis of the reactivity between  $cC_5H_5$  and  $cC_5H_6$ , and between  $cC_5H_5$  and  $cC_5H_5$ .

The PES of the reaction between  $cC_5H_5$  and  $cC_5H_6$  has already been studied by Wang et al.<sup>240</sup> and successively by Kislov and Mebel.<sup>242</sup> Wang et al. investigated four possible reaction pathways that can be originated by the addition of  $cC_5H_5$  to  $cC_5H_6$ , including a C-C  $\beta$  opening pathway and an 'intramolecular' pathway involving the formation of tricyclic intermediates. Successively, this second reaction mechanism has been investigated in greater detail by Kislov and Mebel,<sup>242</sup> who also provided a first estimate of high-pressure channel specific kinetic constants. In the present work, the  $C_{10}H_{11}$  PES has been further re-examined, with the intent of investigating whether the C5-C7

ring expansion mechanism, that has been proposed<sup>174,238</sup> within this group, is active on this PES and if other alternative reactive channels faster than those already identified may exist.

The PES generated by the reaction of two  $cC_5H_5$  radicals, as mentioned before, has been investigated first by Melius et al. and later by Mebel and Kislov. In particular, the last authors proposed that naphthalene could be produced only by a two-step mechanism. Moreover, it was interesting to find that also this mechanism, as the one proposed in their investigation of the  $C_{10}H_{11}$  PES, follows the formation of a tricyclic species. Starting from this standpoint, we revised again the  $C_{10}H_{10}$  PES with the intent of finding whether a reaction mechanism leading to the formation of a direct naphthalene precursor, that is alternative to the mechanisms proposed by Melius et al. and Mebel and Kislov, is possible.

The present chapter is organized as follows. In section 6.2 is presented a brief description of the electronic structure methods and the kinetic theories here adopted. In section 6.3 and 6.4 are reported the analyses of the  $C_{10}H_{11}$  and  $C_{10}H_{10}$  PESs respectively and the estimation of the channel specific rate constants as a function of pressure and temperature. In section 6.5 is reported a comparison between model predictions and experimental measurements. Finally, some concluding remarks will be discussed in section 6.6.

## 6.2. Computational Methodology

### 6.2.1. Electronic Structure Calculations

The  $C_{10}H_{11}$  and  $C_{10}H_{10}$  PESs were investigated determining structures of wells and saddle points using density functional theory (DFT) at the B3LYP/6-31+G(d,p) level.<sup>18,188</sup> Frequency analyses were performed for all the stationary points at the same level of theory. All transitions states were located using a synchronous transit guided saddle point search algorithm<sup>189</sup> and were characterized by a single imaginary frequency.

### $C_{10}H_{11}$ Energies

At a first level of approximation, for the  $C_{10}H_{11}$  PES, the energy of each stationary point has been calculated at the restricted CCSD(T) level using the cc-pVDZ basis set on DFT structures and then extended to the infinite basis set through an MP2 extrapolation scheme as:

$$\begin{aligned}
 E(CCSD(T)/CBS) &= E(CCSD(T)/cc - pVDZ) - E(MP2/cc - pVDZ) \\
 &+ E(MP2/aug - cc - pVDZ) \\
 &+ 0.463[E(MP2/aug - cc - pVTZ) - E(MP2/aug - cc - pVDZ)] \\
 &+ ZPE(B3LYP/6 - 31 + G(d,p))
 \end{aligned}
 \tag{138}$$

The energy calculation scheme of equation ( 138 ) has the purpose of correcting the CCSD(T) energy with the difference between the extrapolated complete basis set (CBS) MP2 energy, calculated as suggested by Martin,<sup>136</sup> and that determined at the MP2/cc-pVDZ level. MP2 calculations have been performed using restricted wave functions and a basis set density fitting procedure to reduce the computational cost.<sup>251</sup> All energies have been corrected with Zero Point Energies (ZPE) determined at the B3LYP/6-31+G(d,p) level. Several test calculations showed that relative energies on the C<sub>10</sub>H<sub>11</sub> PES computed through equation ( 138 ) are comparable within 1.5 kcal/mol with those determined with CCSD(T) energies extrapolated to the CBS limit using the more computationally expensive cc-pVDZ/cc-pVTZ extrapolation scheme we adopted to investigate the C<sub>7</sub>H<sub>6</sub> PES.<sup>183,184</sup>

In order to improve the level of accuracy of the calculations, the energies of the saddle points whose reaction fluxes are rate determining have also been calculated using the ROCBS-QB3 methodology proposed by Wood et al.<sup>252</sup> This computational approach has been designed to improve the level of accuracy of reaction energies calculated using the CBS-QB3 approach when spin contamination is relevant, thus eliminating the need to include the CBS-QB3 empirical corrections factor for spin contamination. This is accomplished performing the calculations using spin restricted wave functions. The mean absolute deviation of bond dissociation energies for a set of 19 severely spin-contaminated species calculated with the ROCBS-QB3 model is  $0.86 \pm 0.36$  kcal/mol, slightly smaller than that of the standard unrestricted CBS-QB3 version,  $1.15 \pm 0.36$  kcal/mol. A few test calculations performed at the UCCSD(T) level showed in fact that spin contamination for several transition states can be high, as indicated by T1 diagnostic values larger than 0.02. There are two further points that indicate that energies calculated with the ROCBS model are more accurate for the case under investigation than those extrapolated through equation ( 138 ). The first is that the ROCBS model, as with all the hybrid methodologies and differently from CCSD(T) extrapolation schemes, uses empirical correction factors tuned over experimental data to account for basis set and other effects. This is particularly relevant when the number of bonds changes in the reaction, as is the case for the formation of W1 from cC<sub>5</sub>H<sub>5</sub> and cC<sub>5</sub>H<sub>6</sub>, a reaction that plays an important role for the system under investigation. The second is that the energy calculation scheme of equation ( 138 ) is based, for computational limitations, on a cc-pVDZ/cc-pVTZ extrapolation, and therefore extrapolates from a relatively small double zeta basis set. In order to test the level of error introduced by the use of a DZ/TZ extrapolation we determined the 0 K cC<sub>5</sub>H<sub>5</sub>-H bond energy using a CCSD(T) cc-pVTZ/cc-pVQZ extrapolation, equation ( 138 ), and the ROCBS-QB3 model. The energies so computed are 81.6 kcal/mol, 82.4 kcal/mol, and 81.1 kcal/mol, respectively. These results show that the DZ-TZ methodology is in error by at least 0.8 kcal/mol with respect to the higher level extrapolation scheme and that the ROCBS-QB3 and the CCSD(T) cc-pVTZ/cc-pVQZ energies are in good agreement. This suggests that the ROCBS-QB3 energies are probably more accu-

rate than those calculated through equation ( 138 ). Because of these considerations, we estimate an uncertainty for the energies computed in this work of 1-2 kcal/mol.

### **C<sub>10</sub>H<sub>10</sub> Energies**

Energies for each stationary point laying on the C<sub>10</sub>H<sub>10</sub> potential energy surface have been calculated at the CBS-QB3 level as proposed by Montgomery et al.<sup>253</sup>, which combines the CBS-Q energy estimation protocol with B3LYP DFT optimized geometries and frequencies. For this PES spin contamination has been found to not be an issue, hence the CBS-QB3 approach has been deemed appropriate to estimate the energies of this system. For reactions without a saddle point we determined the PES scanning the reaction coordinate at the unrestricted B3LYP/6-31+G(d,p) level using a broken symmetry guess for the wave function. Successively this PES has been rescaled over the CBS-QB3 reaction energy.

All DFT, ROCBS-QB3 and CBS-QB3 calculations have been performed using the Gaussian 09 suite of programs<sup>2</sup>, while MP2 and CCSD(T) calculations have been done using Molpro 2008.<sup>3</sup>

### **6.2.2. RRKM/Master Equation Calculations**

Microcanonical rate constants  $k(E,J)$  for each reaction channel have been determined using RRKM theory as a function of energy  $E$  and angular momentum  $J$  from the density of states of reactants and transitions states at energy steps of 1 cm<sup>-1</sup> and  $J$  steps of 1. The  $k(E,J)$  rate constants were then averaged over  $J$  as suggested by Miller et al.<sup>71</sup> to determine 1 cm<sup>-1</sup> spaced  $k(E)$  rate constants. The  $k(E)$  rate constants were successively lumped into energy bins of 100 cm<sup>-1</sup>, which yielded a considerable reduction in the computational cost while retaining good numerical accuracy, as found in previous studies.<sup>70,184</sup>

In the evaluation of the rate constants, the possibility that low frequency vibrations could degenerate into hindered rotors was explicitly considered by investigating the rotational PES. When necessary (i.e. for relatively small rotational energetic barriers) the corresponding partition function was calculated using a hindered rotor model, with energy levels determined by solving the Schrödinger equation for a one dimensional torsional rotation on a rotational potential surface computed at the B3LYP/6-31+G(d,p) level.<sup>79</sup> The moments of inertia for the torsional rotations were calculated with respect to the rotating bond axis and reduced to account for the conjunct rotation of the two moieties as  $I=I_1I_2/(I_1+I_2)$ . This approach corresponds to the I(2,1) level in the East and Radom classification.<sup>78</sup> The calculated densities of states were convoluted when the hindered rotors were more than one.

The microcanonical rate constant  $k_{\text{add}}(E)$  for the entrance channels of PES C<sub>10</sub>H<sub>11</sub> and C<sub>10</sub>H<sub>10</sub> (cC<sub>5</sub>H<sub>5</sub> + cC<sub>5</sub>H<sub>X</sub> giving the W1 adduct, with X being 6 or 5 depending on the reaction considered)

have been computed through microscopic reversibility from the adduct decomposition reaction as explained in section 3.3.5 of Chapter 3. In particular  $k_{\text{add}}(E)$  has been calculated as:

$$k_{\text{add}}(E) = k_{\text{dec}}(E) \cdot \frac{\sigma_{\text{cC}_5\text{H}_5} \sigma_{\text{cC}_5\text{H}_X}}{\sigma_{\text{W1}}} \cdot \frac{g_{\text{W1}}}{g_{\text{cC}_5\text{H}_5} g_{\text{cC}_5\text{H}_X}} \cdot \frac{Q_{\text{W1}}^{\text{tras}}}{Q_{\text{cC}_5\text{H}_5}^{\text{tras}} Q_{\text{cC}_5\text{H}_X}^{\text{tras}}} \cdot \frac{\text{DOS}_{\text{W1}}^{\text{RV}}(E + E_0)}{\sum_{E^*=0}^{E+E_0-E_{\text{rea}}} \text{DOS}_{\text{cC}_5\text{H}_5}^{\text{RV}}(E - E^*) \text{DOS}_{\text{cC}_5\text{H}_X}^{\text{RV}}(E^*)} \quad (139)$$

where  $\sigma_i$  is the rotational symmetry number,  $g_i$  the electronic degeneracy, and  $Q_i^{\text{tras}}$  the translational partition functions of adducts and reactants.  $\text{DOS}_{\text{W1}}^{\text{RV}}(E + E_0)$  is the  $1 \text{ cm}^{-1}$  spaced rovibrational density of states of the adduct, and it is divided by the convoluted density of states of the two reactants. The energy  $E$  of  $k_{\text{dec}}(E)$  is measured from its first non zero term (i.e. at the PES saddle point),  $E_0$  is the activation energy of the reaction calculated with respect to W1, and  $E_{\text{rea}}$  is the reaction energy change.

For the  $\text{C}_{10}\text{H}_{11}$  PES no barrierless reaction has been encountered, while for the  $\text{C}_{10}\text{H}_{10}$  PES both the entrance channel and all the exit channels are characterized by loose transition states. Since the reaction  $\text{cC}_5\text{H}_5 + \text{cC}_5\text{H}_5$  does not have a saddle point,  $k_{\text{dec}}(E)$  has been determined using the E,J resolved variational transition state theory. The transitional modes of the entrance channel have been treated in the harmonic approximation except for the torsional mode, which has been treated as a hindered rotor. The same approach has been adopted to calculate the microcanonical rate coefficients of the H dissociation channels.

In order to determine the level of error associated with the evaluation of the rate of H dissociation reactions using variational transition state theory we computed the kinetic constant for the reaction of addition of H to  $\text{cC}_5\text{H}_5$  using the same approach. The kinetic constant so determined is about a factor of 1.4-1.5 smaller than that determined by Harding et al.<sup>219</sup> using a higher level of theory. Considering the several approximations of this approach, and in particular the estimation of the PES using a single reference theory and the use of the harmonic approximation to calculate the partition functions of the transitional modes, it is reasonable to expect an uncertainty factor of 2-3 for these reaction channels.

For the rate of the entrance channel, although the uncertainty is probably higher, its effect on the calculations is diminished by the fact that this is the main exit channel from the  $\text{C}_{10}\text{H}_{10}$  PES, so that reactants and entrance well are in a pseudo-equilibrium. This translates to a low sensitivity of the overall rate constant to the rate of this reaction. Two test calculations performed at 1500 K confirm that increasing or decreasing the rate of the entrance channel by a factor of 4 affects the RRKM/ME rate constants of the exit channels by a maximum factor of 1.4.

The density of states of  $\text{cC}_5\text{H}_5$ , a molecule that is characterized by Jahn-Teller distortion, was calculated by treating the low frequency mode arising from the Jahn-Teller effect as a free rotor as suggested by Katzer and Sax.<sup>254</sup> The adopted rotational constant,  $230 \text{ cm}^{-1}$ , is the same used by

Katzer and Sax<sup>254</sup> and by Sharma and Green.<sup>233</sup> The  $cC_5H_5$  entropy calculated at 1200 K, is 107.6 cal/mol/k, in good agreement with the 108.1 cal/mol/K calculated by Sharma and Green using a similar approach and the 108.2 cal/mol/K calculated by Kiefer et al.<sup>255</sup> integrating the Schrödinger equation considering explicitly the electronic-vibrational coupling. The  $cC_5H_5$  geometry used in all the calculations is the  $C_{2v}$  ground state structure optimized at the B3LYP/6-31+G(d,p) level, while the rotational symmetry number is 10 and the electronic degeneracy 2.

The contribution of quantum tunneling to microcanonical rate constants was explicitly considered for all reactions with imaginary vibrational frequencies larger than 1300  $cm^{-1}$  using Eckart<sup>87</sup> tunneling probabilities as described in section 3.3.4 of the Methods chapter.

It is worthwhile to mention that each simulation starts from an entrance well at an energy  $E$  determined stochastically by sampling the microcanonical reaction rates calculated assuming a Boltzmann population for the reactants. Channel specific rate constants are then calculated by multiplying the ratio between the number of reacted molecules for each reaction channel and the total number of reacted molecules by the high-pressure rate constant of the entrance channel. An implicit assumption of this approach is that secondary bimolecular reactions involving collisionally stabilized wells do not affect the master equation dynamics, so that the only possible fate of the intermediate wells is either to decompose to reactants or go to the products. The decomposition to reactants is explicitly considered and is in competition with the other possible reaction channels. The kinetic constants so determined however are reaction fluxes and not phenomenological rate coefficients.

### 6.2.3. Kinetic Mechanism and Experimental Data Simulations

The pyrolysis and oxidation mechanism of hydrocarbons up to C16 adopted herein,<sup>256,257</sup> consisting of over 10,000 reactions and more than 300 species, was developed based on hierarchical modularity. Thermochemical data for most species were obtained from the CHEMKIN thermodynamic database<sup>258</sup> and from Goos et al.<sup>259</sup> The group additive method was used to estimate the properties of those species whose thermodynamic data are not available in the literature.<sup>260</sup> The complete kinetic mechanism, with thermodynamic and transport properties, is available in the CHEMKIN format on the web.<sup>261</sup> All numerical simulations were performed with the DSMOKE and OpenSMOKE codes.<sup>262</sup> The BzzMath 6.0 numerical library was adopted.<sup>263</sup>

## 6.3. Kinetics of the $cC_5H_5 + cC_5H_6$ Reaction

The discussion of the results is organized in three sections. The first reports the analysis of two reaction pathways on the  $C_{10}H_{11}$  PES that follows the addition of  $cC_5H_5$  to  $cC_5H_6$  and that was performed using *ab initio* calculations and a simplified analysis of the reaction kinetics. In the second

section the results of the master equation calculations and the estimation of channel specific rate constants are reported, while in the third the calculated kinetic constants are used to simulate the available experimental data using a detailed kinetic mechanism.

### 6.3.1. Analysis of the Potential Energy Surface

The portions of the  $C_{10}H_{11}$  PES investigated in this work are two and reflect two different interpretations of the reactivity of this system. The first reaction pathway studied here has been searched under the assumption that the reaction between  $cC_5H_5$  and  $cC_5H_6$  involves a succession of ring contraction and expansion reactions. It is thus conceptually similar to the ‘intramolecular’ pathway suggested by Wang et al.<sup>240</sup> and further examined by Kislov and Mebel,<sup>242</sup> in which the formation of a tricyclic species plays a dominant role, and resembles the pathway that has been proposed for the reaction between two  $cC_5H_5$  radicals to give naphthalene and two hydrogen atoms.<sup>231</sup> The second reaction pathway has instead been formulated on the basis of the assumption that any progress in the unimolecular reactivity of the  $C_5H_5$ - $C_5H_6$  adduct formed as a result of the addition of  $C_5H_5$  to  $C_5H_6$  requires as a first step a ring opening reaction, and is thus similar to the  $\beta$  opening reaction pathway suggested by Wang et al.<sup>240</sup>

#### C5-C7-C6 Reaction Pathway

The first reaction mechanism investigated is an extension of the C5-C7-C6 mechanism that has been recently proposed as a possible route of conversion of C5 to C6 rings to adducts containing two C5 rings connected by a covalent bond.<sup>174</sup> The C5-C7-C6 mechanism was first proposed to explain experimental evidence showing that  $cC_5H_5$  and acetylene can react to give a  $C_7H_7$  isomer,<sup>236</sup> which has been identified on the basis of successive first principle calculations as the cycloheptatrienyl radical.<sup>238</sup> The mechanism proposed for this reaction involved the formation of a  $C_2H_2$ - $C_5H_5$  adduct, followed by cyclization to a bicyclic intermediate containing C4 and C5 adjacent rings and by a ring expansion to a seven membered ring to give  $cC_7H_7$ . In a successive computational study it has been shown that  $cC_7H_7$  can efficiently be converted to the benzyl radical through the addition and subsequent loss of a hydrogen atom.<sup>174</sup> The extension of the C5-C7-C6 reaction mechanism to the reaction between  $cC_5H_5$  and  $cC_5H_6$  leads to the PES in **Figure 54**.

The reaction mechanism reported in **Figure 54** shows that the reaction between  $cC_5H_5$  and  $cC_5H_6$  is exothermic by about 14.1 kcal/mol and leads to the formation of the W1 adduct, which can further react to form the tricyclic species W2 overcoming an energy barrier that is about 3 kcal/mol smaller than that of the entrance channel TS1. Successively, W2 can undergo ring expansion to form the bicyclic species W3. This reaction has an activation energy that is about 11 kcal/mol higher than that leading to the decomposition to the reactants through TS1, which favors significantly the latter pathway.



dicates that  $cC_5H_5$  and  $cC_5H_6$  start reacting significantly (i.e. above 1100 K). This has been checked directly by calculating energy barriers for several possible H transfer reactions. The only significant exception to this rule will be discussed in the next section.

The reaction mechanism reported in **Figure 54** can be compared at a first level of accuracy with literature mechanisms by comparing the highest energy barriers that must be overcome to convert reactants to products. It can thus be observed that the highest energy barrier characterizing this PES is about 33 kcal/mol, measured with respect to W1, while the pathway indicated by Kislov and Mebel<sup>242</sup> as the major indene formation channel has a maximum energy barrier of about 45 kcal/mol. Also, all the pathways proposed by Wang et al.<sup>240</sup> for this reaction network require overcoming energy barriers of at least 41 kcal/mol. This is an important indication that the C5-C7-C6 reaction pathway is potentially significantly faster than the alternative reaction mechanisms reported in the literature.

A more direct check of the feasibility of this reaction mechanism can be performed calculating reaction fluxes over the PES with respect to W1 using classic transition state theory. Though the rates so calculated are only upper bounds to the real reaction fluxes, this approach can be efficiently used to exclude slow reaction pathways before doing computationally expensive RRKM/ME calculations. The upper bound for the kinetic constant for this reaction pathway calculated assuming that the transition through TS3 is rate limiting and accounting explicitly for decomposition to reactants as a competitive process is  $6.8 \times 10^6 \text{ cm}^3/\text{mol/s}$ . This is significantly slower than the high-pressure rate of the entrance channel,  $3.0 \times 10^{10} \text{ cm}^3/\text{mol/s}$ . The reaction rate for decomposition to reactants through TS1 is much faster than the reaction flux passing through TS3, both because of the lower activation energy and for the much higher pre-exponential factor, since TS1 has a rather loose nature and is characterized by an almost free torsional rotor that is absent in TS3.

The upper limit thus calculated for the rate of the C5-C7-C6 pathway is significantly smaller than the kinetic constant suggested by Butler et al.<sup>249</sup> on the basis of experimental evidences for the production of indene from the reaction between  $cC_5H_5$  and  $cC_5H_6$ ,  $1.5 \times 10^8 \text{ cm}^3/\text{mol/s}$ , and it is also much smaller than that estimated through fitting of experimental indene concentrations at 1200 K in the present study (about  $10^9 \text{ cm}^3/\text{mol/s}$ , see the kinetic section for details).

The rate of indene formation during  $cC_5H_6$  pyrolysis is here taken as an indirect measure of a lower bound for the rate of the reaction between  $cC_5H_5$  and  $cC_5H_6$  since they are, in these conditions, respectively the most abundant radical and chemical species, so that it is most likely that indene is the product of their reaction. The only possible competitive reaction channel, which is the reaction between two  $cC_5H_5$  radicals, is in fact likely to yield as a major product naphthalene, since the lower number of H atoms in the reactants is likely to make the production of indene energetically much less favored than that of naphthalene for stoichiometric reasons. Hence, even considering the uncertainty of the calculations, such a high disagreement between the expected and com-

puted rate of the reaction between  $cC_5H_5$  and  $cC_5H_6$  clearly suggests that a reaction pathway that is alternative not only to the C5-C7-C6 mechanism here proposed, but also to the reaction pathways proposed by Wang et al.<sup>240</sup> and by Kislov and Mebel,<sup>242</sup> must exist. The search for this reaction pathway is the subject of the next section.

### $\beta$ -opening Reaction Pathway

A preliminary analysis of literature reaction pathways of W1 revealed that the opening of the  $C_5H_6$  ring through the  $\beta$ -opening of the C-C bond adjacent to the covalent bond between  $C_5H_6$  and  $C_5H_5$  proceeds at a rate similar to that calculated for the C5-C7-C6 pathway. This is interesting since the activation energy for this reaction, 42.9 kcal/mol, is about 10 kcal/mol higher than that calculated for the C5-C7-C6 pathway. The reason why the two pathways have similar rates is that the high pre-exponential factor of the  $\beta$ -opening reaction, whose transition states maintains the  $C_5H_5\_C_5H_6$  torsional rotor of the W1 well, is significantly larger than that of TS3. Despite this, as mentioned in the previous section, the rate of this reaction is still significantly smaller (about two orders of magnitude) than that consistent with experimental indene formation rates. However an extensive search of the  $C_{10}H_{11}$  PES revealed that the  $\beta$ -opening activation energy can be substantially reduced if the hydrogen bound to the tertiary carbon of the  $C_5H_5$  ring migrates to a neighboring secondary carbon. The PES of this reaction pathway is reported in **Figure 55**.

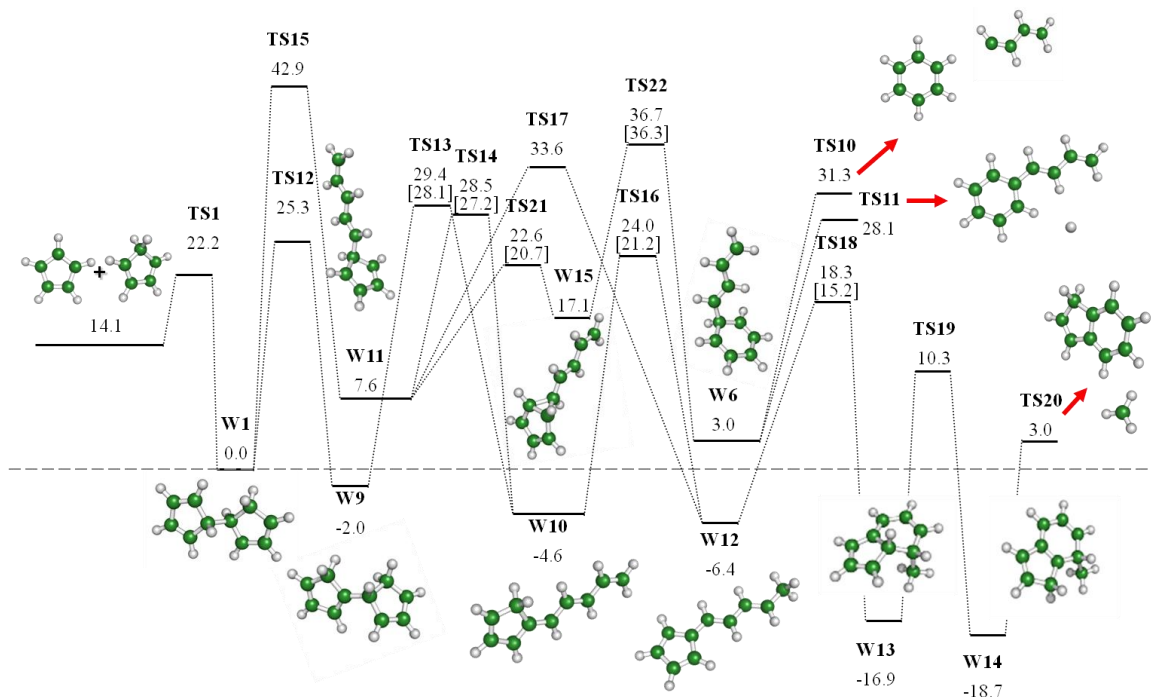


**Figure 55.** Potential energy surface of the  $\beta$ -opening reaction pathway. Energies include ZPE corrections, were computed at the CCSD(T)/cc-pVDZ level, and extrapolated to the CBS as described in equation 138. Energies [kcal/mol] calculated for key transition states at the ROCBS-QB3 level and used in the master equation calculations are reported between square brackets.

Though the molecular structure of W1 and W9 are similar, the  $\beta$ -opening activation energy decreases from 42.9 kcal/mol (TS15) to 29.4 kcal/mol (TS13), which leads to an increase of the rate for this reaction pathway of more than two orders of magnitude at 1200 K, thus making it compatible with experimental evidences. The reason for the significant decrease of the activation energy is that in this molecular configuration, upon opening of the  $C_5H_5$  ring, its two  $\pi$  bonds can conjugate with the two  $\pi$  bonds of the  $C_5H_6$  ring, thus leading to the formation of the very stable W10 well.

The activation energy of the H migration reaction that is necessary to access W9 is 25.3 kcal/mol. Though this value is significantly smaller than that of many other H transfer reactions investigated in this study, it could be expected. Recently, we have in fact extensively investigated the reactivity on PESs that are characterized by the presence of unsaturated C5 rings, such as the  $C_7H_7$  and the  $C_7H_6$  PESs.<sup>180,183,184,187</sup> One of the findings of these studies is that the migration of H atoms on functionalized  $C_5H_5$ -R rings is hindered by relatively low energy barriers. These reactions can be classified as 1,5 sigmatropic H shifts. The facility of 1,5 sigmatropic H migrations in substituted cyclopentadienes has been known for a long time and can be ascribed to the suprafacial nature of the process, which thus stabilizes the transition state through resonance as predicted by the Woodward-Hoffman rules.

From W10 two competitive reaction pathways are possible. The first and faster is started by H transfer to the  $C_5H_6$  linear chain through TS16 and is followed by cyclization to the C5-C6 bicyclic well W13 and, upon a further H transfer, by the loss of methyl to give indene. The second is started by a H transfer to form W11 and then by a ring expansion mechanism that requires passing from TS21 and TS22 and leads to the formation of W6, a  $C_{10}H_{11}$  isomer whose reactivity has been studied for the C5-C7-C6 mechanism that, once formed, decomposes rapidly to benzene and phenylbutadiene. Three alternative reaction channels connecting W6 to  $C_6H_6\_CHCCHCH_3$ ,  $C_6H_5\_CH_2CHCHCH_2$ , and  $C_6H_6\_CHCHCHCH_2$  have been considered. The activation energies computed at the CCSD(T)/CBS level are 83.1 kcal/mol, 29.4, and 27.7 kcal/mol. The two latter reactions have activation energies comparable to those of TS10 and TS11. However, the pre-exponential factors are significantly smaller, so that these reaction channels are not competitive and have not been considered in the RRKM/ME calculations. Transition states parameters are reported as supplementary information in ref<sup>264</sup> under the labels TS34, TS32, and TS33.

A further analysis of the reactivity on this portion of the  $C_{10}H_{11}$  PES showed that, although the main reaction mechanism is the one highlighted in **Figure 55**, several parallel pathways are possible. The three more relevant secondary pathways are shown in **Figure 56** and **Figure 57**.

The first parallel pathway connects W9 and W10 through a reaction mechanism that is different from the one shown in **Figure 55**. This mechanism is initiated by an initial H transfer on the  $C_5H_5$  ring leading from W9 to W16 and is followed by the successive  $C_5H_6$  ring opening reaction through TS25 to W7, which easily isomerizes through H transfer to the more stable W10.

This mechanism represents thus an alternative route with respect to the one reported in **Figure 55** and that requires passing from TS13 and offers a second pathway to form W10, which can compete with the dissociation to reactants through TS1. The key energy barriers of the two steps are given by TS13 and TS25. Although the activation energy of TS25 is about 2 kcal/mol higher than that of TS13, this reaction pathway is expected to contribute about 30% at 1200 K to the overall reaction flux connecting W1 and W10.

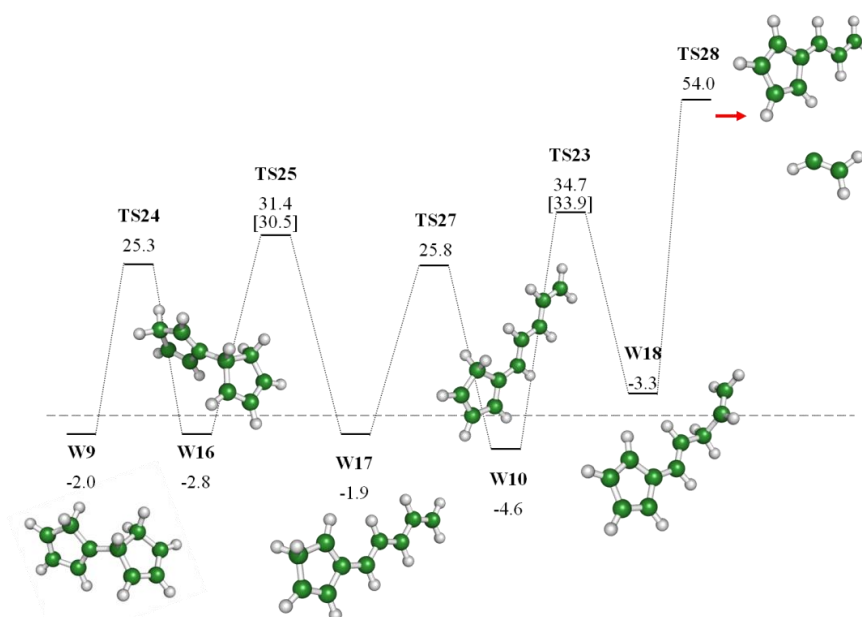


**Figure 56.** Potential energy surface of two mechanisms that proceed in parallel to the main  $\beta$ -opening reaction pathway. The first connects W9 to W10, while the second provides a mechanism for decomposition of W10 alternative to those sketched in **Figure 55**, which leads to 6-vinyl fulvene and the vinyl radical. Energies [kcal/mol] include ZPE corrections, were computed at the CCSD(T)/cc-pVDZ level, and extrapolated to the CBS limit. Energies calculated for key transition states at the ROCBS-QB3 level and used in the master equation calculations are reported between square brackets.

The second parallel reaction pathway is a decomposition mechanism of the  $C_{10}H_{11}$  adduct that is alternative to the pathways leading to indene, phenylbutadiene, and benzene shown in **Figure 55**. The reactions involved in this mechanism are H transfer to the C5 linear chain followed by a loss of the vinyl radical to form 6-vinylfulvene. Despite the high activation energy of TS28, this reaction proceeds rapidly because of the loose nature of the transition state. Unfortunately, the ROCBS-QB3 energy of TS28 could not be computed because of consistency problems related to the spin state during the CCSD(T) restricted open shell calculations. It is thus likely that the reaction rate for this reaction channel used in the master equation calculations is underestimated, as ROCBS-QB3 predicts in general an activation energy that is systematically smaller than that calculated at the other level of theory.

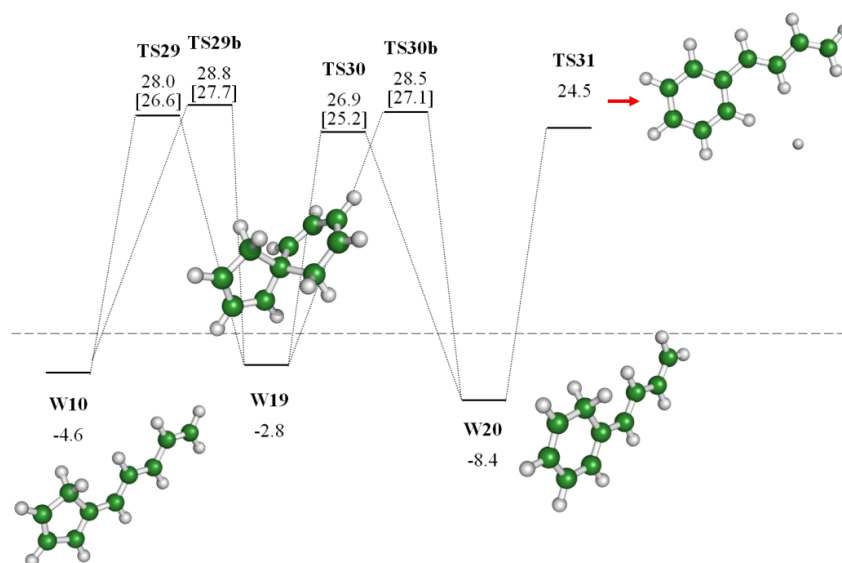


**Figure 57.** Potential energy surface of a mechanism of formation of phenyl butadiene that is parallel to that of **Figure 55**. Energies [kcal/mol] include ZPE corrections, were computed at the CCSD(T)/cc-pVDZ level, and extrapolated to the CBS limit. Energies calculated for key transition states at the ROCBS-QB3 level and used in the master equation calculations are reported between square brackets.

The third mechanism (**Figure 57**) is as well an alternative decomposition mechanism of W10, which involves the formation of a spyrodecatrienyl intermediate (W19), and is followed, upon ring opening, by the loss of a H atom to give phenylbutadiene, which can thus be produced through two different transition states: TS31 and TS11. In addition, in this case, TS31 is the fastest of the several reactions that were studied when investigating the reactivity of the W20 well. In particular, it has been found that any H transfer reaction is likely to be significantly unfavored with respect to the direct H loss process. Two different transition states have been located for TS29 and TS30, which differ for the relative orientations of the two methylene groups.

### 6.3.2. Master Equation Integration and Rate Constant Estimation

Master equation calculations have been performed considering explicitly the whole  $\beta$ -opening reaction mechanism, which is sketched in **Figure 55**, **Figure 56** and **Figure 57**. The C5-C7-C6 pathway was not included in the calculations since, as mentioned above it appears to be too slow to compete with the  $\beta$ -opening pathway. Overall, the PES considered in the calculations consists of 15 wells and 20 transition states.

The master equation has been solved assuming that the bath gas is pure Argon, adopting an exponential down model for the collisional energy transfer, and using as Lennard-Jones collision parameters of the bath gas and of the reactant the literature values of  $\sigma = 3.75 \text{ \AA}$  and  $\varepsilon/k = 113 \text{ K}$  for Argon,<sup>217</sup> and  $\sigma = 8.0 \text{ \AA}$  and  $\varepsilon/k = 600 \text{ K}$  for all the  $C_{10}H_{11}$  isomers, which are the same values used

by Vereecken et al.<sup>265</sup> to model the reactivity of  $C_9H_9$  isomers. Since energy transfer parameters are not well known for these molecules, we assumed that the mean downward transfer energy  $\Delta E_{\text{down}}$  is  $295(T(K)/300)^{0.7} \text{ cm}^{-1}$ , which is the value measured for azulene at 300 K<sup>266</sup> scaled with temperature using the proportionality suggested by Miller and Klippenstein for  $C_6H_6$  isomers.<sup>267</sup>

All parameters used in the simulations, including vibrational frequencies, rotational constants, rotational symmetry numbers, optical isomer numbers, inertia moments for hindered rotors, and rotational PESs for hindered rotors are reported in the supplementary information of ref<sup>264</sup>.

The simulations were continued until at least 250000 molecules had reacted (500000 for temperatures smaller than 1200 K to increase the sampling of slow channels), including also decomposition to reactants among the possible reaction channels. In these conditions for each simulation a minimum of at least 50 reactive events have been observed for each reaction channel. This number has been considered statistically significant as the channel specific rates were converged to a constant value ( $\pm 5\%$ ) for the last 50000 reactive events. The only exception is the 6-vinylfulvene channel at 900 K, in which case only eight reactive events have been observed. The kinetic constant for that channel has been therefore interpolated between 1000 and 2000 K excluding the 900 K data. All the other calculations have been performed at 1 bar at temperatures comprised between 900 and 2000 K.

The results of the calculations are summarized in **Figure 58**, while kinetic constants interpolated to the modified Arrhenius equation as a function of temperature for all the considered reaction channels are reported in **Table 10**.

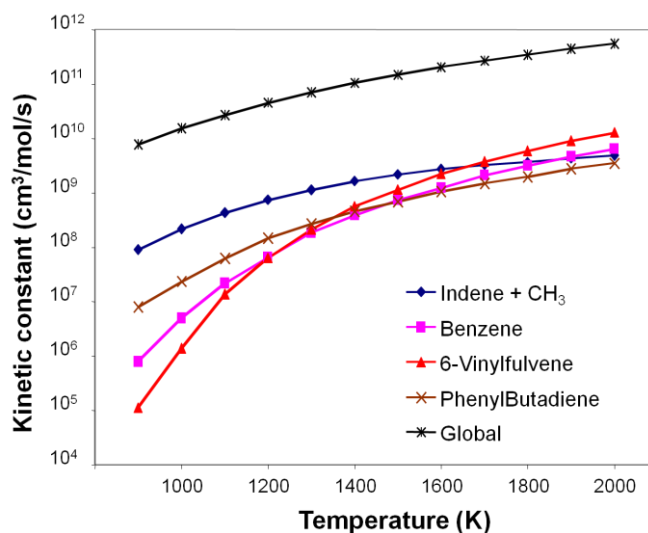


**Figure 58.** Kinetic constants [ $\text{cm}^3 \text{ mol}^{-1} \text{ s}^{-1}$ ] calculated at 1 bar for the reaction between  $cC_3H_5$  and  $cC_3H_6$  for the different reaction channels. The kinetic constant for the reaction of decomposition to reactants is not reported as it is almost superimposed to the global kinetic constant, which is equal to the rate for the addition of  $cC_3H_5$  to  $cC_3H_6$  to give W1.

**Table 10.** Kinetic constants for the reaction between  $cC_5H_5$  and  $cC_5H_6$  interpolated between 900 and 2000 K as  $k = AT^\alpha \exp(-Ea(\text{cal/mol})/RT)$  in  $\text{cm}^3 \text{mol}^{-1} \text{s}^{-1}$ .

Reaction	Log A	$\alpha$	Ea (cal/mol)
$cC_5H_6 + cC_5H_5 \rightarrow \text{Indene} + \text{CH}_3$	25.197	-3.935	23108.
$cC_5H_6 + cC_5H_5 \rightarrow \text{benzene} + \text{C}_4\text{H}_5$	29.172	-4.515	40873.
$cC_5H_6 + cC_5H_5 \rightarrow \text{vinylfulvene} + \text{C}_2\text{H}_3$	65.077	-14.20	74645.
$cC_5H_6 + cC_5H_5 \rightarrow \text{phenylbutadiene} + \text{H}$	16.743	-1.407	23454.

As can be observed, the fastest channel for the W1 adduct is decomposition to reactants, while the main product up to 1600 K is indene. At 1200 K, the temperature at which most of the experimental data simulated in this work were taken, the main reaction products, after indene, are phenylbutadiene, 6-vinylfulvene, and benzene. While indene, phenylbutadiene and benzene were observed by Butler and Glassman<sup>249</sup> among the products of the pyrolysis of  $cC_5H_6$ , this was not the case for 6-vinylfulvene. However both the experimental data of Butler and Glassman and those of Kim et al.<sup>250</sup> report a significant presence of styrene, a stable isomer of 6-vinylfulvene, among the pyrolysis products. Though no data are reported in the literature for the isomerization of 6-vinylfulvene to styrene, a few preliminary *ab initio* calculations performed at the DFT level revealed that no significant barriers hinder its conversion to 1,5 dihydropentalene. The pyrolysis of dihydropentalene has been studied experimentally by Dudek et al.,<sup>268</sup> who found that its major product is styrene and that the kinetic constant for the conversion of dihydropentalene to styrene is  $10^{13.1 \pm 0.3} \exp(-29.1 \pm 1/T)$ . This means that at 1200 K the characteristic time for the conversion of dihydropentalene to styrene is a few ms, which is significantly smaller than the residence time in the experimental set ups considered in this study. This suggests that the vinylfulvene pathway can be reasonably interpreted as a styrene production channel.

Also, it is interesting to observe that, although phenylbutadiene is detected by Butler and Glassman among the chemical species formed during  $cC_5H_6$  pyrolysis, its concentration rapidly reaches a maximum value after which it slowly decreases as a function of the residence time. This suggests that at the temperatures at which  $cC_5H_6$  decomposes to phenylbutadiene, after being formed, it is rapidly converted to more stable species. Considering the phenylbutadiene chemical structure, the most likely decomposition products are styrene and benzene.

## 6.4. The Kinetics of the $C_5H_5 + C_5H_5$ Reaction

### 6.4.1. Analysis of the Potential Energy Surface

The PES investigated here is composed of two parallel and competing pathways. The first reaction pathway corresponds essentially to the first of the two mechanisms proposed by Melius et al.<sup>231</sup> for the formation of naphthalene from the reaction between two  $cC_5H_5$  radicals. In fact, the few new reaction channels located on this portion of the PES do not affect substantially the overall reactivity. This reaction pathway is characterized by numerous hydrogen transfers that can take place on the C5 rings of the W1 adduct and, upon the loss of a hydrogen atom, by the formation of  $n$ -H-fulvalenyl radical species. The second reaction pathway instead leads to the formation of  $n$ -H-azulyl radical species. It follows a mechanism similar to the one proposed for the reaction between  $cC_5H_5$  and  $cC_5H_6$  and involves a ring opening reaction as the key step.

#### $n$ -H-Fulvalenyl Pathway

The first reaction pathway investigated is an extension of the mechanism proposed by Melius and co-workers<sup>231</sup> and successively re-examined by Mebel and Kislov<sup>243</sup>. As mentioned, the mechanism is characterized by the loss of an H atom and the formation of a  $C_5H_5-C_5H_4$  radical, defined as 1-H-fulvalenyl.

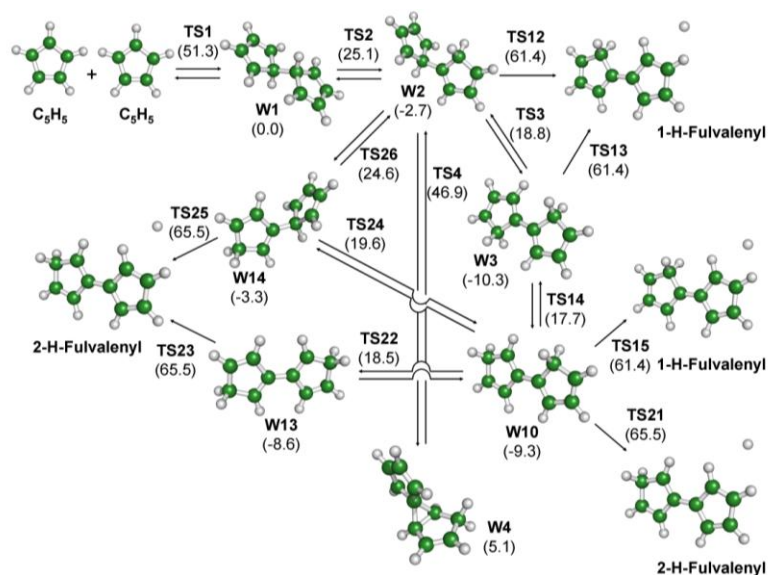


**Figure 59.** Potential energy surface of the  $n$ -H-fulvalenyl mechanism. Energies, expressed in kcal/mol, were computed at the CBS-QB3 level.

In **Figure 59** it is shown the portion of the  $C_{10}H_{10}$  PES in which we analyzed all the possible reactive channels leading to the formation of  $n$ -H-fulvalenyl species. The entrance channel into the  $C_{10}H_{10}$  PES is given by the recombination of two  $cC_5H_5$  radicals, which leads to the formation of the W1 adduct, namely 9,10 dihydrofulvalene. The reaction is exothermic by 51.3 kcal/mol, which

is in reasonable agreement with the values calculated by Melius et al. with the BAC-MP2 method (52.1 kcal/mol) and later by Mebel and Kislov with the G3(MP2,CC) method (52.8 kcal/mol).

The adduct W1 can either dissociate to form the 1-H-fulvalenyl radical and atomic hydrogen or isomerize to the W2 well, which is about 2.7 kcal/mol lower in energy than W1 thanks to the stabilization determined by the migration of the involved hydrogen from a tertiary to a secondary carbon. The migration of the second tertiary hydrogen leads to W3 and is associated with a more consistent stabilization of 10.3 kcal/mol, determined both by the formation of a stronger C-H bond and, more importantly, by the conjugation of the 4  $\pi$  bonds of the two C5 rings. The activation energies for the two H transfer reactions are relatively small, only 25.1 and 18.8 kcal/mol. As mentioned in the previous analysis the facility of 1,5 sigmatropic H migrations in substituted cyclopentadienes has been known for a long time and can be ascribed to the suprafacial nature of the process, which thus stabilizes the transition state through resonance as predicted by the Woodward-Hoffman rules. It is interesting to notice that the activation energy calculated for TS2, 25.1 kcal/mol, is in good agreement with the 23 kcal/mol measured by Mc Lean and Haynes<sup>269</sup>.

The activation energies for all H migration reactions on the bicyclic W1 adduct and its isomers are significantly smaller than those of the competing processes, which are decomposition to reactants and dissociation into the fulvalenyl radical and atomic hydrogen. This indicates that scrambling of H atoms will take place rapidly on this portion of the C<sub>10</sub>H<sub>10</sub> PES.

Among the possible decomposition channels, the direct dissociation of W1 into atomic H and a C<sub>10</sub>H<sub>9</sub> isomer was not considered in this study. The reason is that this reaction was studied and considered improbable by Melius and coworkers<sup>231</sup> as it showed an activation energy of 77.4 kcal/mol, which is more than 15 kcal/mol higher than the alternative dissociation from W2 through TS12, which is barrierless and requires 61.4 kcal/mol. The lower activation energy of TS12 with respect to that for decomposition of W1 is determined by the different resonance of the products. The protonation of the tertiary carbon in the radical produced by W1 dissociation in fact inhibits the conjugation, and therefore the resonance, between the  $\pi$  bonds of the two C5 rings in the product of W1, which is instead present in the 1-H-fulvalenyl radical.

While the decomposition of both W2 and W3 through TS12 and TS13 leads to the same product, W3 can alternatively make a second hydrogen transfer from one of the two CH<sub>2</sub> groups to a vicinal C, thus either giving back W2 or forming W10. In turn, W10 has four possible reaction pathways: dissociation to the 1-H-fulvalenyl radical (TS15), dissociation to the 2-H-fulvalenyl radical (TS21), transfer of the hydrogen in position 1 back to the tertiary carbon leading to W14 (TS24) or to the other neighbor carbon forming W13 through TS22. Isomers W13 and W14 can both lose a hydrogen atom yielding the same product, the 2-H-fulvalenyl radical, through TS23 and TS25, respectively. Moreover W14 can make another H-transfer reaction giving again well W2, thus closing the cycle of the possible hydrogen transfer reactions.

In general, it is interesting to notice that the activation energy leading from well W1 to W2, as well as that of the other H transfer reactions, is half the activation energy for decomposition to reactants, so that all the wells here considered are likely to be visited before leaving the  $C_{10}H_{10}$  PES through a decomposition reaction. Furthermore, we observe that, as anticipated, the path suggested by Melius et al.<sup>231</sup>, i.e. decomposition of W2 through TS12, is among the most probable from an energetic point of view. Firstly because decomposition to 2-H-fulvalenyl is 4 kcal/mol higher with respect to W1 than decomposition to 1-H-fulvalenyl, secondly because isomer W2 is rather unstable (-2.7 kcal/mol) compared to the others that are precursors to dissociation (-10.3 kcal/mol for W3, -9.3 kcal/mol for W10, -8.6 kcal/mol for W13 and -3.3 kcal/mol for W14). These results confirm the conclusions of Melius et al., but do not satisfy the search of an alternative path leading to the direct formation of a naphthalene precursor. The search of this reaction pathway is the subject of the next section.

### ***n*-H-Azulyl Pathway**

The motivation for the investigation of this reaction pathway comes from the intent to test whether the reaction mechanism we proposed to be dominant for the reaction between  $cC_5H_5$  and  $cC_5H_6$  is active also on the  $C_{10}H_{10}$  PES. It is in fact interesting to check whether some reaction mechanisms involving  $cC_5H_5$  as a reactant can be active also for different reaction partners.

In particular in our examination of the  $C_{10}H_{11}$  PES<sup>264</sup> we found that all the literature pathways for the reaction between  $cC_5H_5$  and cyclopentadiene, as well as an extension of a C5-C7-C6 ring expansion-contraction mechanism of recent proposal, lead to a substantial disagreement between the calculated and the expected rate constant for indene formation. Nevertheless, a thorough search of the  $C_{10}H_{11}$  PES performed following this lead revealed that a faster route to indene exists and allowed to obtain good agreement between kinetic simulations and experimental data. This alternative pathway is characterized by a sigmatropic 1,5 H transposition in the  $C_5H_5$ - $C_5H_6$  adduct formed by the addition of  $cC_5H_5$  and cyclopentadiene followed by the beta-opening of one of the C5 rings. Successive reactions easily lead to the formation indene.

For this reason, we searched the  $C_{10}H_{10}$  PES for a reaction route characterized by a ring opening reaction that could lead to naphthalene or one of its precursors. The reaction pathway so located starts from the W2 intermediate described in the previous section and requires the formation of the intermediate tricyclic species W4. W2, in fact, can isomerize to well W4 through a cyclization reaction started by a H migration between the two tertiary carbons that is similar to that found by Melius et al. and that is typical of  $C_5H_5$  rings containing  $-CR(\cdot)-CHR-CR^I=CR^{II}$  moieties. This reaction has an activation energy with respect to W1 of 46.9 kcal/mol, which is comparable but lower than the barrier reaction that leads back to reactants favoring this pathway rather than the latter.

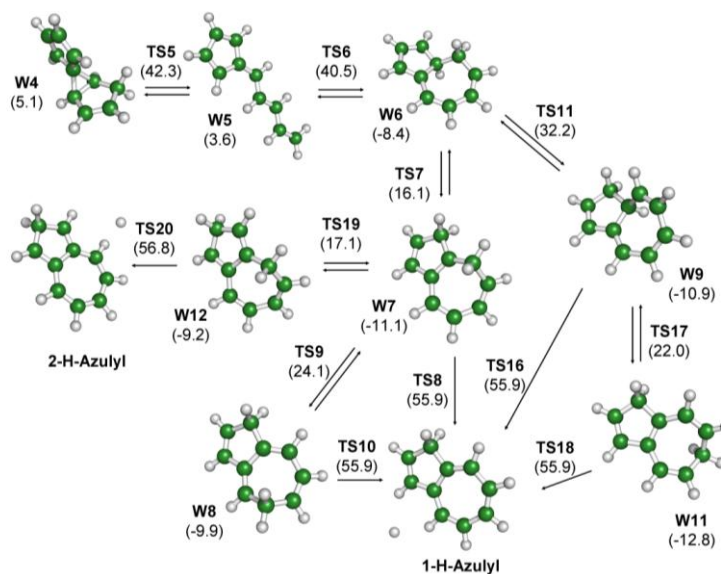


**Figure 60.** Potential energy surface of the *n*-H-azulyl mechanism. Energies, expressed in kcal/mol, were computed at the CBS-QB3 level.

The successive reaction pathway is depicted in **Figure 60** and is started by the conversion of W4 to W5 through the beta opening of the C5 ring. The reaction transition state, TS5, is stabilized by the establishment of conjugation between the  $\pi$  bonds of the surviving C5 ring and those of the linear chain. W5 can successively easily undergo a seven-member ring closure leading to 8,9-dihydroazulene (W6). W6 is further stabilized by H-transfer to the C5 ring, which leads either to W7 or W9 through 1,5 sigmatropic shifts since, differently from cyclopentadiene, 1,7 sigmatropic shifts are symmetry forbidden for cycloheptatriene. Successive hydrogen transfer reactions from W7 and W9 lead to W8 and W11, respectively. Also, W7 can easily isomerize to W12 through a 1,5 H migration on the C5 ring.

As it can be observed, all the bicyclic C5\_C7 wells are interconnected by saddle points having activation energies smaller than that leading back to W4, so that they are all likely to be accessed after W5 is formed. All the C5\_C7 intermediates can dissociate to either 1-H-azulyl or 2-H-azulyl and atomic hydrogen. The decomposition reaction pathways are all barrierless. It is also important to observe that the activation energy for decomposition to azulyl radicals is about 5 kcal/mol faster than decomposition of 1-H-fulvalenyl, making this reaction pathway potentially faster than that proposed by Melius et al.<sup>231</sup>.

Once formed, 1 and 2-H-azulyl radicals are known to straightforwardly interconvert through the spiran pathway to naphthalene, as it has been assessed by Alder et al.<sup>270</sup> in a review of the routes that connect azulene to naphthalene. For this reason, the proposed reaction pathway can be considered as a good candidate to be a direct mechanism for the formation of naphthalene by addition of two cyclopentadienyl radicals. The feasibility of this proposal can however be assessed only through a direct analysis of the reaction dynamics on the C<sub>10</sub>H<sub>10</sub> PES.

### 6.4.2. ME/RRKM Simulations

Master equation calculations of the reactivity on the  $C_{10}H_{10}$  PES accessed through the addition of two  $cC_5H_5$  radicals have been performed considering in the calculation all the reactions reported in **Figure 59** and **Figure 60**. The considered PES comprises 14 wells and 26 transition states. The master equation has been solved assuming that the bath gas is pure Argon adopting an exponential down model for the collisional energy transfer. In particular we used the Lennard-Jones collision parameters  $\sigma = 3.75 \text{ \AA}$  and  $\epsilon/k = 113 \text{ K}$  for Argon proposed by Hippler et al.<sup>217</sup>, while for all the  $C_{10}H_{10}$  species we used the same parameters ( $\sigma = 8.0 \text{ \AA}$  and  $\epsilon/k = 600 \text{ K}$ ) we have also adopted to study the reactivity on the  $C_{10}H_{11}$  PES. Due to the similarity between  $C_{10}H_{10}$  and  $C_{10}H_{11}$  isomers, we employed in the calculations the same mean downward energy transfer. All parameters used in the simulations, including vibrational frequencies, rotational constants, rotational symmetry numbers, optical isomer numbers, inertia moment, and rotational PESs for hindered rotors are reported as supplementary information of ref<sup>271</sup>.

The simulations performed between 1100 K and 2000 K show that the main reaction channel is decomposition to reactants in the whole temperature range investigated and that the azulyl reaction channel is dominant over the fulvalenyl pathway up to 1450 K. Above this temperature decomposition to fulvalenyl becomes faster than decomposition to azulyl. This behavior is determined by the fact that with the increase of the temperature the sum of the rates of the processes of decomposition to fulvalenyl becomes faster than the rate of access to the portion of the PES leading to the formation of azulyl, which bottleneck is given by TS4.

The analysis of the internal energy distribution among the states of the key wells, performed monitoring the time spent at each well in a specific energy bin, showed that in the conditions examined the energy has prevalently a Boltzmann distribution. This means that collisional stabilization is dominant in these conditions. A set of simulations performed at 1200 K at different pressures (0.01, 0.1, 1, and 10 bar) supports this conclusion, as the kinetic constants calculated for the four possible reactions channels exhibit only a slight dependence from the pressure. The maximum deviation with respect to the 1 bar data is in fact the increase of a factor of 1.3 observed for the rate of formation of the azulyl isomers, which can be ascribed to a slight depletion of the population of the highest energy levels. These conclusions indicate that an effective approach for the insertion of this reaction network in a kinetic mechanism would be to include all the elementary reactions here identified using high-pressure values. For this purpose, the forward and backward high-pressure kinetic constants for each reaction channel interpolated in the Arrhenius form are given in **Table 11**. However, if it is assumed that no well visited in the course of the reaction has a secondary reactivity it means that the kinetic constants here calculated are a good approximation of the overall rate of conversion of the reactants into azulyl and fulvalenyl radicals.

**Table 11.** High-pressure kinetic constants of the overall reacting system investigated interpolated between 1000 and 2000 K as  $k = A T^\alpha \exp(-E_a(\text{kcal/mol})/RT)$  in  $\text{s}^{-1}$  for unimolecular reactions and  $\text{cm}^3 \text{mol}^{-1} \text{s}^{-1}$  for bimolecular reactions.

Forward reaction	Log A	$\alpha$	Ea	Backward reaction	Log A	$\alpha$	Ea
$\text{C}_5\text{H}_5 + \text{C}_5\text{H}_5 \rightarrow \text{W1}$	7.87	1.46	1.467	$\text{W1} \rightarrow \text{C}_5\text{H}_5 + \text{C}_5\text{H}_5$	20.47	-1.55	55.440
$\text{W1} \rightarrow \text{W2}$	13.20	0.16	24.834	$\text{W2} \rightarrow \text{W1}$	12.25	0.33	27.349
$\text{W2} \rightarrow \text{1H-fulvalenyl} + \text{H}$	13.66	0.19	65.392	---	---	---	---
$\text{W2} \rightarrow \text{W3}$	12.11	0.37	21.606	$\text{W3} \rightarrow \text{W2}$	13.41	0.05	29.372
$\text{W3} \rightarrow \text{1H-fulvalenyl} + \text{H}$	13.46	0.35	72.946	---	---	---	---
$\text{W3} \rightarrow \text{W10}$	12.87	0.19	27.833	$\text{W10} \rightarrow \text{W3}$	12.41	0.32	26.627
$\text{W10} \rightarrow \text{1H-fulvalenyl} + \text{H}$	15.51	-0.23	72.417	---	---	---	---
$\text{W10} \rightarrow \text{2H-fulvalenyl} + \text{H}$	16.63	-0.45	79.354	---	---	---	---
$\text{W10} \rightarrow \text{W13}$	12.69	0.24	27.455	$\text{W13} \rightarrow \text{W10}$	12.42	0.31	26.574
$\text{W13} \rightarrow \text{2H-fulvalenyl} + \text{H}$	16.04	-0.32	76.356	---	---	---	---
$\text{W10} \rightarrow \text{W14}$	13.05	0.15	28.710	$\text{W14} \rightarrow \text{W10}$	12.35	0.31	22.490
$\text{W14} \rightarrow \text{2H-fulvalenyl} + \text{H}$	14.34	0.05	70.323	---	---	---	---
$\text{W14} \rightarrow \text{W2}$	12.50	0.29	27.237	$\text{W2} \rightarrow \text{W14}$	12.33	0.34	26.870
$\text{W2} \rightarrow \text{W4}$	10.66	0.76	49.533	$\text{W4} \rightarrow \text{W2}$	13.64	0.27	43.555
$\text{W4} \rightarrow \text{W5}$	14.27	0.04	38.981	$\text{W5} \rightarrow \text{W4}$	11.12	0.34	38.243
$\text{W5} \rightarrow \text{W6}$	11.01	0.33	36.544	$\text{W6} \rightarrow \text{W5}$	13.69	0.16	50.885
$\text{W6} \rightarrow \text{W7}$	11.93	0.39	24.760	$\text{W7} \rightarrow \text{W6}$	12.06	0.25	27.538
$\text{W7} \rightarrow \text{1H-azulyl} + \text{H}$	20.89	-1.75	71.064	---	---	---	---
$\text{W7} \rightarrow \text{W8}$	11.36	0.45	35.378	$\text{W8} \rightarrow \text{W7}$	11.37	0.47	34.305
$\text{W8} \rightarrow \text{1H-azulyl} + \text{H}$	19.26	-1.31	68.787	---	---	---	---
$\text{W7} \rightarrow \text{W12}$	12.00	0.26	28.559	$\text{W12} \rightarrow \text{W7}$	11.94	0.33	26.524
$\text{W12} \rightarrow \text{2H-azulyl} + \text{H}$	16.09	-0.48	68.211	---	---	---	---
$\text{W6} \rightarrow \text{W9}$	11.28	0.45	40.702	$\text{W9} \rightarrow \text{W6}$	11.35	0.44	43.294
$\text{W9} \rightarrow \text{1H-azulyl} + \text{H}$	11.84	0.66	75.960	---	---	---	---
$\text{W9} \rightarrow \text{W11}$	11.33	0.46	33.221	$\text{W11} \rightarrow \text{W9}$	11.45	0.42	34.937
$\text{W11} \rightarrow \text{1H-azulyl} + \text{H}$	17.47	-0.96	68.594	---	---	---	---

The kinetic constants so determined are sketched in **Figure 61** and are reported in **Table 12**.

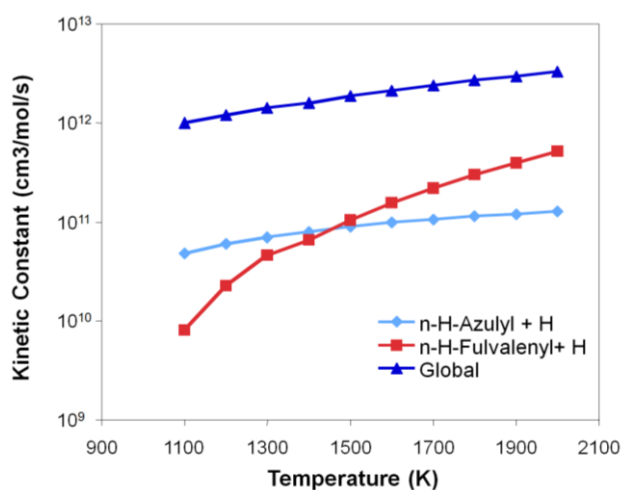


**Figure 61.** Kinetic constants [ $\text{cm}^3 \text{mol}^{-1} \text{s}^{-1}$ ] calculated at 1 bar for the reaction between  $c\text{C}_5\text{H}_5$  and  $c\text{C}_5\text{H}_5$ . The kinetic constant for the decomposition to reactants is not reported as it is almost superimposed to the global kinetic constant, which is equal to the high-pressure rate of the entrance channel.

**Table 12.** Kinetic constants for the reaction between  $cC_5H_5$  and  $cC_5H_5$  interpolated between 1100 and 2000 K as  $k = AT^\alpha \exp(-Ea(\text{cal/mol})/RT)$  in  $\text{cm}^3 \text{mol}^{-1} \text{s}^{-1}$ .

Reaction	Log A	$\alpha$	Ea (cal/mol)
$cC_5H_5 + cC_5H_5 \rightarrow \text{n-H-Azulyl} + \text{H}$	14.72	-0.853	7254.
$cC_5H_6 + cC_5H_5 \rightarrow \text{n-H-Fulvalenyl} + \text{H}$	10.30	0.951	15793.

In order to check the impact of a change of the rate of the H loss channels within the range of its uncertainty a specific set of simulations has been performed increasing all H loss rates by a factor of 3. Simulations have been performed at 1400 K and 1 bar. It has been found that the rate of both reaction channels increases, and in particular that the rate of the fulvalenyl channel increases by a factor of 3, and that the ratio of the reaction fluxes of the two reaction channels changes by a factor of 2 in favor of the fulvalenyl channel (from 1.2 to 0.6). Similar results with opposite trends would be expected if the H loss rates were decreased.

## 6.5. Comparisons between Model Predictions and Experimental Data

The kinetic parameters for the critical interactions of cyclopentadiene and cyclopentadienyl radical reported in **Table 10** and those corresponding to the reaction between two cyclopentadienyl radicals reported in **Table 12** have been included in the overall kinetic model POLIMI\_1202.<sup>261</sup>

The kinetic constants and products of each reaction channel were however slightly modified as follows to make the agreement with experimental data quantitative. First it has been assumed that vinylfulvene converts rapidly to styrene, as suggested at the end of the  $cC_5H_5 + cC_5H_6$  section, and the rate of this reaction channel was increased by factor of 2. The increase of the rate of the styrene channel is consistent with the fact that all simulations were performed with the CCSD(T) extrapolated energies, which are systematically higher than the ROCBS-QB3 energies used for the reaction bottlenecks of the other channels. The reason behind this choice is that we were not able to calculate the ROCBS-QB3 energy for this reaction for the reasons mentioned in section 6.3.1. A decrease of 1-2 kcal/mol of the activation energy of TS28 would easily translate to an increase in the rate of this channel by a factor of about 2 in the investigated temperature range. Then, it was assumed that phenylbutadiene rapidly decomposes with equal probability to benzene and styrene, as motivated at the end of the previous section.

Though a detailed list of the kinetic parameters used in the simulations is reported in POLIMI\_1202, it is here interesting to highlight that the kinetic constant for naphthalene production through the recombination of two  $cC_5H_5$  radicals used in the simulations,  $10^{12} \cdot \exp(-3020/T(\text{K})) \text{ cm}^3/\text{mol/s}$ , is similar to the value used by Robinson and Lindstedt<sup>272</sup> ( $2.5 \cdot 10^{12} \cdot \exp(-4174/T(\text{K})) \text{ cm}^3/\text{mol/s}$ ) to simulate the same experimental data set. At 1200 K, the temperature at which most experiments were performed, the two kinetic constants are almost equal ( $8.1 \cdot 10^{10}$  vs

$7.7 \cdot 10^{10} \text{ cm}^3/\text{mol/s}$ ). These rate constants yield a calculated naphthalene concentration that is in good quantitative agreement with experimental data, thus defining a consensus value for the rate of a reaction whose initial value, first proposed in 1996, was about one order of magnitude higher.<sup>244,245</sup> Model predictions with the upgraded kinetic parameters are here compared with two different sets of recent experimental measurements. The former set relates to the cyclopentadiene pyrolysis in a flow reactor operating between 800-1200 K.<sup>250</sup> The second is a study of cyclopentadiene pyrolysis and oxidation of Butler and Glassman<sup>249,273</sup> in Princeton's adiabatic, atmospheric pressure flow reactor.

### 6.5.1. Pyrolysis in Georgia Flow Reactor

Kim et al.<sup>250</sup> studied the pyrolysis of cyclopentadiene from 800 K up to 1200 K in a laminar flow reactor, 48 cm long and 1.7 cm in diameter, at a nominal residence time of 3 s. Nitrogen was used as a carrier gas, and the gas stream entering the reactor consisted of 0.7% molar  $\text{C}_5\text{H}_6$  in nitrogen. The gas temperature in the reaction zone of  $\sim 30$  cm was nearly constant ( $\pm 10$  K of the set value) and radial variation of temperature was negligible. These experimental data support the pyrolytic growth and constitute a useful test for the kinetic modeling of polycyclic aromatics via  $\text{C}_5\text{H}_5$  recombination and addition reactions. Benzene, indene, and naphthalene were the major pyrolysis products. **Figure 62** shows the good comparisons between experimental measurements and model predictions versus the reactor temperature at  $\sim 3$  s.

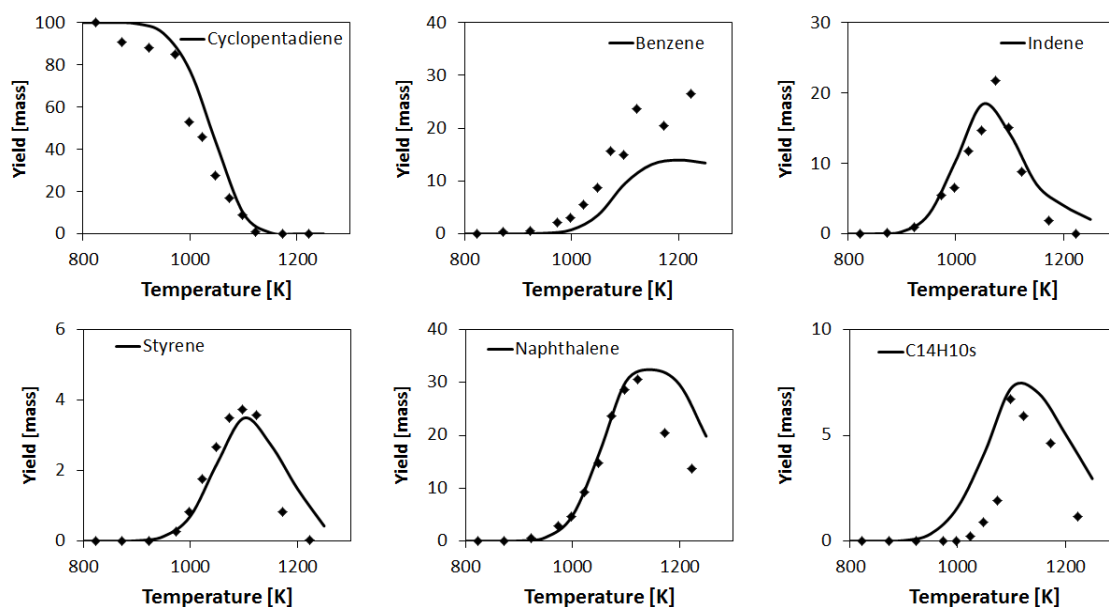


**Figure 62.** Cyclopentadiene conversion and yields of major aromatic products versus reactor temperature.<sup>250</sup>

The model correctly predicts naphthalene, indene, and styrene properly locating their maximum yields. The profiles of these species highlight the importance of the parallel and successive reactions involving  $cC_5H_5$  and heavy molecules and radicals. Phenanthrene is here considered as a lumped species  $C_{14}H_{10}$  grouping also anthracene. At moderate cyclopentadiene conversions (<50%), the main reaction channel for its formation is the recombination of  $cC_5H_5$  with indenyl radicals, which has been implemented in the kinetic mechanism using the same kinetic parameters of the similar  $cC_5H_5$  radical recombination reaction:  $10^{12} \cdot \exp(-3000/T(K)) \text{ cm}^3/\text{mol}\cdot\text{s}$ .

At higher temperatures and cyclopentadiene conversions, also the reactions of  $cC_5H_5$  and indenyl radicals with naphthalene and naphthyl radicals contribute to phenanthrene formation. The maximum yield of phenanthrene correctly peaks at  $\sim 7\%$ , whilst in the previous kinetic scheme<sup>[44]</sup>, where higher kinetic values were assumed for the recombination reactions of resonantly stabilized radicals, there was an over prediction by a factor of  $\sim 2$

### 6.5.2. Pyrolysis and Oxidation Study in Princeton Flow Reactor

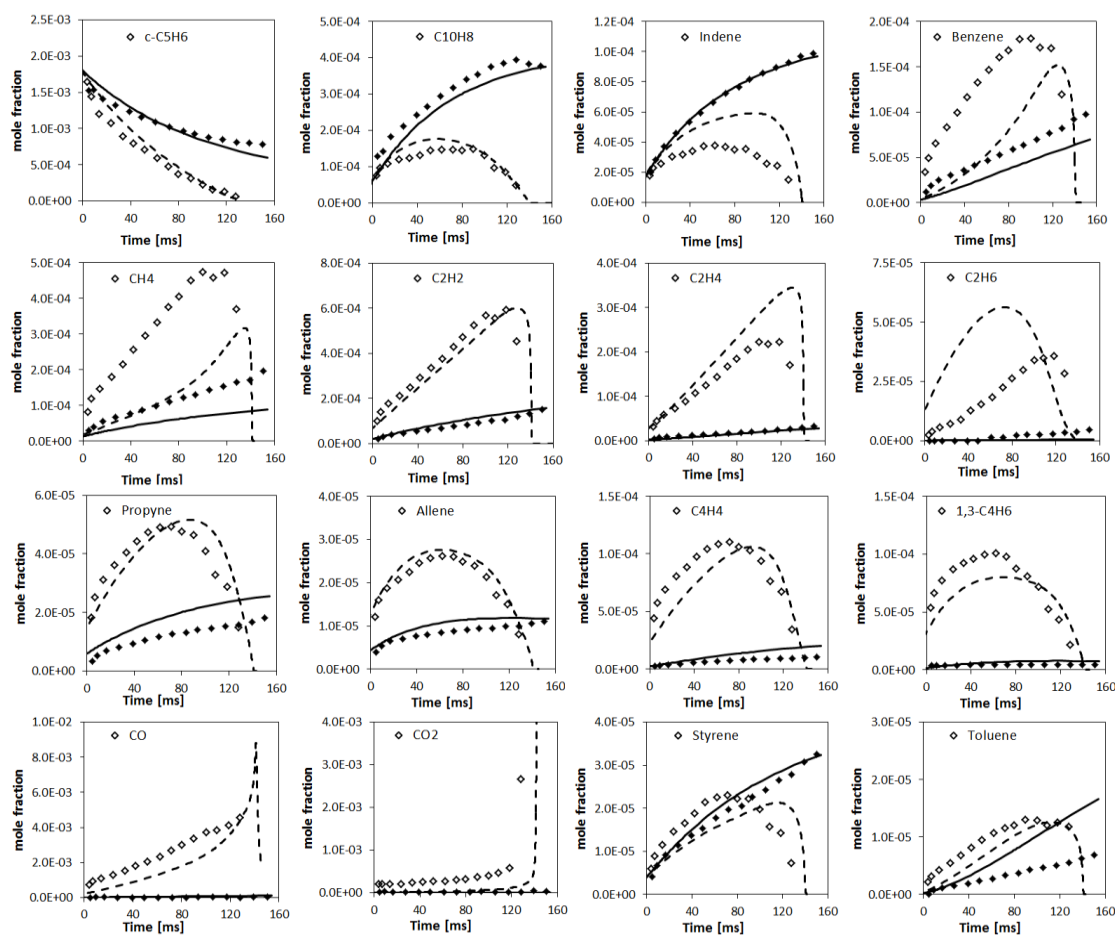


**Figure 63.** Concentration profiles of major species for the pyrolysis (lines and filled symbols) and oxidation at  $\Phi \sim 1$  (dashed lines and empty symbols) of cyclopentadiene.<sup>249,273</sup> (Experimental runs #7 and #12. Initial temperature = 1190-1200 K, initial fuel =  $\sim 2000$  ppmv.)

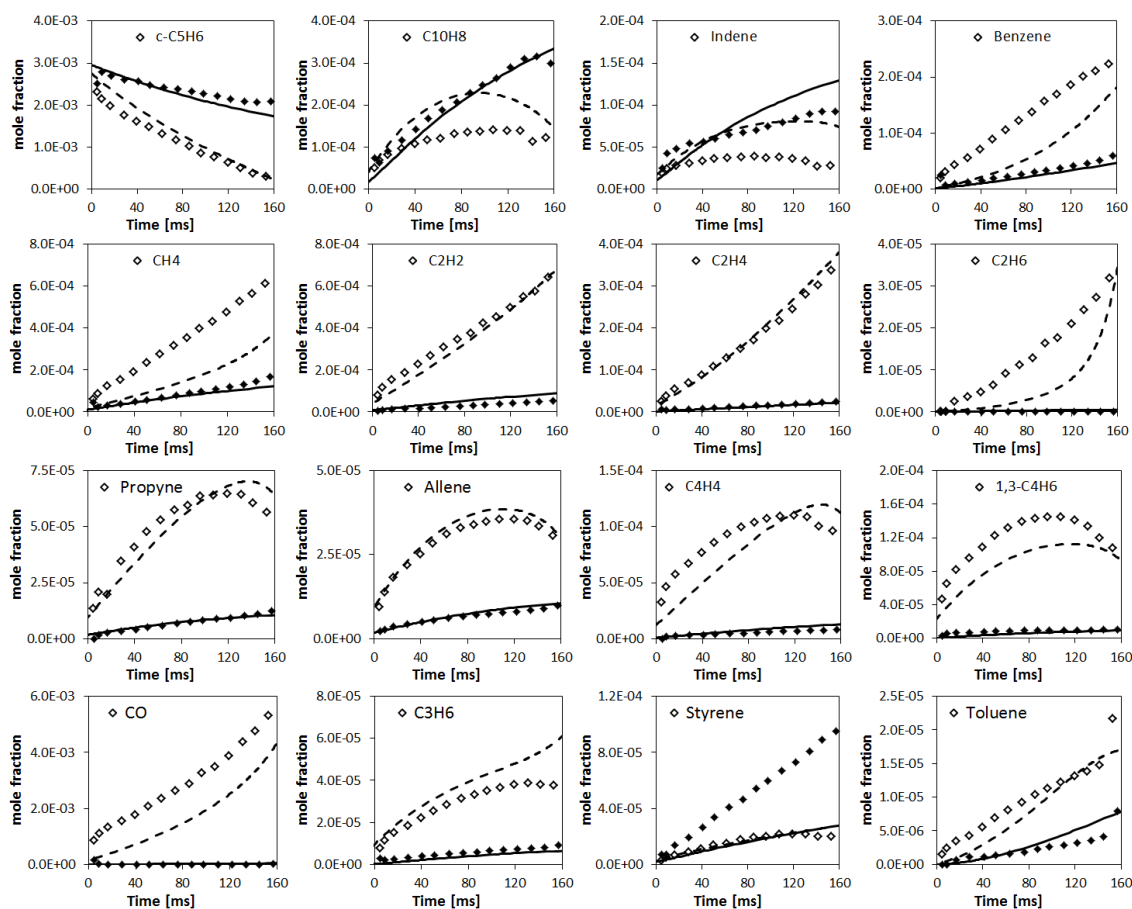


**Figure 64.** Concentration profiles of major species for the pyrolysis (lines and filled symbols) and oxidation at  $\Phi = \sim 1$  (dashed lines and empty symbols) of cyclopentadiene.<sup>249,273</sup> (Experimental runs #3 (a) and #10 (b). Initial temperature =  $\sim 1150$  K, initial fuel =  $\sim 3000$  ppmv.)

Butler and Glassman<sup>249,273</sup> analyzed several pyrolysis and oxidation conditions by varying the concentration, equivalence ratio, and initial temperature in the Princeton flow reactor. The change of the equivalence ratio, from pyrolysis to oxidation conditions, had the largest effect on the reaction products, while the concentration change had only a minor impact. Under all conditions, the growth of the molecular weight confirms the significant role of recombination and condensation reactions of  $cC_5H_5$ .

**Figure 63** and **Figure 64** compare four sets of experimental measurements and model predictions in pyrolysis and oxidation conditions. Note that, following usual practice employed for comparison with Princeton flow reactor data, predicted mole fraction profiles are shifted by 20 ms in order to match the fuel conversion. This approach and similar corrections, due to non-ideal reactant mixing, were discussed and verified both numerically and experimentally in the literature.<sup>274</sup>

Model predictions agree well with the experimental measurements, mainly in pyrolysis conditions, while the model seems to underestimate slightly the consumption of cyclopentadienyl radi-

cals in the oxidation environment. Therefore, the initial formation of naphthalene and indene is partially over predicted, with a corresponding under prediction of CO and methane, mainly at intermediate decomposition. The interactions of  $cC_5H_5$  with oxygen and oxygenated radicals, systematically discussed by Robinson and Lindsted,<sup>272</sup> could thus require a further revision.

Finally, **Figure 65** shows a simple reaction path analysis in pyrolysis conditions. The thermal decomposition of cyclopentadiene with H formation accounts for 10.5% and the dominant H abstraction reactions to form cyclopentadienyl radicals  $\sim 71\%$ . The thermal decomposition to form  $C_2H_2$  and  $C_3H_4$ s accounts for 3.7%. The recombination reaction of cyclopentadienyl radicals to form naphthalene explains more than 50% of the overall decomposition. The interactions of  $cC_5H_5$  radical with cyclopentadiene to form indene (12.4), styrene (2.8), and benzene (2.4) also play a relevant role in this system. As already mentioned, further interactions of cyclopentadienyl radical with indene, naphthalene, and mainly indenyl radical, explain the successive formation of heavier species, like phenanthrene, anthracene, and pyrene.

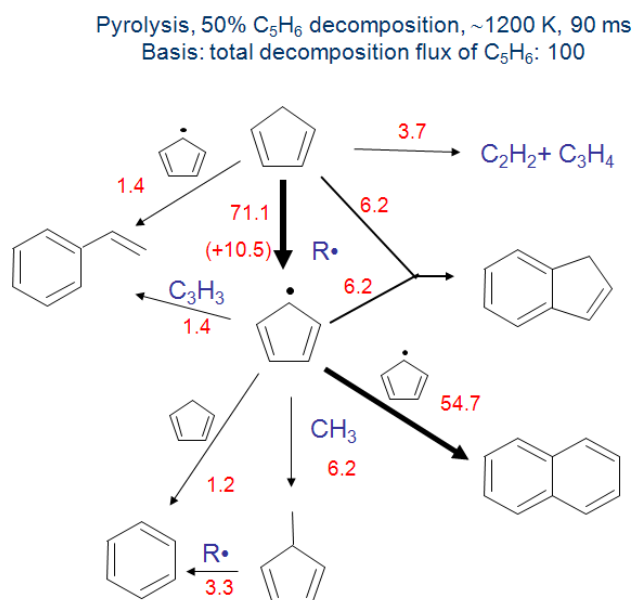


**Figure 65.** Major reaction paths of cyclopentadiene pyrolysis at 1200 K and 50% conversion. Conditions of experimental run #12.<sup>249</sup>

## 6.6. Concluding Remarks

The purpose of this work was to improve our understanding of the gas phase reactivity of the cyclopentadienyl radical through the study of the kinetics of cyclopentadiene pyrolysis. A preliminary analysis showed that the key to the comprehension of this system is the evaluation of the rate constants of the reaction between the cyclopentadienyl radical and cyclopentadiene and the self-recombination of cyclopentadienyl radical.

Our investigation of the PES of the  $C_5H_5 + C_5H_6$  reaction revealed that the preferred reaction mechanism requires the  $\beta$  opening of one of the two C5 rings of the adduct, which is formed by the addition of  $cC_5H_5$  to  $cC_5H_6$ . This reaction pathway, facilitated by an H migration to a carbon center that allows conjugation between the  $\pi$  bonds of the two C5 rings in the transition state, is both entropically and energetically favored over alternative mechanisms involving the formation of tricyclic species as intermediates.

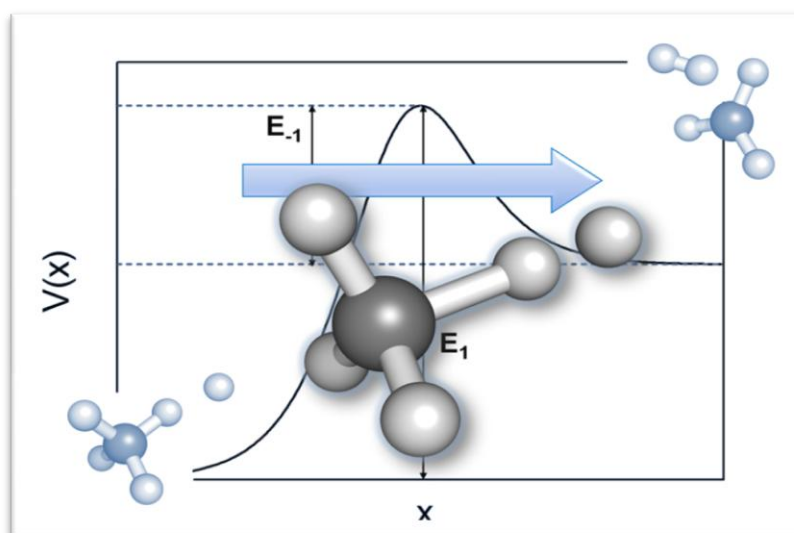
The master equation simulations performed over the  $C_{10}H_{11}$  PES revealed that the favored reaction channel is decomposition to reactants, a reaction pathway often ignored in the analysis of the feasibility of reaction mechanisms requiring intramolecular rearrangements over complex PESs. The major reaction product is indene up to 1700 K. Above this temperature vinylfulvene, a most probable styrene precursor, becomes the dominant species. The calculated rate constant for the production of indene allows quantitative fitting of the experimental data for two different sets of measurements.

Moreover, a new mechanism has been proposed for the conversion of two cyclopentadienyl radicals into naphthalene, which is characterized by a beta-opening reaction, facilitated by a stabilization effect due to conjugation, and by the formation of azulyl radicals as reaction products. As known, the conversion of azulyl to naphthalene is a relatively fast process, so that the mechanism here proposed is an effective route for the formation of naphthalene.

The channel specific rate constants calculated integrating the master equation are in good agreement with literature data that fit well naphthalene concentrations measured during cyclopentadiene pyrolysis and oxidation at 1200 K. Our calculations predict that above 1450 K the dominant reaction product is the fulvalenyl radical, in agreement with other theoretical studies. However, the fate of the fulvalenyl radical is uncertain, as it has been recently proposed that its main reaction channel is decomposition to fulvalene. If the reaction mechanism here proposed is the dominant pathway of formation of naphthalene from  $cC_5H_5$  precursors, it becomes thus interesting to understand what is likely to be the main reaction pathway for fulvalene, whether decomposition to reactants through an inverse pathway or as a building block for PAH growth.

# 7 Quantum Tunneling in Hydrogen Transfer Reactions: A Study on the $\text{CH}_4 + \text{H}$ Reaction

---



## 7.1. Introduction

Hydrogen transfer reactions and more generally hydrogen abstractions, hydrogen shifts, or isomerizations play a relevant role in a large variety of chemical and biochemical processes, such as combustion chemistry, peptide rearrangements, and radical polymerization. For example, in the combustion of hydrocarbons, both isomerizations via intramolecular hydrogen transfer and hydrogen abstraction reactions are important classes of alkyl radical reactions. Thus, the determination of the rate coefficients of these reactions is a prerequisite for the modeling of combustion devices, such as engines and furnaces operating with hydrocarbon fuel.

Despite the importance of hydrogen transfer reactions, few data on the kinetics of these reactions are available in literature. The difficulties related to the experimental investigation of hydrogen transfer reactions are mainly due to the high instability of the produced intermediates that complicates the direct measurement of their reaction rates. In these complex processes, for which a theoretical investigation of the kinetics is often necessary to interpret experimental evidences, computational studies represent a new tool for the determination of the rate coefficients of hydrogen transfer reactions.

However, a critical aspect characterizes the theoretical analysis of the reactivity of these reactions, which is the evaluation of the tunneling contribution to the rate constant. Quantum tunneling, in fact, is a common feature of all reactions involving hydrogen atom transfers. When active, the hydrogen atom is able to tunnel through the energetic barrier, because its small mass is associated with a wavelength comparable to the barrier width typical of such transfer reactions. For example, the role of quantum tunneling in alkyl radical isomerizations has been recently highlighted by Tsang and co-workers.<sup>275-277</sup> In particular, they concluded that a large body of literature data at low-temperatures (with small pre-exponential factors and activation energies) could be reconciled with high-temperature data by taking into account the quantum tunneling correction.<sup>278</sup>

A number of methods have been developed to determine the tunneling effect contribution in reaction rates estimation. Among these, one of the most popular is the method proposed by Eckart.<sup>87</sup> This approach is based on the solution of the 1D Schrödinger equation in which the potential has been described with a functional form able to approximate the shape of the potential energy barrier and its asymptotic properties. Notably, Eckart not only proposed such a functional form, but also provided the analytical solution of the associated Schrödinger equation, leading to the formulation of a relatively simple expression for the microcanonical transmission probability.

Lately, Truhlar and coworkers proposed a new theory named Small Curvature Tunneling theory (SCT), which is currently probably the most effective approach for the calculation of accurate quantum tunneling effects.<sup>90</sup> This theory came as an extension of the idea proposed by Marcus and Coltrin.<sup>88</sup> Briefly, they demonstrated that the integration of the 1D Schrödinger equation over the standard transition state theory path, which is the minimum energy path (MEP), leads to significant underestimations of the tunneling coefficient. Thus, to explain this effect they proposed for the H + H<sub>2</sub> reaction an alternative path called tunneling path, that is removed from the MEP by an orthogonal displacement equal to the maximum vibrational amplitude. Truhlar and co-workers successively extended this path to a multi-atomic system using the generalized harmonic vibrational frequencies obtained following the reaction path Hamiltonian proposed by Miller, Handy and Adams.<sup>89</sup>

More accurate theories based on quantum dynamics simulations have been proposed in the literature.<sup>279</sup> However, these theories require as input a large number of *ab initio* data as it is necessary to span a wide range of configurational space and are therefore unfeasible for reacting systems with more than 6 atoms.

Comparing the Eckart model and SCT theory the latter is deemed to be more reliable between the two especially at lower temperatures (300 – 800 K); Eckart corrections come close to the SCT values only at higher temperatures. For this reason the Eckart model is usually adopted to correct the rate coefficients of the many hydrogen transfer reactions encountered in combustion systems, which significance increase at high temperatures (>800 K). The same however cannot be said for

example for polymerization systems; in fact, intramolecular hydrogen transfer reactions (in this field also known as back-biting reactions) play a major role in these chemical processes, that are characterized by a very high reactivity, which means that polymerizations occur at relatively low temperature (300 – 400 K). In order to address both problems, we have implemented in our code as described in the Method chapter both approaches: the Eckart model and SCT theory.

In this chapter however we will appraise the ability of the SCT method to adequately correct the rate coefficients of hydrogen transfer reactions and for this purpose we revisited the reactivity of a fundamentally important reaction, namely the  $\text{CH}_4 + \text{H} \rightarrow \text{CH}_3 + \text{H}_2$  reaction.

The  $\text{CH}_4 + \text{H} \rightarrow \text{CH}_3 + \text{H}_2$  reaction and its reverse have served as a prototype reaction involving a polyatomic molecule and have played an important role in the theoretical and experimental development of chemical kinetics. Thermal rate constants for both the forward and reverse reactions have been measured by different groups since the late 1950's; however, when compared also large discrepancies can be detected. In order to overcome these ambiguities, which could affect the correct measurements of other important reactions, in 2001 Sutherland et al.<sup>280</sup> measured directly the rate coefficient performing a Laser Photolysis-Shock Tube experiment coupled with H-atom ARAS detection on a wide temperature range (928 – 1697 K). Then they extended it to a larger temperature range (348 – 1950 K) introducing in their fitting procedure also the data of seven previous studies. The result of their work is shown in **Figure 66** and is compared with earlier literature data.<sup>281-298</sup>

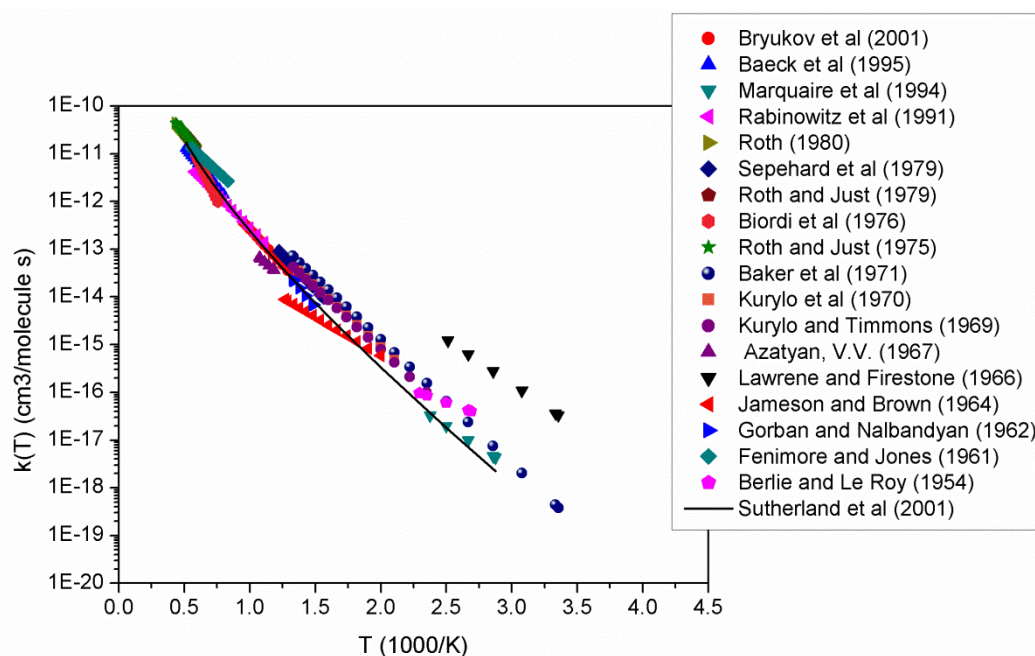


**Figure 66.** Experimental literature rate coefficients for the  $\text{CH}_4 + \text{H}$  reaction.

Given its relatively simple nature, the  $\text{CH}_4 + \text{H}$  reaction has been used also as an important benchmark system in a number of theoretical investigations. These include studies using various

forms of classic transition state theory with tunneling corrections,<sup>299-305</sup> as well as more sophisticated quantum transition state approaches.<sup>306,307</sup> A number of quantum dynamics studies have also been focused on this reaction to test the ability of such methods to treat reactions involving polyatomic molecules. Among these we found full dimensional quantum dynamics studies, such as the multi-configurational time dependent Hartree (MCTDH) method,<sup>307-311</sup> or the alternative approach that has been recently introduced as ring polymer molecular dynamics<sup>312</sup> (RPMD) which is an approximate quantum mechanical method able to address much larger systems. Next to these are quantum dynamics and quantum reaction scattering treatments with reduced dimensionality.<sup>313-320</sup>

In this work, we calculated the rate of the  $\text{CH}_4 + \text{H}$  reactions adopting transition state theory with the tunneling correction evaluated with the SCT theory. We carried out a number of calculations in order to assess the reliability of the SCT code implemented; we analyzed in particular the effect that the method, the basis set, the number and the spacing of the points used to calculate the potential energy surface, the gradient and the hessian have on the final result. We then compared our results with the recommended value of Sutherland et al.<sup>280</sup> and with the results obtained adopting other more accurate theoretical approaches.

## 7.2. Computational Methodology

The geometries and vibrational frequencies of the stationary points (reactants, products and transition states) were optimized using different methods and basis sets. Given the recent development of new DFT methods, which are able to recover the effect of dispersion interactions, we choose to investigate the outcome of several different DFT methods and in particular, we focused on the popular B3LYP<sup>17,18</sup> and the new MPW1PW91,<sup>321</sup> BMK,<sup>322</sup> WB97XD<sup>323</sup> and M062X<sup>19</sup> functionals. For completeness, also calculations at the MP2 level<sup>324</sup> were carried out. In addition, also the effect of the basis set has been investigated. Specifically, we compared the results obtained at the 6-311+G(2d,2p)<sup>325,326</sup> level with those obtained with the Dunning aug-cc-pVTZ basis set.<sup>327</sup> The activation energy of the title reaction was calculated also with Coupled Cluster theory<sup>15</sup> specifically at the CCSD(T)/aug-cc-pVTZ and CCSD(T)/aug-cc-pVQZ levels and then extrapolated to the infinite basis set limit (CBS) adopting Martin's extrapolation procedure.<sup>136</sup>

The minimum energy path was obtained using two different algorithms that are implemented in the last version of Gaussian 09. The Hessian-based Predictor-Corrector (HPC) integrator,<sup>328,329</sup> which is a very accurate algorithm that uses the Hessian-based local quadratic approximation as the predictor component and a modified Bulirsch-Stoer integrator for the corrector portion and the LQA algorithm,<sup>99,330</sup> which uses the local quadratic approximation for the predictor step. Moreover, also minimum energy path calculations were performed adopting all the methods previously men-

tioned: B3LYP, MPW1PW91, BMK, WB97XD, M062X and MP2. For each of these methods we calculated the minimum energy path with two basis sets: 6-311+G(2d,2p) and aug-cc-pVTZ. Generally, all internal reaction coordinate (IRC) calculations were carried out in mass weighted Cartesian coordinates with a step size of 0.01 amu<sup>1/2</sup>bohr and a maximum distance from the TS of 1 amu<sup>1/2</sup>bohr in both directions.

The tunneling correction factor was evaluated using the small curvature tunneling method. A detailed description of the theory and its implementation is given in section 3.3.4 of Chapter 3.

Since the calculation of tunneling correction factors using SCT theory requires information on the curvature of the reaction path, the rate coefficients were also calculated within the canonical variational transition state theory (CVT/SCT) that is given by:<sup>331</sup>

$$k^{CVT}(T) = \min_s k^{GT}(T, s) \quad (140)$$

where

$$k^{GT}(T, s) = \frac{k_B T}{h} \frac{Q^{GT}(T, s)}{Q^R(T)} \exp\left(-\frac{V_{MEP}(s)}{RT}\right) \quad (141)$$

Here  $k^{GT}(T, s)$  is the generalized transition state theory rate constant at the dividing surface  $s$ ,  $k_B$  is the Boltzmann's constant,  $h$  is the Planck's constant,  $Q^R(T)$  is the reactants partition function per unit volume,  $Q^{GT}(T, s)$  is the partition function of a generalized transition state at  $s$  and  $V_{MEP}(s)$  is the classical potential energy along the MEP with the zero of energy at the reactants.

All calculations were performed with the Gaussian 09 program suite.<sup>2</sup>

### 7.3. Sensitivity Analyses

To assess the reliability and robustness of the SCT theory implemented we carried out an exploratory analysis on the effect that several parameters have on the predicted rate coefficient.

One of our goals was to determine how the accuracy of different levels of *ab initio* theory might affect the final rate coefficient, in terms of both electronic structure method and basis set typology and size. The level of *ab initio* theory plays a role on various aspects of the rate coefficient prediction. Firstly, the choice of *ab initio* theory establishes the accuracy of the geometries, vibrational frequencies and energies of the reactants and transition state, which determine the accuracy of the TST rate coefficient. Secondly, the theory level may affect significantly the accuracy of the SCT tunneling correction.

As described in the method section, SCT calculations need information about the energy, the gradient and the hessian along the MEP in order to compute the curvature and the generalized vibrational frequencies along the reaction path. Initial SCT calculations showed how both parameters are very sensitive to the precision of the input data (energy, gradient and hessian). Therefore, we

decided to investigate the role that electronic structure methods and basis sets play on the accuracy of the minimum energy path and its properties.

IRC calculations, moreover, are characterized by other input parameters, such as the step size and the number of points considered along the path, which were investigated. Lastly, as Gaussian gives the possibility to choose among several reaction path following algorithms, we explored also the possibility to use a different method than the one given as default (HPC).

### 7.3.1. Level of *Ab Initio* Theory

#### Electronic Structure Methods

Six electronic structure methods were tested for the calculation of the SCT correction factor as a function of temperature; five of them are DFT based methods while the sixth is MP2 theory, the simplest post Hartree-Fock based method that takes into account electronic correlation through a second order perturbation of the Hamiltonian.

First, it is interesting to evidence the accuracy of each method in predicting the activation energy of the title reaction. The activation energies without the zero point energy (ZPE) correction obtained adopting a 6-311+G(2d, 2p) basis set are compared with the value obtained at the CCSD(T)/CBS level in **Table 13**.

**Table 13.** Activation energies (kcal/mol) without ZPE correction of the  $CH_4 + H$  reaction calculated with different electronic structure methods adopting the 6-311+G(2d,2p) basis set.

	<b>B3LYP</b>	<b>BMK</b>	<b>MPW1PW91</b>	<b>WB97XD</b>	<b>M062X</b>	<b>MP2</b>	<b>CCSD(T)/CBS</b>
$E_A$	9.74	15.50	12.10	13.70	15.72	18.87	14.80

It is evident from the energy results that both B3LYP and MP2 fail to describe correctly the energy barrier of the title reaction. Only the DFT methods BMK, WB97XD and M062X, which include dispersion effects, are comparable with CCSD(T)/CBS being within  $\pm 1$  kcal/mol of its value.

**Table 14.** CVT/SCT rate coefficients for the  $CH_4 + H$  reaction calculated using different electronic structure methods and adopting the 6-311+G(2d,2p) basis set compared with the suggested value of Sutherland et al.<sup>280</sup>

<b>T (K)</b>	<b>B3LYP</b>	<b>BMK</b>	<b>MPW1PW91</b>	<b>WB97XD</b>	<b>M062X</b>	<b>MP2</b>	<b>Sutherland</b>
250	3.11E-17	1.06E-21	3.29E-19	2.88E-20	1.91E-21	5.85E-25	5.56E-21
300	2.53E-16	4.45E-20	5.79E-18	6.69E-19	5.96E-20	5.39E-23	1.87E-19
350	1.29E-15	7.77E-19	5.07E-17	7.42E-18	8.67E-19	1.76E-21	2.47E-18
400	4.75E-15	7.31E-18	2.80E-16	4.99E-17	7.29E-18	2.79E-20	1.82E-17
500	3.33E-14	1.90E-16	3.44E-15	8.29E-16	1.75E-16	1.74E-18	3.33E-16

These results are reflected also on the predicted rate coefficients calculated with the same levels of theory in the 250-500 K temperature range, which are compared in **Table 14** with the values suggested by Sutherland et al.<sup>280</sup> based on experimental evidences.

As expected, the methods that failed to describe correctly the activation energy, B3LYP and MP2, also fail in the prediction of the rate coefficient. In particular, B3LYP largely overestimates the value suggested by Sutherland et al. and this is easily ascribed to the underestimation of the activation energy (9.74 vs 14.80 kcal/mol). The same can be said about the results obtained at the MP2/6-311+G(2d,2p) level, where in the specific case the activation energy overestimates the reference value by 4 kcal/mol. It is noteworthy to point out that a difference of 5 kcal/mol in the activation energy, for the temperature range considered here, leads to a difference in the rate coefficient ranging from 4 orders of magnitude at 250 K to 2 orders of magnitude at 500 K.

The MPW1PW91 DFT functional underestimates the activation energy of about 2.7 kcal/mol and this leads to an overestimation of the rate coefficient of a factor of 60 at 250 K that is reduced to a factor of 10 at 500 K. Among the other DFT methods, which activation energies were within 1 kcal/mol of the reference value, we found different results. BMK underestimates the rate coefficient by a factor of 5 going down to a less than factor 2 at 500 K, while WB97XD overestimates Sutherland et al. values by a factor of 5 at 250 K going to a factor of 2 at 500 K. The rate coefficient predicted with M062X, finally, also underestimates the rate coefficient given by Sutherland et al. with a maximum deviation of a factor of 3 at 300 K.

From these results we have assessed that the activation energy has a major influence on the results. In order to remove the effect given by the accuracy of the activation energy we calculated the rate coefficients with the different methods using the activation energy calculated at the CCSD(T)/CBS level for all of them. The results are reported in **Table 15**.

**Table 15.** CVT/SCT rate coefficients for the CH<sub>4</sub> + H reaction calculated using different electronic structure methods adopting the 6-311+G(2d,2p) basis set for structures, vibrational frequencies and ZPE. The CCSD(T)/CBS activation energy was adopted for all cases. Results are compared with the suggested values of Sutherland et al.<sup>280</sup>

T (K)	B3LYP	BMK	MPW1PW91	WB97XD	M062X	MP2	Sutherland
250	1.19E-21	4.44E-21	1.42E-21	3.10E-21	1.13E-020	3.85E-20	5.56E-21
300	5.29E-20	1.47E-19	6.18E-20	1.05E-19	2.63E-019	5.58E-19	1.87E-19
350	9.03E-19	2.16E-18	1.03E-18	1.51E-18	3.09E-018	4.85E-18	2.47E-18
400	8.25E-18	1.79E-17	9.29E-18	1.24E-17	2.22E-017	2.86E-17	1.82E-17
500	2.06E-16	3.89E-16	2.26E-16	2.72E-16	4.28E-016	4.46E-16	3.33E-16

Using an activation energy evaluated at a higher level leads to a general improvement of the results; however, some differences can still be evidenced and they are largely ascribed to the differences found in the SCT tunneling correction, that are presented in **Table 16**.

**Table 16.** SCT tunneling corrections evaluated using different electronic structure methods adopting the 6-311+G(2d, 2p) for the  $\text{CH}_4 + \text{H}$  reaction.

T (K)	B3LYP	BMK	MPW1PW91	WB97XD	M062X	MP2
250	10.79	35.70	16.02	23.85	59.89	276.51
300	4.99	12.64	6.99	8.67	15.84	43.60
350	3.19	7.13	4.26	4.83	7.46	14.66
400	2.43	4.99	3.12	3.37	4.68	7.39
500	1.78	3.25	2.15	2.23	2.82	3.48

Comparing the two tables it is possible to notice that in the cases of B3LYP and MPW1PW91 the tunneling corrections at very low temperature (250 – 300 K) are lower compared to those corresponding to the other methods, while the MP2 tunneling correction is significantly higher. The same behavior is found for the rate constant. In fact, both B3LYP and MPW1PW91 underestimate the reference rate coefficient at 250 and 300 K by about a factor of 4 and 3 respectively. MP2 on the other hand overestimates the rate coefficient at 250 and 300 K by a factor of 7 and 3.

In the other cases we registered a better agreement. In particular, WB97XD slightly underestimates the rate of Sutherland et al. with a maximum deviation of 80% at 250 K that is reduced to a 22% at 500 K. Also BMK and M062X, which show similar SCT corrections, are found to be in good agreement with the reference values; with M062X overestimating Sutherland suggested value by a factor of 2 only at 250 K.

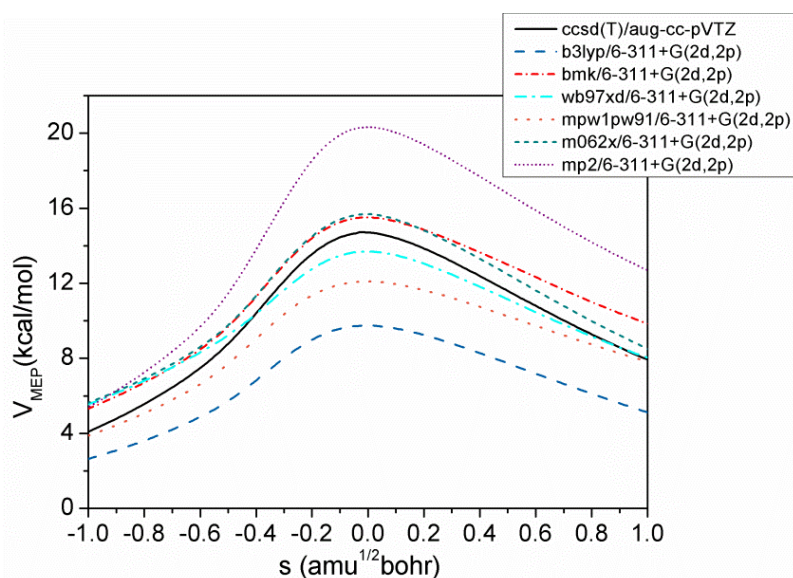


**Figure 67.** The potential energy along the MEP ( $V_{\text{MEP}}(s)$ ) as function of the reaction coordinate  $s$  calculated at different levels of theory.

Since SCT correction seems to be strongly influenced by the choice of the electronic structure method, we investigated the source of these discrepancies by comparing the potential energy curves

obtained with the different methods with an energy surface calculated at the CCSD(T)/aug-cc-pVTZ level using the structures obtained from WB97XD/6-311+G(2d,2p) calculations.

From the plot in **Figure 67** it is possible to notice how the MEP evaluated at the B3LYP and MPW1PW91 level are lower than the potential energy evaluated at the CCSD(T)/aug-cc-pVTZ//WB97XD/6-311+G(2d,2p) level and have larger width. In contrast, the MP2 potential reaches higher values and presents a narrower width compared to the more accurate CCSD(T) curve. These observations explain why the SCT corrections estimated with B3LYP and MPW1PW91 are lower compared to the other methods, while the MP2 based SCT correction is higher. BMK, WB97XD and M062X curves, conversely, are much closer to the CCSD(T) potential and this explains their ability to predict rate coefficients that are in better agreement with experiments.

These evidences show how the accuracy of the minimum potential energy surface influences the SCT tunneling correction and consequently the rate coefficient estimation. Thus, to obtain the optimum results we recalculated the SCT corrections adopting the CCSD(T)/aug-cc-pVTZ//WB97XD/6-311+G(2d,2p) minimum energy path. In this way, it was possible to assess also the relevance that has the accuracy of the other input parameters: geometries, gradients and Hessians evaluated along the MEP. The results are reported in **Table 17**.

**Table 17.** CVT/SCT rate coefficients for the CH<sub>4</sub> + H reaction calculated using different electronic structure method adopting the 6-311+G(2d,2p) basis set for structures, vibrational frequencies and ZPE. The CCSD(T)/CBS activation energy and the CCSD(T)/aug-cc-pVTZ//WB97XD/6-311+G(2d,2p) MEP were adopted for all cases. The results are compared with the suggested values of Sutherland et al.<sup>280</sup>

T (K)	B3LYP	BMK	MPW1PW91	WB97XD	M062X	MP2	Sutherland
250	8.13E-21	1.09E-20	1.53E-20	9.92E-21	9.36E-21	1.17E-20	5.56E-21
300	1.84E-19	2.52E-19	3.12E-19	2.21E-19	2.35E-19	2.49E-19	1.87E-19
350	2.14E-18	3.04E-18	3.31E-18	2.53E-18	2.89E-18	2.76E-18	2.47E-18
400	1.54E-17	2.24E-17	2.21E-17	1.80E-17	2.14E-17	1.90E-17	1.82E-17
500	3.00E-16	4.41E-16	3.85E-16	3.39E-16	4.18E-16	3.45E-16	3.33E-16

As expected, the introduction of a higher level of accuracy in the evaluation of the minimum energy path generally improves the agreement with the suggested rate coefficients of Sutherland et al. However, there are different degrees of agreement and these differences at this point can be ascribed to the ability of each method to describe correctly structures, frequencies and gradients along the minimum energy path.

The maximum deviation from the reference values is detected in each case at 250 K. The MPW1PW91 presents the larger deviation, overestimating the rate constant at 250 K by a factor of 3. This result is closely followed by the MP2 and BMK based predicted rates, which overestimate

the reaction rate at 250 K by a factor of 2. B3LYP, WB97XD and M062X show the better agreement with an overestimation at 250 K of respectively about 46%, 78% and 68%. For temperatures higher than 300 K, all the results are within 50% of the suggested value of Sutherland et al. with the best agreement obtained with the WB97XD DFT method.

These results suggest that the new WB97XD and M062X DFT methods can adequately describe structures, vibrational frequencies and energy gradients.

## Basis Sets

Two basis sets have been compared in order to judge the effect that the size of the basis set can have on the final prediction: the 6-311+G(2d, 2p) and the aug-cc-pVTZ basis sets. In the specific case of the  $\text{CH}_4 + \text{H}$  reaction we found that to the 6-311+G(2d, 2p) basis set correspond 72 basis functions, while to the larger aug-cc-pVTZ basis set correspond 161 basis functions.

We calculated TST based reaction rates and SCT correction factors for each method with the two basis sets. The results obtained without correcting the activation energy for the aug-cc-pVTZ were very similar to those obtained with the 6-311+G(2d,2p) reported in **Table 14**. Thus, here we will focus on the rate coefficients calculated using the best CCSD(T)/CBS value for the activation energy and also introducing the CCSD(T)/aug-cc-pVTZ minimum energy path for SCT calculations. In **Table 18** are compared the rate coefficients obtained using the 6-311+G(2d,2p) and the aug-cc-pVTZ basis sets, which are expressed as ratios over the reference values of Sutherland et al.<sup>280</sup>

**Table 18.** Ratio of CVT/SCT rate constants over the reference value calculated for the  $\text{CH}_4 + \text{H}$  reaction using different electronic structure methods and adopting the 6-311+G(2d,2p) (BS1) and the aug-cc-pVTZ (BS2) basis sets for structures, vibrational frequencies and ZPE. The CCSD(T)/CBS activation energy and the CCSD(T)/aug-cc-pVTZ//WB97XD/6-311+G(2d,2p) MEP were adopted for all cases.

T (K)	B3LYP		BMK		MPW1PW91		WB97XD		M062X		MP2	
	BS1	BS2	BS1	BS2	BS1	BS2	BS1	BS2	BS1	BS2	BS1	BS2
250	1.46	1.46	1.96	1.13	2.76	0.94	1.78	2.81	1.68	1.30	2.11	1.81
300	0.99	0.98	1.35	0.82	1.67	0.69	1.18	1.68	1.26	0.99	1.33	1.17
350	0.87	0.87	1.23	0.76	1.34	0.66	1.03	1.37	1.17	0.92	1.12	0.99
400	0.85	0.85	1.23	0.77	1.22	0.69	0.99	1.28	1.18	0.93	1.04	0.94
500	0.90	0.91	1.32	0.84	1.16	0.80	1.02	1.27	1.25	1.00	1.04	0.97

From the results reported in **Table 18** it is possible to notice how generally rate coefficients calculated using the more accurate aug-cc-pVTZ basis set have a lower value. However, the agreement of the predictions remains largely unchanged. It is interesting to notice that B3LYP based predictions are not affected by the change of basis set, while reaction rates based on WB97XD/aug-cc-pVTZ calculations are slightly increased, in contrast to the behavior detected in the other cases. Finally, M062X is the DFT method that offers the best overall agreement.

## Ultrafine Grid

In light of these evidences, we deemed the M062X/6-311+G(2d, 2p) method suitable to explore also the effects that the introduction of an ultrafine integration grid in the computation of the gradients and Hessians along the MEP may have on the accuracy of the SCT tunneling correction. A first effect due to the introduction of the ultrafine grid is the smoothing of the reaction path curvature expressed as functions of the reaction coordinate  $s$ . Consequently, the smoothing of the reaction path curvature produces some changes in the effective reduced mass, as evidenced in **Figure 68**.

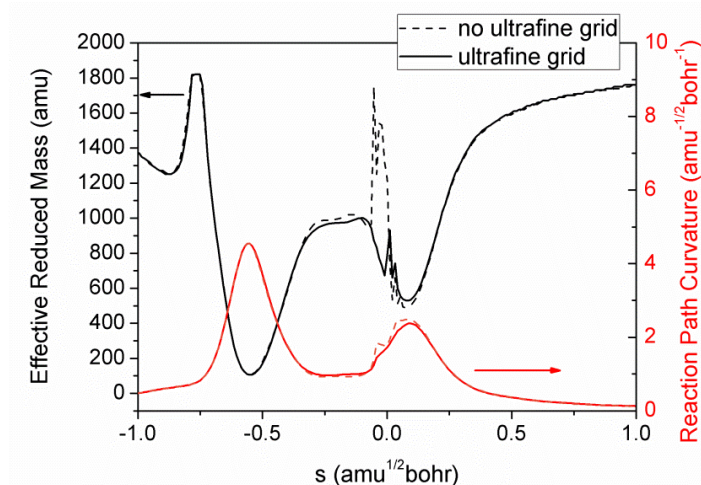


**Figure 68.** Plot of the reaction path curvature and effective reduced mass as functions of the reaction coordinate  $s$ .

The same smoothing effect has been identified observing the plots of the generalized vibrational frequencies as functions of the reaction coordinate  $s$ . In particular, in **Figure 69** we show the behavior of the two lowest frequencies, which are associated with the bending of the H bonding atom, with and without the introduction of the ultrafine grid.

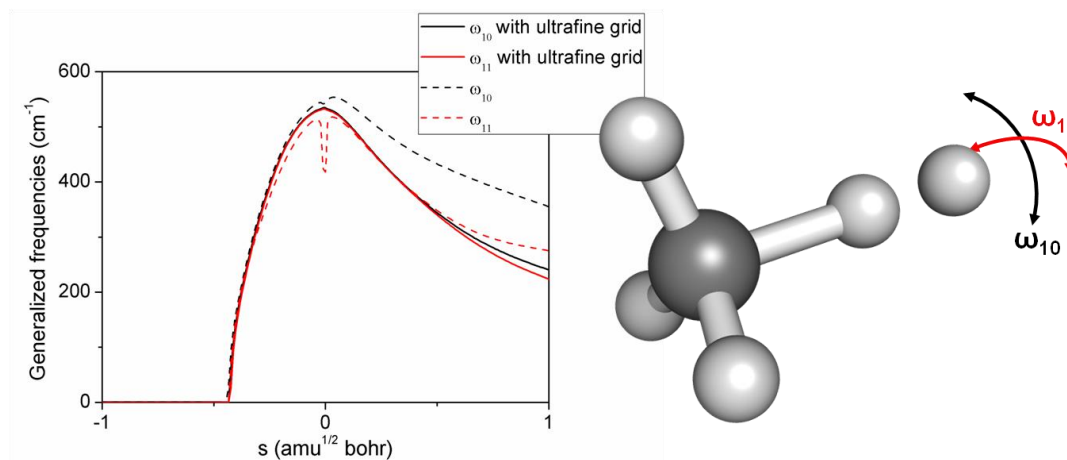


**Figure 69.** Plots of the two lowest generalized vibrational frequencies ( $\omega_{10}$  and  $\omega_{11}$ ) as function of the reaction coordinate  $s$  corresponding to the bending motions of the H atom as illustrated on the right.

The plots in **Figure 69** shows again that with a better level of approximation of the Hessian along the MEP it is possible to attain a more proper description of the properties of the reactive system. In correspondence of the TS, in fact, where the gradients and Hessians are subject to a higher degree of uncertainty, the description of the generalized vibrational frequencies without the ultrafine grid is rather poor. With the introduction of this option, in contrast, the discontinuity previously observed is eliminated and the generalized frequencies are properly described.

Given the improvement of the description of the system, we expect also an improvement in our prediction of the rate coefficient. We calculated TST based reaction rates and SCT correction factors with and without the ultrafine option. The results obtained without introducing any correction for the activation energy and for the MEP are reported in **Table 19**.

**Table 19.** SCT tunneling correction and ratio of CVT/SCT rate constants over the reference value<sup>280</sup> ( $k_{ref}$ ) calculated for the  $CH_4 + H$  reaction using the M062X method and adopting the 6-311+G(2d,2p) basis set without (case 1) and with the ultrafine grid (case 2).

T (K)	SCT tunneling correction		$k(CVT/SCT)/k_{ref}$	
	Case 1	Case 2	Case 1	Case 2
250	59.89	104.35	0.34	0.63
300	15.84	22.02	0.32	0.46
350	7.46	9.02	0.35	0.44
400	4.68	5.22	0.40	0.46
500	2.82	2.84	0.53	0.55

It is evident from the data reported that the ultrafine grid option improves the agreement of the reaction rate in particular at 250 K with the ratio passing from 0.34 to 0.63. The ultrafine option, in fact, affects the SCT correction factor majorly at low temperature, where it increases by a factor of two. At higher temperatures, the effect is less significant; this observation suggests that the level of approximation of the hessian around the TS region can become an issue especially when one is interested in very low temperature reaction rates. However, ultrafine grid calculations should give in any case solutions that are more reliable and robust.

### 7.3.2. Level of Approximation for IRC Calculations

As mentioned previously the accuracy of the rate coefficient and specifically the accuracy of the tunneling correction is affected by the level of approximation of IRC calculations that are performed to determine the minimum energy path. Thus, we decided to carry out a sensitivity analysis on the input parameters of IRC calculations. In particular, here we explored the effect of the step and interval size and the algorithm chosen to follow the reaction path. Calculations were performed at the M062X/6-311+G(2d, 2p) level.

### Step Size and Reaction Coordinate Interval Size

First, we investigated the role that the step size plays in the calculation of the SCT tunneling correction. The step size adopted to perform IRC simulations determines also the number of points that describe the MEP used for SCT calculations. The reference we adopted is a step size of 0.01 bohr, which has been used to obtain the results discussed up to now. We then explored the possibility to use larger step sizes, of 0.02 and 0.05 bohr, thus reducing the density of points used to describe the MEP. Here in **Figure 70** we analyze how the step size affects the effective reduced mass and consequently the tunneling correction.

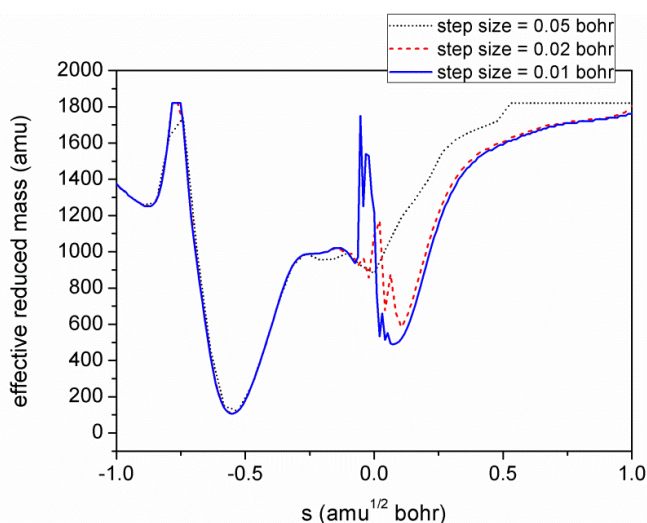


**Figure 70.** Plots of the effective reduced mass calculated with different step sizes as a function of the reaction coordinate expressed in mass weighted coordinates.

From the graph, it is evident how the reduced mass computed with a step size of 0.02 bohr reproduces fairly well the reduced mass calculate with a step size of 0.01 bohr. Moving to a larger step size of 0.05 bohr, however, we found that the curve of the reduced mass on the right side of the TS is systematically higher and also the minimum located in the other two cases in correspondence of  $s \sim 0.1$  ( $\text{amu}^{1/2}$  bohr) is lost. Successively we verified how the differences in the description of the effective reduced mass affect the tunneling factors, which are reported in **Table 20**.

**Table 20.** SCT tunneling corrections evaluated adopting different step sizes for the calculation of the MEP.

T (K)	Step Size = 0.01 bohr	Step Size = 0.02 bohr	Step Size = 0.05 bohr
250	59.89	59.85	53.13
300	15.84	15.46	14.16
350	7.46	7.09	6.61
400	4.68	4.38	4.12
500	2.82	2.53	2.32

The tunneling corrections calculated reflect the behavior of the reduced masses associated. In fact, passing from a step size of 0.01 bohr to 0.02 bohr the SCT outcome does not change significantly, with a maximum deviation at 500 K of 11%. Moving to a step size of 0.05 bohr we find a slightly larger deviation from the values obtained with step size equal to 0.01 bohr, which is about ~13% at 250 K and goes to ~22% at 500 K. Overall, we can deduce that the degree of sensitivity of the SCT coefficient with the step size is rather small. On the other hand, passing to larger steps significantly reduces the computational costs and this signifies that, if needed, larger step sizes may be adopted without a significant loss of accuracy.

In addition, we investigated also the effect that an expansion of the reaction coordinate interval considered may have on the tunneling correction. So far, we have considered a total interval of  $-1.0 - 1.0 \text{ amu}^{1/2} \text{ bohr}$ . Thus, we decided to extend the interval to  $-1.5 - 1.5 \text{ amu}^{1/2} \text{ bohr}$ . The tunneling corrections so calculated are given in **Table 21**.

**Table 21.** *SCT tunneling corrections evaluated adopting different reaction coordinate intervals for the calculation of the MEP and adopting a step size of 0.01 bohr.*

<b>T (K)</b>	<b>s = -1.0, 1.0 amu<sup>1/2</sup> bohr</b>	<b>s = -1.5, 1.5 amu<sup>1/2</sup> bohr</b>
250	59.89	73.90
300	15.84	17.62
350	7.46	7.97
400	4.68	4.90
500	2.82	2.90

The results reported in the table show how the SCT factors increase when a larger interval of the reaction coordinate is taken in consideration, the maximum increment is about 20%, which is registered at 250 K. Going to higher temperatures this deviation is reduced to just 3% at 500 K. Furthermore, if we increase the interval dimensions and we adopt larger step sizes, then the tunneling correction increment is even less pronounced with a maximum deviation of only 13% and 11% registered at 250 K for step sizes of 0.02 and 0.05 bohr respectively.

With these observations, we can deduce that it is reasonable to adopt an interval size of  $-1.0 - 1.0 \text{ amu}^{1/2} \text{ bohr}$  knowing that we are introducing an error of about 20% only at very low temperatures, as the adoption of larger intervals would increase the computational costs.

### **Reaction Path Following Algorithms: HPC and LQA**

To complete the sensitivity analysis performed on the level of approximation of the IRC calculations we explored the possibility to adopt different algorithms to follow the reaction path. Thus far, we have employed the Hessian based Predictor Corrector algorithm of Schlegel and coworkers. Gaussian however gives the possibility to choose among several algorithms available in the litera-

ture and in particular, we opted for the LQA method because, like HPC, it already calculates the hessian at every step, since both need its information.

SCT calculations performed with the input data obtained from the two IRC simulations gave very similar results in terms of tunneling correction. The plots of the effective reduced mass obtained in the two cases are almost superimposed along the entire reaction coordinate interval, save for the TS region. Here in fact the LQA method finds a deeper minimum near  $s = 0.0 \text{ amu}^{1/2} \text{ bohr}$ , as is evident from **Figure 71**.

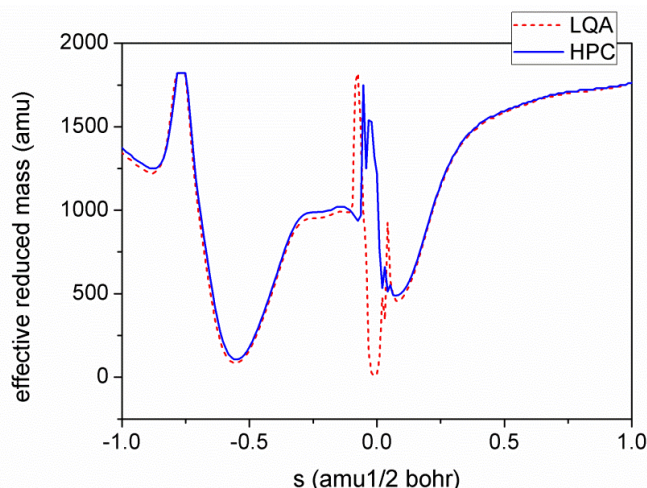


**Figure 71.** Plots of the effective reduced mass calculated from LQA and HPC based IRC calculations.

The SCT results reported in **Table 22** demonstrate that the differences in the effective reduced mass leads to a systematic deviation between the two results of about 16%. The results are very close to each other, thus we cannot say if one is preferable to the other.

**Table 22.** SCT tunneling corrections evaluated adopting LQA and HPC based IRC solutions.

T (K)	HPC	LQA
250	59.89	70.06
300	15.84	18.50
350	7.46	8.65
400	4.68	5.45
500	2.82	3.22

## 7.4. Comparison with Experiments and Accurate Theories

Our best result for the rate coefficient was obtained with the CVT/SCT model calculating structures and vibrational frequencies at the M062X/aug-cc-pVTZ level and the energies at the CCSD(T)/CBS level. SCT calculations were carried out using as input data the results obtained

through IRC calculations performed at the M062X/aug-cc-pVTZ level. Energies were recalculated at the CCSD(T)/aug-cc-pVTZ level for each point along the MEP individuated.

Here in **Figure 72** we compare our predicted rate coefficient with the experimental measurements presented in the first section.<sup>281-298</sup>

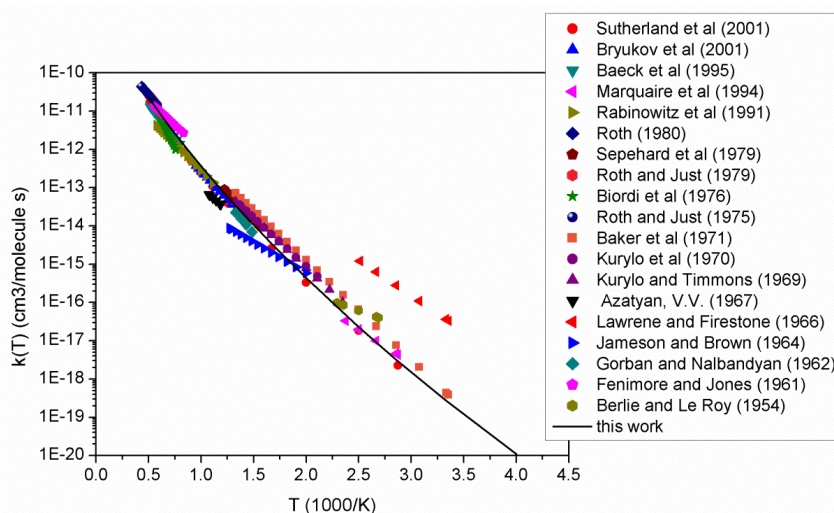


**Figure 72.** Experimental literature rate coefficient compared with our predicted rate.

Our prediction is very close to the measured values, also reproducing very well the temperature dependence of the reaction rate coefficient. Furthermore, we deemed interesting to compare our results also with more accurate theoretical predictions available in the literature, like quantum instanton (QI) rate predictions,<sup>306</sup> RPMD based calculations,<sup>312</sup> the accurate multiconfigurational time dependent Hartree-Fock method,<sup>307</sup> quantum scattering rates<sup>320</sup> and previous CVT/ $\mu$ OMT calculations.<sup>300,307</sup> In **Figure 73** we plot our rate coefficient with the results obtained with these methods for the  $\text{CH}_4 + \text{H}$  reaction.

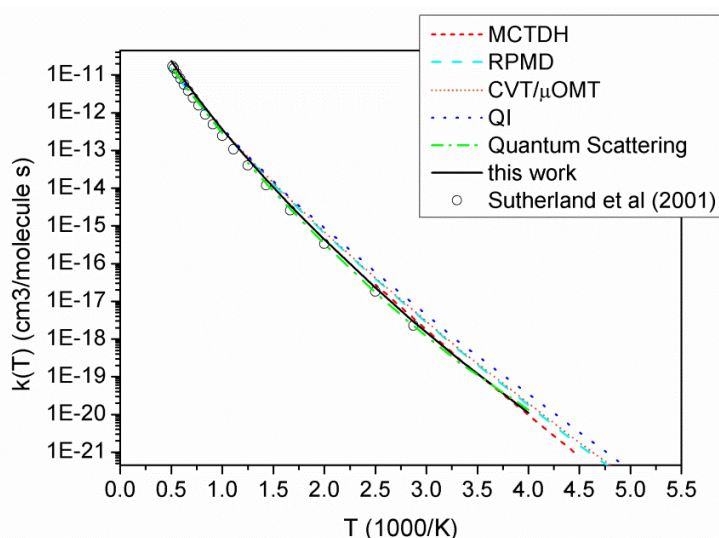


**Figure 73.** Plots of the theoretical literature rate coefficients compared with our predicted rate and the experimental data of Sutherland et al.

The graph shows that our predictions are in good agreement with the experimental values of Sutherland et al. and with the more accurate MCTDH predictions. Overall, all the theoretical results are very close, being within a factor of 3 from each other at very low T (250 K). This result thus confirms the reliability of our methodology and evidences the importance of the accuracy of the electronic structure method adopted. In fact only using an high level method such as CCSD(T) to determine activation energies and energy potential surfaces allowed us to correctly predict the rate coefficient of the CH<sub>4</sub> + H reaction.

## 7.5. Concluding Remarks

In this work, we implemented the CVT/SCT methodology and we assessed its reliability studying the CH<sub>4</sub> + H benchmark reaction. In particular, we performed a sensitivity analysis on the main parameters that enter as input data in this approach and comparing the results against the suggested values of Sutherland et al. based on experimental evidences that we used as reference.

Our sensitivity analysis revealed the importance that the accuracy of the electronic structure method adopted to calculate the activation energy and the minimum energy path has on the prediction of the rate coefficient. Especially, we found that combining the M062X DFT method for structures, energy gradients and Hessians and the CCSD(T) methods for the energies leads to a rate coefficient that is in good agreement with both experimental and high level quantum dynamics results.

In addition, also the effect of other parameters on the SCT tunneling correction was investigated; namely the introduction of an ultrafine grid, the size of the step used in the minimum energy path calculations, the size of the interval considered around the TS and the role of the algorithm chosen to follow the reaction path. This sensitivity analysis showed that the SCT tunneling correction is mainly affected by the precision of the hessian and the introduction of an ultrafine grid in IRC calculations can become important. The other parameters, in contrast, did not affect significantly the SCT outcomes with the maximum deviation being around ~20%. Overall, the methodology implemented is reliable and robust and thus in the future it may be applied with confidence to other reactions of interest.



# 8 Singlet Methylene Addition to Unsaturated Hydrocarbons

---

## 8.1. Introduction

The addition of singlet methylene ( $^1\text{CH}_2$ ) to unsaturated hydrocarbons is an important class of reactions in combustion chemistry as they play a key role in the formation and growth of polycyclic aromatic hydrocarbons (PAH). Miller and Melius<sup>332</sup> were the first to consider in their combustion models the insertion of  $^1\text{CH}_2$  into acetylene ( $\text{C}_2\text{H}_2$ ) leading to propargyl radical ( $\text{C}_3\text{H}_3$ )



and to propose that in turn the recombination of propargyl radicals is likely the dominant route for the formation of the “first” aromatic ring under most conditions. Importantly, the first ring formation is believed to be a precursor to subsequent PAH growth and ultimately soot formation. This reaction sequence is now included in essentially all kinetic schemes for PAH growth in combustion modeling.<sup>333-337</sup>

The central importance of the propargyl radical is related to its resonantly stabilized character coupled with its resistance to further dehydrogenation or other decompositions. The insertion of singlet methylene,  $^1\text{CH}_2$ , into other unsaturated hydrocarbons should similarly yield other resonantly stabilized radicals, which can also play important roles in hydrocarbon growth through their recombination reactions. For instance, the addition of  $^1\text{CH}_2$  to ethylene leads to allyl radical (either directly or via subsequent abstractions from propene), whose dimerization and recombination with propargyl have been postulated to play significant roles in the formation of the first aromatic ring under some conditions.<sup>335,338-342</sup> Even more importantly, addition to benzene yields benzyl radical and/or toluene with the latter also readily converting to benzyl radical via H abstractions. Notably, just as with propargyl, benzyl radical is resistant to further decomposition,<sup>165,179,181,186,187,343-345</sup> and so its recombination reactions may be key steps in the formation of the larger PAHs<sup>346</sup> Analogous reactions of  $^1\text{CH}_2$  with larger PAHs would similarly contribute to further growth in PAH size.<sup>347</sup> Hence, information about the rates of  $^1\text{CH}_2$  addition to a variety of unsaturated hydrocarbon compounds would be of great value to the development of combustion models for soot formation.

Singlet methylene is the first excited state of methylene and lies just 9.0 kcal/mol above the triplet ground state ( $^3\text{CH}_2$ ).<sup>348</sup> The removal of singlet methylene in the presence of hydrocarbons can occur via two competing processes: chemical reaction and physical deactivation through collision induced intersystem crossing to the triplet.<sup>349</sup> Singlet methylene is generally several orders of mag-

nitude more reactive than the triplet, with its reactions commonly taking place over barrierless potential energy surfaces.<sup>350</sup> The barrierless nature of its reaction paths allows its reaction to be competitive with the deactivation process. Nevertheless, the competition between reaction and deactivation complicates the extraction of chemical reaction rate constants from experimental studies of the singlet methylene removal rates.

The reaction of  $^1\text{CH}_2$  with acetylene has served as a benchmark reaction for the study of the reactivity of carbenes with unsaturated species. Its key role in the formation of propargyl radical has led to a large number of theoretical<sup>351-353</sup> and experimental<sup>354-362</sup> studies aimed at delineating the temperature and pressure dependence of its kinetics. Its overall kinetics has been experimentally investigated by several authors at room temperature,<sup>354,355,357,358</sup> with reported values ranging from  $2.5$  to  $3.7 \times 10^{-10} \text{ cm}^3 \text{ molecule}^{-1} \text{ s}^{-1}$ . Only a few studies have examined the temperature-dependence of the kinetics (195-798 K).<sup>360,362</sup> Böhland and Temps<sup>363</sup> and Hack et al.<sup>355</sup> also determined, by direct detection of  $^3\text{CH}_2$  via laser magnetic resonance (LMR), that the physical deactivation contribution counts for  $\sim 20\%$  at room temperature. Later, Gannon et al.<sup>362</sup> obtained a similar result by analyzing the H atom yield for the  $^1\text{CH}_2 + \text{C}_2\text{H}_2$  reaction. Theoretical predictions of the rate coefficient for this reaction have been reported by Guadagnini et al.<sup>351</sup> using variational RRKM theory and by Yu and Muckermann<sup>353</sup> with direct *ab initio* molecular dynamics simulations using the “scaling all correlation” (SAC) method of Truhlar et al.<sup>364-366</sup> Notably, the theoretical predictions of a nearly temperature independent rate constant are in sharp contrast with the experimental results, which show a significant decay with increasing temperature. Furthermore, this discrepancy cannot be explained by a temperature dependent contribution from deactivation.

In the case of ethylene, a number of authors<sup>354,357,367-369</sup> measured the room temperature rate coefficient for its addition to singlet methylene, obtaining results ranging from  $1.5$  to  $2.5 \times 10^{-10} \text{ cm}^3 \text{ molecule}^{-1} \text{ s}^{-1}$ . Temperature dependent studies were carried out by Wagener et al.<sup>356</sup> and Hayes et al.<sup>359</sup> over the range 250-500 K, and more recently by Gannon et al.<sup>362</sup> over the range 195-798 K. Hack and coworkers<sup>368</sup> found that the relaxation contribution to the overall  $^1\text{CH}_2$  removal rate at room temperature is  $0.20 \pm 0.04$ , which is very similar to the value they determined for acetylene ( $0.22 \pm 0.07$ ).

There have been only a few studies of the kinetics of singlet methylene reacting with larger hydrocarbons. Wagner's group used laser induced fluorescence (LIF) to measure the removal rate of  $^1\text{CH}_2$  for a large set of olefins and aromatic species at room temperature.<sup>355,356,368,370</sup> In these studies, they also evaluated the branching ratios for physical deactivation at room temperature and the temperature dependence for the overall removal rate with methane, ethane, ethylene, and benzene. Hayes et al.<sup>359</sup> also determined the room temperature removal rate constant for a large number of saturated and unsaturated hydrocarbons, with laser flash photolysis/laser absorption experiments.

Finally, Gannon et al.<sup>362</sup> have recently reported a temperature dependent rate coefficient for the reaction of methylene with propene.

The most important temperature range for combustion modeling is  $\sim 800$  to  $2000$  K. Unfortunately, there have been no experimental studies performed in this temperature range. Furthermore, the difficulty of deconvolving the relaxation and reaction contributions combined with the considerable discrepancy between the available theoretical and experimental studies implies that there is considerable uncertainty in the proper temperature dependence of the chemical reaction rate even over the studied range of  $200$  to  $700$  K. Gannon et al.<sup>362,371</sup> analyzed the H atom yields from the reaction of  $^1\text{CH}_2$  with acetylene and ethylene and found that the reaction contribution to the total removal of methylene increases from  $\sim 0.3$  to nearly  $1$  as the temperature increased from  $195$  to  $398$  K for both reactants. Their experimental result was confirmed with non-adiabatic transition state theory<sup>75</sup> based calculations of the rate coefficient for intersystem crossing. In contrast, a few other studies indicate that the rate coefficient for deactivation shows a slightly positive temperature dependence with inert gas collision partners.<sup>363,372</sup> Hence, although a number of works have been dedicated to this class of reactions, there are still uncertainties about the temperature dependence for the addition of singlet methylene to unsaturated hydrocarbons, especially for larger alkenes and alkynes.

The direct variable reaction coordinate transition state theory (VRC-TST) approach<sup>53,54,56,57</sup> has been shown to yield accurate predictions for the kinetics of barrierless radical-radical recombination reactions.<sup>12-14,58</sup> Here we have chosen to apply this approach to the study of the high-pressure rate constant for the reaction of  $^1\text{CH}_2$  with a series of unsaturated hydrocarbons. Although these reactions are barrierless, they are not simple radical-radical reactions. Thus, we begin by testing the methodology for the reaction of  $^1\text{CH}_2$  with  $\text{C}_2\text{H}_2$  and  $\text{C}_2\text{H}_4$ . These tests involve extensive consideration of various correction factors and detailed comparison of the predictions with the available experimental data. Subsequent investigations of the association of  $^1\text{CH}_2$  with propyne and propene illustrate the effect of adding a methyl substituent to both  $\text{C}_2\text{H}_2$  and  $\text{C}_2\text{H}_4$ . Predictions for the reaction with 2-butene help distinguish the opposite effects of greater steric repulsion and increased attractiveness along the minimum energy path for the methyl substituent. Further consideration of the additions to allene and butadiene illustrate the effect of multiple double bonds. Finally, predictions for the  $^1\text{CH}_2 + \text{benzene}$  reaction provide valuable information regarding the reactivity of carbenes with aromatic compounds. Each of these reactions are important prototypes for combustion modeling.

For simplicity, in this work we consider only the addition kinetics. Prior studies have established<sup>353,362</sup> that the addition of singlet methylene to  $\text{C}_2\text{H}_2$  leads initially to the formation of cyclopropene, which is followed by isomerization to either allene or propyne. Subsequently, in the absence of stabilizing collisions, both allene and propyne decompose to  $\text{C}_3\text{H}_3$  and atomic hydrogen.

Similar ring formations followed by isomerizations that lead to stable closed shell products and further decompositions to resonantly stabilized radicals are expected for each of the reactions studied here. Complete kinetic analyses of the temperature and pressure dependent branching between these channels<sup>352</sup> is important, but is beyond the scope of this work.

It is perhaps worth mentioning that Blitz and co-workers,<sup>360</sup> and later Frankcombe and Smith,<sup>352</sup> noted, through ME/RRKM analysis of the recombination of  $^1\text{CH}_2$  with  $\text{C}_2\text{H}_2$ , that the rate coefficient for the overall reaction is pressure independent. Due to the large reaction exothermicity, the microcanonical rate coefficient for proceeding on to formation of propargyl was many orders of magnitude larger than that for dissociation back to reactants. Notably, all singlet methylene addition reactions are highly exothermic because  $^1\text{CH}_2$  is a very unstable species. Hence, given that the reaction step leading back to the reactants is expected to be much slower than other decomposition processes, it is reasonable to presume that the overall rate for reaction of singlet methylene with other unsaturated hydrocarbons will also be pressure independent.

The outline of this paper is as follows: in section 2 we provide the details of the electronic structure and TST methods used here. Then, in section 3, the predictions for the high-pressure addition rate coefficients are presented, discussed, and compared in detail with the available experimental data. This discussion initially focuses (section 3.1) on the prototypical  $^1\text{CH}_2 + \text{C}_2\text{H}_2$  and  $^1\text{CH}_2 + \text{C}_2\text{H}_4$  reactions, which are used to illustrate the sensitivity of the predictions to various aspects of the theoretical analysis. The predictions for the remaining reactions are presented in sections 3.2, while some general observations are made in section 3.3. Finally, some concluding remarks are given in section 4.

## 8.2. Methodology

In this section we first review the kinetic theory employed here and then discuss the electronic structure methods used to generate the interaction energies that are needed in the kinetic theory.

### 8.2.1. Kinetic Theory

The present calculations implement the direct variable reaction coordinate transition state theory (VRC-TST) approach. This approach has been described in detail in previous investigations on hydrogen atom addition to alkyl<sup>13</sup> and alkenyl radicals<sup>54</sup> and on alkyl + alkyl combination reactions.<sup>12,14</sup> Thus, we provide only a brief review of the methodology focusing primarily on the details relevant to its application to the addition of singlet methylene to unsaturated hydrocarbons.

A separation into conserved and transitional modes is a key simplifying assumption within the VRC-TST approach. The conserved modes are taken to be the vibrational modes of the reacting fragments, while the remaining transitional modes describe their rotational and translational mo-

tions. The contribution to the transition state partition function from the conserved modes is readily evaluated via a direct sum over the vibrational levels, which are typically treated as harmonic oscillators. The VRC-TST approach then focuses on an accurate evaluation of the transitional mode contribution to the transition state partition function via Monte Carlo integration of classical phase space integral representations.

An important feature of the VRC-TST protocol for the transitional modes is the definition of the transition state dividing surface in terms of a set of pivot point locations and separations. These pivot points define the location of the origin for the effective fragment rotations within the transition state. A fixed distance between a pivot point on one fragment and one on the other fragment defines a dividing surface separating reactants from products. Hence, in accord with the variational principle of TST, the rate coefficient is minimized with respect to both the pivot point locations and separations. For the present study of  $^1\text{CH}_2$  + alkene/alkyne reactions we employ the multi-faceted dividing surface approach,<sup>53</sup> where multiple pivot points are specified for each fragment. The overall dividing surface is then composed of the set of faces corresponding to fixed distances between each pair of pivot points.

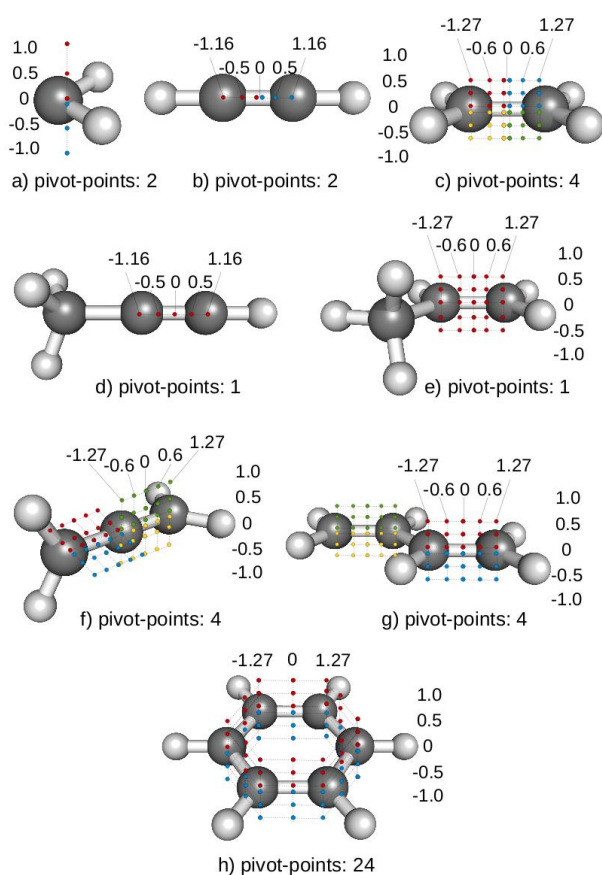


**Figure 74.** *Pivot points number and locations used for each fragment a) methylene, b) acetylene, c) ethylene, d) propyne, e) propene, f) allene, g) butadiene, h) benzene. Distances are in bohr.*

Previous studies have demonstrated that at large separations the optimum position for the pivot point is at the center-of-mass (CoM). Meanwhile, at short separations orbital centered pivot points are preferred. For the singlet methylene fragment we used two pivot points, positioning them along the direction perpendicular to the plane formed by the three atoms and passing from the CoM of the fragment (c.f., **Figure 74a**). We located one point on each side of the plane in order to take into account the possibility that the  $^1\text{CH}_2$  can attack the unsaturated bond from either of its sides. The distance of these two pivot points from the CoM was varied from 0.01 to 0.5 and 1.0 bohr in the optimizations.

For all other reactive fragments the pivot point positions are summarized in **Figure 74(b-h)**. Notably, our choice of pivot points accounts for all manner of additions including ring formation via addition to the center of the unsaturated bond and addition to the C atom. This range of addition possibilities provides the motivation for locating the pivot points across the full length of the unsaturated bond, from its center all the way to the C atoms forming the bond.

Importantly, within the multifaceted dividing surface VRC-TST approach, it is possible to take advantage of the symmetry properties of the fragments. For example, in the case of acetylene plus methylene, two pivot points were employed for each fragment and the pair of pivot points for each fragment are identical. Thus, by symmetry, the dividing surfaces generated by their combination are also identical. Hence, we calculate the flux corresponding to one dividing surface and then simply multiply it by a factor of 4.

For the pivot point to pivot point distance, a grid spacing of 0.26 Å was employed for short separations, while a grid spacing ranging from 0.26 to 1.1 Å was used for larger separations. As a consequence, on the order of 100 to 500 dividing surfaces have been considered for each addition reaction investigated here. The evaluation of the transitional mode contribution to the partition function is then accomplished via Monte Carlo integration over the transitional mode orientations, with up to a few thousand samplings per dividing surface. The Monte Carlo simulations were terminated when the estimated integration error bars were below the threshold of 10%. Finally, based on the results of previous studies,<sup>13,14</sup> a temperature independent dynamical correction factor of 0.85 was applied. This correction factor accounts for the limited recrossing of the transition state dividing surface observed in trajectory studies for radical-radical reactions.

### 8.2.2. Electronic Structure Methods

The Monte Carlo integration over the transitional mode coordinates requires accurate estimates of the interfragment interaction energies for approximately ten thousand geometries. The development of analytic representations for the, generally 6-dimensional, transitional mode potential energy surface is difficult and time consuming. Instead, we evaluate the transitional mode interaction energies on the fly using an approach that is similar to the one employed in our previous studies for

reactions such as the addition of atomic hydrogen to alkyl radicals and the recombination of two alkyl radicals.<sup>13,14</sup> In particular, we employ a CASPT2 approach, which yields accurate energies very efficiently, to evaluate directly the orientation dependence of the interaction energies. Additional calculations are performed along the minimum energy path to yield one-dimensional corrections based on higher-level evaluations and to account for the effects of the relaxation of the fragment geometries at shorter separations.

To begin, the reactant geometries were optimized at the CASPT2/cc-pVDZ level.<sup>8-11,373</sup> For singlet methylene a two electron two orbital (2e,2o) active space was used. For the unsaturated hydrocarbons the  $\pi$  bonding and  $\pi^*$  anti-bonding orbitals are strongly correlated and so we included each of these orbitals in the active space for their geometry optimization. Thus, for example a four electron four orbital (4e,4o) active space was considered for acetylene.

The orientation dependent interfragment interaction potentials were generally determined with a CASPT2(2e,2o)/cc-pVDZ approach, where the (2e,2o) active space correlates with the singlet methylene orbitals. For computational expediency, the  $\pi$  and  $\pi^*$  orbitals of the unsaturated hydrocarbons were generally not included in the active space for this orientational sampling. As described below, test calculations for acetylene demonstrate that their exclusion is acceptable. However, for ethylene and propylene, certain wavefunction convergence problems were encountered with the (2e,2o) active space. For these cases, we instead employ a (4e,4o) active space that includes the  $\pi$  and  $\pi^*$  orbitals of ethylene/propene because it yields a more consistent set of interaction energies.

The one-dimensional, orientation-independent correction ( $\Delta V_{corr}$ ) to the CASPT2/cc-pVDZ potential is obtained from the expression:

$$\Delta V_{corr} = [E(CCSD(T)/CBS)_{fixed} - E(CASPT2/cc - pVDZ)_{fixed}] + [E(CASPT2/cc - pVDZ)_{relaxed} - E(CASPT2/cc - pVDZ)_{fixed}] \quad (142)$$

In this expression, the subscript “fixed” means that the calculations were carried out while keeping the geometries fixed at their asymptotic equilibrium geometries, while the subscript “relaxed” corresponds to energy evaluations allowing for the relaxation of the internal degrees of freedom of the two fragments. The term in the first brackets accounts for limitations in the accuracy of the CASPT2/cc-pVDZ method, and from here on we will call it the “method correction”. This correction is based on CCSD(T)/CBS(cc-pVTZ;cc-pVQZ)<sup>15,373</sup> one-dimensional orientation independent evaluations along the minimum energy path. The extrapolation to the complete basis set limit was obtained using the scaling coefficient proposed by Martin.<sup>374</sup> The term in the second brackets accounts for the contribution due to the relaxation of the conserved modes, and from now on, it will be referred to as the “relaxation correction”. To obtain this correction we optimized the internal fragment geometries (at the CASPT2/cc-pVDZ level) at various points along the reaction coordi-

nate, while also constraining the relative orientation of the two fragments. All the calculations carried out in this work were performed with the MOLPRO package.<sup>4</sup>

## 8.3. Results and Discussion

### 8.3.1. Tests for $^1\text{CH}_2 + \text{C}_2\text{H}_2$ and $\text{C}_2\text{H}_4$

The small size of  $\text{C}_2\text{H}_2$  and  $\text{C}_2\text{H}_4$ , together with the availability of a number of high quality experimental data sets, allows us to use their reactions to assess the accuracy of various aspects of the present rate predictions. In particular, we systematically explore the accuracy of the reference electronic structure methods via comparisons with calculations employing larger basis sets and/or higher level methods for both the orientational sampling and the one-dimensional corrections. Meanwhile, the experimental data provides compelling tests for the overall rate predictions.

First, to test the suitability of the CASPT2(2e,2o)/cc-pVDZ method we computed one-dimensional potential energy surfaces (PES) for  $^1\text{CH}_2 + \text{C}_2\text{H}_2$  using a variety of methods and basis sets. These calculations were performed at various fixed distances,  $R_{\text{C-CoM}}$ , between the carbon atom of methylene and the center of mass (CoM) of acetylene, with the geometries of the two fragments kept fixed at their asymptotic equilibrium geometries. The resulting one-dimensional potentials correlate qualitatively with the potential along the minimum energy path for addition to form a 3-membered ring.

For the present reactions, the CCSD(T) method is expected to provide an accurate description of the interaction energies because the T1 diagnostic is reasonably small, being 0.02 or less. Meanwhile, the Davidson corrected multireference configuration interaction method<sup>139,191</sup> (CAS+1+2+QC) provides an alternative to the CASPT2 approach that is potentially more accurate and still reasonably computational efficient.

In **Figure 75** results are shown for calculations of the approximate minimum energy path potential at the CASPT2, CAS+1+2+QC, and CCSD(T) levels. The CASPT2 results are in remarkably good agreement with the CCSD(T) results with a deviations of less than 5%. The CAS+1+2+QC results are also in good agreement with the CCSD(T) ones, but with a somewhat larger maximum deviation of about 13%. These results provided the motivation for our decision to employ the CASPT2 method in our direct evaluation of the interaction energies within the VRC-TST simulations. The accuracy of the reference frozen-core CCSD(T) method was examined via CCSDT(Q)/cc-pVDZ<sup>375</sup> calculations of the T(Q) correction for the effect of higher order excitations and CCSD(T)/cc-pCVDZ calculations of the correction for core-valence correlation. Notably, these energy corrections were each less than 2%, indicating that the reference frozen-core CCSD(T) method and correspondingly the CASPT2 results are of high accuracy. For simplicity, these corrections were not included in our protocol for this or other reactions.

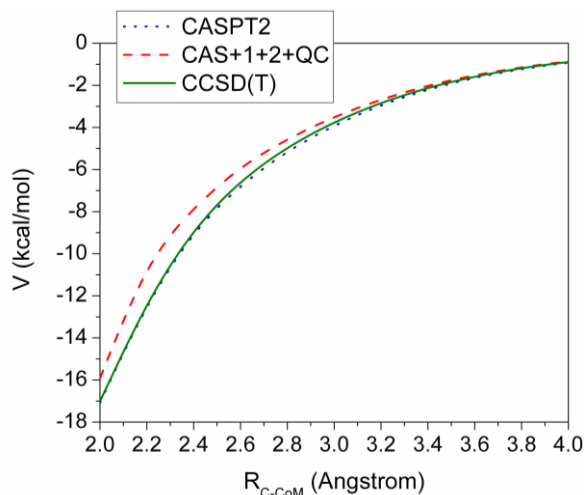


**Figure 75.** One-dimensional potential energy surface for  $^1\text{CH}_2 + \text{C}_2\text{H}_2$  with CASPT2/cc-pVDZ (blue dotted), CAS+1+2+QC/cc-pVDZ (red dashed) and CCSD(T)/cc-pVDZ (green solid) calculations.

The excellent agreement between the CASPT2(2e,2o) and CCSD(T) calculations suggests that the (2e,2o) active space is adequate. Nevertheless, it is interesting to examine the effect on the CASPT2 predictions of including the  $\pi$  and  $\pi^*$  orbitals of acetylene to obtain a (6e,6o) active space. As illustrated in **Figure 76**, the dimension of the active space has only a minor affect on the potential energy surface, further confirming the appropriateness of the (2e,2o) space.

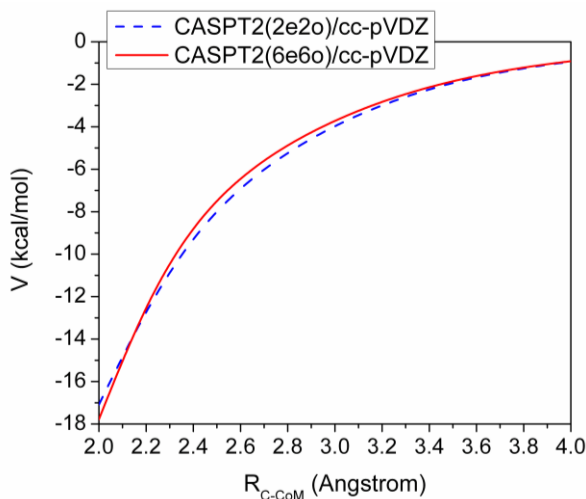


**Figure 76.** Potential energy surface for  $^1\text{CH}_2 + \text{C}_2\text{H}_2$  with CASPT2/cc-pVDZ calculations using either a (2e2o) active space (blue dotted) or a (6e6o) active space (red solid).

Finally, we investigated the dependence on the size of the basis set with CASPT2(2e,2o) calculations using Dunning's correlation consistent polarized valence double, triple and quadruple- $\zeta$  basis sets. The results are illustrated in **Figure 77** where it can be seen that increasing the basis set from double- $\zeta$  to triple- $\zeta$  yields a significantly more attractive potential, with a maximum deviation

of 20% at a C-CoM distance of 2 Å. In contrast, the increase from triple- $\zeta$  to quadruple- $\zeta$  does not substantially modify the PES, with a maximum deviation of only 4%. The relatively modest extent of the increased attractiveness for the basis set limit implies that the present scheme based on explicit cc-pVDZ orientational samplings coupled with one-dimensional corrections for the effect of the basis set on the minimum energy path potential should be satisfactory.

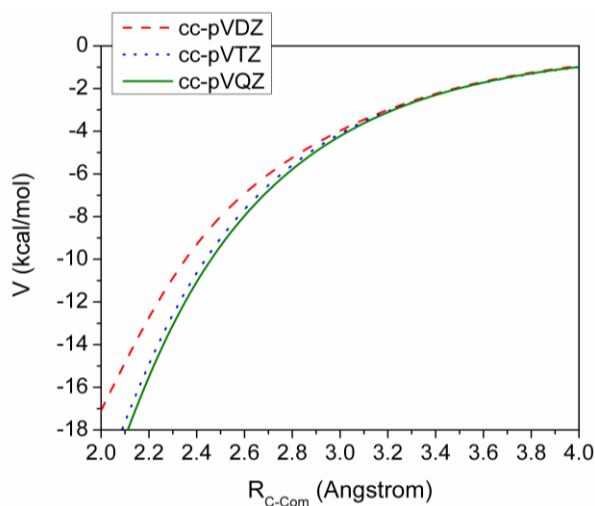


**Figure 77.** Potential energy surface for  $^1\text{CH}_2 + \text{C}_2\text{H}_2$  with CASPT2(2e,2o) calculations employing a cc-pVDZ (blue dotted), cc-pVTZ (red dashed) or cc-pVQZ (green solid) basis set.

Similar comparisons were performed for the addition of singlet methylene to ethylene. These comparisons yielded essentially identical results, further confirming the appropriateness of the CASPT2(2e,2o)/cc-pVDZ based approach.

Further indications of the accuracy of the present CASPT2/cc-pVDZ based sampling can be obtained from comparisons of the full rate coefficient calculations employing different methods for the orientational sampling. Correspondingly, we have also implemented the full VRC-TST analysis for CASPT2/cc-pVTZ direct evaluations of the interaction energies for the addition of methylene to both acetylene and ethylene and for CCSD(T)/cc-pVDZ direct evaluations for the addition to acetylene. For the CASPT2/cc-pVTZ case we also reevaluate both the method and relaxation corrections to be relative to the CASPT2/cc-pVTZ energies, while for the CCSD(T)/cc-pVDZ case we reevaluate the method correction and presume that the relaxation correction is invariant.

The predicted rate coefficients for the reactions of  $^1\text{CH}_2$  with acetylene and ethylene are illustrated in **Figure 78** for calculations using either CASPT2/cc-pVDZ or CASPT2/cc-pVTZ direct samplings and with or without the one-dimensional correction. The relatively large deviation of the uncorrected cc-pVDZ results from the uncorrected cc-pVTZ results indicates that the basis set correction is quite significant, especially at high temperature. Nevertheless, the good agreement between the two calculations incorporating the one-dimensional corrections (maximum deviation of 13%) implies that the one-dimensional scheme for correcting for limitations in the basis set is satis-

factory. The limitation to the cc-pVDZ basis set for the direct orientational sampling is expected to increase the uncertainties in the predicted rates by only about 10% to 20%.

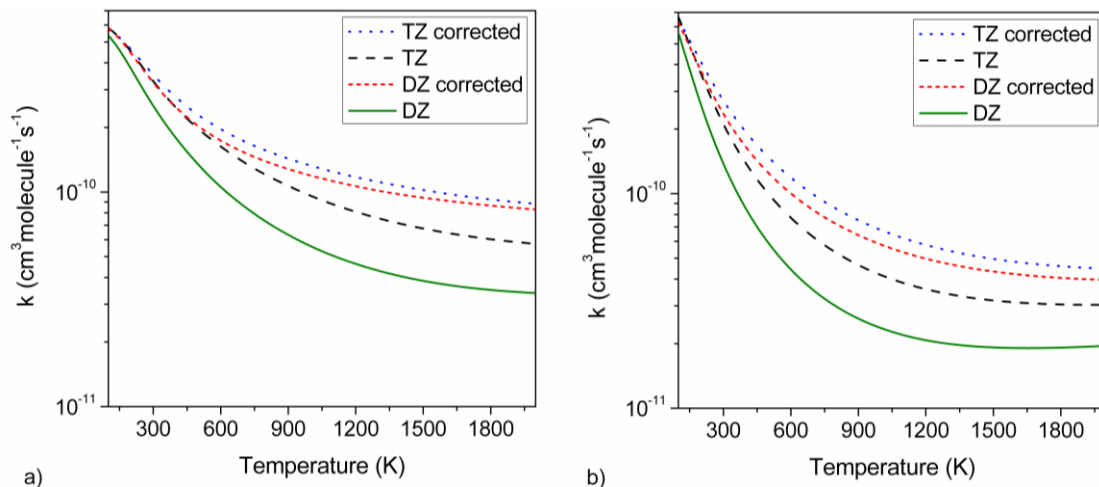


**Figure 78.** Comparison of the VRC-TST calculated rate coefficients for (a)  $^1\text{CH}_2 + \text{C}_2\text{H}_2$  and (b)  $^1\text{CH}_2 + \text{C}_2\text{H}_4$  reactions using CASPT2/cc-pVDZ (green solid), CASPT2/cc-pVDZ+Corr (red fine-dashed), CASPT2/cc-pVTZ (black dashed) and CASPT2/cc-pVTZ+Corr (blue dotted) interaction energies.

The corresponding comparison between calculations employing either CASPT2(2e,2o)/cc-pVDZ or CCSD(T)/cc-pVDZ direct evaluations of the orientation dependent energies is provided in **Figure 79**. The small deviation between the two results, which is at most 20%, further confirms the reliability of the present CASPT2/cc-pVDZ based approach.

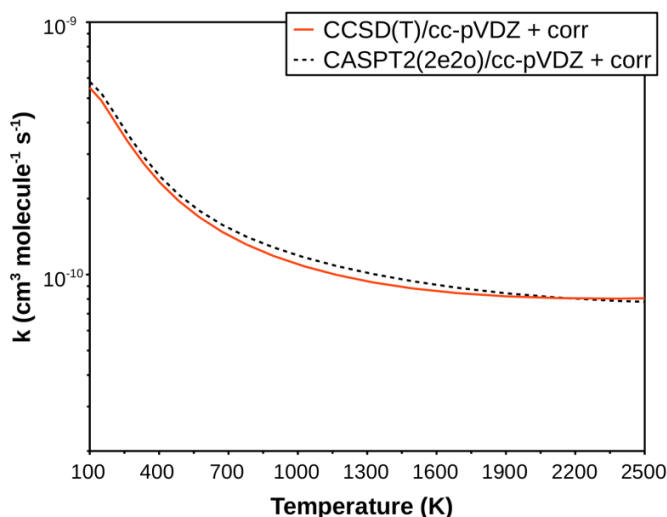


**Figure 79.** VRC-TST rate predictions for  $^1\text{CH}_2 + \text{C}_2\text{H}_2$  with CASPT2(2e2o)/cc-pVDZ (black fine-dashed) and CCSD(T)/cc-pVDZ energies (red solid) including the potential correction.

It is interesting to highlight the relative sizes of the method and relaxation corrections to the VRC-TST rate coefficients. For simplicity, we consider these effects for only the addition to acety-

lene. As shown in **Figure 80a**, for the cc-pVDZ direct sampling the predicted rate increases by more than a factor of 2 for temperatures between 800 and 2500 K when the full correction is included. This result is better highlighted in **Figure 80c**, where the ratio between the corrected and the uncorrected rate coefficient is plotted as a function of temperature. From **Figure 80a** and **c**, we also see that for the cc-pVDZ case, although both contributions are important, the method correction plays a dominant role. In contrast, for the CASPT2/cc-pVTZ direct sampling, the two contributions play an equally important role. Overall, the relaxation correction is clearly significant and so it has been included in our protocol for the VRC-TST analysis of methylene addition to other unsaturated hydrocarbons.

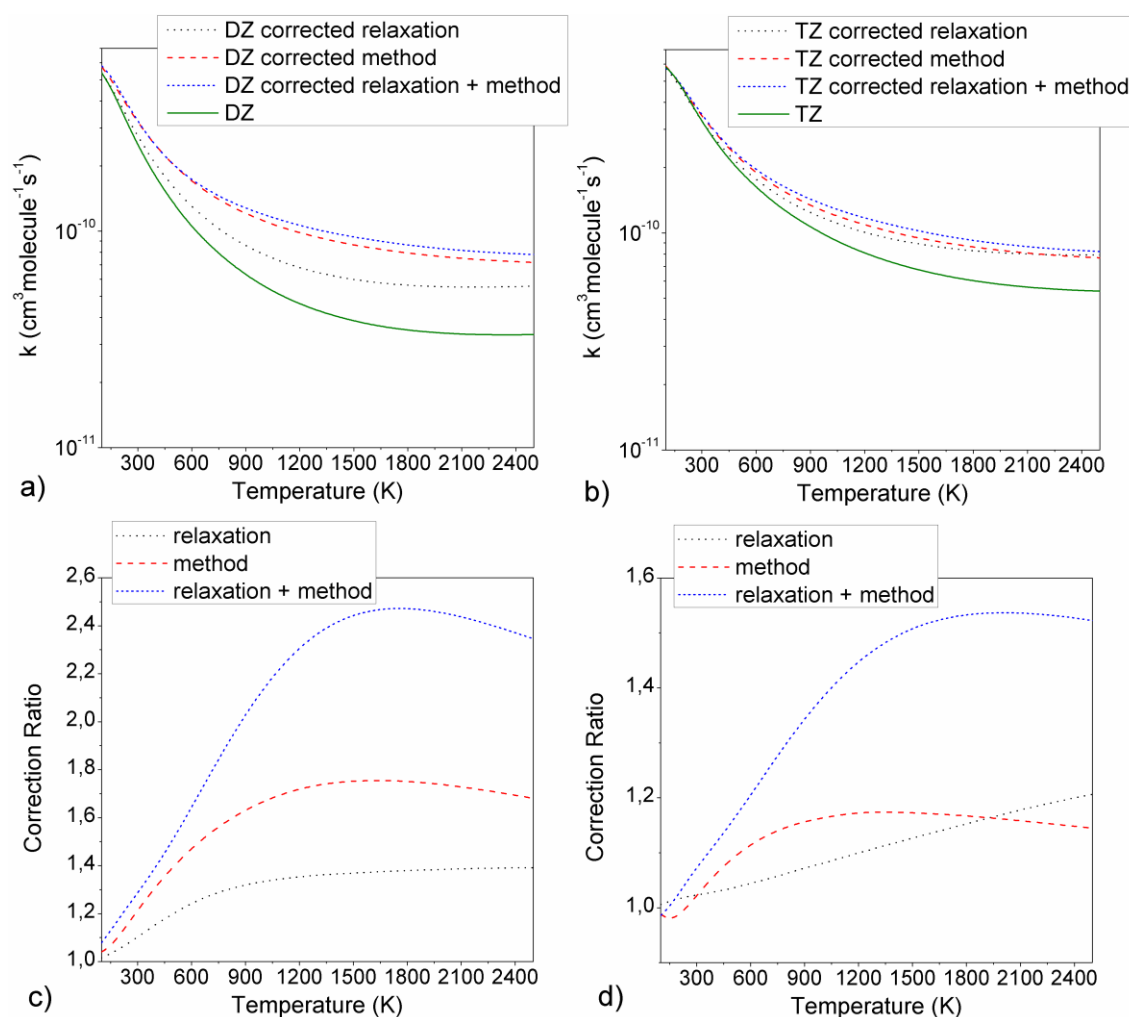


**Figure 80.** VRC-TST rate predictions for  ${}^1\text{CH}_2 + \text{C}_2\text{H}_2$  with (a) CASPT2/cc-pVDZ and (b) CASPT2/cc-pVTZ direct sampling including only the relaxation correction (black dotted), only the method correction (red dashed), both relaxation and method corrections (blue fine-dashed) and no correction (green solid). Correction ratio evaluated for (c) CASPT2/cc-pVDZ and (d) CASPT2/cc-pVTZ direct sampling based VRC-TST rate coefficients.

For both cases, the relaxation correction increases with increasing temperature because the deviation between the relaxed and the fixed potential increases with decreasing separation distances, as illustrated in **Figure 81**. With increasing temperature, the transition state moves to shorter separations and so the effective deviations are increased. The plots in **Figure 81** illustrate the percent change to the interaction potential along the approximate minimum energy path (MEP) for the various correction terms. Interestingly, the percent correction to the potential roughly corresponds to the percent correction to the predicted rate coefficients.

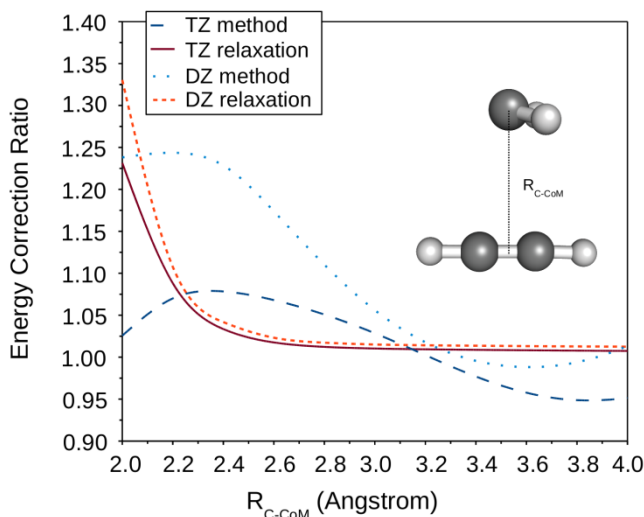


**Figure 81.** Energy correction ratio for the  ${}^1\text{CH}_2 + \text{C}_2\text{H}_2$  reaction accounting for the method correction at the *cc-pVTZ* level (blue dashed) and *cc-pVDZ* level (light blue dotted) and for the relaxation correction at the *cc-pVTZ* level (dark red solid) and at the *cc-pVDZ* level (red fine-dashed).

In cases where the relaxation correction is significant changes in the conserved mode zero point energy (ZPE) along the MEP may also be significant. Here, we evaluated the effect of the changing ZPE for the  ${}^1\text{CH}_2 + \text{C}_2\text{H}_2$  reaction, and found it to be negligible yielding a correction of less than 2%. This effect was neglected in our studies of the other  ${}^1\text{CH}_2$  reactions.

The present dynamically corrected VRC-TST predictions for the temperature dependent rate coefficient, based on the corrected CASPT2/*cc-pVTZ* energies, are plotted in **Figure 82** for the addition reaction of  ${}^1\text{CH}_2$  with acetylene. These rate predictions are plotted together with a  $\pm 10\%$  confidence limit that reflects the uncertainty level adopted for the Monte Carlo simulations. The variations in the various correction terms discussed above suggest that the overall uncertainty in the rate predictions is on the order of 20-30%. The experimental data and theoretical results available in the literature are also compared with these predictions. The calculated VRC-TST rate coefficient is in very good agreement with the numerous experimental rates measured at room temperature.

Moreover, our predictions quantitatively reproduce the temperature dependence found in the experimental work of Blitz et al.<sup>360</sup> and Gannon et al.<sup>362</sup>

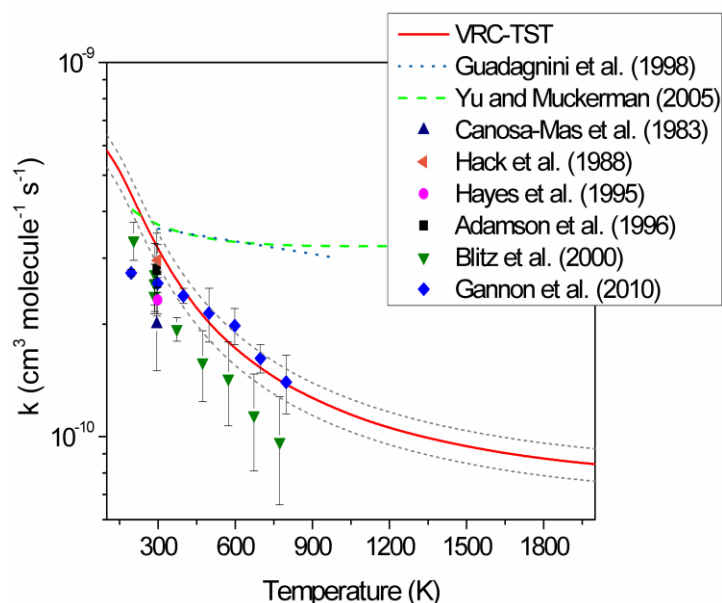


**Figure 82.** VRC-TST high-pressure limit rate coefficient for the  $^1\text{CH}_2 + \text{C}_2\text{H}_2$  reaction (solid red line) with 10% confidence limit compared with experimental measurements (symbols) and other theoretical predictions (lines).

It is important to point out that all the experimental data are based on removal measurements of  $^1\text{CH}_2$  and thereby contain information about both reaction with acetylene and physical deactivation to the triplet ground state. As mentioned in the introduction, Hack et al.<sup>355</sup> measured the contribution from relaxation to the total removal rate of singlet methylene in the presence of acetylene to be  $0.22 \pm 0.07$  at room temperature. Hence, all experimental results shown in **Figure 82** were plotted after subtracting this contribution, which was maintained constant for all temperatures. This choice is motivated by the lack of experimental data on the temperature dependence of physical deactivation.

Previous theoretical predictions made by Guadagnini et al.<sup>351</sup>, and more recently by Yu and Muckerman,<sup>353</sup> reproduce well the room temperature experimental data, but fail to predict the negative temperature dependence found by Blitz et al.<sup>360</sup> and Gannon et al.<sup>362</sup> By necessity, the early study of Guadagnini et al. was based on relatively low-level electronic structure evaluations for the vibrational frequencies (CASSCF/DZ), and furthermore presumed rigid rotor harmonic oscillator behavior in the transition state region. Thus, it is perhaps not surprising that the present predictions yield quite different predictions for the temperature dependence. Yu and Muckerman, on the other hand, carried out *ab initio* trajectory simulations using forces calculated at the UCCSD/cc-pVDZ level and then extrapolated to the UCCSD(T)/CBS level with the “SAC” approach of Truhlar et al.<sup>364-366</sup> However, they employ a 300 K canonical ensemble for their rotational sampling, apparent-

ly even for their high temperature evaluations of the rate coefficient. This inappropriate restriction in rotational states is likely responsible for their discordant prediction for the temperature dependence of the addition kinetics.

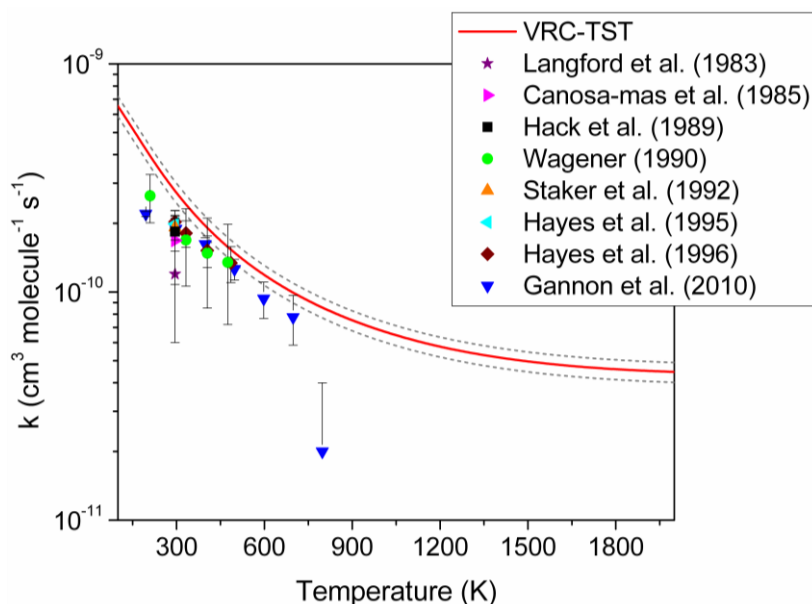


**Figure 83.** VRC-TST high-pressure limit rate coefficient for the  $^1\text{CH}_2 + \text{C}_2\text{H}_4$  reaction (solid red line) with 10% confidence limit compared with experimental measurements (symbols).

The present dynamically corrected VRC-TST predictions for the temperature dependent rate coefficient in the reaction of singlet methylene with ethylene is plotted in **Figure 83** together with the available experimental data. These calculations also employed a corrected CASPT2/cc-pVTZ potential. However, in this case it was necessary to introduce a 4 electron 4 orbital CAS active space in order to correctly follow the potential energy surface. The present a priori predictions again show good agreement with both the rate values measured at room temperature, and also the temperature dependence found by Gannon et al.<sup>362</sup> The plotted experimental values were again reduced by a temperature independent factor of 20%, in order to account for the contribution from deactivation to the measured total removal rates.

### 8.3.2. Comparison with Experiment for $^1\text{CH}_2 + \text{pC}_3\text{H}_4$ , $\text{C}_3\text{H}_6$ , $\text{aC}_3\text{H}_4$ , $\text{C}_4\text{H}_6$ , $\text{C}_6\text{H}_6$

Variable reaction coordinate TST calculations were performed for the addition of singlet methylene to a series of unsaturated hydrocarbons that are commonly present in combustion environments: propyne, propene ( $\text{pC}_3\text{H}_4$ ), allene ( $\text{aC}_3\text{H}_4$ ), butadiene and benzene. For each of these reactions the orientation dependent interaction potentials were evaluated with the CASPT2/cc-pVDZ method and one dimensional corrections based on CCSD(T)/CBS and relaxed CASPT2/cc-pVDZ calculations were employed. For completeness, the potential energy surface corrections for all of

the considered reactions are given as supplementary information. As already discussed in the methods section a (2e,2o) CAS active space was adopted for most of the calculations. Unfortunately, this choice could not be applied to all of the reactions that were investigated. For propene, as for ethylene, a (4e,4o) active space was required in order to correctly estimate the interaction energies at shorter distances. Meanwhile, for the allene and butadiene cases, it was necessary to employ a (6e,6o) active space, which includes the  $\pi$  spaces for both of the double bonds.

For these reactions, only limited comparisons with experimental data are possible. The complete series of hydrocarbons has only been studied by the Wagner group<sup>355,368,370</sup> and only at room temperature. All experimental data were again scaled by a constant correction factor that approximately accounts for the contribution to the singlet methylene removal rate from the physical deactivation of singlet to triplet methylene. Correction factors were mainly obtained from the experimental values measured by Wagner and coworkers and are presented in **Table 23**.

**Table 23.** Contributions of physical deactivation to the removal of  $^1\text{CH}_2$  by the reactants considered in this study.

Reactant	$k_d/k_{\text{tot}}$
$\text{C}_2\text{H}_2$	0.22 <sup>a</sup>
$\text{C}_2\text{H}_4$	0.20 <sup>b</sup>
p $\text{C}_3\text{H}_4$	0.24 <sup>c</sup>
$\text{C}_3\text{H}_6$	0.24 <sup>b</sup>
a $\text{C}_3\text{H}_4$	0.30 <sup>b</sup>
$\text{C}_4\text{H}_6$	0.20 <sup>d</sup>
$\text{C}_6\text{H}_6$	0.30 <sup>a</sup>

<sup>a</sup>Ref. [355], <sup>b</sup>Ref. [368], <sup>c</sup>Ref. [370], <sup>d</sup>Assumed equal to the value corresponding to ethylene.

### $^1\text{CH}_2$ + Propyne and Propene

A comparison of the VRC-TST based predictions with the available experimental data for the reaction of singlet methylene with propyne is presented in **Figure 84a** and with propene in **Figure 84b**. The room temperature rate coefficient measured by Koch et al.<sup>370</sup> is only slightly overestimated by our predictions (a factor of 1.3) and is generally very close to the rate constant for addition of methylene to acetylene. For the propene case, there are a larger number of experimental works. Among them, Gannon et al.<sup>362</sup> extended their measurements to a range of temperatures between 195 and 798 K. For this reaction, we again found very good agreement between our theoretical predictions and the experimental results at room temperature. However, our predictions show a sharper temperature dependence than that measured by Gannon et al. This modest discrepancy may be indicative of an increase in the rate of the physical deactivation process with increasing tempera-

ture or alternatively it can be attributed to an additional contribution to the total reaction rate arising from abstraction. Otherwise, there may be some inaccuracy in the predictions arising perhaps from the use of the double- $\zeta$  basis set or a failure of the CASPT2 method. Nevertheless, overall our predictions are still in reasonable agreement with the experimental data.

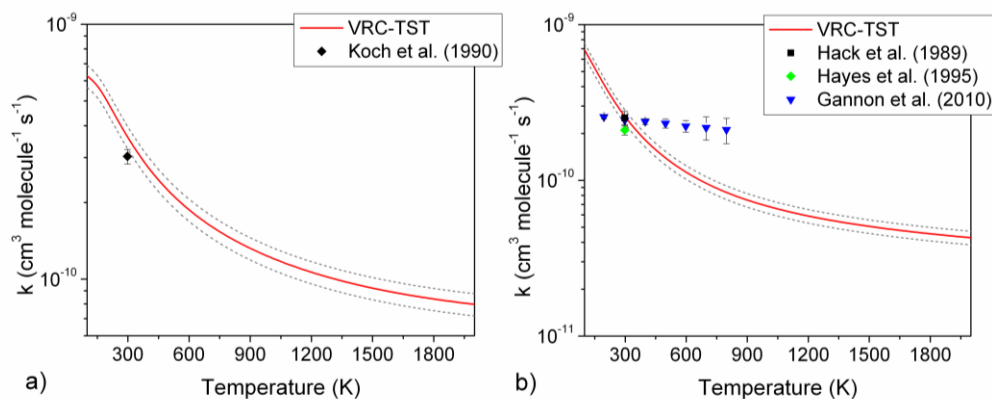


**Figure 84.** VRC-TST high-pressure limit rate coefficient (solid red line) for (a)  $^1\text{CH}_2 + p\text{C}_3\text{H}_4$  and (b)  $^1\text{CH}_2 + \text{C}_3\text{H}_6$  with 10% confidence limit compared with experimental measurements (symbols).

### $^1\text{CH}_2 + \text{Allene and Butadiene}$

In

**Figure 85a and b** the results of our VRC-TST simulations are plotted for the reaction of singlet methylene with allene and butadiene, respectively. These predicted rate coefficients show a slightly larger discrepancy with experiment as compared to the reactions previously analyzed. Nevertheless, our predictions are still fairly consistent with the experimental measurements as we overestimate the values determined by Hack et al.<sup>368</sup> and Hayes et al.<sup>357</sup> by only a factor of 1.4 to 1.5.

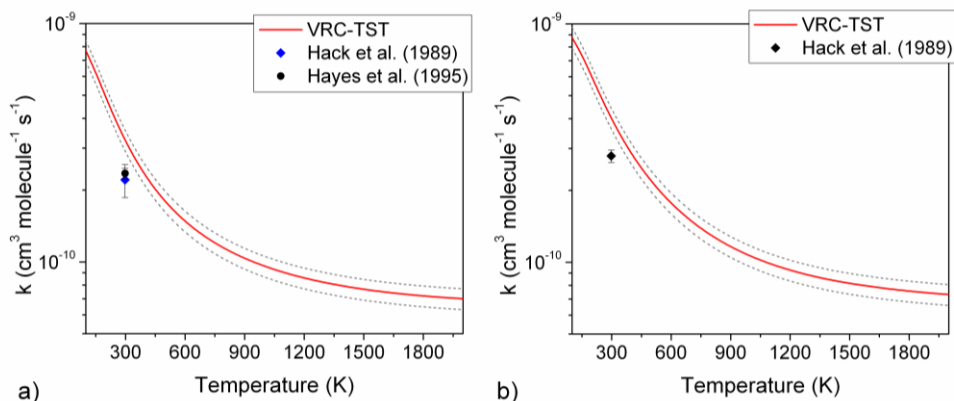


**Figure 85.** VRC-TST high-pressure limit rate coefficient (solid red line) for (a)  $^1\text{CH}_2 + a\text{C}_3\text{H}_4$  and (b)  $^1\text{CH}_2 + \text{C}_4\text{H}_6$  with 10% confidence limit compared with experimental measurements (symbols).

$^1\text{CH}_2 + \text{benzene}$ 

In our analysis of the potential energy surface for the addition of singlet methylene to benzene we found that the magnitude of the interaction energy does not increase smoothly along the reaction coordinate. Instead, it shows a slope change at a distance of 2.3-2.4 Å, suggesting the presence of a saddle point, as illustrated in **Figure 86**. This behavior can be ascribed to the necessity to break the resonance within the aromatic ring in order to form a new bond with the methylene carbon atom. Furthermore, the difficulty of forming bicyclic compounds may also contribute to this change in the form of the potential energy surface. Saddle point searches at the CASPT2/cc-pVDZ level were unsuccessful, while CCSD(T)/CBS calculations along the minimum energy path showed a reduced variation of the slope, confirming the absence of a saddle point. Thus, the variable reaction coordinate TST approach was again used to predict the high-pressure addition rate coefficient as described in section 8.2.

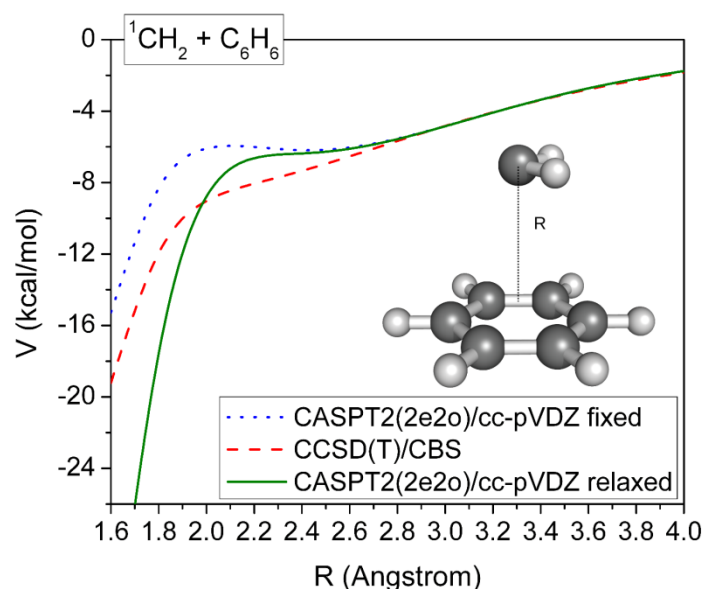


**Figure 86.** Potential energy surface for the  $^1\text{CH}_2 + \text{C}_6\text{H}_6$  reaction evaluated at the CASPT2/cc-pVDZ level (blue fine dashed) and CCSD(T)/CBS level (red dashed) keeping the geometries of the approaching fragments fixed, and at the CASPT2/cc-pVDZ level (green solid) allowing the relaxation of the internal degrees of freedom of the two reactants.

The predicted addition rate constant is plotted in **Figure 87** along with the experimental data from the works of Hack et al.,<sup>355</sup> Wagener,<sup>356</sup> and Hayes et al.<sup>359</sup> Again, the agreement with their measurements is satisfactory, as we underestimate their values by less than a factor of two, which is essentially within the error bars. Yet again, it is possible that abstraction here plays an important role due to the greatly reduced addition rate

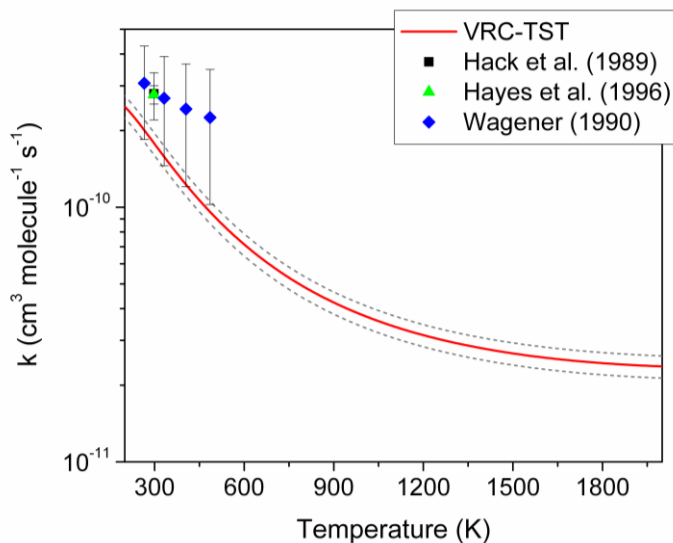


**Figure 87.** VRC-TST predicted high-pressure limit rate coefficient (solid red line) for  $^1\text{CH}_2 + \text{C}_6\text{H}_6$  with 10% limit confidence compared with experimental measurements (symbols).

### 8.3.3. General observations

The generally good agreement found in the comparisons with experimental data suggests that the dynamically corrected VRC-TST approach adopted in this study provides a reliable treatment of the high-pressure rate coefficients for the addition of singlet methylene to unsaturated hydrocarbons. The reliability of the present predictions suggests that it may also be worthwhile to analyze the reactivity trends for singlet methylene addition across the series of alkenes and alkynes investigated.

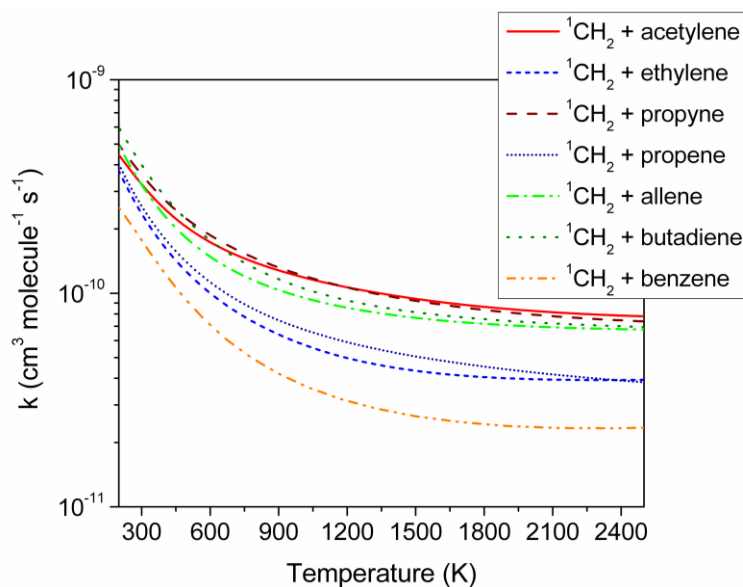


**Figure 88.** Temperature dependent VRC-TST high-pressure limit rate coefficients for all the  $^1\text{CH}_2 + \text{R}$  reactions considered in this work.

In **Figure 88** the calculated rate coefficients are plotted as function of temperature for all of the studied reactions. Examining this figure leads to the following observations:

- (i) While the rate coefficients for  $^1\text{CH}_2$  + acetylene and ethylene are very similar at room temperature, the relative reactivity of acetylene increases by up to a factor of two for temperatures above 900 K. Hence, the presence of the triple bond enhances the rate for addition of singlet methylene. This increase is likely related to the fact that the methylene can now attack the bond from all sides. Furthermore, there is also less steric hindrance.
- (ii) The addition of a  $\text{CH}_3$  substituent to acetylene does not significantly affect the rate for addition of methylene to the triple bond. In fact only a deviation of 10% is registered, which falls within the confidence limit used in our Monte Carlo simulations.
- (iii) When we add a  $\text{CH}_3$  substituent to ethylene (e.g. calculating the rates of methylene recombination with propene) the reactivity increases slightly (by up to about 20%). This result is in contrast with what we expected. In fact, the presence of a methyl group should increase the steric hindrances to the formation of the new bond and reduce the rate constant, as was found for the alkyl + alkyl recombination reactions. However, inspection of the two potential energy surfaces reveals a more attractive character for the propene +  $^1\text{CH}_2$  potential along its minimum energy path as compared to that for ethylene +  $^1\text{CH}_2$ . This effect can be attributed to the methyl group being an electron-donor substituent, which leads to an increase of the electron density of the double bond, thereby facilitating its addition to the lowest unoccupied pi orbital of methylene. Furthermore, the increased molecular size correlates with greater dispersion interactions. Overall, the increased attractiveness largely cancels the effect of the increased steric hindrance and the two rate coefficients are rather similar.
- (iv) The reactivity of allene and butadiene gives important information on the effect that the presence of a second double bond has on the reactivity of methylene with olefins. With two double bonds, there are two points of attack, and so we expect their rate of addition to be  $\sim 2$  times higher than for ethylene. This hypothesis was confirmed at high temperatures (above 1000 K) for which the  $^1\text{CH}_2$  + allene and butadiene rate coefficients are greater than for ethylene by factors of 1.7 and 1.8, respectively. As was found for the combination of alkyl radicals, at very low temperatures, the rate coefficients are instead predicted to be nearly independent of size.
- (v) For the recombination of methylene with benzene, the predicted rate coefficient is the lowest for the whole series of unsaturated hydrocarbons for the full range of temperatures considered. At high temperatures, the addition of singlet methylene to benzene is slower than that to acetylene and ethylene by factors of 3 and 1.6, respectively. This

result is a consequence of the less attractive potential energy surface and suggests that the reactivity of carbenes with aromatic species is in general lower than for other classes of unsaturated hydrocarbons.

This reduced rate coefficient also correlates with a decreased bond energy for the bicyclic complex that is formed by the direct addition to benzene. For comparison purposes we report in **Table 24** the zero-point corrected bond energies for a number of  $^1\text{CH}_2$  addition complexes. These bond energies were obtained at the RQCISD(T)/CBS//B3LYP/6-311++G(d,p) level based on explicit calculations for the cc-pVTZ and cc-pVQZ basis sets. Notably, for benzene the bond energy is about 30 kcal/mol less for the other alkene cases. Interestingly, the bond energies for the alkynes are also about 10 kcal/mol lower, although this does not appear to have a similar bearing on the rate coefficient.

**Table 24.** Direct addition bond strengths for  $^1\text{CH}_2 + \text{unsaturated hydrocarbons}$ .

Reactant	$D_0$ (kcal/mol)
$\text{C}_2\text{H}_2$	87.1
$\text{C}_2\text{H}_4$	99.4
p $\text{C}_3\text{H}_4$	87.2
$\text{C}_3\text{H}_6$	98.8
a $\text{C}_3\text{H}_4$	99.1
$\text{C}_4\text{H}_6$	96.9
$\text{C}_6\text{H}_6$	69.9
$\text{C}_6\text{H}_{10}$	92.9

## 8.4. Conclusion

The present theoretical approach has proven to be an effective strategy for the estimation of the high-pressure rate coefficients for the addition of singlet methylene to unsaturated hydrocarbons. Specifically, the CASPT2 method was demonstrated to yield a valid procedure for the direct evaluation of the interaction energies within variable reaction coordinate transition state theory. The introduction of the one-dimensional correction potential yields predicted rate coefficients that are in good agreement with the available experimental data. The effects due to the relaxation of the conserved modes are particularly significant. Overall, we estimate the present rate predictions to be accurate to within about +/- 25%.

The present dynamically corrected VRC-TST rate coefficients are reproduced reasonably well (errors <10%) by the following modified Arrhenius expressions:

$2.74 \times 10^{-9} T^{-0.474} \exp(155.6/T)$	${}^1\text{CH}_2 + \text{C}_2\text{H}_2$
$9.29 \times 10^{-10} T^{-0.444} \exp(329/T)$	${}^1\text{CH}_2 + \text{C}_2\text{H}_4$
$6.39 \times 10^{-9} T^{-0.589} \exp(131.9/T)$	${}^1\text{CH}_2 + \text{pC}_3\text{H}_4$
$2.82 \times 10^{-9} T^{-0.570} \exp(239.1/T)$	${}^1\text{CH}_2 + \text{C}_3\text{H}_6$
$7.98 \times 10^{-10} T^{-0.345} \exp(298/T)$	${}^1\text{CH}_2 + \text{aC}_3\text{H}_4$
$2.27 \times 10^{-9} T^{-0.476} \exp(272.8/T)$	${}^1\text{CH}_2 + \text{C}_4\text{H}_6$
$1.35 \times 10^{-9} T^{-0.559} \exp(323.9/T)$	${}^1\text{CH}_2 + \text{C}_6\text{H}_6$

In these expressions, T is the temperature in K, and the rate coefficients are in  $\text{cm}^3 \text{ molecule}^{-1} \text{ s}^{-1}$ . These expressions are valid over the 250-2000 K temperature range.

These theoretical results provide new insight into the reactivity of singlet methylene with unsaturated hydrocarbons. The faster addition of  ${}^1\text{CH}_2$  to acetylene and propyne indicates a higher reactivity of the triple bond as compared with the double bond of ethylene and propene. Moreover, it has been found that this reactivity is not strongly affected by the size of the unsaturated reactant. Comparison between the reaction of methylene with allene or butadiene and the reaction with ethylene showed that the presence of two double bonds increases the total rate of addition by nearly a factor of 2. The rate coefficient for the recombination of methylene with benzene is the slowest of the series, showing that addition of singlet methylene to aromatic species is less favored, compared to other unsaturated hydrocarbons.

Notably, each of the rate coefficients is predicted to decrease by a factor of 5 to 10 as the temperature increases from 300 to 2000 K. Nevertheless, all reactions present a very high rate of recombination suggesting the importance of these reactions in combustion environments.

The present study has focused on the addition of the simplest carbene ( ${}^1\text{CH}_2$ ), but the reliability of the present approach opens the possibility to extend the same procedure to the addition of other important carbenes to unsaturated hydrocarbons, such as ethylidene ( $\text{CH}_3\text{CH}$ ) and vinylidene ( $\text{CH}_2\text{C}$ ). Barrierless reactions of such carbenes with other unsaturated hydrocarbons are also expected to be of importance in combustion and pyrolysis environments.

# 9 Conclusions

---

In this PhD thesis, the major limitations of transition state theory have been assessed and ad hoc methodologies that overcome these limits have been studied and implemented. In particular, we have been able to address spin forbidden reactions, hindered rotors, multi-well and multi-channel potential energy surfaces, tunneling corrections and a microcanonical description of bimolecular reactions. The methods implemented allowed us to study a number of reactions of scientific interest.

In particular, in the course of the present project, we first investigated the dissociation kinetics of germane and its decomposition products. It was found that the main decomposition channel leads to the formation of germylene, which rapidly decomposes to atomic Ge and H<sub>2</sub>. The dissociation of GeH<sub>2</sub> to Ge and H<sub>2</sub> is a formally spin forbidden reaction. Thus, the intersystem crossing probability was explicitly included in the microcanonical simulations through Landau–Zener theory. Kinetic constants of the main decomposition channels were determined as a function of pressure and temperature between 0.0013 and 10 bar and 1100 and 1700 K and a quantitative agreement with experimental data for GeH<sub>4</sub> decomposition was obtained.

This study was followed by a thorough investigation of the reaction pathways active within toluene pyrolysis secondary chemistry, which allowed us to assess the approach implemented to treat multi-well reactions. Specifically, the reactivity and decomposition kinetics on the C<sub>7</sub>H<sub>6</sub> potential energy surface were first investigated. This analysis revealed that two main decomposition channels are possible with equal probability after visiting a potential energy surface comprised of 10 wells and 11 transition states. The first is active on the singlet PES leading to the formation of the fulvenallenyl radical and atomic hydrogen. The second instead requires intersystem crossing to the triplet PES and leads to acetylene and cyclopentadienylidene. Channel specific rate coefficients were determined as a function of temperature and pressure.

After this investigation, due to inconsistencies between our theoretical results and new experimental evidences, we were directed to re-explore benzyl decomposition mechanism. This research allowed us to individuate a new pathway active during benzyl decomposition, which yields benzyne and a methyl radical. The reaction dynamics that take place over the new PES was simulated through ME/RRKM calculations and channel specific rate coefficients were calculated. These findings allowed us to build a new kinetic scheme able to reproduce fairly well the experimental data reported by different authors on toluene and benzyl decomposition.

Afterwards, two reactions active during cyclopentadiene pyrolysis were studied: the recombination of two cyclopentadienyl radicals and the addition of a cyclopentadienyl radical to a

cyclopentadiene molecule. New routes to the production of naphthalene in the first case and indene in the second have been proposed. The rate coefficients calculated with the methodology developed here were included in the overall POLIMI\_1202 kinetic model and allowed to reproduce properly the experimental concentration profiles of key species, such as naphthalene, indene and styrene. This study permitted us to appraise the ability of our treatment to describe correctly microcanonical bimolecular reactions.

Later, we concentrated on hydrogen transfer reactions, which are characterized by the tunneling phenomenon. Specifically, we implemented the SCT theory of Truhlar and coworkers to calculate the tunneling correction. The ability of this method to properly describe tunneling effects was tested by studying the  $\text{CH}_4 + \text{H}$  benchmark reaction. A sensitivity analysis was also performed on the main parameters that enter as input data and the results were compared with the rate coefficient suggested by Sutherland and coworkers. Our analysis revealed the critical role that the accuracy of the activation energy and the minimum energy path plays on the prediction of the rate coefficient. Overall, the methodology implemented provided a rate coefficient that is in good agreement with the reference value of Sutherland et al. and with the predictions obtained with other theoretical approaches that are more sophisticated.

Finally, a study on a specific class of reactions was performed in collaboration with Dr. Stephen J. Klippenstein, which confirmed the reliability of the multifaceted VRC-TST approach. The present theoretical approach in fact has proven to be an effective strategy for the estimation of the high-pressure rate coefficients for the addition of singlet methylene to unsaturated hydrocarbons. Specifically, the CASPT2 method was demonstrated to yield a valid procedure for the direct evaluation of the interaction energies within variable reaction coordinate transition state theory. Moreover, the introduction of the one-dimensional correction potential yielded predicted rate coefficients that are in good agreement with the available experimental data.

As evidenced by the investigations performed during the course of this PhD thesis, the methods studied and implemented permitted us to improve our understanding of a number of reactions of scientific interest. However, the methodology presented can be still subject to development. One of the aspects that can be improved, for example, is the solution of the master equation for multi-well PES. A limit common to all the master equation solvers available in the literature in fact consists in the inability to treat a 2D master equation in which, number of states, microcanonical rate coefficients and energy transfer probabilities depend not only on the energy level but also on the angular momentum. Another area where there is space to improvement is the kinetics of reactions involving macromolecules, such as polymers. In these cases in fact the entropic factor corresponding to the number of configurations available to the molecule in the course of the reaction may be important, thus an appropriate method is needed.

In conclusion, we can say that great progress has been achieved in our ability to model the kinetics of gas phase reactions, but we anticipate that continued improvements will follow this research project.



# References

---

- (1) Frisch, M. J.; Trucks, G. W.; Schlegel, H. B.; Scuseria, G. E.; Robb, M. A.; Cheeseman, J. R.; Montgomery, J. A.; Vreven, T.; Kudin, K. N.; Burant, J. C.; Millam, J. M.; Iyengar, S. S.; Tomasi, J.; Barone, V.; Mennucci, B.; Cossi, M.; Scalmani, G.; Rega, N.; Petersson, G. A.; Nakatsuji, H.; Hada, M.; Ehara, M.; Toyota, K.; Fukuda, R.; Hasegawa, J.; Ishida, M.; Nakajima, T.; Honda, Y.; Kitao, O.; Nakai, H.; Klene, M.; Li, X.; Knox, J. E.; Hratchian, H. P.; Cross, J. B.; Bakken, V.; Adamo, C.; Jaramillo, J.; Gomperts, R.; Stratmann, R. E.; Yazyev, O.; Austin, A. J.; Cammi, R.; Pomelli, C.; Ochterski, J. W.; Ayala, P. Y.; Morokuma, K.; Voth, G. A.; Salvador, P.; Dannenberg, J. J.; Zakrzewski, V. G.; Dapprich, S.; Daniels, A. D.; Strain, M. C.; Farkas, O.; Malick, D. K.; Rabuck, A. D.; Raghavachari, K.; Foresman, J. B.; Ortiz, J. V.; Cui, Q.; Baboul, A. G.; Clifford, S.; Cioslowski, J.; Stefanov, B. B.; Liu, G.; Liashenko, A.; Piskorz, P.; Komaromi, I.; Martin, R. L.; Fox, D. J.; Keith, T.; Al-Laham, M. A.; Peng, C. Y.; Nanayakkara, A.; Challacombe, M.; Gill, P. M. W.; Johnson, B.; Chen, W.; Wong, M. W.; Gonzalez, C.; Pople, J. A. Gaussian 03 (Revision B.05); Gaussian, Inc.: Pittsburgh, PA, 2003.
- (2) Frisch, M. J. T., G. W.; Schlegel, H. B.; Scuseria, G. E.; Robb, M. A.; Cheeseman, J. R.; Scalmani, G.; Barone, V.; Mennucci, B.; Petersson, G. A.; Nakatsuji, H.; Caricato, M.; Li, X.; Hratchian, H. P.; Izmaylov, A. F.; Bloino, J.; Zheng, G.; Sonnenberg, J. L.; Hada, M.; Ehara, M.; Toyota, K.; Fukuda, R.; Hasegawa, J.; Ishida, M.; Nakajima, T.; Honda, Y.; Kitao, O.; Nakai, H.; Vreven, T.; Montgomery, Jr., J. A.; Peralta, J. E.; Ogliaro, F.; Bearpark, M.; Heyd, J. J.; Brothers, E.; Kudin, K. N.; Staroverov, V. N.; Kobayashi, R.; Normand, J.; Raghavachari, K.; Rendell, A.; Burant, J. C.; Iyengar, S. S.; Tomasi, J.; Cossi, M.; Rega, N.; Millam, N. J.; Klene, M.; Knox, J. E.; Cross, J. B.; Bakken, V.; Adamo, C.; Jaramillo, J.; Gomperts, R.; Stratmann, R. E.; Yazyev, O.; Austin, A. J.; Cammi, R.; Pomelli, C.; Ochterski, J. W.; Martin, R. L.; Morokuma, K.; Zakrzewski, V. G.; Voth, G. A.; Salvador, P.; Dannenberg, J. J.; Dapprich, S.; Daniels, A. D.; Farkas, Ö.; Foresman, J. B.; Ortiz, J. V.; Cioslowski, J.; Fox, D. J. . Gaussian 09, Revision A.1; Gaussian Inc.: Wallingford CT, 2009.
- (3) Werner, H.-J.; Knowles, P. J.; Lindh, R.; Manby, F. R.; Schütz, M.; Celani, P.; Korona, T.; Mitrushenkov, A.; Rauhut, G.; Adler, T. B.; Amos, R. D.; Bernhardsson, A.; Berning, A.; Cooper, D. L.; Deegan, M. J. O.; Dobbyn, A. J.; Eckert, F.; Goll, E.; Hampel, C.; Hetzer, G.; Hrenar, T.; Knizia, G.; Köppl, C.; Liu, Y.; Lloyd, A. W.; Mata, R. A.; May, A. J.; McNicholas, S. J.; Meyer, W.; Mura, M. E.; Nicklaß, A.; Palmieri, P.; Pflüger, K.; Pitzer, R.; Reiher, M.; Schumann, U.; Stoll, H.; Stone, A. J.; Tarroni, R.; Thorsteinsson, T.; Wang, M.; Wolf, A. MOLPRO 2008.1.
- (4) Werner, H.-J.; Knowles, P. J.; Knizia, G.; Manby, F. R.; M. Schütz, M.; Celani, P.; Korona, T.; Lindh, R.; Mitrushenkov, A.; Rauhut, G.; Shamasundar, K. R.; Adler, T. B.; Amos, R. D.; Bernhardsson, A.; Berning, A.; Cooper, D. L.; Deegan, M. J. O.; Dobbyn, A. J.; Eckert, F.; Goll, E.; Hampel, C.; Hesselmann, A.; Hetzer, G.; Hrenar, T.; Jansen, G.; Köppl, C.; Liu, Y.; Lloyd, A. W.; Mata, R. A.; May, A. J.; McNicholas, S. J.; Meyer, W.; Mura, M. E.; Nicklass, A.; O'Neill, D. P.; Palmieri, P.; Pflüger, K.; Pitzer, R.; Reiher, M.; Shiozaki, T.; Stoll, H.; Stone, A. J.; Tarroni, R.; Thorsteinsson, T.; Wang, M.; Wolf, A. MOLPRO, version 2010.1, a package of ab initio programs, see <http://www.molpro.net>.
- (5) Schmidt, M. W.; Baldridge, K. K.; Boatz, J. A.; Elbert, S. T.; Gordon, M. S.; Jensen, J. H.; Koseki, S.; Matsunaga, N.; Nguyen, K. A.; Su, S. J.; Windus, T. L.; Dupuis, M.; Montgomery, J. A. *Journal of Computational Chemistry* **1993**, *14*, 1347.
- (6) Gordon, M. S.; Schmidt, M. W. Advances in electronic structure theory: GAMESS a decade later. In *Theory and Applications of Computational Chemistry: the first forty years*;

- Dykstra, C. E., G., F., Kim, K. S., Scuseria, G. E., Eds.; Elsevier: Amsterdam, 2005; pp 1167.
- (7) Jensen, F. *Introduction to Computational Chemistry*; John Wiley & Sons: Chichester, 1999.
- (8) Knowles, P. J.; Werner, H. J. *Chemical Physics Letters* **1985**, *115*, 259.
- (9) Werner, H. J.; Knowles, P. J. *J. Chem. Phys.* **1985**, *82*, 5053.
- (10) Werner, H. J. *Molecular Physics* **1996**, *89*, 645.
- (11) Celani, P.; Werner, H. J. *J. Chem. Phys.* **2000**, *112*, 5546.
- (12) Georgievskii, Y.; Miller, J. A.; Klippenstein, S. J. *Physical Chemistry Chemical Physics* **2007**, *9*, 4259.
- (13) Harding, L. B.; Georgievskii, Y.; Klippenstein, S. J. *Journal of Physical Chemistry A* **2005**, *109*, 4646.
- (14) Klippenstein, S. J.; Georgievskii, Y.; Harding, L. B. *Physical Chemistry Chemical Physics* **2006**, *8*, 1133.
- (15) Raghavachari, K.; Trucks, G. W.; Pople, J. A.; Headgordon, M. *Chemical Physics Letters* **1989**, *157*, 479.
- (16) Hohenberg, P.; Kohn, W. *Physical Review* **1964**, *136*, B864.
- (17) Lee, C.; Yang, W.; Parr, R. G. *Physical Review B* **1988**, *37*, 785.
- (18) Becke, A. D. *J. Chem. Phys.* **1993**, *98*, 5648.
- (19) Zhao, Y.; Truhlar, D. G. *Theoretical Chemistry Accounts* **2008**, *120*, 215.
- (20) Curtiss, L. A.; Jones, C.; Trucks, G. W.; Raghavachari, K.; Pople, J. A. *J. Chem. Phys.* **1990**, *93*, 2537.
- (21) Curtiss, L. A.; Raghavachari, K.; Pople, J. A. *J. Chem. Phys.* **1995**, *103*, 4192.
- (22) Curtiss, L. A.; Raghavachari, K.; Redfern, P. C.; Rassolov, V.; Pople, J. A. *J. Chem. Phys.* **1998**, *109*, 7764.
- (23) Curtiss, L. A.; Raghavachari, K.; Trucks, G. W.; Pople, J. A. *J. Chem. Phys.* **1991**, *94*, 7221.
- (24) Curtiss, L. A.; Redfern, P. C.; Raghavachari, K. *J. Chem. Phys.* **2007**, *127*.
- (25) Curtiss, L. A.; Redfern, P. C.; Raghavachari, K. *J. Chem. Phys.* **2007**, *126*.
- (26) Curtiss, L. A.; Redfern, P. C.; Rassolov, V.; Kedziora, G.; Pople, J. A. *J. Chem. Phys.* **2001**, *114*, 9287.
- (27) Montgomery, J. A.; Frisch, M. J.; Ochterski, J. W.; Petersson, G. A. *J. Chem. Phys.* **1999**, *110*, 2822.
- (28) Montgomery, J. A.; Frisch, M. J.; Ochterski, J. W.; Petersson, G. A. *J. Chem. Phys.* **2000**, *112*, 6532.
- (29) Montgomery, J. A.; Ochterski, J. W.; Petersson, G. A. *J. Chem. Phys.* **1994**, *101*, 5900.
- (30) Nyden, M. R.; Petersson, G. A. *The Journal of Chemical Physics* **1981**, *75*, 1843.
- (31) Ochterski, J. W.; Petersson, G. A.; Montgomery, J. A. *J. Chem. Phys.* **1996**, *104*, 2598.
- (32) Petersson, G. A.; Allaham, M. A. *J. Chem. Phys.* **1991**, *94*, 6081.
- (33) Petersson, G. A.; Tensfeldt, T. G.; Montgomery, J. A. *J. Chem. Phys.* **1991**, *94*, 6091.
- (34) Boese, A. D.; Oren, M.; Atasoylu, O.; Martin, J. M. L.; Kallay, M.; Gauss, J. *J. Chem. Phys.* **2004**, *120*, 4129.
- (35) Karton, A.; Rabinovich, E.; Martin, J. M. L.; Ruscic, B. *J. Chem. Phys.* **2006**, *125*.
- (36) Martin, J. M. L.; de Oliveira, G. *J. Chem. Phys.* **1999**, *111*, 1843.
- (37) Martin, J. M. L.; De Oliveira, G. *Abstracts of Papers of the American Chemical Society* **2000**, *219*, U591.
- (38) Parthiban, S.; Martin, J. M. L. *J. Chem. Phys.* **2001**, *114*, 6014.
- (39) Karton, A.; Martin, J. M. L. *J. Chem. Phys.* **2012**, *136*.
- (40) Bomble, Y. J.; Vazquez, J.; Kallay, M.; Michauk, C.; Szalay, P. G.; Csaszar, A. G.; Gauss, J.; Stanton, J. F. *J. Chem. Phys.* **2006**, *125*.
- (41) Harding, M. E.; Vazquez, J.; Ruscic, B.; Wilson, A. K.; Gauss, J.; Stanton, J. F. *J. Chem. Phys.* **2008**, *128*.
- (42) Tajti, A.; Szalay, P. G.; Csaszar, A. G.; Kallay, M.; Gauss, J.; Valeev, E. F.; Flowers, B. A.; Vazquez, J.; Stanton, J. F. *J. Chem. Phys.* **2004**, *121*, 11599.

- (43) Gilbert, R. G.; Smith, S. C. *Theory of Unimolecular and Recombination Reactions*; Blackwell Scientific Publications: Oxford, 1990.
- (44) Alexander, M. H. *Science* **2011**, *331*, 411.
- (45) Eyring, H. *The Journal of Chemical Physics* **1935**, *3*, 107.
- (46) Evans, M. G.; Polanyi, M. *Transactions of the Faraday Society* **1935**, *31*, 875.
- (47) Wigner, E. *Transactions of the Faraday Society* **1938**, *34*, 29.
- (48) Lindemann, F. A.; Arrhenius, S.; Langmuir, I.; Dhar, N. R.; Perrin, J.; McC. Lewis, W. C. *Transactions of the Faraday Society* **1922**, *17*, 598.
- (49) Rice, O. K.; Ramsperger, H. C. *Journal of the American Chemical Society* **1927**, *49*, 1617.
- (50) Kassel, L. S. *The Journal of Physical Chemistry* **1927**, *32*, 1065.
- (51) Kassel, L. S. *The Journal of Physical Chemistry* **1927**, *32*, 225.
- (52) Marcus, R. A. *The Journal of Chemical Physics* **1952**, *20*, 359.
- (53) Georgievskii, Y.; Klippenstein, S. J. *Journal of Physical Chemistry A* **2003**, *107*, 9776.
- (54) Georgievskii, Y.; Klippenstein, S. J. *J. Chem. Phys.* **2003**, *118*, 5442.
- (55) Klippenstein, S. J. *J. Chem. Phys.* **1991**, *94*, 6469.
- (56) Klippenstein, S. J. *J. Chem. Phys.* **1992**, *96*, 367.
- (57) Klippenstein, S. J.; Allen, W. D. *Berichte der Bunsen-Gesellschaft fuer Physikalische Chemie* **1997**, *101*, 423.
- (58) Klippenstein, S. J.; Georgievskii, Y.; Harding, L. B. *Proceedings of the Combustion Institute* **2002**, *29*, 1229.
- (59) Klippenstein, S. J.; Harding, L. B.; Georgievskii, Y. *Proceedings of the Combustion Institute* **2007**, *31*, 221.
- (60) Glowacki, D. R.; Liang, C.-H.; Morley, C.; Pilling, M. J.; Robertson, S. H. *The Journal of Physical Chemistry A* **2012**, *116*, 9545.
- (61) Barker, J. R. *International Journal of Chemical Kinetics* **2001**, *33*, 232.
- (62) Vereecken, L.; Huyberechts, G.; Peeters, J. *The Journal of Chemical Physics* **1997**, *106*, 6564.
- (63) Klippenstein, S. J.; Wagner, A. F.; Dunbar, R. C.; Wardlaw, D. M.; Robertson, S.; Miller, J. A. VARIFLEX; 1.14m ed., 2005.
- (64) Frankcombe, T. J.; Smith, S. C. *The Journal of Chemical Physics* **2003**, *119*, 12729.
- (65) Sherrill, C. D.; Schaefer Iii, H. F. The Configuration Interaction Method: Advances in Highly Correlated Approaches. In *Advances in Quantum Chemistry*; Per-Olov Löwdin, J. R. S. M. C. Z., Erkki, B., Eds.; Academic Press, 1999; Vol. Volume 34; pp 143.
- (66) Schmidt, M. W.; Gordon, M. S. *Annu. Rev. Phys. Chem.* **1998**, *49*, 233.
- (67) Møller, C.; Plesset, M. S. *Physical Review* **1934**, *46*, 618.
- (68) Bartlett, R. J. *The Journal of Physical Chemistry* **1989**, *93*, 1697.
- (69) Barbato, A. Multiscale simulations of the production process of advanced materials by chemical vapor deposition. PhD Thesis, Politecnico di Milano, 2008.
- (70) Barbato, A.; Seghi, C.; Cavallotti, C. *J. Chem. Phys.* **2009**, *130*, 074108.
- (71) Miller, J. A.; Klippenstein, S. J.; Raffy, C. *Journal of Physical Chemistry A* **2002**, *106*, 4904.
- (72) Reid, R. C.; Prausnitz, J. M.; Sherwood, T. K. *The Properties of Gases and Liquids*, 3rd ed.; McGraw-Hill: New Yoork, 1977.
- (73) Zener, C. *Proceedings of the Royal Society of London. Series A* **1932**, *137*, 696.
- (74) Landau, L. D. *Phys. Z. Sowjetunion* **1932**, *2*, 46.
- (75) Harvey, J. N. *Physical Chemistry Chemical Physics* **2007**, *9*, 331.
- (76) Pitzer, K. S.; Gwinn, W. D. *The Journal of Chemical Physics* **1942**, *10*, 428.
- (77) Pfaendtner, J.; Yu, X.; Broadbelt, L. *Theoretical Chemistry Accounts* **2007**, *118*, 881.
- (78) East, A. L. L.; Radom, L. *The Journal of Chemical Physics* **1997**, *106*, 6655.
- (79) Fascella, S.; Cavallotti, C.; Rota, R.; Carra, S. *Journal of Physical Chemistry A* **2004**, *108*, 3829.
- (80) Van Speybroeck, V.; Van Neck, D.; Waroquier, M.; Wauters, S.; Saeys, M.; Marin, G. B. *The Journal of Physical Chemistry A* **2000**, *104*, 10939.
- (81) Astholz, D. C.; Troe, J.; Wieters, W. *J. Chem. Phys.* **1979**, *70*.

- (82) Widom, B. *Science* **1965**, *148*, 1555.
- (83) Miller, J. A.; Klippenstein, S. J. *The Journal of Physical Chemistry A* **2006**, *110*, 10528.
- (84) Shavitt, I. *The Journal of Chemical Physics* **1959**, *31*, 1359.
- (85) Wigner, E. *The Journal of Chemical Physics* **1937**, *5*, 720.
- (86) Bell, R. P. *The Tunnel Effect in Chemistry*; Chapman and Hall: London, 1980.
- (87) Eckart, C. *Phys. Rev.* **1930**, *35*, 1303.
- (88) Marcus, R. A.; Coltrin, M. E. *J. Chem. Phys.* **1977**, *67*, 2609.
- (89) Miller, W. H.; Handy, N. C.; Adams, J. E. *J. Chem. Phys.* **1980**, *72*, 99.
- (90) Skodje, R. T.; Truhlar, D. G.; Garrett, B. C. *Journal of Physical Chemistry* **1981**, *85*, 3019.
- (91) Lu, D.-h.; Truong, T. N.; Melissas, V. S.; Lynch, G. C.; Liu, Y.-P.; Garrett, B. C.; Steckler, R.; Isaacson, A. D.; Rai, S. N.; Hancock, G. C.; Lauderdale, J. G.; Joseph, T.; Truhlar, D. G. *Computer Physics Communications* **1992**, *71*, 235.
- (92) Marcus, R. A. *J. Chem. Phys.* **1965**, *43*, 1598.
- (93) Miller, W. H. *Faraday Discussions of the Chemical Society* **1977**, *62*, 40.
- (94) Razavy, M. *Quantum Theory of Tunneling*, 1st ed.; World Scientific Publishing Company, 2003.
- (95) Connor, J. N. L. *Molecular Physics* **1968**, *15*.
- (96) Porter, R. N.; Karplus, M. *J. Chem. Phys.* **1964**, *40*, 1105.
- (97) Marcus, R. A. *J. Chem. Phys.* **1964**, *41*, 610.
- (98) Kuppermann, A.; Truhlar, D. G. *Journal of the American Chemical Society* **1971**, *93*, 1840.
- (99) Page, M.; McIver, J. J. W. *J. Chem. Phys.* **1988**, *88*, 922.
- (100) Klippenstein, S. J. *Journal of Physical Chemistry* **1994**, *98*, 11459.
- (101) Wardlaw, D. M.; Marcus, R. A. *The Journal of Chemical Physics* **1985**, *83*, 3462.
- (102) Miller, W. H. *The Journal of Chemical Physics* **1976**, *65*, 2216.
- (103) Smith, S. C. *The Journal of Chemical Physics* **1999**, *111*, 1830.
- (104) Robertson, S.; Wagner, A. F.; Wardlaw, D. M. *The Journal of Chemical Physics* **2000**, *113*, 2648.
- (105) Cavallotti, C.; Di Stanislao, M.; Carrà, S. *Progress in Crystal Growth and Characterization of Materials* **2004**, *48–49*, 123.
- (106) Binning, R. C.; Curtiss, L. A. *J. Chem. Phys.* **1990**, *92*, 1860.
- (107) Chambreau, S. D.; Zhang, J. S. *Chemical Physics Letters* **2002**, *351*, 171.
- (108) Dakternieks, D.; Henry, D. J.; Schiesser, C. H. *Organometallics* **1998**, *17*, 1079.
- (109) Das, K. K.; Balasubramanian, K. *J. Chem. Phys.* **1990**, *93*, 5883.
- (110) Duchowicz, P. R.; Cobos, C. J. *Journal of Physical Chemistry A* **2008**, *112*, 6198.
- (111) Dylla, K. G. *J. Chem. Phys.* **1992**, *96*, 1210.
- (112) Grev, R. S.; Schaefer Iii, H. F.; Baeins, K. M. *Journal of the American Chemical Society* **1990**, *112*, 9458.
- (113) Gunn, S. R.; Green, L. G. *Journal of Physical Chemistry* **1961**, *65*, 779.
- (114) Karolczak, J.; Harper, W. W.; Grev, R. S.; Clouthier, D. J. *J. Chem. Phys.* **1995**, *103*, 2839.
- (115) Koizumi, H.; Davalos, J. Z.; Baer, T. *Chemical Physics* **2006**, *324*, 385.
- (116) Li, Q. S.; Lu, R. H.; Xie, Y. M.; Schaefer Iii, H. F. *Journal of Computational Chemistry* **2002**, *23*, 1642.
- (117) Mayer, P. M.; Gal, J. F.; Radom, L. *International Journal of Mass Spectrometry* **1997**, *167*, 689.
- (118) Noble, P. N.; Walsh, R. *International Journal Of Chemical Kinetics* **1983**, *15*, 547.
- (119) Ricca, A.; Bauschlicher, C. W. *Journal of Physical Chemistry A* **1999**, *103*, 11121.
- (120) Ruscic, B.; Schwarz, M.; Berkowitz, J. *J. Chem. Phys.* **1990**, *92*, 1865.
- (121) Su, M. D.; Chu, S. Y. *Journal of the American Chemical Society* **1999**, *121*, 11478.
- (122) Su, M. D.; Chu, S. Y. *Journal of the American Chemical Society* **1999**, *121*, 4229.
- (123) Wang, L. M.; Zhang, J. S. *Journal of Physical Chemistry A* **2004**, *108*, 10346.
- (124) Wu, Y.; Ding, Y. H.; Xiao, J. F.; Li, Z. S.; Huang, X. R.; Sun, C. C. *Journal of Computational Chemistry* **2002**, *23*, 1366.
- (125) Yockel, S.; Mintz, B.; Wilson, A. K. *J. Chem. Phys.* **2004**, *121*, 60.
- (126) Su, M. D.; Chu, S. Y. *Journal of the Chinese Chemical Society* **2000**, *47*, 135.

- (127) Reed, K. J.; Brauman, J. I. *J. Chem. Phys.* **1974**, *61*, 4830.
- (128) Berkowitz, J.; Ellison, G. B.; Gutman, D. *Journal of Physical Chemistry* **1994**, *98*, 2744.
- (129) Simka, H.; Hierlemann, M.; Utz, M.; Jensen, K. F. *Journal of the Electrochemical Society* **1996**, *143*, 2646.
- (130) Newman, C. G.; Dzarnoski, J.; Ring, M. A.; O'Neal, H. E. *International Journal Of Chemical Kinetics* **1980**, *2*, 661.
- (131) Smirnov, V. N. *Kinetics and Catalysis* **2007**, *48*, 615.
- (132) Votintsev, V. N.; Zaslanko, I. S.; Mikheev, V. S.; Smirnov, V. N. *Kinetics and Catalysis* **1986**, *26*, 1114.
- (133) Wilson, A. K.; Woon, D. E.; Peterson, K. A.; Dunning, T. H. *J. Chem. Phys.* **1999**, *110*, 7667.
- (134) Finley, J.; Malmqvist, P. A.; Roos, B. O.; Serrano-Andres, L. *Chemical Physics Letters* **1998**, *288*, 299.
- (135) Roos, B. O.; Andersson, K.; Fulscher, M. P.; Malmqvist, P. A.; Serrano-Andres, L.; Pierloot, K.; Merchán, M. Multiconfigurational perturbation theory: Applications in electronic spectroscopy. In *Advances in Chemical Physics, Vol Xciii*, 1996; Vol. 93; pp 219.
- (136) Martin, J. M. L. *Chemical Physics Letters* **1996**, *259*, 669.
- (137) Matsunaga, N.; Koseki, S.; Gordon, M. S. *The Journal of Chemical Physics* **1996**, *104*, 7988.
- (138) Werner, H. J.; Knowles, P. J. *J. Chem. Phys.* **1988**, *89*, 5803.
- (139) Knowles, P. J.; Werner, H. J. *Chemical Physics Letters* **1988**, *145*, 514.
- (140) Berning, A.; Schweizer, M.; Werner, H.-J.; Knowles, P. J.; Palmieri, P. *Molecular Physics* **2000**, *98*, 1823.
- (141) Becerra, R.; Boganov, S. E.; Egorov, M. P.; Faustov, V. I.; Nefedov, O. M.; Walsh, R. *Canadian Journal of Chemistry-Revue Canadienne De Chimie* **2000**, *78*, 1428.
- (142) Boganov, S. E.; Egorov, M. P.; Faustov, V. I.; Krylov, I. V.; Nefedov, O. M.; Becerra, R.; Walsh, R. *Russ Chem Bull* **2005**, *54*, 483.
- (143) Glushko, V. P.; Gurvich, L. V.; Bergman, G. A.; Veits, I. V.; Medvedev, V. A.; Khachukuruzov, G. A.; Yungman, V. S.; *Termodinamicheski Svoistva Individual' nikh Veshchestv*; Nauka: Moscow, 1979.
- (144) Becerra, R.; Boganov, S.; Walsh, R. *Journal of the Chemical Society, Faraday Transactions* **1998**, *94*, 3569.
- (145) Matsumoto, K.; Klippenstein, S. J.; Tonokura, K.; Koshi, M. *Journal of Physical Chemistry A* **2005**, *109*, 4911.
- (146) Dollet, A.; de Persis, S. *Journal of Analytical and Applied Pyrolysis* **2007**, *80*, 460.
- (147) Tanaka, T.; Hiramatsu, M.; Nawata, M.; Kono, A.; Goto, T. *Journal of Physics D: Applied Physics* **1994**, *27*, 1660.
- (148) Becerra, R.; Boganov, S. E.; Egorov, M. P.; Faustov, V. I.; Promyslov, V. M.; Nefedov, O. M.; Walsh, R. *Physical Chemistry Chemical Physics* **2002**, *4*, 5079.
- (149) Becerra, R.; Boganov, S. E.; Egorov, M. P.; Faustov, V. I.; Krylova, I. V.; Nefedov, O. M.; Promyslov, V. M.; Walsh, R. *Physical Chemistry Chemical Physics* **2007**, *9*, 4395.
- (150) Ackermann, L.; Hippler, H.; Pagsberg, P.; Reihs, C.; Troe, J. *Journal of Physical Chemistry* **1990**, *94*, 5247.
- (151) Astholz, D. C.; Durant, J.; Troe, J. *Proceedings of the Combustion Institute* **1980**, *18*, 809.
- (152) Braun-Unkoff, M.; Frank, P.; Just, T. *Proceedings of the Combustion Institute* **1988**, *22*, 1053.
- (153) Braun-Unkoff, M.; Frank, P.; Just, T. *Berichte Der Bunsen-Gesellschaft-Physical Chemistry Chemical Physics* **1990**, *94*, 1417.
- (154) Brooks, C. T.; Cummins, C. P. R.; Peacock, S. J. *Transactions of the Faraday Society* **1971**, *67*, 3265.
- (155) Colket, M. B.; Seery, D. J. *Proceedings of the Combustion Institute* **1994**, *25*, 883.
- (156) D'Alessio, J.; Lazzaro, M.; Massoli, P.; Moccia, V. *Optics and Lasers in Engineering* **2002**, *37*, 495.

- (157) Hippler, H.; Reihs, C.; Troe, J. *Zeitschrift Fur Physikalische Chemie Neue Folge* **1990**, *167*, 1.
- (158) Ikeda, N.; Nakashima, N.; Yoshihara, K. *J. Chem. Phys.* **1985**, *82*, 5285.
- (159) Luther, K.; Troe, J.; Weitzel, K. M. *Journal of Physical Chemistry* **1990**, *94*, 6316.
- (160) Pamidimukkala, K. M.; Kern, R. D.; Patel, M. R.; Wei, H. C.; Kiefer, J. H. *Journal of Physical Chemistry* **1987**, *91*, 2148.
- (161) Price, S. J. *Canadian Journal of Chemistry* **1962**, *40*, 1310.
- (162) Rao, V. S.; Skinner, G. B. *Proceedings of the Combustion Institute* **1986**, *21*, 809.
- (163) Sivaramakrishnan, R.; Brezinsky, K.; Vasudevan, H.; Tranter, R. S. *Combustion Science and Technology* **2006**, *178*, 285.
- (164) Sivaramakrishnan, R.; Tranter, R. S.; Brezinsky, K. *Journal of Physical Chemistry A* **2006**, *110*, 9388.
- (165) Sivaramakrishnan, R.; Tranter, R. S.; Brezinsky, K. *Journal of Physical Chemistry A* **2006**, *110*, 9400.
- (166) Smith, R. D. *Journal of Physical Chemistry* **1979**, *83*, 1553.
- (167) Badger, G. M.; Spotswood, T. M. *Journal of the Chemical Society* **1960**, 4420.
- (168) Errede, L. A.; Cassidy, J. P. *Journal of the American Chemical Society* **1960**, *82*, 3653.
- (169) Szwarc, M. *J. Chem. Phys.* **1948**, *16*, 128.
- (170) Brouwer, L. D.; Muller-Markgraf, W.; Troe, J. *Journal of Physical Chemistry* **1988**, *92*, 4905.
- (171) Eng, R. A.; Gebert, A.; Goos, E.; Hippler, H.; Kachiani, C. *Physical Chemistry Chemical Physics* **2002**, *4*, 3989.
- (172) Rao, V. S.; Skinner, G. B. *Journal of Physical Chemistry* **1989**, *93*, 1864.
- (173) Sivaramakrishnan, R.; Michael, J. V. *Proceedings of the Combustion Institute* **2011**, *33*, 225.
- (174) Cavallotti, C.; Mancarella, S.; Rota, R.; Carra, S. *Journal of Physical Chemistry A* **2007**, *111*, 3959.
- (175) Jarzecki, A. A.; Gajewski, J.; Davidson, E. R. *Journal of the American Chemical Society* **1999**, *121*, 6928.
- (176) Moon, J. H.; Choe, J. C.; Kim, M. S. *Journal of Physical Chemistry A* **2000**, *104*, 458.
- (177) Frochtenicht, R.; Hippler, H.; Troe, J.; Toennies, J. P. *Journal of Photochemistry and Photobiology, A: Chemistry* **1994**, *80*, 33.
- (178) Hippler, H.; Riehn, C.; Troe, J.; Weitzel, K. M. *Journal of Physical Chemistry* **1990**, *94*, 6321.
- (179) Oehlschlaeger, M. A.; Davidson, D. F.; Hanson, R. K. *Journal of Physical Chemistry A* **2006**, *110*, 6649.
- (180) Cavallotti, C.; Derudi, M.; Rota, R. *Proceedings of the Combustion Institute* **2009**, *32*, 115.
- (181) da Silva, G.; Cole, J. A.; Bozzelli, J. W. *Journal of Physical Chemistry A* **2009**, *113*, 6111.
- (182) Dettelleux, V.; Vandoooren, J. *Journal of Physical Chemistry A* **2009**, *113*, 10913.
- (183) Polino, D.; Famulari, A.; Cavallotti, C. *Journal of Physical Chemistry A* **2011**, *115*, 7928.
- (184) Polino, D.; Cavallotti, C. *Journal of Physical Chemistry A* **2011**, *115*, 10281.
- (185) da Silva, G.; Bozzelli, J. W. *Journal of Physical Chemistry A* **2009**, *113*, 12045.
- (186) Sivaramakrishnan, R.; Su, M.-C.; Michael, J. V. *Proceedings of the Combustion Institute* **2011**, *33*, 243.
- (187) Derudi, M.; Polino, D.; Cavallotti, C. *Physical Chemistry Chemical Physics* **2011**, *13*, 21308.
- (188) Ditchfield, R.; Hehre, W. J.; Pople, J. A. *J. Chem. Phys.* **1971**, *54*, 724.
- (189) Peng, C. Y.; Ayala, P. Y.; Schlegel, H. B.; Frisch, M. J. *Journal of Computational Chemistry* **1996**, *17*, 49.
- (190) Woon, D. E.; Dunning, T. H. *J. Chem. Phys.* **1995**, *103*, 4572.
- (191) Werner, H. J.; Knowles, P. J. *J. Chem. Phys.* **1988**, *89*, 5803.
- (192) Johnson, R. P. *Chemical Reviews* **1989**, *89*, 1111.
- (193) Brown, W. T.; Jones, W. M. *Journal of Organic Chemistry* **1979**, *44*, 3090.
- (194) Harris, J. W.; Jones, W. M. *Journal of the American Chemical Society* **1982**, *104*, 7329.

- (195) Billups, W. E.; Lin, L. P.; Chow, W. Y. *Journal of the American Chemical Society* **1974**, *96*, 4026.
- (196) Wentrup, C.; Wilczek, K. *Helvetica Chimica Acta* **1970**, *53*, 1459.
- (197) Schissel, P.; Kent, M. E.; McAdoo, D. J.; Hedaya, E. *Journal of the American Chemical Society* **1970**, *92*.
- (198) West, P. A.; Chapman, O. L.; LeRoux, J.-P. *Journal of the American Chemical Society* **1982**, *104*, 1779.
- (199) McMahon, R. J.; Abelt, C. J.; Chapman, O. L.; Johnson, J. W.; Kreil, C. L.; Leroux, J. P.; Mooring, A. M.; West, P. R. *Journal of the American Chemical Society* **1987**, *109*, 2456.
- (200) Chapman, O. L.; LeRoux, J. P. *Journal of the American Chemical Society* **1978**, *100*, 282.
- (201) Wong, M. W.; Wentrup, C. *Journal of Organic Chemistry* **1996**, *61*, 7022.
- (202) Schreiner, P. R.; Karney, W. L.; Schleyer, P. V.; Borden, W. T.; Hamilton, T. P.; Schaefer, H. F. *Journal of Organic Chemistry* **1996**, *61*, 7030.
- (203) Matzinger, S.; Bally, T.; Patterson, E. V.; McMahon, R. J. *Journal of the American Chemical Society* **1996**, *118*, 1535.
- (204) Platz, M. S. *Accounts Chem. Res.* **1995**, *28*, 487.
- (205) Nguyen, T. L.; Kim, G. S.; Mebel, A. M.; Nguyen, M. T. *Chemical Physics Letters* **2001**, *349*, 571.
- (206) Wentrup, C. *Topics in Current Chemistry* **1976**, *62*, 173.
- (207) Joines, R. C.; Turner, A. B.; Jones, W. M. *Journal of the American Chemical Society* **1969**, *91*, 7754.
- (208) Jones, W. M.; Ennis, C. L. *Journal of the American Chemical Society* **1967**, *89*, 3069.
- (209) Mukai, T.; Nakazawa, T.; Isobe, K. *Tetrahedron Letters* **1968**, *9*, 565.
- (210) Tyner, R. L.; Jones, W. M.; Ohm, Y.; Sabin, J. R. *Journal of the American Chemical Society* **1974**, *96*, 3765.
- (211) Bofill, J. M.; Bru, N.; Farras, J.; Olivella, S.; Sole, A.; Vilarrasa, J. *Journal of the American Chemical Society* **1988**, *110*, 3740.
- (212) Collins, C. L.; Davy, R. D.; Schaefer, H. F. *Chemical Physics Letters* **1990**, *171*, 259.
- (213) Wentrup, C.; Muller, P. *Tetrahedron Letters* **1973**, *14*, 2915.
- (214) Acosta-Silva, C.; Branchadell, V. *Theoretical Chemistry Accounts* **2009**, *123*, 59.
- (215) Sakai, S. *Journal of Molecular Structure-Theochem* **2003**, *630*, 177.
- (216) Shin, K. S.; Michael, J. V. *The Journal of Physical Chemistry* **1991**, *95*, 5864.
- (217) Hippler, H.; Troe, J.; Wendelken, H. J. *J. Chem. Phys.* **1983**, *78*, 6709.
- (218) Jones, J.; Bacskay, G. B.; Mackie, J. C. *Journal of Physical Chemistry A* **1997**, *101*, 7105.
- (219) Harding, L. B.; Klippenstein, S. J.; Georgievskii, Y. *Journal of Physical Chemistry A* **2007**, *111*, 3789.
- (220) Ranzi, E.; Frassoldati, A.; Granata, S.; Faravelli, T. *Industrial & Engineering Chemistry Research* **2005**, *44*, 5170.
- (221) Wang, H.; Laskin, A.; Moriarty, N. W.; Frenklach, M. *Proceedings of the Combustion Institute* **2000**, *28*, 1545.
- (222) Kern, R. D.; Zhang, Q.; Yao, J.; Jursic, B. S.; Tranter, R. S.; Greybill, M. A.; Kiefer, J. H. *Proceedings of the Combustion Institute* **1998**, *27*, 143.
- (223) Ranzi, E.; Faravelli, T. *User's Manual Dsmoke Program, Release 6.0, CMIC Politecnico di Milano, 2006*. <http://creckmodeling.chem.polimi.it>.
- (224) Moskaleva, L. V.; Madden, L. K.; Lin, M. C. *Physical Chemistry Chemical Physics* **1999**, *1*, 3967.
- (225) Zhang, L. D.; Cai, J. G.; Zhang, T. C.; Qi, F. *Combustion and Flame* **2010**, *157*, 1686.
- (226) Polino, D.; Cavallotti, C. **2011, in press**.
- (227) Deng, W.-Q.; Han, K.-L.; Zhan, J.-P.; He, G.-Z. *Chemical Physics Letters* **1998**, *288*, 33.
- (228) Burcat, A.; Dvinyaninov, M. *International Journal of Chemical Kinetics* **1997**, *29*, 505.
- (229) Roy, K.; Braun-Unkhoff, M.; Frank, P.; Just, T. *International Journal of Chemical Kinetics* **2001**, *33*, 821.
- (230) Tokmakov, I. V.; Moskaleva, L. V.; Lin, M. C. *International Journal of Chemical Kinetics* **2004**, *36*, 139.

- (231) Melius, C. F.; Colvin, M. E.; Marinov, N. M.; Pitz, W. J.; Senkan, S. M. *Proceedings of the Combustion Institute* **1996**, *26*, 685.
- (232) Moskaleva, L. V.; Mebel, A. M.; Lin, M. C. *Proceedings of the Combustion Institute* **1996**, *26*, 521.
- (233) Sharma, S.; Green, W. H. *Journal of Physical Chemistry A* **2009**, *113*, 8871.
- (234) Ikeda, E.; Tranter, R. S.; Kiefer, J. H.; Kern, R. D.; Singh, H. J.; Zhang, Q. *Proceedings of the Combustion Institute* **2000**, *28*, 1725.
- (235) Bacskay, G. B.; Mackie, J. C. *Physical Chemistry Chemical Physics* **2001**, *3*, 2467.
- (236) Knyazev, V. D.; Slagle, I. R. *Journal of Physical Chemistry A* **2002**, *106*, 5613.
- (237) Moskaleva, L. V.; Lin, M. C. *Journal of Computational Chemistry* **2000**, *21*, 415.
- (238) Fascella, S.; Cavallotti, C.; Rota, R.; Carra, S. *Journal of Physical Chemistry A* **2005**, *109*, 7546.
- (239) da Silva, G.; Cole, J. A.; Bozzelli, J. W. *Journal of Physical Chemistry A*, *114*, 2275.
- (240) Wang, D.; Violi, A.; Kim, D. H.; Mullholland, J. A. *Journal of Physical Chemistry A* **2006**, *110*, 4719.
- (241) Kislov, V. V.; Mebel, A. M. *Journal of Physical Chemistry A* **2007**, *111*, 9532.
- (242) Kislov, V. V.; Mebel, A. M. *Journal of Physical Chemistry A* **2008**, *112*, 700.
- (243) Mebel, A. M.; Kislov, V. V. *Journal of Physical Chemistry A* **2009**, *113*, 9825.
- (244) Castaldi, M. J.; Marinov, N. M.; Melius, C. F.; Huang, J. M.; Senkan, S. M.; Pitz, W. J.; Westbrook, C. K. *Proceedings of the Combustion Institute* **1996**, 693.
- (245) Marinov, N. M.; Pitz, W. J.; Westbrook, C. K.; Vincitore, A. M.; Castaldi, M. J.; Senkan, S. M.; Melius, C. F. *Combustion and Flame* **1998**, *114*, 192.
- (246) Goldaniga, A.; Faravelli, T.; Ranzi, E. *Combustion and Flame* **2000**, *122*, 350.
- (247) Lindstedt, P.; Maurice, L.; Meyer, M. *Faraday Discussions* **2001**, *119*, 409.
- (248) Richter, H.; Howard, J. B. *Progress in Energy and Combustion Science* **2000**, *26*, 565.
- (249) Butler, R. G.; Glassman, I. *Proceedings of the Combustion Institute* **2009**, *32*, 395.
- (250) Kim, D. H.; Mullholland, J. A.; Wang, D.; Violi, A. *Journal of Physical Chemistry A* **2010**, *114*, 12411.
- (251) Werner, H.-J.; Manby, F. R.; Knowles, P. J. *J. Chem. Phys.* **2003**, *118*, 8149.
- (252) Wood, G. P. F.; Radom, L.; Petersson, G. A.; Barnes, E. C.; Frisch, M. J.; Montgomery, J. A. *J. Chem. Phys.* **2006**, *125*, 094106.
- (253) Montgomery Jr., J. A.; Frisch, M. J.; Ochterski, J. W.; Petersson, G. A. *J. Chem. Phys.* **1999**, *110*, 2822.
- (254) Katzer, G.; Sax, A. F. *J. Chem. Phys.* **2002**, *117*, 8219.
- (255) Kiefer, J. H.; Tranter, R. S.; Wang, H.; Wagner, A. F. *International Journal of Chemical Kinetics* **2001**, *33*, 834.
- (256) Ranzi, E.; Dente, M.; Goldaniga, A.; Bozzano, G.; Faravelli, T. *Progress in Energy and Combustion Science* **2001**, *27*, 99.
- (257) Ranzi, E. *Energy & Fuels* **2006**, *20*, 1024.
- (258) Kee, R. J.; Rupley, F.; Miller, J. A. "Chemkin II: A Fortran Chemical Kinetics Package for the Analysis of Gas-Phase Chemical Kinetics," Sandia National Laboratories, 1989.
- (259) Goos, E.; Burcat, A.; Ruscic, B. "Third Millennium Thermodynamic Database for Combustion and Air Pollution Use," <http://garfield.chem.elte.hu/Burcat/BURCAT.THR>, 2009.
- (260) Benson, S. W. *Thermochemical Kinetics (2nd edition)*; Wiley: New York, 1976.
- (261) POLIMI\_1111 "Kinetic version 2011, November," <http://creckmodeling.chem.polimi.it>, 2011.
- (262) Cuoci, A.; Frassoldati, A.; Faravelli, T.; Ranzi, E. OpenSMOKE: Numerical Modeling of Reacting Systems with Detailed Kinetic Mechanisms. In *XXXIV Meeting of the Italian Section of the Combustion Institute Rome (Italy)*, 2011.
- (263) Buzzi-Ferraris, G. BzzMath 6.0 Numerical Libraries. Available at: <http://homes.chem.polimi.it/gbuzzi/index.htm>, 2010.
- (264) Cavallotti, C.; Polino, D.; Frassoldati, A.; Ranzi, E. *The Journal of Physical Chemistry A* **2012**, *116*, 3313.

- (265) Vereecken, L.; Bettinger, H. F.; Peeters, J. *Physical Chemistry Chemical Physics* **2002**, *4*, 2019.
- (266) Hippler, H.; Otto, B.; Troe, J. *Berichte der Bunsen-Gesellschaft fuer Physikalische Chemie* **1989**, *93*, 428.
- (267) Miller, J. A.; Klippenstein, S. J. *Journal of Physical Chemistry A* **2003**, *107*, 7783.
- (268) Dudek, D.; Glanzer, K.; Troe, J. *Berichte der Bunsen-Gesellschaft fuer Physikalische Chemie* **1979**, *83*, 776.
- (269) Mc Lean, S.; Haynes, P. *Tetrahedron Letters* **1964**, *5*, 2385.
- (270) Alder, R. W.; East, S. P.; Harvey, J. N.; Oakley, M. T. *Journal of the American Chemical Society* **2003**, *125*, 5375.
- (271) Cavallotti, C.; Polino, D. *Proceedings of the Combustion Institute* **2013**, in press.
- (272) Robinson, R. K.; Lindstedt, R. P. *Combustion and Flame* **2011**, *158*, 666.
- (273) Butler, R. G. *Combustion Chemistry of 1–3 Cyclopentadiene*, Ph.D. thesis, Princeton University, Princeton, NJ, 2001.
- (274) Zhao, Z.; Chaos, M.; Kazakov, A.; Dryer, F. L. *International Journal of Chemical Kinetics* **2008**, *40*, 1.
- (275) Tsang, W.; McGivern, W. S.; Manion, J. A. *Proceedings of the Combustion Institute* **2009**, *32*, 131.
- (276) Tsang, W.; Walker, J. A.; Manion, J. A. *Proceedings of the Combustion Institute* **2007**, *31*, 141.
- (277) Tsang, W.; Walker, J. A.; Manion, J. A. *Symposium (International) on Combustion* **1998**, *27*, 135.
- (278) Sirjean, B.; Dames, E.; Wang, H.; Tsang, W. *The Journal of Physical Chemistry A* **2011**, *116*, 319.
- (279) Wu, T.; Werner, H.-J.; Manthe, U. *Science* **2004**, *306*, 2227.
- (280) Sutherland, J. W.; Su, M. C.; Michael, J. V. *International Journal Of Chemical Kinetics* **2001**, *33*, 669.
- (281) Berlie, M. R.; Roy, D. J. L. *Canadian Journal of Chemistry* **1954**, *32*, 650.
- (282) Fenimore, C. P.; Jones, G. W. *The Journal of Physical Chemistry* **1961**, *65*, 2200.
- (283) Gorban, N. I.; Nalbandyan, A. B. *Russian Journal of Physical Chemistry* **1962**, *36*, 946.
- (284) Jamieson, J. W. S.; Brown, G. R. *Canadian Journal of Chemistry* **1964**, *42*, 1638.
- (285) Lawrence, R. H.; Firestone, R. F. *Journal of the American Chemical Society* **1966**, *88*, 4564.
- (286) Azatyan, V. V. *Arm. Khim. Zh.* **1967**, *20*, 577.
- (287) Kurylo, M. J.; Timmons, R. B. *The Journal of Chemical Physics* **1969**, *50*, 5076.
- (288) Kurylo, M. J.; Hollinden, G. A.; Timmons, R. B. *The Journal of Chemical Physics* **1970**, *52*, 1773.
- (289) Baker, R. R.; Baldwin, R. R.; Walker, R. W. *Symposium (International) on Combustion* **1971**, *13*, 291.
- (290) Roth, P.; Just, T. *Berichte der Bunsengesellschaft für physikalische Chemie* **1975**, *79*, 682.
- (291) Biordi, J. C.; Lazzara, C. P.; Papp, J. F. *Journal Name: Combust. Flame; (United States); Journal Volume: 26:1* **1976**, Medium: X; Size: Pages: 57.
- (292) Roth, P.; Just, T. H. *Natl. Bur. Stand. Spec. Publ. (U.S.)* **1979**, *10*, 1339.
- (293) Sepehrad, A.; Marshall, R. M.; Purnell, H. *Journal of the Chemical Society, Faraday Transactions 1: Physical Chemistry in Condensed Phases* **1979**, *75*, 835.
- (294) Roth, P. *Forsch Ing-Wes* **1980**, *46*, 93.
- (295) Rabinowitz, M. J.; Sutherland, J. W.; Patterson, P. M.; Klemm, R. B. *The Journal of Physical Chemistry* **1991**, *95*, 674.
- (296) Marquaire, P.-M.; Dastidar, A. G.; Manthorne, K. C.; Pacey, P. D. *Canadian Journal of Chemistry* **1994**, *72*, 600.
- (297) Baeck, H. J.; Shin, K. S.; Yang, H.; Qin, Z.; Lissianski, V.; Gardiner, W. C. *The Journal of Physical Chemistry* **1995**, *99*, 15925.
- (298) Bryukov, M. G.; Slagle, I. R.; Knyazev, V. D. *The Journal of Physical Chemistry A* **2001**, *105*, 3107.

- (299) Corchado, J. C.; Bravo, J. L.; Espinosa-Garcia, J. *The Journal of Chemical Physics* **2009**, *130*, 184314.
- (300) Espinosa-Garcia, J. *The Journal of Chemical Physics* **2002**, *116*, 10664.
- (301) Espinosa-Garcia, J.; Nyman, G.; Corchado, J. C. *The Journal of Chemical Physics* **2009**, *130*, 184315.
- (302) Pu, J.; Corchado, J. C.; Truhlar, D. G. *The Journal of Chemical Physics* **2001**, *115*, 6266.
- (303) Pu, J.; Truhlar, D. G. *The Journal of Chemical Physics* **2002**, *116*, 1468.
- (304) Pu, J.; Truhlar, D. G. *The Journal of Chemical Physics* **2002**, *117*, 1479.
- (305) Pu, J.; Truhlar, D. G. *The Journal of Chemical Physics* **2002**, *117*, 10675.
- (306) Zhao, Y.; Yamamoto, T.; Miller, W. H. *The Journal of Chemical Physics* **2004**, *120*, 3100.
- (307) Andersson, S.; Nyman, G.; Arnaldsson, A.; Manthe, U.; Jónsson, H. *The Journal of Physical Chemistry A* **2009**, *113*, 4468.
- (308) Huarte-Larranaga, F.; Manthe, U. *The Journal of Chemical Physics* **2000**, *113*, 5115.
- (309) Huarte-Larranaga, F.; Manthe, U. *The Journal of Chemical Physics* **2002**, *116*, 2863.
- (310) Schiffel, G.; Manthe, U. *The Journal of Chemical Physics* **2010**, *132*, 084103.
- (311) Huarte-Larrañaga, F.; Manthe, U. *The Journal of Physical Chemistry A* **2001**, *105*, 2522.
- (312) Suleimanov, Y. V.; Collepardo-Guevara, R.; Manolopoulos, D. E. *The Journal of Chemical Physics* **2011**, *134*, 044131.
- (313) Kerkeni, B.; Clary, D. C. *The Journal of Chemical Physics* **2004**, *120*, 2308.
- (314) Wang, D.; Bowman, J. M. *The Journal of Chemical Physics* **2001**, *115*, 2055.
- (315) Wang, M. L.; Zhang, J. Z. H. *The Journal of Chemical Physics* **2002**, *117*, 3081.
- (316) Yang, M.; Zhang, D. H.; Lee, S.-Y. *The Journal of Chemical Physics* **2002**, *117*, 9539.
- (317) Yu, H.-G.; Nyman, G. *The Journal of Chemical Physics* **1999**, *111*, 3508.
- (318) Zhang, L.; Lu, Y.; Lee, S.-Y.; Zhang, D. H. *The Journal of Chemical Physics* **2007**, *127*, 234313.
- (319) Palma, J.; Echave, J.; Clary, D. C. *The Journal of Physical Chemistry A* **2002**, *106*, 8256.
- (320) von Horsten, H. F.; Banks, S. T.; Clary, D. C. *The Journal of Chemical Physics* **2011**, *135*, 094311.
- (321) Adamo, C.; Barone, V. *The Journal of Chemical Physics* **1998**, *108*, 664.
- (322) Boese, A. D.; Martin, J. M. L. *The Journal of Chemical Physics* **2004**, *121*, 3405.
- (323) Chai, J.-D.; Head-Gordon, M. *Physical Chemistry Chemical Physics* **2008**, *10*, 6615.
- (324) Head-Gordon, M.; Pople, J. A.; Frisch, M. J. *Chemical Physics Letters* **1988**, *153*, 503.
- (325) McLean, A. D.; Chandler, G. S. *The Journal of Chemical Physics* **1980**, *72*, 5639.
- (326) Krishnan, R.; Binkley, J. S.; Seeger, R.; Pople, J. A. *The Journal of Chemical Physics* **1980**, *72*, 650.
- (327) Dunning, J. T. H. *The Journal of Chemical Physics* **1989**, *90*, 1007.
- (328) Hratchian, H. P.; Schlegel, H. B. *The Journal of Chemical Physics* **2004**, *120*, 9918.
- (329) Hratchian, H. P.; Schlegel, H. B. *Journal of Chemical Theory and Computation* **2004**, *1*, 61.
- (330) Page, M.; Doubleday, C.; McIver, J. J. W. *The Journal of Chemical Physics* **1990**, *93*, 5634.
- (331) Truhlar, D. G.; Isaacson, A. D.; Garrett, B. C. Generalized Transition State Theory. In *Theory of Chemical Reaction Dynamics*; Baer, M., Ed.; CRC Press: Boca Raton, FL, 1985; Vol. 4; pp 65.
- (332) Miller, J. A.; Melius, C. F. *Combustion and Flame* **1992**, *91*, 21.
- (333) Leung, K. M.; Lindstedt, R. P. *Combustion and Flame* **1995**, *102*, 129.
- (334) Fournet, R.; Bauge, J. C.; Battin-Leclerc, F. *International Journal of Chemical Kinetics* **1999**, *31*, 361.
- (335) Pope, C. J.; Miller, J. A. *Proceedings of the Combustion Institute* **2000**, *28*, 1519.
- (336) Richter, H.; Howard, J. B. *Physical Chemistry Chemical Physics* **2002**, *4*, 2038.
- (337) Dias, V.; Vandooren, J. *Combustion and Flame* **2011**, *158*, 848.
- (338) Miller, J. A.; Klippenstein, S. J.; Georgievskii, Y.; Harding, L. B.; Allen, W. D.; Simmonett, A. C. *Journal of Physical Chemistry A* **2010**, *114*, 4881.

- (339) Georgievskii, Y.; Miller, J. A.; Klippenstein, S. J. *Physical Chemistry Chemical Physics* **2007**, *9*, 4259.
- (340) Hansen, N.; Li, W.; Law, M. E.; Kasper, T.; Westmoreland, P. R.; Yang, B.; Cool, T. A.; Lucassen, A. *Physical Chemistry Chemical Physics* **2010**, *12*, 12112.
- (341) Hansen, N.; Miller, J. A.; Kasper, T.; Kohse-Höinghaus, K.; Westmoreland, P. R.; Wang, J.; Cool, T. A. *Proceedings of the Combustion Institute* **2009**, *32*, 623.
- (342) McEnally, C. S.; Pfefferle, L. D.; Atakan, B.; Kohse-Höinghaus, K. *Prog. Energy Combust. Sci.* **2006**, *32*, 247.
- (343) Cavallotti, C.; Derudi, M.; Rota, R. *Proceedings of the Combustion Institute* **2009**, *32*, 115.
- (344) Braun-Unkloff, M.; Frank, P.; Just, T. *Berichte der Bunsen-Gesellschaft fuer Physikalische Chemie* **1990**, *94*, 1417.
- (345) Hippler, H.; Reihs, C.; Troe, J. *Zeitschrift fuer Physikalische Chemie (Muenchen, Germany)* **1990**, *167*, 1.
- (346) Matsugi, A.; Miyoshi, A. *International Journal of Chemical Kinetics* **2012**, *44*, 206.
- (347) Slavinskaya, N. A.; Frank, P. *Combustion and Flame* **2009**, *156*, 1705.
- (348) Jensen, P.; Bunker, P. R. *J. Chem. Phys.* **1988**, *89*, 1327.
- (349) Pilling, M. J. *Proceedings of the Combustion Institute* **2009**, *32*, 27.
- (350) Bauschlicher, C. W.; Haber, K.; Schaefer, H. F.; Bender, C. F. *Journal of the American Chemical Society* **1977**, *99*, 3610.
- (351) Guadagnini, R.; Schatz, G. C.; Walch, S. P. *Journal of Physical Chemistry A* **1998**, *102*, 5857.
- (352) Frankcombe, T. J.; Smith, S. C. *Faraday Discussions* **2001**, *119*, 159.
- (353) Yu, H. G.; Muckerman, J. T. *Journal of Physical Chemistry A* **2005**, *109*, 1890.
- (354) Canosamas, C. E.; Frey, H. M.; Walsh, R. *Journal of the Chemical Society-Faraday Transactions II* **1985**, *81*, 283.
- (355) Hack, W.; Koch, M.; Wagner, H. G.; Wilms, A. *Berichte der Bunsen-Gesellschaft fuer Physikalische Chemie* **1988**, *92*, 674.
- (356) Wagener, R. *Zeitschrift fuer Naturforschung, A: Physical Sciences* **1990**, *45*, 649.
- (357) Hayes, F.; Gutsche, G. J.; Lawrance, W. D.; Staker, W. S.; King, K. D. *Combustion and Flame* **1995**, *100*, 653.
- (358) Adamson, J. D.; Morter, C. L.; DeSain, J. D.; Glass, G. P.; Curl, R. F. *Journal of Physical Chemistry* **1996**, *100*, 2125.
- (359) Hayes, F.; Lawrance, W. D.; Staker, W. S.; King, K. D. *Journal of Physical Chemistry* **1996**, *100*, 11314.
- (360) Blitz, M. A.; Beasley, M. S.; Pilling, M. J.; Robertson, S. H. *Physical Chemistry Chemical Physics* **2000**, *2*, 805.
- (361) Davis, H. F.; Shu, J. N.; Peterka, D. S.; Ahmed, M. *J. Chem. Phys.* **2004**, *121*, 6254.
- (362) Gannon, K. L.; Blitz, M. A.; Liang, C. H.; Pilling, M. J.; Seakins, P. W.; Glowacki, D. R. *Journal of Physical Chemistry A* **2010**, *114*, 9413.
- (363) Bohland, T.; Temps, F.; Wagner, H. G. *Berichte der Bunsen-Gesellschaft fuer Physikalische Chemie* **1985**, *89*, 1013.
- (364) Gordon, M. S.; Nguyen, K. A.; Truhlar, D. G. *Journal of Physical Chemistry* **1989**, *93*, 7356.
- (365) Gordon, M. S.; Truhlar, D. G. *Journal of the American Chemical Society* **1986**, *108*, 5412.
- (366) Gordon, M. S.; Truhlar, D. G. *International Journal of Quantum Chemistry* **1987**, *31*, 81.
- (367) Langford, A. O.; Petek, H.; Moore, C. B. *J. Chem. Phys.* **1983**, *78*, 6650.
- (368) Hack, W.; Koch, M.; Wagener, R.; Wagner, H. G. *Berichte der Bunsen-Gesellschaft fuer Physikalische Chemie* **1989**, *93*, 165.
- (369) Staker, W. S.; King, K. D.; Gutsche, G. J.; Lawrance, W. D. *Journal of the Chemical Society-Faraday Transactions* **1991**, *87*, 2421.
- (370) Koch, M.; Temps, F.; Wagener, R.; Wagner, H. G. *Berichte der Bunsen-Gesellschaft fuer Physikalische Chemie* **1990**, *94*, 645.
- (371) Gannon, K. L.; Blitz, M. A.; Liang, C.-H.; Pilling, M. J.; Seakins, P. W.; Glowacki, D. R.; Harvey, J. N. *Faraday Discussions* **2010**, *147*, 173.

## References

---

- (372) Gannon, K. L.; Blitz, M. A.; Kovacs, T.; Pilling, M. J.; Seakins, P. W. *J. Chem. Phys.* **2010**, *132*.
- (373) Dunning, T. H. *J. Chem. Phys.* **1989**, *90*, 1007.
- (374) Martin, J. M. L.; Uzan, O. *Chemical Physics Letters* **1998**, *282*, 16.
- (375) MRCC, a string-based quantum chemical program suite written by M. Kállay. See also M. Kállay, P. R. Surján, *J. Chem. Phys.* 115 2945 (2001) as well as: [www.mrcc.hu](http://www.mrcc.hu).